Control of As and Cr speciation by reactive iron mineral-mediated redox reactions: Development of in situ remediation methods

Einfluss redox-reaktiver Eisenminerale auf die Speziationen von Arsen und Chrom: Entwicklung von in situ Sanierungsmethoden

Zur Erlangung des akademischen Grades eines
DOKTORS DER NATURWISSENSCHAFTEN (Dr. rer. Nat.)
von der KIT-Fakultät für
Bauingenieur-, Geo- und Umweltwissenschaften

des Karlsruher Instituts für Technologie (KIT)
genehmigte
DISSERTATION
von
M.Sc.-Umweltwissenschaften Andrew Thomas
M.Sc. Environmental Sciences, University of Arizona

Tag der mündlichen Prüfung: 31.07.2020

Referent: Prof. Dr. Thomas Neumann
Korreferent: Prof. Dr. Jochen Kolb

Karlsruhe (2020)

Erklärung

Hiermit erkläre ich, dass ich die vorliegende Dissertation, abgesehen von der Benutzung der von mir vollständig und genau bezeichneten Hilfsmittel, selbstständig verfasst und die Grundsätze des Karlsruher Instituts für Technologie (KIT) zur Sicherung guter wissenschaftlicher Praxis in ihrer aktuell gültigen Fassung beachtet habe.

Karlsruhe den _____

gez. Andrew Thomas

Preliminary Statement and Attached Publications

   This dissertation consists of 4 scientific papers, including two first-author publications and two to which I made second-author contributions, as well as a summary of the results obtained. The publication references and author contributions are summarized below, while the full texts can be found in this dissertation's appendix.

First-author Scientific Publications

Thomas, A., Eiche, E., Göttlicher, J., Steininger, R., G. Benning, L., M. Freeman, H., … Neumann, T. (2018). **Products of Hexavalent Chromium Reduction by Green Rust Sodium Sulfate and Associated Reaction Mechanisms.** *Soil Systems*, *2*(4), 58. https://doi.org/10.3390/soilsystems2040058

Authorship Statement: This peer-reviewed scientific article was written by me and based on lab experiments performed from February to November 2017 at the Institute for Applied Geosciences at Karlsruhe Institute of Technology, the ANKA synchrotron facility in Eggenstein-Leopoldshafen, Germany, and the Interface Geochemistry group at the Geoforschungszentrum in Potsdam, Germany. I was responsible for conducting the experiments with green rust at KIT and sample preparation and analysis during XAS beamtime at ANKA, in addition to synthesis of mineral reference standards with the help of Nadine Wittmann. In addition, I assisted with sample preparation and imaging while performing transmission electron microscopy (TEM) analyses at GFZ. Elisabeth Eiche and Thomas Neumann provided lab space at KIT as well as assistance with planning of the experiments, interpretation of the results of X-ray absorption spectroscopy, X-ray diffraction and electron microscopy analyses, and review of this publication. Jörg Göttlicher and Ralph Steininger were responsible for maintaining and running the SUL-X beamline at ANKA during measurements. Liane Benning provided lab space and access to the TEM instrument

at GFZ, while Helen Freeman assisted with TEM imaging and other analyses. Knud

Dideriksen assisted with interpretation of all results and elucidation of the mechanism of

action. All authors critically-reviewed this manuscript and agreed to its publication.

Thomas, A. N., Eiche, E., Göttlicher, J., Steininger, R., Benning, L. G., Freeman, H. M., … Neumann, T.

(2020). **Effects of metal cation substitution on hexavalent chromium reduction by green rust**.

Geochemical Transactions, *21*(1), 2. https://doi.org/10.1186/s12932-020-00066-8

Authorship statement: This publication, currently in preparation, was written by me based

on experiments performed between August 2018 and August 2019 at the Institute for Applied

Geosciences at Karlsruhe Institute of Technology, the ANKA synchrotron facility in

Eggenstein-Leopoldshafen, Germany, the Nanogeoscience Center at Copenhagen University,

and the Interface Geochemistry group at the Geoforschungszentrum in Potsdam, Germany. I

was responsible for conducting the experiments with green rust at KIT and sample

preparation and analysis during XAS beamtime at ANKA. In addition, I assisted with sample

preparation and imaging while performing transmission electron microscopy (TEM) analyses

at GFZ and scanning electron microscopy (SEM) measurements at Copenhagen University.

Other analyses performed at KIT include X-ray diffraction (XRD) measurements with

assistance from Beate Oetzel and ICP-OES measurements with assistance from Gesine Preuß.

Elisabeth Eiche and Thomas Neumann provided lab space and KIT as well as assistance

planning of the experiments, interpretation of the results of X-ray absorption spectroscopy,

X-ray diffraction and electron microscopy analyses and review of this publication. Jörg

Göttlicher and Ralph Steininger were responsible for maintaining and running the SUL-X

beamline at ANKA during measurements. Liane Benning provided lab space and access to

the TEM instrument at GFZ, while Helen Freeman assisted with TEM imaging and other

analyses. Dominique Tobler provided lab space at KU in order to continue experiments, and Marco Mangayayam performed high-energy scattering analyses of selected samples. Knud Dideriksen assisted with interpretation of all results and elucidation of the mechanism of action. All authors critically-reviewed this manuscript and agreed to its publication.

Coauthored Scientific Publications

Perez, J. P. H., Tobler, D. J., **Thomas, A. N.**, Freeman, H. M., Dideriksen, K., Radnik, J., & Benning, L. G. (2019). **Adsorption and Reduction of Arsenate during the Fe^{2+}-Induced Transformation of Ferrihydrite**. *ACS Earth and Space Chemistry*, *3*(6), 884–894. https://doi.org/10.1021/acsearthspacechem.9b00031

Authorship Statement: This peer-reviewed scientific article is based on laboratory experiments performed by Jeffrey Paulo Perez in 2019. My contribution consisted of planning and carrying out XAS experiments at ANKA, as well as processing and analysis of the data generated in these investigations. Overall, my contribution to this publication is approximately 15%.

Wang, H.Y., Byrne, J.M., Perez, J.P.H., **Thomas, A.N.**, Göttlicher, J., Höfer, H.E., Mayanna, S., Kontny, A., Kappler, A., Guo, H.M., and others (2020) **Arsenic sequestration in pyrite and greigite in the buried peat of As-contaminated aquifers.** Geochimica et Cosmochimica Acta, 284, 107–119.

Authorship Statement: This peer-reviewed scientific article is based on laboratory experiments performed by Hongyan Wang in 2018 and 2019. My contribution consisted of planning and carrying out XAS experiments at ANKA, as well as processing and analysis of the data generated in these investigations. Overall, my contribution to this publication is approximately 15%.

Abstract

  Arsenic and chromium are elemental contaminants often introduced into soil and groundwater from an array of natural and anthropogenic sources. Because of their distributions and serious consequences for human health, both arsenic and chromium are considered contaminants of concern by environmental authorities in the United States and European Union and therefore are targets for soil and groundwater remediation. Remediation using pump-and-treat methods is effective but costly; *in situ* methods can remediate contamination without requiring its removal from the site, and therefore can decrease these costs substantially if applied effectively. As metallic and metalloid contaminants cannot be broken down into less toxic forms, *in situ* methods can take advantage of differences in mobility and toxicity between oxidation states of each substance and reduce or oxidize chromium and/or arsenic to a less toxic and/or less mobile state. Knowledge of the reaction mechanisms governing these redox transformations is essential to their successful application in the field. In the original research studies presented in this dissertation, other researchers and I investigated the behavior of arsenic and chromium in contact with redox-active Fe and Mn mineral surfaces in laboratory experiments. These studies resulted in three papers (Thomas et al. 2018, Perez et al. 2019, Thomas et al. 2020). In addition, As-contaminated peat samples obtained from a dry paleolake basin in China were characterized in order to determine the ultimate fate of As following diagenesis in various redox environments (Wang et al. 2020).

  Between 2016 and 2019, I carried out a series of laboratory experiments examining the reduction of hexavalent chromium to its more benign trivalent form by green rust sulfate, a layered Fe(II, III) hydroxide mineral. First, pure green rust sulfate was reacted with hexavalent chromium at a range of concentrations typical of groundwater contaminant plumes in order to determine the effect of chromium concentration on the eventual Cr carrier phase following the reaction, as determined by X-ray absorption spectroscopy (XAS). This study indicated that the primary Cr carrier phase produced by Cr (VI) reduction by green rust was Cr(III) hydroxide, which is unsuitable because its solubility is higher than other Cr(III)-bearing phases. Next, , in order to determine the effect of the chemical composition of green rust on the properties of the solid products of its reaction with Cr (VI), green rust sulfate batches with isomorphically-substituted Al, Mg and Zn were synthesized and reacted with identical chromate solutions. The dominant Cr carrier phases were again determined by XAS, and the particle structure and morphology were determined by X-ray diffraction (XRD), pair distribution function (PDF) analysis, and transmission electron microscopy (TEM). Furthermore, the lability of Cr in the reacted samples was assessed by reacting them with synthetic δ-MnO_2 because

oxidation of trivalent chromium in soils primarily occurs at the surface of biogenic manganese oxides. Al and Mg substitution was found to substantially decrease the lability of Cr in the layered Fe(III) oxyhydroxysulfate product, a phenomenon attributed to the effect of these substitutions on electron conductivity in green rust. The lability of Cr was also found to be correlated to the fraction of Cr bound in poorly-crystalline Cr (III) hydroxide phases, suggesting that Al and Mg substitution in green rust favor the formation of a Cr (III)-bearing Fe (III) (oxyhydr)oxide product, and that this reaction pathway is responsible for sequestering Cr into a less-labile solid phase.

In addition, several studies of the redox behavior of As in laboratory experiments and natural samples are included in this dissertation because I assisted with EXAFS data collection and interpretation. Perez et al. (2019) demonstrated the reduction of As(V) by aqueous Fe^{2+} at the surface of synthetic Fe(III) oxyhydroxides by reacting As (V) with mixtures of Fe^{2+} and ferrihydrite. Fe^{2+} was found to reduce As(V) to As(III) at the surface of ferrihydrite, and this mechanism, which was coupled to the Fe^{2+}-promoted transformation of ferrihydrite to more-crystalline phases, may drive the As mobilization observed in groundwater at various locations in south and southeast Asia. Wang et al (2020) collected As-affected peat samples from paleolake sediments in the Hetao Basin in northern China and identified the primary As carrier phases in each sample, which differed depending on the redox conditions. XAS and μ-X-ray fluorescence analyses of these samples showed that As was primarily sequestered by Fe sulfide minerals under reducing conditions, but oxidation of these sulfide minerals redistributes As into secondary phases such as Fe(III) (oxyhydr)oxides. When bound in these phases, As may then be vulnerable to reduction and mobilization via the mechanism tested by Perez et al (2019).

Zusammenfassung

Arsen und Chrom sind Schadstoffe die häufig aus unterschiedlichen natürlichen und anthropogenen Quellen in Böden und Grundwässer eingetragen werden. Wegen ihrer negativen Wirkung auf die menschliche Gesundheit werden sie von den Umweltbehörden der USA und EU als gefährliche Schadstoffe eingestuft. Die Entfernung bzw. Immobilisierung dieser Stoffe aus der Umwelt ist daher ein verbreitetes Sanierungsziel. Ex situ Sanierungsverfahren, wie beispielsweise die „Pump and Treat" Grundwasserreinigung, sind wirksam aber teuer. Demgegenüber können in situ Methoden Böden und Grundwässer weitaus kosteneffizienter sanieren. Im Gegensatz zu organischen Schadstoffen, können toxische Metalle allerdings nicht abgebaut werden. In situ Sanierungsmethoden zielen daher darauf ab, den Oxidationszustand (Speziation) der Schadstoffe zu modifizieren und somit die Mobilität und die toxische Wirkung zu senken. Das übergeordnete Ziel dieser Dissertation ist es, ein umfassendes Verständnis über den Einfluss von redox-reaktiven Eisenmineralen über die Änderungen der Speziationen von As und Cr zu erlangen und damit Grundlagen für eine erfolgreiche Anwendung von in situ Sanierungstechnologien zu legen.

Die vorgelegte Dissertation besteht aus insgesamt vier Publikationen. Drei dieser Veröffentlichungen behandeln die Wirkung redoxreaktiver Fe- und Mn-Mineralphasen auf das Verhalten von toxischen Arsen- und Chrom-Speziationen. In einer weiteren Veröffentlichung Torfproben aus Sedimenten eines Paläosees in China untersucht, um den Einfluss der Diagenese auf die redox-gesteuerte Retardation von Arsen zu erfassen.

Im Rahmen der Dissertation wurden von 2016 bis 2019 eine Reihe von Laborversuchen durchgeführt, in denen die Umwandlung von toxischem sechswertigen Chrom zu nicht-toxischem dreiwertigen Chrom durch "Grünen Rost", ein geschichtetes Eisen(II,III)-haltiges Doppelhydroxid, untersucht wurde. Dabei wurde die Phase Grüner Rost mit Schadstoffkonzentrationen, die typisch für Chrom-belastete Grundwässer sind, in Kontakt gebracht, um die Wirkung der anfänglichen Chromkonzentration auf die potenzielle Chromträgerphase zu bestimmen. Die primären Chromträgerphasen wurden mittels Röntgenabsorptionsspektroskopie als Chrom(III)-Hydroxide identifiziert. Aufgrund ihrer hohen Löslichkeit sind diese allerdings für Sanierungszwecke ungeeignet. Da die Oxidation von dreiwertigem Chrom in natürlichen Systemen hauptsächlich an den Oberflächen biogener Manganoxide erfolgt, wurde die Mobilität von Chrom in den reagierten Proben durch die Addition von synthetischer δ-MnO_2 betrachtet (Thomas et al. 2018). Die stabilste Chromträgerphase wurde durch die Oxidation von magnesiumhaltigem „Grünem Rost" produziert und hat ähnelt dem Mineral Feroxyhyt.

Analog zur ersten Studie wurden in einem zweiten Ansatz Grüner Rost mit Al, Mg und Zn substituiert und anschließend mit Chrom(VI)-Lösungen behandelt. Die dominanten Chromträgerphasen wurden wieder durch Röntgenabsorptionsspektroskopie bestimmt und deren Struktur und Morphologie durch Röntgendiffraktion, Pair Distribution Function-Analyse und Transmissionselektronenmikroskopie charakterisiert. Die isomorphe Substitution von Al und Mg mit Fe(II) verringert die Chrommobilität im Reaktionsprodukt signifikant (Thomas et al., 2020). Dies ist auf die Verringerung des Elektronentransports in der Mineralstruktur zurückzuführen und der damit auf der Oberfläche erfolgenden Reduzierung von sechswertigem Chrom. Insgesamt helfen diese Erkenntnisse, das Anwendungsspektrum von Grünem Rost für Sanierungszwecken abzuschätzen. Weiterhin gibt die Arbeit Einblicke in die Mechanismen, die das Redoxverhalten von Chrom in Böden bestimmen.

In einer weiteren Studie wurden EXAFS Analysen zum Redoxverhalten von Arsen mit Eisenmineralen durchgeführt, die zu zwei Veröffentlichungen beigetragen haben (Perez et al 2019, Wang et al. 2020). Die erste Arbeit demonstriert die Reduktion von fünfwertigem Arsen durch gelöstes Fe^{2+} an den Oberflächen synthetischer Eisen(III)-oxide. Dieser Mechanismus könnte die Mobilisierung von toxischem Arsen, die in Grundwässern in Süd- und Südostasien beobachtet wird, senken. In der zweiten Studie wurden die primären Arsenträgerphasen in Arsen belasteten Torfproben aus Paläoseesedimenten im nordchinesischen Hetaobecken identifiziert. Diese Phasen unterschieden sich in Abhängigkeit von den Redoxbedingungen der entsprechenden Sedimente: Unter reduzierenden Bedingungen wird Arsen durch Eisensulfidminerale sequestriert. Die Oxidation dieser Sulfidminerale führt zur Bildung von arsenführenden Sekundärphasen, wie z. B. Fe(III)-Oxide. Die Stabilität dieser Phasen wurde durch Perez et al. (2019) untersucht.

Die verschiedenen Studien dieser Dissertation zeigen, dass sich das Verhalten und die Mobilität von Arsen und Chrom in Böden und Grundwässern durch Variationen der Redoxeigenschaften schnell verändern können. Für den Erfolg einer Sanierungsmethode, die auf der Basis einer in-situ Oxidation oder Reduktion erfolgt, ist es entscheidend, dass eine Trägerphase produziert wird, die den Schadstoff nachhaltig retardiert und vor Redoxtransformationen schützt. Dies kann durch den Einbau von Chrom und Arsen in die sekundäre Mineralphase erfolgen. Auf diese Art und Weise kann die Mobilisierung von toxischem Arsen und Chrom unter variablen Redoxbedingungen unterbunden werden. Die hier gewonnenen Erkenntnisse vermitteln neue Einblicke in die komplexen Wechselwirkungen von Arsen und Chrom mit Eisenoxiden und -sulfiden, sowie deren Stabilität. Auf dieser Grundlage können die Erfolgsaussichten von in-situ Sanierungsmethoden besser abgeschätzt werden.

Table of Contents

List of Figures

1. Introduction and Scientific Background

1.1   Motivation, Background and Scope of Study

Most of the studies described in this dissertation were carried out in the context of the Metal-Aid project, a European Union Horizon 2020 Marie Sklodowska Curie Innovative Training Network. Participants from 11 universities, industry partners and governmental agencies across Europe performed research with the goal of developing a particle-based *in situ* remediation reagent, with topics ranging from molecular-scale interactions of trace elements with iron oxide surfaces to the kinetics of contaminant removal from solution and a pilot project testing particle injection into a sediment media. This research network focused primarily on the use of green rust sulfate and sulfidized zero valent iron for remediation, although additional studies of the remediative activity of siderite, sepiolite, naturally-occurring Fe oxides and oxidant-intercalated layered double hydroxides were also performed. The Metal Aid project-based portion of this dissertation will focus on the interactions of arsenic and chromium, two commonly-occurring groundwater contaminants, with green rust sulfate. An additional study characterizing the sequestration of arsenic in subsurface sediments is also presented.

Chromium and arsenic are common soil and groundwater contaminants widely distributed throughout the world, and pose a significant danger to human health (Hughes 2002; Duker et al. 2005; Hossain 2006; Saha et al. 2011; Postma et al. 2012). However, their toxicity and mobility depend on their speciation and interactions with minerals found in soil and sediments, so the actual danger posed by Cr and As contamination varies depending on site conditions (Savage et al. 2000; Mandaliev et al. 2014). Remediation typically requires the use of pump-and-treat technology, which is effective but expensive and long-lasting (Higgins and Olson 2009). *In situ* chemical remediation methods, on the other hand, can immobilize

contaminants without requiring groundwater extraction, which can significantly decrease the costs and lifetimes of groundwater remediation projects (Wilkin et al, 2018). These methods often take advantage of differences in solubility and/or mobility between different oxidation states of a metal(loid) contaminant(Ludwig et al., 2007; Puls et al, 1999), an approach which is particularly effective for chromium and arsenic because their mobility is speciation dependent (Bowell et al, 2014; Saha et al., 2011). Fe(II)-bearing oxide and sulfide minerals can be used to catalyze or induce redox transformations, and trace elements can easily be incorporated into the Fe(III) (oxyhydr)oxide oxidation products of these mineral phases.

While the interactions of Fe-bearing minerals with chromium and arsenic have been investigated extensively in lab- and field-based studies (Bond & Fendorf, 2003; Rittle et al, 1995; Skovbjerg et al, 2006; Wilkin & Ford, 2006), this dissertation features studies that specifically investigated the mechanisms of these interactions in the following systems: hexavalent chromium with pure and cation-substituted green rust sulfate, arsenic with ferrihydrite and Fe^{2+}, and arsenic in natural, high-S peat deposits. The results of these experiments provide valuable information on the redox transformations driving sequestration of chromium and arsenic in iron oxide and sulfide phases and the predominant As and Cr carrier phases following the redox transformations. To provide a sufficient theoretical background for understanding of this study, this dissertation includes an introduction to Fe (oxyhydr) oxide and sulfide mineralogy, arsenic and chromium behavior in the environment, applicable remediation techniques, and the analysis methods used in the included experiments.

1.2 Formation and Properties of Fe Oxide and Sulfide Minerals

1.2.1 Iron oxide formation and structure

The term "iron oxides" refers to a broad category of iron-bearing minerals ranging from the pure oxides such as magnetite (Fe_3O_4) and hematite (α-Fe_2O_3) to the oxyhydroxides such as goethite (α-FeOOH) and hydroxides (i.e. green rust). For simplicity, the terms iron oxides and iron (oxyhydr)oxides will be used here to define this class of mineral. Fe(II) and Fe(III) (oxyhydr)oxide minerals are commonly found in soils, typically as secondary surface precipitates following weathering of Fe-bearing parent material (Allen and Hajek 1989; Cornell and Schwertmann 2003); however, formation in other environments such as mafic magmas (Reynolds 1985), hydrothermal vents (Tazaki 2000), and serpentinization (Moody 1976) have been observed. Because of the low solubility of Fe^{3+} under typical surface conditions, crystalline Fe (oxyhydr)oxides are insoluble and unlikely to undergo further transformations. Therefore, incorporation of trace elements such as arsenic and chromium during the formation of these phases can effectively remove them from solution. When iron oxides form, they typically undergo several transformation steps, as there is a significant activation energy barrier to precipitation of crystalline (oxyhydr)oxides such as hematite and goethite because of the decrease in entropy associated with the formation of a solid-solution interface at the surfaces of these particles (Schwertmann & Cornell, 2008). Poorly-crystalline Fe(III) oxyhydroxides such as ferrihydrite precipitate first via a hydrolysis mechanism, followed by rapid polymerization of octahedrally coordinated Fe(III) units (Spiro et al. 1966). These phases can then transform to more crystalline phases via several mechanisms such as dissolution and reprecipitation (which forms goethite) and dehydration coupled to an internal rearrangement (Cudennec & Lecerf, 2006; Yee et al, 2006). The latter mechanism leads to transformation to hematite, which typically

14

forms in warmer and drier conditions than goethite. Other iron (oxyhydr)oxides are also known to form from poorly-crystalline intermediates, some of which require oxidative transformation (i.e. green rust oxidation to lepidocrocite, Schwertmann and Fechter 1994).

The structures of iron (oxyhydr)oxides are typically characterized by hexagonal (ABAB) or cubic (ABCABC) close packed stacking of oxide and hydroxide groups; Fe then occupies the octahedral and, in some cases, tetrahedral sites within these structures (Cornell and Schwertmann 2003). The structures are best visualized as chains or sheets of FeO_6 octahedra linked by monodentate corner-sharing, bidentate edge-sharing or tridentate face-sharing linkages bridged by shared oxide or hydroxide ligands (Cornell and Schwertmann 2003). In some iron oxides, particularly magnetite and (possibly) ferrihydrite, tetrahedrally-coordinated Fe is also present in the structure (Hargrove and Kündig 1970; Maillot et al. 2011; Peak and Regier 2012). If a portion of these tetrahedral sites are unoccupied, they can also serve as potential interstitial sites for incorporation of trace elements into the iron (oxyhydr)oxide structure. Substitution of Al, Cr, Mn, Ni, Zn, V, Co and other elements at both octahedral and tetrahedral sites has been observed
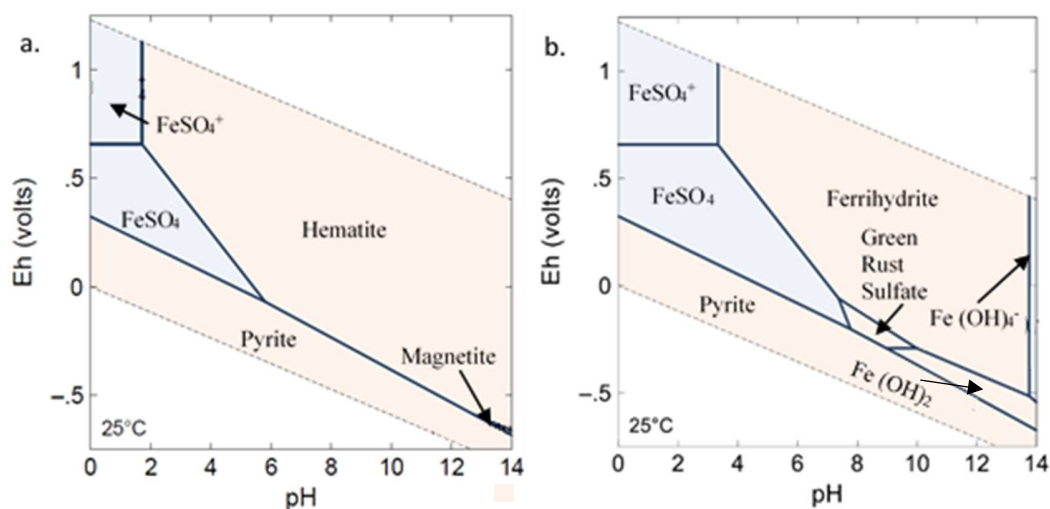
Figure 1 Fe speciation diagrams at 25°C, with [Fe] = 0.001 M, [SO$_4$] = 0.01 M. When no phases are suppressed (a), hematite is dominant under oxidizing conditions, while ferrihydrite and green rust sulfate can form as metastable phases in a controlled synthesis batch (b). Diagrams generated using the Geochemist's workbench software.

in the laboratory and natural samples (Cornell and Schwertmann 2003 and references therein).

Figure 1a shows the dependence of Fe speciation on pH and Eh. The dominant phases in this diagram are magnetite (Fe_3O_4) and hematite (Fe_2O_3). The modified phase predominance diagram shown in Figure 1b shows the predominant metastable phases (i.e. green rust and ferrihydrite) likely to form when more crystalline phases such as goethite, hematite and magnetite are suppressed. This is an acceptable model for the applied synthesis conditions because the more crystalline phases are unlikely to form under surface conditions on such short timescales (Schwertmann & Cornell, 2008).

1.2.2   Structure and properties of iron oxides relevant to the present study

Goethite is commonly encountered in soils and a common sink for trace elements in soils and sediments (Refait et al, 2017; Schwertmann & Carlson, 1994; Singh et al, 2002). It has an orthorhombic unit cell and is characterized by hexagonal close packing of oxide and hydroxide ligands (Sampson 1969). Fe only occupies octahedral sites in the structure, while the tetrahedral sites are empty. In terms of FeO_6 complexes, the structure of goethite consists of double chains of edge-sharing octahedra oriented in the [100] direction. Each double chain is linked to four adjacent double chains by corner sharing between $FeO_3(OH)_3$ octahedra (Cornell and Schwertmann 2003). Many studies of trace element incorporation into goethite have been performed: Al-for-Fe substitution as high as 30% have been observed (Schwertmann & Carlson, 1994), while up to 12% Cr substitution has been observed in the laboratory (Schwertmann et al. 1989). In addition, $FeO_3(OH)_3$ structures at the particle edges are ideal bonding sites for solution anions and cations. Sorption of silicate, phosphate and arsenate has been investigated in

laboratory studies (Gimenez et al., 2007; Jordan et al., 2007; Strauss et al., 1997), and all are capable of forming stable surface complexes with high surface coverages.

Ferrihydrite is a poorly-crystalline Fe(III) oxyhydroxide that does not exhibit long-range structure in the same sense as other, more-crystalline iron oxides. Nevertheless, structural motifs characteristic of many iron oxides are present (Cornell and Schwertmann 2003). Most natural ferrihydrite resembles 2-line ferrihydrite (Cismasu et al., 2011), which features two characteristic broad reflections in its diffraction pattern. Ferrihydrite has a low degree of order, so diffraction studies have yielded different interpretations of its structure. The oxide and hydroxide stacking sequence is believed to resemble that of hematite with significant irregularities, but the Fe distribution throughout the structure is poorly ordered, and a significant amount of water is present (Manceau and Drits 1993; Michel et al. 2007). Nevertheless, because of its poor crystallinity and high specific surface area, ferrihydrite is a highly effective sink for trace elements. Although trace element substitution for Fe in ferrihydrite and trace element sorption to a ferrihydrite nanoparticle are very difficult to distinguish spectroscopically, ferrihydrite-like solids with very high trace element concentrations have been synthesized and observed (Cornell and Schwertmann 2003). For example, ferrihydrite with very high chromium levels has been synthesized in the laboratory (Papassiopi et al., 2014; Tang et al., 2010), and arsenate incorporation into ferrihydrite is also possible, although X-ray absorption fine structure spectroscopy studies of As incorporation into ferrihydrite (Waychunas et al., 1993) suggest that this incorporation is better described as sorption to an interior nanoparticle. The poorly-crystalline and possibly nanoparticulate structure of natural ferrihydrite also means that it has a high specific surface area (≥ 300 m^2/g) (Cismasu et al. 2011), so sorption is also a potential sink for trace substances, including arsenate.

Green rust is a mixed-valence Fe(II, III) hydroxide with a structure significantly different from other Fe(III) (oxyhydr)oxides, as it more closely resembles a phyllosilicate without a tetrahedral layer. Green rust consists of an octahedral layer with hexagonal symmetry occupied by a mix of octahedrally-coordinated Fe(II) and Fe(III) cations, which give it a positive layer charge balanced by an interlayer anion (most commonly chloride, carbonate or sulfate). Green rusts are classified according to the identity of this interlayer anion, although the different forms of green rust exhibit other structural differences in unit cell symmetry and the Fe(II)/Fe(III) molar ratio in the octahedral layer (Refait et al. 1998; Trolard et al. 2007; Christiansen et al. 2009). In Figure 1b, the stability of green rust sulfate is shown because it is the form of green rust used in the experiments described in this dissertation. Green rust is typically found in slightly reducing environments such as redox transition zones in soils and iron metal corrosion shells, where it most likely plays a role in mediating cycles of trace elements. Lab-synthesized green rust has been found to reduce common groundwater contaminants such as hexavalent chromium (Williams and Scherer 2001; Bond and Fendorf 2003; Skovbjerg et al. 2006), hexavalent uranium (O'Loughlin et al. 2003), neptunium (Skovbjerg et al. 2010; Christiansen et al. 2011) as well as several other actinides (Bach et al. 2014), nitrate (Hansen and Koch 1998), and selenium (Myneni 1997). Because of green rust's heterogeneous structure and relatively high electrical conductivity (Wander et al. 2007), it has multiple potential reaction sites allowing engineering of the particle to favor a particular mechanism that produces a more stable product, i.e. reduction in the interlayer and subsequent co-precipitation. In addition, the high surface area (if interlayer sites are included in the calculation) (Randall et al. 2001) and exchange capacity of green rust suggest that it has a high capacity for adsorption and incorporation of oxyanions not reducible by structural Fe(II).

Finally, feroxyhyte is a poorly-crystalline Fe(III) oxyhydroxide whose formation has been associated with rapid oxidation of Fe^{2+} (Sestu et al., 2015). In natural environments, feroxyhyte forms as a byproduct of rapidly-flowing, Fe^{2+}-rich water passing through a porous, oxidizing sediment (Carlson and Schwertmann 1980). Like ferrihydrite, feroxyhyte is poorly-crystalline and its crystal structure is disputed. It is generally accepted that the phase has a hexagonal unit cell with a disordered ABAB array of oxide and hydroxide groups (Patrat et al. 1983; Drits et al. 1993). These studies also proposed that half of the associated octahedral sites were vacant, leading to stacked sheets of edge-sharing octahedra similar to brucite, although other features such as face-sharing octahedra and partial occupation of tetrahedral sites (Drits et al. 1993) were also proposed. Studies of the short-range structure of feroxyhyte have also yielded conflicting results. Previous studies utilizing EXAFS (Manceau and Drits 1993) and simulation of XRD patterns from a structural model (Drits et al. 1993) described its short-range structure as a mix of hematite and ferrihydrite. However, a later study (Sestu et al. 2015) was able to model the feroxyhyte diffraction pattern using goethite-based motifs. Natural feroxyhyte (Carlson and Schwertmann 1980) differs from the ideal structure constructed by studies of synthetic samples. The anion packing is significantly more disordered and cations are distributed randomly across interstitial sites, causing a loss of the periodic edge-sharing octahedral layers present in the idealized structure (Cornell and Schwertmann 2003).

1.2.3   Iron Oxide Surface-Solution Interactions

Secondary iron oxides typically exist as small crystals with sizes in the micron to nanometer range. Therefore, the surface area to volume ratios of these minerals are high, and interactions at the interface between the particle surface and the surrounding solution play an important role in controlling trace element mobility. Fe atoms located at mineral surfaces act as

Lewis acids and are hydroxylated and/or hydrated in the presence of water (Cornell and Schwertmann 2003). Depending on the structure of the iron oxide particle, these surface hydroxyl groups can be singly, doubly or triply coordinated to surface Fe atoms. In addition, as the hydroxyl groups can donate or accept protons from solution, the minerals have a pH-dependent surface charge that mediates the interactions of the surface with chemical species in solution (Schindler and Stumm 1987). In order to balance this surface charge, ionic species of the opposite charge (counter-ions) and hydrogen-bonded water molecules are concentrated in the region near the mineral surface. This region is called the electrical double layer, the thickness of which depends on the magnitude of the surface charge and the counter-ion concentration.

Bonding of a solution species to the surface of a solid particle is referred to as adsorption. Because the rates of mineral precipitation and growth as well as surface-mediated redox reactions are controlled by an adsorption step (Cornell and Schwertmann 2003), adsorption is central to our understanding of the results observed in the scientific studies presented in this dissertation. A finite number of surface sites is available for adsorption, so adsorption thermodynamics are often represented by isotherms, or mathematical models that relate the surface site coverage to the equilibrium adsorbate concentration at constant pH (Kinniburgh 1986). Alternatively, surface complexation models use the calculated thermodynamic constants of a defined surface complexation reaction with corrections for the effects of surface charge and the electrical double layer (Dzombak and Morel 1990). Adsorption thermodynamics are pH-dependent due to the effect of pH on the surface charge of the adsorbent material and speciation of the aqueous species. This effect is clearly visible when considering the adsorption of arsenate, arsenite and chromate on iron oxides surfaces.

The mechanisms and thermodynamic constraints of the adsorption of oxyanions such as chromate (CrO_4^{2-}) and arsenate (AsO_4^{3-}) as well as other species such as arsenite ($As(OH)_3$) to iron oxide surfaces have been extensively characterized. Arsenate (Fuller et al., 1993; Raven et al., 1998; Waychunas et al., 1993) and chromate (Mamun et al., 2017) adsorption to ferrihydrite surfaces is highly favorable, and ferrihydrite is the primary sink for these species in many environments. In the case of chromate, adsorption to magnetite and green rust surfaces was found to be coupled to reduction to trivalent chromium (Kendelewicz et al., 2000; Loyaux-Lawniczak et al., 2000). Arsenite also displays affinity for various iron oxide surfaces, but because arsenite deprotonation is not thermodynamically favorable under neutral and acidic conditions, less of this species adsorbs to iron (oxyhydr)oxide surfaces than arsenate and adsorption has a weaker dependence on pH (Raven et al. 1998). In addition, other oxyanions such as silicate and phosphate compete with chromium and arsenic for potential adsorption sites on the iron oxide surfaces (Zachara et al. 1987; Swedlund and Webster 1999; Liu et al. 2001). Because borosilicate glassware was used in the experiments in this dissertation, trace amounts of silicate in solution most likely impacted these experiments, providing some insight into the potential course of these reactions in natural systems, where silicate exists in groundwater at similar concentrations.

The kinetics of arsenate and chromate sorption on mineral surfaces have also been investigated extensively (Fuller et al., 1993; Garman et al., 2004; Raven et al., 1998). In the case of sorption to minerals such as ferrihydrite or layered minerals such as phyllosilicates or layered double hydroxides (Prasanna et al., 2006), the overall kinetics vary depending on the stage of the adsorption reaction and the saturation of more easily accessible adsorption sites (Cornell and Schwertmann 2003). Adsorption in this case can be simplified to a model with two reactions

taking place simultaneously. In the first reaction, arsenate and chromate adsorb rapidly to the mineral surface in the early stages of reaction, when these surface sites are not yet saturated, while a smaller portion of the solution species is adsorbed by sites within the ferrihydrite aggregates or layered mineral interlayers. However, after saturation of the surface sites, the adsorption kinetics are controlled by sorption to the "interior" sites, which is in turn dependent on the rate of sorbate diffusion to these sites. In this way, the mechanism of adsorption and the ability of the sorbate to access surface complexation sites can control the kinetics of adsorption and any associated crystal growth and or charge transfer reactions.

Aqueous species such as chromate, arsenite and arsenate can adsorb to mineral surfaces in the form of an inner-sphere or outer-sphere surface complex. In the case of an inner-sphere complex, one or more of the oxide and/or hydroxyl ligands bound to the As or Cr exchanges for a hydroxyl group on the mineral surface (Cornell and Schwertmann 2003). In this way, the ion's oxide and/or hydroxyl ligands are bound directly to a metal cation on the surface without any intervening water molecules. These surface complexes are classified according to the number of hydroxyl groups bound to the surface (Dzombak and Morel 1990); monodentate, bidentate and tridentate surface complexes are comprised of one, two and three bonds, respectively. On the other hand, outer-sphere complexes are mediated by intervening hydroxyl groups and are electrostatic in nature. In the case of arsenate, arsenite and chromate, the predominant surface complex is a function of pH and surface coverage. An EXAFS-based study by Waychunas et al. (1993) found that arsenate adsorbs to ferrihydrite surfaces in the form of a bidentate, bridging (bound to two FeO_6 octahedra) surface complex, with traces of a monodentate complex at low surface coverages, while Ona-Nguema et al. (2005) found that arsenite adsorbs to the surfaces of iron (oxyhydr)oxides via similar bidentate complexes. A study of chromate adsorption on

ferrihydrite (Mamun et al. 2017) suggested that chromate forms a mixture of outer- and inner-sphere bidentate surface complexes on ferrihydrite's surface. Inner-sphere complexes are more common at Cr/Fe ratios above 0.5 (compared to the ratio of 0.25 used in these experiments). Formation of these surface complexes mediates the redox transformations in the experiments presented in this dissertation, particularly inner-sphere surface complexes, as coupling of electron spin states by a shared ligand increases the rate of electron transfer.

1.2.4 Electronic Structure and Charge Transfer in Iron Oxides

Some Fe (oxyhydr)oxides, like many similar minerals, are semiconducting materials, and transfer of electrons to and away from particle surfaces may allow them to participate in redox reactions. The conduction pathway is described in detail by Sherman (1990) as a series of intervalence charge transfer (IVCT) steps. According to the crystal field theory, octahedral coordination of an Fe(II) or Fe(III) atom by oxide or hydroxide ligands causes a splitting of the Fe 3d orbitals into two energy levels based on their t_{2g} or e_g symmetry. Depending on the magnitude of d-orbital splitting relative to the energy cost of pairing electrons in the same orbital, the electronic states of these octahedral complexes may enter high-spin or low-spin configurations. For example, in the case of Fe^{3+} octahedrally coordinated by oxide and hydroxide ligands, the energy cost of pairing electrons in the 3d t_{2g} orbitals is higher than the cost of the electron entering a higher-energy e_g orbital, so the electron configurations of these octahedrally-coordinated ions are invariably in a high-spin state. For this reason, when the orbital energy levels are calculated using molecular orbital theory (this calculation requires single-electron occupation of each orbital), spin-up (α) electron configurations are lower-energy than spin-down (β) configurations. The spin-down configurations are better characterized as anti-bonding orbitals and comprise the conduction band in iron oxide phases (Sherman 1985). There are two

types of transitions to the conduction band: O 2p→Fe 2t_{2g} (β) ligand-metal charge transfer (LMCT) and spin-forbidden ligand-field transitions between 3d orbitals.

The LMCT transitions are spin-allowed and typically occur at about 38,000 cm^{-1} (~4.7 eV), while ligand field transitions are spin-forbidden because of the change in spin quantum number (Sherman 1990). However, the spin selection rules can be relaxed in an iron oxide or clay mineral as a result of a process called superexchange coupling (Goodenough 1955, 1958; Kanamori 1959), which magnetically couples adjacent Fe cations. Because covalent bonding is spin-dependent, if a (hydr)oxide-coordinated Fe cation is α spin-dominated, the electron spin states of the shared O^{2-} and OH^- ligands are polarized, leading to a predominantly β spin state in the nearest-neighbor Fe cation; therefore, adjacent Fe cations in Fe(III) oxyhydroxides are antiferromagnetically coupled. The strength of this coupling depends on several factors including the covalent character of the ligand-metal bond (coupling by OH^- is weaker than O^{2-}), the number of shared ligands, and the magnitude of α or β spin-polarization of the coordinated metal cation. This superexchange coupling also controls intervalence charge transfer (IVCT), the mechanism by which electrons are conducted through an iron oxide particle.

In some Fe (oxyhydr)oxides such as magnetite and green rust, multiple Fe valences (i.e. Fe(II) and Fe(III)) are present. Fe^{2+}→Fe^{3+} IVCT takes place within these phases and controls electron conduction within their interiors. Understanding of this process requires understanding of the electronic transitions involved. When in octahedral coordination environments, both Fe^{2+} and Fe^{3+} have the high-spin electron configuration described earlier, while the Fe^{2+} 3d t_{2g} (β) antibonding orbitals are partially occupied by the sixth 3d electron (Sherman 1990). Within a $(Fe_2O_{10})^{15-}$ cluster, the Fe^{2+} 3d t_{2g} (β) orbitals are reclassified as Fe^{2+}-Fe^{3+} bonding, while all Fe^{3+} 3d (β) orbitals are still antibonding orbitals in the cluster's conduction band. IVCT can take place

due to the aforementioned superexchange coupling effects, but the rate of electron transfer depends on the band gap (in this case an activation energy barrier), which is controlled by the strength of superexchange coupling. In the case of magnetite, Fe^{2+} and Fe^{3+} both occupy edge-sharing octahedral sites coupled by O^{2-}-mediated superexchange, which is particularly strong when the bond is highly covalent. As a result, magnetite is ferromagnetic and has a very narrow band gap (0.1 eV, similar to metals), and electron transfer can be thermally induced (Schlegel et al. 1979), accounting for its black color (as all visible light wavelengths can be absorbed). In green rust, on the other hand, coupling between hydroxyl-coordinated Fe^{2+} and Fe^{3+} is weaker and inconstant. These weak coupling interactions mean that the band gap is broader, estimated at about 1.7 eV based on optical spectroscopy analyses of Fe-bearing silicates of similar structure (Lear and Stucki 1987); there is therefore a significant activation energy barrier to $Fe^{2+} \rightarrow Fe^{3+}$ electron transfer (Figure 2) in native green rust. However, when an electron hole (i.e. Fe^{3+}) is introduced at a Fe^{2+} site, $Fe^{2+} \rightarrow Fe^{3+}$ charge transfer transitions become more favorable, as electron hole placement at sites Fe1 and Fe2 in Figure 2 is energetically equivalent, lowering the activation energy barrier. Density functional theory (DFT) modelling of electron hole propagation in a brucite-like sheet (Wander et al. 2007) showed that superexchange coupling of Fe electronic states was the primary factor controlling the rates of various charge transfer mechanisms. Charge transfer between next-nearest neighbors, separated by a distance of 5.67 Å and bound to two shared Fe-centered octahedra, was the most rapid charge transfer mechanism at 8.33×10^{10} s^{-1}, eight orders of magnitude faster than any other transfer geometry. In the case of Wander et al., (2007), modelling of the brucite sheet suggests that indirect superexchange coupling can also occur between Fe octahedra (Fe1 and Fe2) coupled to the same one or two cations (Fe^{2+}, Fe^{3+}). These rapid charge transfer steps are therefore able to regenerate Fe(II)

oxidized at green rust's solid-solution interfaces, suggesting that electron charge transfer steps

control redox reactions mediated by the surfaces of green rust and other iron oxides, and

knowledge of the physical processes controlling these reaction mechanisms is essential for our

understanding of the results obtained in the experiments presented below.

$Fe_{(aq)}$ and iron oxide mediation of redox reactions

The conductivity implied by the electron transfer mechanisms outlined in the previous

section suggests that iron oxides can mediate redox reactions in soils. Aqueous Fe^{2+} and its
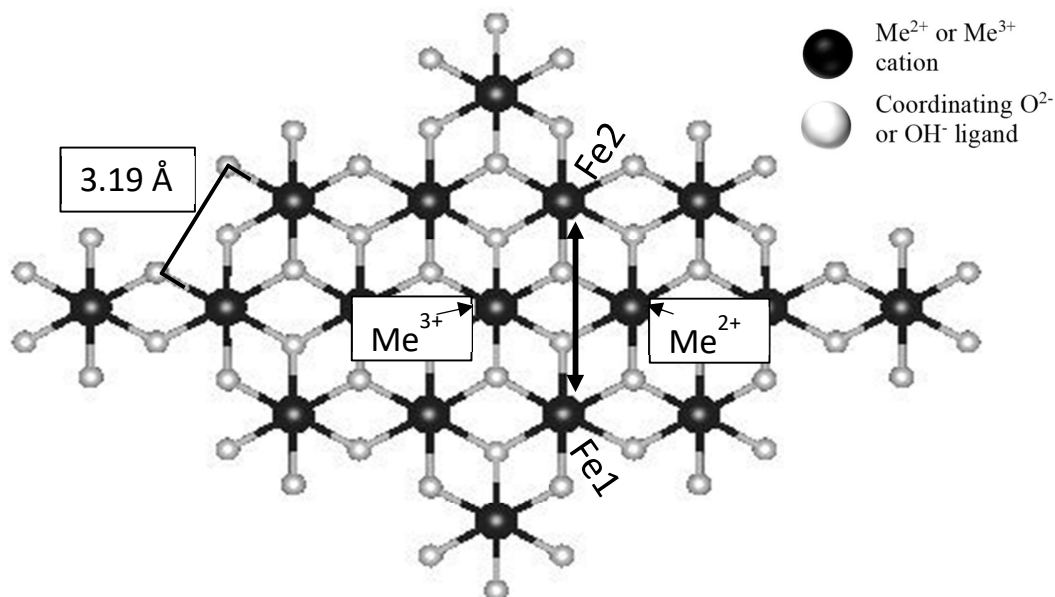
Figure 2 Brucite-like sheet used to demonstrate electron transfer between Fe-centered octahedra. Electron transport is between next-nearest neighbor Fe sites labelled Fe1 and Fe2, which are coupled via superexchange with atoms at the neighboring sites Me^{2+} and Me^{3+}.

interactions with Fe oxide minerals is a topic of ongoing research, and aqueous Fe^{2+} has been

found to promote Fe (oxyhydr)oxide dissolution (Cornell & Schwertmann, 2003; Litter & Blesa,

1988; Litter & Blesa, 1992), phase transformation via dissolution and reprecipitation or

topotactic recrystallization (Fischer 1972; Bechine et al. 1982), redox transformations to Fe(II)-

bearing minerals such as magnetite and green rust (Tamaura et al 1984; Usman et al., 2012), and

reduction of other chemical substances using an Fe oxide as a catalyst (Amstaetter et al., 2010;

Daus et al., 2000; Kendelewicz et al., 2000; Ona-Nguema et al., 2010; Scott et al., 2005). Reductive dissolution is a well-characterized dissolution method of Fe oxides (Cornell and Schwertmann 2003), as it is the most important dissolution mechanism in natural systems.

When combined with an acid or complexing agent, aqueous Fe^{2+} accelerates dissolution by reducing a Fe(III) atom at the mineral surface, destabilizing it within the lattice and favoring detachment following protonation or complexation (Litter & Blesa, 1988; Litter & Blesa, 1992). In this context, Fe^{2+} acts as a catalyst rather than a reducing agent, as the reduced surficial Fe(II) complex is an unstable transition state. The ability of aqueous Fe^{2+} to accelerate dissolution of Fe (oxyhydr)oxides also implies that it is able to accelerate mineral transformations that utilize a dissolution-reprecipitation mechanism, such as the transformation of less-crystalline Fe(III) oxyhydroxides to goethite. For example, aqueous Fe^{2+} has been found to accelerate transformation of iron oxides such as lepidocrocite (Bechine et al. 1982) and ferrihydrite (Fischer 1972) to goethite. In addition, exposure of certain Fe(III) oxyhydroxides to high concentrations of aqueous Fe^{2+} can cause transformation to mixed-valence Fe(II, III) oxides such as magnetite and green rust, whose formation is thermodynamically favored at high Fe^{2+} concentrations. Transformation to magnetite proceeds via a dissolution-precipitation mechanism (Tamaura et al. 1984). On the other hand, transformation of lepidocrocite, goethite and ferrihydrite (Tamaura et al. 1984; Usman et al. 2012) to green rust is topotactic but requires charge transfer on a larger scale (~500 nm) than reductive dissolution.

In addition to its interactions with iron oxides, aqueous Fe^{2+} is also capable of participating in redox reactions with other solution species, often at the surface of iron oxide particles. Fe(II) bound in mineral phases can also act as a reductant in similar reactions. In some cases, Fe^{2+} can reduce species such as chromate (Buerge and Hug 1997) and nitrate (Buresh and

Moraghan 1976) directly in solution, although it is impossible to distinguish reduction by Fe^{2+} from reduction by Fe(II, III)-bearing intermediate phases such as green rust that form in the course of these reactions (Skovbjerg et al. 2006). Fe^{2+} can also reduce other species by utilizing mechanisms that take advantage of its ability to destabilize Fe(III) (oxyhydr)oxide structures and surfaces following an IVCT electron transfer. Aqueous Fe^{2+} has been found to promote reduction of As(V) under anoxic conditions (Daus et al. 2000; Ona-Nguema et al. 2010) and oxidation of As(III) (Amstaetter et al. 2010) under oxic conditions in the presence of Fe(III) oxyhydroxide surfaces, and can also reduce As incorporated into jarosite during the Fe^{2+}-promoted transformation of this mineral to goethite (Karimian et al., 2017).

Similarly, Fe(II)-bearing minerals are capable of trace element reduction via mechanisms that require intraparticular electron transport, as these reactions can only take place at the particle surfaces. For example, magnetite reduction of chromate (He & Traina, 2005; Kendelewicz et al., 2000; Peterson et al., 1996) and U(VI) (Missana et al., 2003; Scott et al., 2005) has been the subject of multiple investigations. Green rust minerals can also reduce a variety of trace element contaminants, and may be more efficient because of their layered clay mineral-like structure (Christiansen et al. 2009), which provides a higher reactive surface area for reduction of aqueous species that can enter the interlayer, limiting passivation and potentially sequestering the reduced contaminant in the interior of the reaction product. Green rust reduction of nitrate (Hansen & Koch, 1998; Hansen et al., 2001), U(VI) (Latta et al., 2015; O'Loughlin et al., 2003), Se(VI) (Myneni 1997), Np (Christiansen et al. 2011), and Cr(VI) (Bond & Fendorf, 2003; Legrand et al., 2004; Loyaux-Lawniczak et al., 1999; Loyaux-Lawniczak et al., 2000; Skovbjerg et al., 2006) has been observed in laboratory studies. As Fe (oxyhydr)oxides are widespread in soils

and sediments, these reactions likely play an essential role in mediating trace element speciation and distribution in soils.

1.2.5 Formation and Properties of Iron Sulfide Minerals

Iron sulfide minerals are also a common component of soils and sediments, particularly under anoxic conditions (Rickard and Luther 2007). Because it is the dominant iron sulfide formation process in soils and sediments, the microbially-driven formation mechanism will be discussed here. Sulfate-reducing bacteria (SRB) drive formation of sulfide (S^{2-}) by sulfate reduction in the subsurface. Sulfate is a less effective electron acceptor than other oxidants such as O_2, NO_3^-, MnO_2 and Fe^{3+}, so sulfate reduction by SRBs, which utilize it primarily for oxidation of organic carbon and molecular hydrogen, occurs under anoxic conditions where other potential electron acceptors are depleted (Liamleam and Annachhatre 2007). Sulfide is primarily in the form of HS^- under these conditions, but other species such as hydrogen sulfide (H_2S), disulfide (S_2^{2-}), polysulfide (S_n^{2-}) and elemental sulfur can also form at low concentrations, particularly when sulfur is not fully reduced to the (-II) oxidation state. Fe is primarily in the form of Fe^{2+} under anoxic conditions (Rickard and Luther 2007), providing a potential pathway for formation of Fe sulfide minerals. Common Fe(II) sulfide minerals include mackinawite, which is poorly crystalline and likely a precursor for formation of other Fe(II) sulfide phases (Lennie et al., 1995a;Lennie et al., 1997), greigite (Skinner et al., 1964), marcasite (Schoonen and Barnes 1991), pyrrhotite (Lennie et al., 1995b) and pyrite (Wilkin & Barnes, 1997). Other metal(loid) sulfide minerals are also expected to form using similar mechanisms, including As-bearing phases such as realgar, orpiment and arsenopyrite (Rittle et al. 1995). Simultaneous dissimilatory reduction of arsenate and sulfate in laboratory- and field-based studies has been identified as a potential pathway for removal of arsenic from soil and

groundwater (Rittle et al. 1995; Newman et al. 1997; Oremland et al. 2000). Sulfide minerals

have also been tested as potential *in situ* chemical reduction reagents for contaminants such as

hexavalent chromium (Patterson et al. 1997), and likely play a role in controlling speciation and

distribution of trace elements in natural environments.

1.3   Chromium contamination and remediation

1.3.1   Origin, distribution and applications

Chromium is a first-row transition metal frequently encountered in the earth's crust,

where it is estimated to be the 19th most common element, with an average concentration of 126

ppm (Wedepohl 1995). Although relatively common, chromium is not distributed uniformly

across the earth's surface. It is primarily associated with mafic and ultramafic rocks, particularly

ophiolites, or regions of oceanic crust that has been uplifted and/or emplaced in continental crust

regions (Nriagu and Simmons 1988). As a result, in these ophiolites and their weathering

products, chromium is often associated with other elements common in mafic rocks, such as iron

and manganese, both of which play a role in determining the speciation and environmental

impacts of chromium. The most commonly-mined chromium ore is chromite ((Fe^{2+}, Mg) O·(Cr,

Al, Fe^{3+})$_2$O$_3$), a spinel mineral of variable composition encountered in stratiform and podioform

ophiolite deposits (Anger et al. 2000).

Once extracted, chromium has many industrial applications, including leather tanning,

metal plating, pigmentation, wood preservation, and catalysis, although many of these

applications have been phased out in developed countries because of chromium's toxicity

(Barceloux and Barceloux 1999). Of particularly concern is the widespread use of chromium in

the tanning industry, which has caused severe contamination of ground- and surface water in the

developing world, particularly in regions with active tanning industries such as northern India,

Bangladesh and Central America (Guo et al., 2006). Although Cr^{3+} compounds with low toxicity

are used in the tanning process, these can be oxidized to the more toxic and carcinogenic form

(hexavalent chromium) during this process or in the soil, potentially endangering human health

in areas impacted by these activities (Apte et al., 2005; Milacic & Stupar, 1995).

1.3.2 Toxicity and Environmental and Health Effects
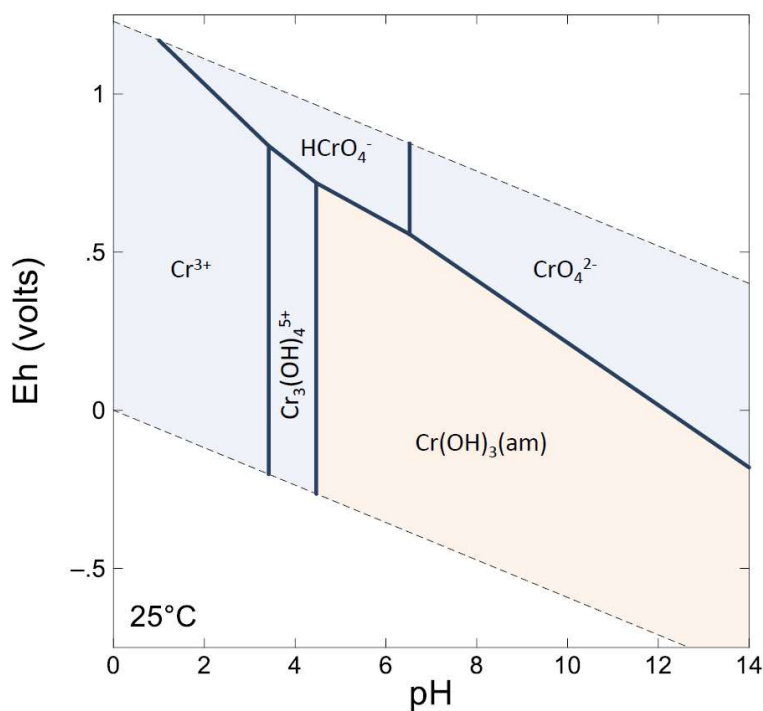
Figure 3 Phase diagram for Cr at a concentration of 1.0 mM, in the absence of sulfur. Diagram generated using the Geochemist's Workbench software. Crystalline Cr(III) oxide phases are excluded because they are not known to precipitate under surface conditions. Cr (OH)₃ (am) refers to a poorly-crystalline Cr(III) (oxyhydr) oxide solid.

The environmental and health effects of chromium depend primarily on its speciation in

environmental media (see Figure 3). The metal has many oxidation states, but two are commonly

encountered under surface conditions: the trivalent (Cr^{3+}) and hexavalent (Cr^{6+}) forms, the latter

of which typically occurs in the form of the interconvertible anions chromate (CrO_4^{2-}) and

dichromate ($Cr_2O_7^{2-}$) (Barceloux and Barceloux 1999). Trivalent chromium has low toxicity and

is poorly soluble; while hexavalent chromium, on the other hand, is toxic and carcinogenic.

Chromate's high toxicity is a result of its high solubility, ability to enter cells using sulfate and phosphate channels, and its mutagenicity, although the mechanism of mutagenicity is still undetermined (von Burg and Liu 1993; Saha et al. 2011). Chronic and occupational exposure to hexavalent chromium is carcinogenic and can lead to other symptoms such as contact dermatitis. These symptoms are highly prevalent in areas affected by poorly-regulated releases of chromium into the environment, such as the city of Kanpur and the Sukinda Valley in India (Naz et al., 2016; Sharma et al., 2012).
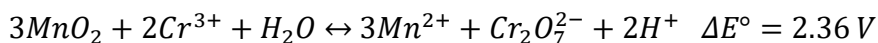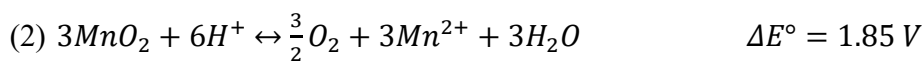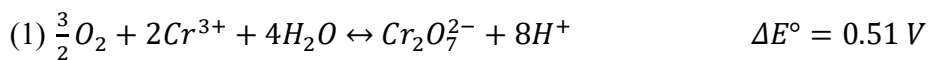
1.3.3 Chromium behavior in soils and groundwater

The speciation, solubility and distribution of chromium in soil and groundwater depend on the degree of weathering, the redox conditions, and the minerals present. Prior to chemical weathering of chromium-bearing parent material, chromium is primarily bound in a variety of host phases, including silicates such as pyroxenes (particularly spinels), amphiboles, and olivines (Shiraki 1997), as well as the aforementioned chromite, which also often contains Cr in the form of (oxyhydr)oxides such as eskolaite (α-Cr_2O_3) and guyanaite ($CrOOH$) (Anger et al. 2000). Native Cr has also been identified in some deposits, but is rarely encountered (Saha et al. 2011). After weathering, under circumneutral pH conditions, the trivalent form can precipitate as $Cr(OH)_3$, a very poorly-crystalline phase that is metastable in soils (Papassiopi et al., 2014; Rai et al., 2007). However, unlike similarly-structured Fe(III) oxides, transformation to crystalline Cr(III) (oxyhydr)oxide phases such as eskolaite and guyanaite has not been observed under surface conditions. Instead, X-ray absorption spectroscopy studies of Cr-bearing soils and sediments suggest that Cr(III) is primarily bound as a minor component of secondary silicate and Fe(III) oxide phases (Rose et al. 2006; Fandeur et al. 2009; Elzinga and Cirmo 2010), both in adsorbed and co-precipitated forms. Similarly, Fe (oxyhydr)oxides were suggested by Landrot et

al. (2012b) as the primary chromium host phase in soils affected by anthropogenic chromium contamination.

Thermodynamic modelling predicts the oxidation of Cr^{3+} to Cr^{6+} under oxic conditions. Although Cr^{3+} oxidation by dissolved O_2 is thermodynamically favorable under standard conditions (Eqn. 1), the rate of Cr^{3+} oxidation by dissolved O_2 is too slow to play a significant role in this transformation, so the transformation requires a MnO_2 intermediate (Eqn. 2). Biogenic Mn(IV) oxides, which have a similar structure to synthetic vernalite (δ-MnO_2) (Villalobos et al. 2003), form under oxic conditions and are believed to be the primary reagent mediating hexavalent chromium formation in soils and groundwater based on the results of lab- and field-based studies (Landrot et al. 2012a; Hausladen and Fendorf 2017; Pan et al. 2017). Oxidation occurs following dissolution of the Cr(III)-bearing solid and diffusion of Cr^{3+} to the oxidation site at the Mn(IV) oxide surface. The redox potential of this reaction is calculated in equations 1 and 2 using standard reduction potentials taken from Rumble et al. (2020). Once hexavalent chromium is produced, its high solubility means that precipitation as a solid phase is unlikely. Instead, chromate either remains in the aqueous phase or is incorporated into a solid phase such as an iron oxide.

(1) $\frac{3}{2}O_2 + 2Cr^{3+} + 4H_2O \leftrightarrow Cr_2O_7^{2-} + 8H^+$ $\qquad\qquad \Delta E° = 0.51\ V$

(2) $3MnO_2 + 6H^+ \leftrightarrow \frac{3}{2}O_2 + 3Mn^{2+} + 3H_2O$ $\qquad\qquad \Delta E° = 1.85\ V$

$3MnO_2 + 2Cr^{3+} + H_2O \leftrightarrow 3Mn^{2+} + Cr_2O_7^{2-} + 2H^+$ $\quad \Delta E° = 2.36\ V$

1.3.4 Remediation of chromium contamination

Groundwater chromium concentrations above approximately 50-100 µg/L (depending on the maximum contaminant level assigned by the governing body) require remediative efforts to reduce these concentrations to below the maximum contaminant level (World Health Organization 2017). Pump-and-treat, which utilizes a groundwater extraction well to remove chromium-contaminated groundwater from the subsurface, is the technology most often used, as it removes chromium from the system, is a mature technology that site remediation experts are familiar with, and is more effective when the targeted element is highly soluble (Palmer and Wittbrodt 1991; Nivas et al. 1996). However, characterizations of Cr-contaminated sites (Rose et al. 2006) have revealed that a majority of the Cr is bound in solid phases, as Cr(VI) adsorbs to mineral surfaces and Cr(III) is bound in various oxide and/or silicate phases. Therefore, it is possible that after pump-and-treat remediation is concluded, solid phase-bound Cr is released by dissolution and/or desorption and oxidized via the Mn(IV) oxide-mediated reactions outlined in Equations. 1 and 2, again increasing chromate concentrations to above the maximum contaminant level and necessitating continued remediation. *In situ* chemical reduction (ISCR) technologies, which remove chromium from groundwater by reducing it to Cr(III) with a chemical reagent (James 1996), therefore show promise as a means of converting chromium to a recalcitrant solid phase resistant to oxidation.

In situ chemical reduction technologies applied to remediation of hexavalent chromium typically rely on aqueous or structural Fe-mediated redox reactions, although there are exceptions. Simple addition of Fe^{2+} has been found to rapidly reduce chromate (Buerge and Hug 1997), and reduction is also effective when Fe^{2+} is paired with dithionite (Ludwig et al. 2007). In addition, many Fe(0) and Fe(II)-bearing particles have been tested as potential ISCR reagents for

chromium, with varying degrees of effectiveness. Both microscale and nanoscale zero-valent iron (ZVI) have been tested extensively in lab and field-scale experiments and are already widely-used commercially for these purposes, although lab-scale experiments indicated passivation of the ZVI surface (Wilkin et al. 2005; Lai and Lo 2008). Fe sulfides, including pyrite (Patterson et al. 1997), also were able to reduce chromate in lab-scale experiments. Finally, the chromate reduction ability of several Fe(II)-bearing oxides and phyllosilicates have been investigated, and reduction by oxides was the focus of the chromium remediation studies performed in the experiments presented below.

Magnetite (Kendelewicz et al. 2000) can reduce hexavalent chromium on relatively rapid timescales because of the high conductivity of electrons in its interior. However, the magnetite reactive surface is eventually passivated, and this study did not identify the Cr(III) carrier phase in the product. Chromate reduction by natural (Brigatti et al. 2000) and microbially-generated (Bishop et al. 2019) Fe(II)-bearing phyllosilicates occurs as a result of nanoscale electron transfer, which allows reduction of chromate in the interlayers and at the edges of the silicate particles. Reduction in the interlayer is expected to more effectively sequester the Cr(III) in the reaction product. Green rust sulfate, however, is the most promising Fe(II)-bearing potential ISCR reagent for treatment of hexavalent chromium, as its layered, clay-like structure and large pool of structural Fe(II) minimize the effects of passivation and can potentially allow incorporation of Cr(III) in the interior of the Fe(III) (oxyhydr)oxide reaction product.
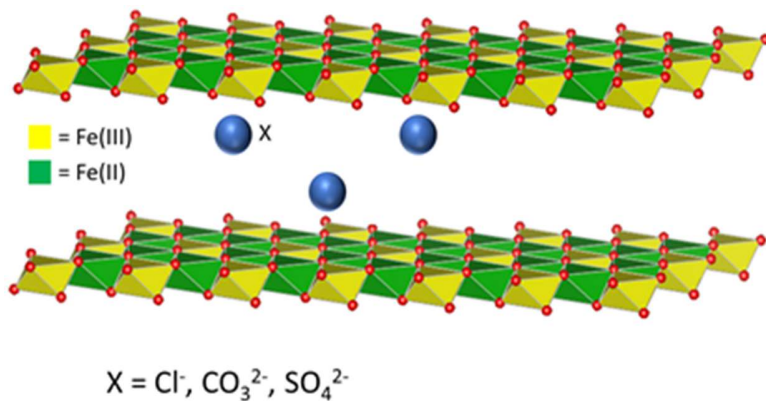
= Fe(III) (yellow)
= Fe(II) (green)

$X = Cl^-, CO_3^{2-}, SO_4^{2-}$

Figure 4 Crystal structure of green rust. Cr(VI) is reduced by structural Fe(II), which can be accessed by continual charge transfer to the crystal edges or exchange for interlayer sulfate. The second mechanism allows chromate to access the mineral's interior directly.

Green rust has a structure that allows access to the interlayer at its edges, potentially allowing reduction of chromium in the interlayer and formation of an insoluble, Cr(III)-bearing Fe (oxyhydr)oxide (Figure 4). Therefore, ISCR treatment of hexavalent chromium using green rust as a reagent has been investigated extensively, but the resulting product characterizations and mechanism descriptions vary, most likely because inconsistent synthetic and analytical methods were used. The twin studies of Loyaux-Lawniczak et al. (1999) and Loyaux-Lawniczak et al. (2000) examined the solid byproducts of green rust chloride and sulfate reacted with CrO_4^{2-} using X-ray diffraction (XRD), Raman spectroscopy, and X-ray photoelectron spectroscopy (XPS) and identified the product as a poorly ordered Cr(III)-Fe(III) oxyhydroxide resembling 2-line ferrihydrite. Bond and Fendorf (2003) reduced chromate with green rust sulfate, carbonate and chloride and proposed a dominant interlayer-exchange reaction mechanism. This was the first study to utilize extended X-ray absorption fine structure spectroscopy (EXAFS) to analyze the speciation of Cr in the reaction product; it identified a poorly ordered Cr(III)-Fe(III) oxyhydroxide. Williams and Scherer (2001) and Legrand et al. (2004) measured the kinetics of chromate reduction by green rust carbonate and identified the product as a Fe(III) oxyhydroxycarbonate. Finally, Skovbjerg et al. (2006) reacted concentrated chromate solutions with freshly prepared, untreated green rust sulfate and analyzed both partially and fully reacted solid samples. This study used transmission electron microscopy

and X-ray diffraction to identify Cr(III)-bearing goethite as the primary reaction product in the partially-reacted samples, formed via chromate exchange for sulfate in the interlayer. In this case, the unreacted Fe^{2+} remaining after the reaction most likely catalyzed the transformation of the poorly-crystalline product to goethite. In this dissertation, X-ray absorption spectroscopy (XAS) and XRD were used to characterize the structure and Cr speciation of the products of this reaction and relate these parameters to the lability of Cr bound within the products.

1.4   Arsenic Contamination and Remediation

1.4.1   Origin, distribution and applications

Arsenic, a Group 5 metalloid, is estimated to be the 47th most common element in the Earth's crust with an average concentration of 1.7 ppm (Wedepohl 1995). As a chalcophile, arsenic is concentrated in sulfide ore deposits, and weathering of this parent material is the primary mechanism by which environmental media can be contaminated by arsenic (Bowell et al. 2014). Within sulfide deposits, arsenic is found in a variety of forms, most commonly within sulfide minerals, the most common of which is arsenopyrite (FeAsS) (Craw et al. 2003). However, other sulfides such as orpiment (As_2S_3) and realgar (α-As_4S_4) are also significant sources (Mullen and Nowacki 1972). When exposed to oxidizing conditions at earth's surface, arsenic is transformed to either As(III) or As(V) (Savage et al. 2000), both of which exist in oxyanionic form [i.e. arsenite (H_3AsO_3) and arsenate (H_3AsO_4)]. Like chromium, the speciation of arsenic controls its solubility and bioavailability in environmental media (Bowell et al. 2014).

Arsenic has few industrial uses, most of which take advantage of its toxicity to insects, bacteria and fungi. Although many of these applications have been phased out in developed countries, arsenic has been used in wood treatment reagents (chromated copper arsenate)

(Rahman et al. 2004), insecticides (Peryea and Kammereck 1997), and animal feed additives

(Nachman et al. 2005). It is also an important component of several important alloys and

semiconductors, including lead components of car batteries and gallium arsenide, a

semiconductor used in integrated circuits (Blakemore 1982). However, most arsenic enters

environmental media via weathering of parent material with high As concentrations or as a waste

product of hardrock mining.

1.4.2 Toxicity, Environmental and Health Effects and Mobility
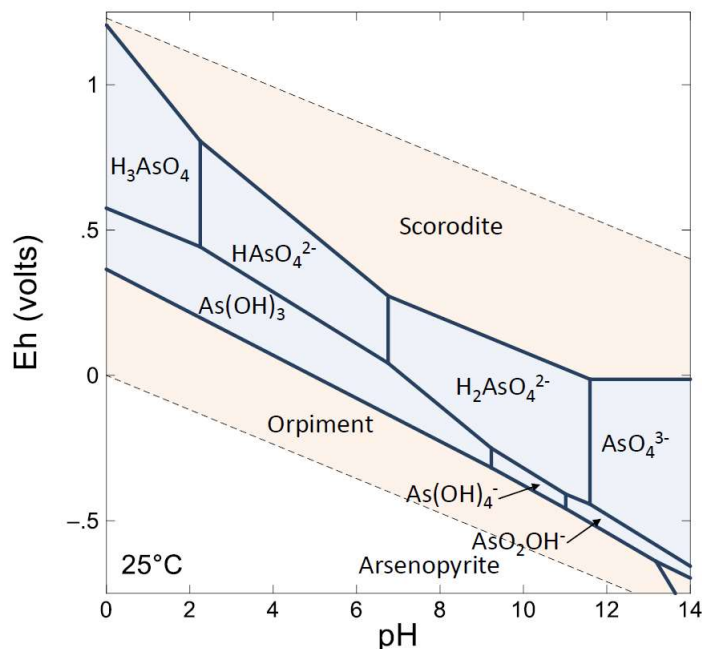
Figure 5 Phase diagram for As at a concentration of 0.1 mM As, Fe and S concentrations of 1.0 and 10.0 mM, respectively. Diagram generated using the Geochemist's Workbench software.

Figure 5 shows a phase diagram of arsenic in a Fe-As-S system. Under surface conditions

where sulfide concentrations are low, As exists primarily in one of two oxyanion forms: arsenite

(dominant under reducing conditions) and arsenate (dominant under oxidizing conditions).

Arsenic has several proposed mechanisms of toxicity. Trivalent arsenic has a known affinity for

thiols (Scott et al. 1993; Delnomdedieu et al. 1994), which are located at the active sites of many

enzymes and cofactors, allowing it to inhibit many cell functions. Pentavalent arsenic, on the other hand, can mimic phosphate and therefore disrupts cellular respiration via inhibition of the participating enzymes and spontaneous hydrolysis of arsenated intermediates (Lagunas 1980; Dixon 1996).

Occupational exposure and chronic consumption of contaminated drinking water are the most common arsenic exposure pathways, potentially leading to health problems such as cancer (Hughes 2002) and skin lesions (Cebrián et al. 1983). In particular, drinking water in south and southeast Asia is often contaminated by As released from sediments below the water table in response to varying pH and redox conditions (Nickson et al. 1998; Hossain 2006; Postma et al. 2012). Arsenic contamination derived from natural sediments and weathered mine tailings is a serious enough problem in the United States that the Agency for Toxic Substances and Disease Research (ATSDR) ranked it as the number one contaminant of concern at Superfund sites (ATSDR 2017). Based on toxicological studies, the WHO and most governmental bodies have set its allowable groundwater concentration at 0.01 mg/L (World Health Organization 2017).

Arsenic released by oxidative weathering of As-bearing sulfide minerals is primarily in the form of either arsenite or arsenate (Savage et al. 2000; Mandaliev et al. 2014), although organic arsenic compounds can be produced by microbes (Páez-Espino et al. 2009), but typically only make up a small portion of the total arsenic in a soil or groundwater sample. The mobility of these species is controlled by their interactions with the surrounding mineral assemblage Arsenite and arsenate species have a high affinity for iron oxides (Raven et al. 1998). Since both arsenic and iron oxides are common weathering products of sulfide ore deposits, these phases are usually the primary arsenic sink in soils and sediments (Arčon et al. 2005; Voegelin et al. 2007; Landrot et al. 2012a). Arsenate in particular has a high affinity for iron oxides, while arsenite is

more soluble in environmental media because of its lower affinity for these surfaces (Raven et al. 1998). In addition, other phases such as scorodite ($FeAsO_4 \cdot 2H_2O$) are known to precipitate at high arsenic concentrations (Arčon et al. 2005; Flemming et al. 2005). In acidic mine tailings, arsenate has been found to substitute for sulfate in secondary precipitates such as schwertmannite [$Fe_8O_8(OH)_6SO_4 \cdot nH_2O$] (Regenspurg and Peiffer 2005) and jarosite [$KFe_3(OH)_6(SO_4)_2$] (Paktunc and Dutrizac 2003; Savage et al. 2005).

The affinities of arsenite and arsenate for secondary iron oxide precipitates depend on the pH and redox characteristics of the groundwater. For example, the surface charge of iron oxides and the protonation states of arsenate and arsenite are pH-dependent. As a result, the strength of electrostatic interactions and the stability of inner-sphere surface complexes are pH-dependent, which manifests as a pH-dependent affinity of arsenic for Fe oxide surfaces (Bowell 1994; Raven et al. 1998). In addition, under reducing conditions, reductive dissolution of the iron oxide host phases or reduction of arsenate can result in release of arsenic to the aqueous phase. Fe oxides can catalyze the partial reduction of arsenate by an excess of aqueous Fe^{2+} (Nickson et al. 1998; Amstaetter et al. 2010; Ona-Nguema et al. 2010), particularly under acidic conditions (Eqn. 3). On the other hand, oxidation of arsenite to arsenate by O_2 is accelerated by microbial activity and the presence of Mn(IV) oxides (Manning et al. 2002), as is the case for Cr(III) oxidation (Eqns. 1-2).

(3) $H_3AsO_4 + 2H^+ + Fe^{2+} \leftrightarrow H_3AsO_3 + H_2O + Fe^{3+}$ ΔE° = -0.21 V
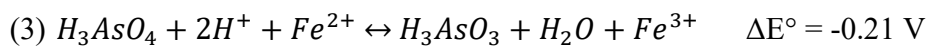
1.4.3   Techniques used for remediation of arsenic contamination

Traditional pump-and-treat methods are effective at removal of the labile fraction of arsenic from groundwater. However, other methods have been investigated and applied in the

field, including *in situ* chemical oxidation, bioremediation and phytoremediation. *In situ* chemical oxidation reagents such as Fenton's reagent (Fe^{2+}/H_2O_2) (Krishna et al. 2001), permanganate (MnO_4^-) (Sorlini and Gialdini 2010) and Mn(IV) oxides (Manning et al. 2002) can oxidize arsenite in groundwater to arsenate far more rapidly than O_2, increasing its affinity for Fe oxides in the soil. Certain microbial species can also oxidize arsenite to arsenate by using it as an electron donor under anoxic conditions. Alternatively, sulfate-reducing bacteria can use sulfate as an electron acceptor under anoxic conditions to produce sulfide (Rittle et al. 1995; Newman et al. 1997; Oremland et al. 2000; Omoregie et al. 2013), favoring the formation of As(III) sulfides as an As sink in reducing environments. Finally, phytoremediation utilizes plants resistant to arsenic poisoning to sequester As found near the soil surface. Plant exudates typically used to increase iron bioavailability also release As from near-surface iron oxide phases, causing uptake and sequestration of As by these plants (Fitz and Wenzel 2002; Rahman and Hasegawa 2011). However, application of these *in situ* techniques is only technically and economically feasible on a small scale; for large areas affected by groundwater As contamination such as the Bengal Delta, more-scalable strategies such as large-scale treatment of extracted groundwater or replacement of contaminated water supplies by other sources is more feasible.

1.5 Methods used and their environmental geochemistry applications

A variety of techniques have been utilized to characterize mineral phases in soil, including X-ray absorption spectroscopy for trace element speciation (Calvin 2013), X-ray diffraction for phase identification, characterization and quantification (Moore and Reynolds 1989), and electron microscopy methods for characterization of particle morphology as well as crystallographic and element analysis of small particles (Utsunomiya and Ewing 2003). The

following section outlines the potential applications and theoretical underpinnings of the applied techniques and explains how usage of each technique contributed to the present study.

1.5.1 X-ray absorption spectroscopy (XAS)

An X-ray absorption spectrum, which is obtained by measuring the absorption coefficient of a sample at a series of X-ray wavelengths above and below an ionization energy (referred to as an absorption edge), describes the average bonding environment of a selected element in the sample (Calvin 2013). The method is unique in its ability to identify trace element sequestration in amorphous phases, quantify the distribution of a trace element across multiple phases in a soil, identify phases present in a sample at concentrations below the limit of detection of X-ray diffraction (1-2%), and determine element-specific coordination environments (Manceau et al. 2002). XAS is best applied to measurements of high-Z elements, but low-Z elements can also be measured. Because a high-intensity source of X-rays with a wide range of photon energies is required to produce a useful XAS spectrum, these measurements are almost always performed at a synchrotron radiation facility.

After collecting and processing the raw data, the possible analyses depend on what is known about the sample (Calvin 2013). Analysis of the extended X-ray absorption fine structure spectroscopy (EXAFS) region (Gurman 1995), found in the oscillating portion of the spectrum far beyond the absorption edge, can reveal information about a trace element's structural environment within a range of approximately 10 Å, particularly if the researcher can postulate the most likely carrier phases based on what is known about the chemical behavior of the target element. For example, in the case of trivalent Cr bound in an Fe oxyhydroxide phase, it is likely that Cr replaces Fe in the oxyhydroxide structure and is octahedrally coordinated by (hydr)oxide groups, and the surrounding structure is characterized by motifs typical of iron oxide structures

such as edge- and corner-sharing octahedra. This allows fitting of a theoretical structure to the Fourier-transformed spectrum or linear combination fitting of a set of reference spectra. Alternatively, the X-ray near-edge spectroscopy (XANES) region near the absorption edge can provide information on the dominant oxidation state and immediate ($\leq$3.0 Å) coordination environment of the element of interest, which may be sufficient to identify the phase in which the element of interest is incorporated. Fitting of a theoretical structure to this region is also possible but beyond the scope of the present studies.

XAS is most useful when performed in combination with other techniques. For example, the technique is not able to identify phases not containing the target element, and electron-based techniques are better suited for nm- and Å-scale measurements, as they can be magnetically focused down to this scale and have de Broglie wavelengths of approximately 1 Å, an appropriate wavelength for high-resolution imaging and diffraction (Fultz and Howe 2013). In addition, there are other techniques such as μ-XAS that combine XAS measurements with mapping of element concentrations throughout the sample, therefore giving some spatial resolution to the analysis instead of simply measuring the average bonding environment (Majumdar et al. 2012).

XAS uses a tunable synchrotron X-ray source to produce a spectrum with variable absorption depending on the energy of the incident photon (Bunker 2010; Calvin 2013). An example of a typical normalized XAS spectrum is shown in Figure 6a. At the absorption K-edge (7127 eV), which corresponds to the energy required to remove one 1s electron from the investigated atom (Siegbahn 1916), absorption increases dramatically as the incident beam reaches a high enough energy to eject bound-state electrons from the central atom as a photoelectron, leaving a core-hole vacancy behind. Because this photoelectron has kinetic energy at incident beam energies higher than the edge, it scatters off of nearby atoms and returns to the
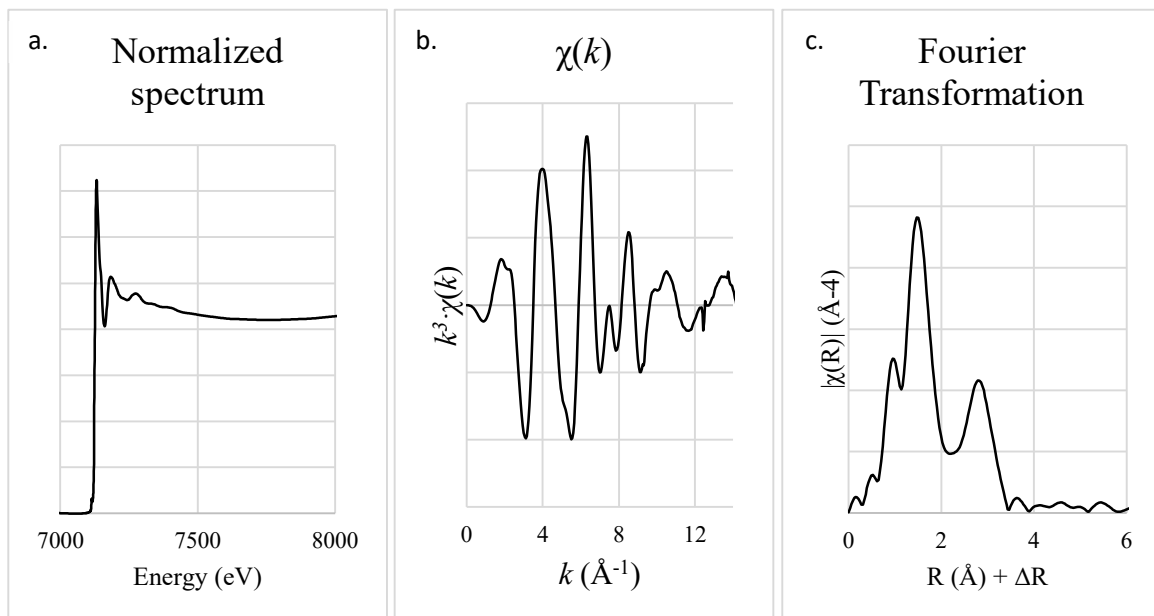
Figure 6 Normalized (a), $\chi(k)$ (b), and Fourier-transformed (c) Fe K-edge EXAFS spectrum.

"central atom" (Gurman 1995). Because the photoelectron exhibits wave-like properties as predicted by the de Broglie equation, it constructively or destructively interferes with itself at the central atom depending on its amplitude. Therefore, the absorption at a given incident beam energy depends on the electron's amplitude at the central atom, giving rise to a sinusoidal oscillation pattern in the post-edge region as photoelectrons with steadily decreasing de Broglie wavelengths are scattered in the surrounding lattice. This sinusoidal oscillation can be seen in

Figure 6b, where it is expressed as a multiple of $\chi(k)$, or the deviation from a background function in terms of the photoelectron wavenumber (Teo 2012). Figure 6c shows the Fourier transformation of this spectrum, which represents regions of high electron density surrounding the central atom at distances corresponding to the scattering path half-length (minus a phase shift). Potential scattering pathways identified in a theoretical structure can then be fit to the Fourier transformation.

A successful XAS analysis requires a high-flux, tunable X-ray source with a broad range of photon energies, a monochromator to select the desired photon energy, optics to control the beam width and flux, and detectors to quantify the absorption or fluorescence at each chosen measurement energy. These measurements must be performed at synchrotron facilities, which generate X-ray beams with a wide range of photon energies and sufficient intensity. First, electrons from an X-ray tube source are accelerated to relativistic velocities within a booster ring, then injected into a storage ring, where the experiments are actually conducted. A circular path is maintained by a series of bending magnets and insertion devices in the electron beam pathway, which simultaneously generate a tangential, high-intensity X-ray beam (Willmott 2011). For simplicity, only beam propagation by a bending magnet is described here; wigglers and undulators generate radiation by a similar mechanism but at a higher intensity (Elleaume 1992). Bending magnets are dipole magnets installed along curved sections of the storage ring. When an external magnetic field is applied to a moving electron, the Lorentz force ($e\vec{v} \times \vec{B}$) accelerates the electron in a direction perpendicular to both the direction of motion and the applied magnetic field (Margaritondo 1995), causing emission of high-intensity bremsstrahlung radiation, which is and adequate for XAS experiments. At relativistic electron velocities, there is an enormous Doppler shift from the point of view of an observer looking at an electron moving

in his direction, as the electron is moving nearly as fast as the emitted wavefront. As a result, radiation is emitted in a direction tangential to the storage ring.

The beam first passes through a series of filters, which remove low-energy photons to prevent overheating of the beamline components, and apertures, which limit the diameter of the beam (Willmott 2011). A double-crystal monochromator is then used to control the energy of light passing through the sample (Tohji and Udagawa 1988). XAS spectra are collected by measuring the absorbance in transmission or fluorescence mode at a series of regularly-spaced photon energies chosen by the monochromator. Two or three spectra are usually collected to check for inhomogeneity effects and beam damage, and to increase the signal-to-noise ratio in the averaged spectrum (Bunker 2010; Calvin 2013). The detectors used vary from simple ionization chambers used in transmission mode to large, multi-element, energy-discriminating fluorescence detectors (Cramer et al. 1988) capable of collecting multiple spectra simultaneously to increase the signal-to-noise ratio in the averaged spectrum. In addition, a reference foil with an edge within the energy range of the obtained spectrum is placed between two detectors downstream of the sample. This reference spectrum is used to calibrate the photon energy.

Prior to data analysis, the raw data must be processed. First, the incident photon energy is calibrated using the reference foil spectrum. Replicate scans are then averaged and the spectrum is normalized (Figure 6a) by subtracting pre- and post-edge background functions (Teo 2012). More detailed explanations of this procedure are available in the instruction manuals of software used for this purpose (i.e. Athena, WinXAS, etc.) (Ravel and Newville 2005; Webb 2005).

After the data is processed, linear combination fitting of a set of reference standards to the XANES region of this normalized spectrum or its derivative can be used for quantitative speciation of the target element. This kind of analysis is best suited for determining the dominant

oxidation states of the target element as well as the short-range (i.e. <2.5-3.0 Å) bonding

environment surrounding it (Wilke et al. 2001; Bare 2005; Yamamoto 2008). Fitting of the

XANES region is sometimes the only available option for analysis, as signal-to-noise ratios are

much higher in this region than in the EXAFS region (Calvin 2013). For analysis of the EXAFS

region, the spectrum is transformed to $\chi(k)$ (Figure 6b) by displaying the deviations from the

post-edge background function in terms of k, the wavenumber of the photoelectron (Teo 2012).

This transforms the spectrum into a function equal to a linear combination of sinusoidal

functions, each of which corresponds to a single photoelectron scattering pathway represented by

the EXAFS equation (Stern et al. 1980), a parameterized representation used to model EXAFS

spectra (Eqn. 4). Therefore, if the sample is composed of several phases that each contain the

target element, a linear combination fit of the EXAFS region quantifies the proportion of the

target element that is bound in each phase. This analysis depends on the availability of reference

spectra, so a great deal must already be known about the sample to perform it (Calvin 2013).

(Eqn. 4) $\qquad X(k) = S_0^2 \sum_i N_i \frac{f_i(k)}{k D_i^2} e^{i\frac{2D_i}{\lambda(k)}} e^{-2k^2\sigma_i^2} sin\left(2k D_i + \delta_i(k)\right)$

Finally, the technique most commonly used for XAS analysis is fitting of the Fourier-

transformed EXAFS spectrum to a theoretical structure (Teo 2012; Calvin 2013). This technique

requires less knowledge about the composition of the sample than other techniques, and does not

require collection of reference standard spectra. To perform an EXAFS fit using this method, the

fitting software starts with one or more theoretical photoelectron scattering path lengths extracted

from a model structure and systematically varies parameters from the EXAFS equation so that

the Fourier-transformed model and sample spectra match as closely as possible. The FEFF code

(Newville 2001) included in most software packages calculates the scattering amplitudes of each

potential pathway and can be used to identify which pathways are most likely to contribute to the

sample spectrum. If the sample deviates from the model structure, fitting components such as the coordination number (N_i), half path length (D_i) and Debye-Waller factor (σ^2) of a shell can quantify these differences and give a more accurate description of the structure surrounding the target element in a sample (Stern et al. 1980). However, there are disadvantages to this technique: it can be difficult to find an appropriate model structure if not much is known about the sample, correlations between parameters may require one or more to be fixed (lowering the quality of the fit), and it requires more theoretical knowledge of XAS than the linear combination fitting methods (Bunker 2010; Calvin 2013).

XAS was used in all of the scientific publications presented in this dissertation, and all XAS measurements were performed at the SUL-X beamline at the ANKA synchrotron facility in Karlsruhe. Thomas et al. (2018) and Thomas et al. (2020) used all three of the outlined analysis techniques to determine Fe and Cr speciation in the reacted green rust samples. In Thomas et al. (2018), the Fe K-edge $\chi(k)$ spectra were fit to a linear combination of feroxyhyte, goethite and lepidocrocite reference spectra. Although these discrete phases were not detected by other methods such as XRD, EXAFS fitting allowed the identification of short-range order structural motifs characteristic of these phases (i.e. edge- and corner-sharing octahedra) that were also found in the measured samples. Linear combination fitting showed that all samples after 7 days of reaction time were 80-90% feroxyhyte, with small contributions from goethite and lepidocrocite. The goethite contribution increased with the initial chromium concentration. As the samples were primarily composed of a feroxyhyte-like phase, we were able to conclude that the reaction of green rust with hexavalent chromium produced a layered product with a structure similar to green rust. Feroxyhyte has a similar structure to green rust, but the unit cell is smaller because of Fe^{3+} has a smaller ionic radius. To characterize the speciation of Cr, the Fourier-

transformed Cr K-edge spectra were fit to a theoretical standard. Based on previous EXAFS

analyses of poorly-crystalline Cr(III) hydroxides (Tang et al. 2010; Papassiopi et al. 2014a), the

fit was performed using three scattering path half-lengths at 1.97 Å (Cr-O), 3.05 Å (Cr-Cr edge-

sharing) and 3.9 Å (Cr-Cr corner sharing). The actual structure of Cr(III) hydroxide is undefined,

so similar scattering paths identified in goethite and lepidocrocite were used. The parameter

values determined in this fit showed that the primary Cr carrier phase in these samples resembled

Cr(III) hydroxide, suggesting that reduction of hexavalent chromium occurred at green rust's

surface, leading to precipitation of Cr(III) hydroxide at the surface and the rapid, topotactic

oxidation of green rust sulfate to a phase resembling feroxyhyte. Since the solubility of Cr in a

sample is linked to the fraction oxidizible by biogenic Mn(IV) oxides in soil (Landrot et al.

2012b; Hausladen and Fendorf 2017; Pan et al. 2017), identification of the primary Cr-bearing

phase using X-ray absorption spectroscopy can help determine the efficacy of *in situ* remediation

techniques in the laboratory.

Thomas et al. (2020) determined the Fe and Cr speciation of the reaction products of

hexavalent chromium and cation-substituted green rust sulfates using a different approach. The

Fourier-transformed Fe K-edge spectra were fit to a feroxyhyte theoretical standard and

compared to an actual feroxyhyte XAS spectrum, as linear combination fitting suggested that this

was again the predominant phase in the samples. Theoretical scattering paths with half path

lengths of 1.98 Å (Fe-O), 3.04 Å (Fe-Fe edge-sharing) and 3.4 Å (Fe-Fe corner-sharing) were

used to perform the fit. The reacted Al- and Mg-substituted green rusts most closely resembled

feroxyhyte, and X-ray diffraction patterns also showed reflections characteristic of feroxyhyte.

Cr speciation was analyzed by linear combination fitting of the XANES region. The features in

this region reflect the predominant oxidation state and short-range coordination environment

surrounding the central atom. Cr(III) hydroxide is easily distinguished from more crystalline Cr carrier phases using XANES, as it is octahedrally coordinated by hydroxide ligands in a symmetrical configuration as opposed to the more distorted octahedra found when Cr substitutes for Fe in ferrihydrite and goethite. XANES linear combination fitting of the Cr K-edge spectra showed that the proportion of Cr bound in Cr(III) hydroxide varied from 0.54 to 0.66. Substitution of Al and Mg within green rust's structure led to the formation of a Cr(III)-substituted Fe oxide product following reduction. Determination of the Cr(III) hydroxide fraction in the reaction products, when combined with treatment with δ-MnO_2 to determine the labile fraction of Cr in the reaction products, allowed assessment of the efficacy of green rust sulfate as a reagent for remediation.

XANES was also used to determine the speciation and carrier phases of arsenic in the two relevant publications presented in this dissertation. Perez et al. (2019) reacted arsenate adsorbed to ferrihydrite with aqueous Fe^{2+} at a series of concentrations. Linear combination fitting of the As K-edge XANES spectra, along with X-ray photoelectron spectroscopy, revealed that a portion of the arsenate was reduced to arsenite. The arsenite was adsorbed to ferrihydrite and goethite, which formed in the course of the experiment. The XAS analysis performed in this study was relatively simple, but was able to determine the proportion of As in each measured oxidation state (+3 and +5), an application that is possible even at very low elemental concentrations. In Wang et al. (2020), As K-edge XAS measurements were performed on diagenetically-altered peat sediment samples from northern China, with arsenic concentrations equal to or below 20 mg kg^{-1}. Because of the low signal to noise ratio of spectra obtained from samples with such low arsenic concentrations, only the XANES region of the spectra was usable. Nevertheless, linear combination XANES fitting was enough to determine the dominant arsenic

carrier phases in each sample when performed in combination with other techniques such as

μXRF (Voegelin et al. 2007; Landrot et al. 2012a). As a result of the differences in coordination

of arsenic within various Fe sulfide and oxide carrier phases, differentiation of these phases

using linear combination fitting in the XANES region was possible. Identification of specific

carrier phases was assisted by the application of μXRF, which was able to identify pyrite,

greigite and Fe(III) oxyhydroxide particles with detectable arsenic concentrations. The results of

this publication are a good example of how XAS measurements are most useful when the results

or compared to the results of other techniques, particularly when analysis of the spectra is

hindered by low elemental concentrations or adverse measurement conditions.

1.5.2   X-ray diffraction (XRD)

X-ray diffraction is used to identify mineral phases in a sample and to characterize these

phases (Rietveld 1969), as well as quantitative analysis of the mineralogical composition of a

sample (Ufer et al. 2008). XRD is most useful for analysis of crystal phases, which possess a

highly-ordered, periodic structure that extends in all directions (West 2014). The repeating unit

of a crystal is known as the unit cell. Within the unit cell is a set of atoms known as the basis,

while the Bravais lattice is an infinite array of points extending in all directions (Aroyo et al.

2006). These points are defined by translations of the unit cell in all crystallographic directions

and define the crystal's periodic structure. This periodicity, specifically the distance between

parallel planes defined by the unit cell coordinates, can be detected and quantified using X-ray

diffraction. Diffraction occurs because of scattering of the incident X-ray beam from atoms

within a crystal (Bish and Post 2018). As a result of the crystal's periodicity, photons scattered at

angles not equal to the Bragg angle (defined by Bragg's law, Eqn. 5) undergo deconstructive

interference, while Bragg peaks are detected because of constructive interference at angles where

this condition is met. In the Bragg equation, *d* is the periodic spacing, θ is the angle between the incident beam and the crystallographic plane, λ is the wavelength of the incident beam and *n* is the diffraction order. Other characteristics of a crystal can also be analyzed and quantified using XRD and an analysis technique called Rietveld refinement (Rietveld 1969). For example, the width of the Bragg peaks is a function of the crystallite size and its internal disorder (Patterson 1939), and poorly-crystalline phases such as ferrihydrite and amorphous silica produce broad diffraction patterns with no distinct peaks (Bish and Post 2018).

(Eqn. 5) $2dsin\theta = n\lambda$

When X-ray diffraction is performed on a powder sample, the resulting diffractogram shows the diffracted intensity as a function of 2θ. Bragg's law defines the positions of the diffraction peaks, but the basis, or the atoms within the unit cell and their positions, determines the intensity of these peaks (Als-Nielsen and McMorrow 2011). The diffractogram itself can be viewed as a Fourier transformation of the crystal structure, as each Bragg peak corresponds to a periodic structure within the crystal. A Fourier transformation of the lattice yields the positions of the Bragg peaks, while a Fourier transformation of the basis gives the structure factor (F_{hkl}), a function of the positions and form factors of its constituents (Warren 1969). A full mathematical treatment of this topic is beyond the scope of this dissertation, as the publications presented here used X-ray diffraction for phase identification.

Powder XRD is the preferred technique for experiments in geochemistry (Bish and Post 2018 and references therein) and is almost always performed using Bragg-Bentano geometry. The sample is loaded onto a sample holder, which is rotated while an X-ray source and a detector are rotated in an arc with the sample at the center. X-rays are generated by X-ray tubes, which emit radiation at a characteristic wavelength that depends on the metal used to construct the

tube's anode. These instruments return XRD patterns that show the intensity of the detected beam as a function of 2θ. Alternatively, diffraction patterns can be collected on imaging plates located perpendicular to the incident beam, similar to the first X-ray diffraction analyses, which used photographic plates to collect diffraction patterns from single-crystal and powdered samples. Today, this setup is primarily used for synchrotron-based XRD measurements. The patterns generated consist of a series of rings each corresponding to a Bragg peak. Conversion of this pattern to a Bragg-Bentano diffraction pattern requires integration of the detected intensity along each ring. Recalculation of 2θ is required for comparison to patterns collected using lab-based instruments because a different incident beam wavelength is used when collecting XRD patterns.

Powder XRD was performed on the pure and cation-substituted green rusts prior to and following reaction with hexavalent chromium. This data was used for a qualitative assessment of the composition of the unreacted and reacted reagents. XRD patterns of the green rust sulfate reagents were collected using a Bruker D8 diffractometer, which collects XRD patterns using Bragg-Bentano geometry. The unreacted green rusts were loaded onto a standard plastic sample holder and measured while they were still wet to prevent oxidation. Benchtop XRD patterns were collected using a Cu Kα source (λ = 1.5418 Å) between 2 and 82° 2θ with a step size of 0.2° and a measurement time of one second per step. Diffraction patterns of the reaction products were collected at beamline 11-ID-B at the Advanced Photon Source (APS) at Argonne National Laboratory. Samples were loaded into glass capillaries sealed with paraffin, and the diffraction patterns were collected using a beam with a photon energy of 58.66 keV (λ = 0.2113 Å) and an amorphous Si 2d detector located 100 cm from the sample. The 2D Laue patterns were converted to 1D diffraction patterns using the Fit2d software after calibrating the geometry using a CeO_2

standard. The GSAS-II software was then used to remove the background of the diffraction pattern and convert the photon energy to Cu Kα for comparison with the benchtop XRD patterns.

In Thomas et al. (2018), the XRD patterns suggested that the reagent used was in fact green rust sulfate and that suspension of green rust in water caused transformation to a mixture of ferrihydrite and magnetite. In addition, the reflections diffraction patterns measured after aging the reaction products for 11 months (Figure 7) are consistent with poorly-crystalline goethite, suggesting that the initial reaction products eventually transform to a mixture of Cr(III)-bearing goethite and Cr(III) hydroxide. It is likely that mineral transformation processes are able to sequester a portion of the reduced chromium in a stable phase. However, it may be possible to modify the reaction conditions in order to form these phases more quickly or sequester a larger proportion of chromium within them. The experiments in Thomas et al. (2020) were planned with this goal in mind. The diffraction patterns in Figure 7 are not included in Thomas et al. (2018) because they were obtained after this paper was published.
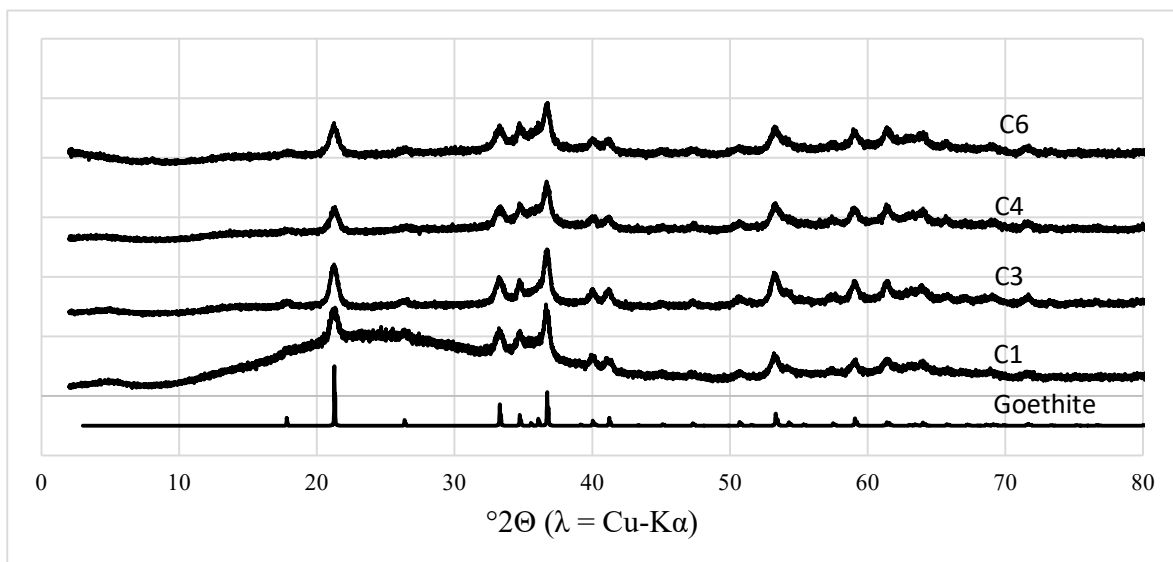

Figure 7 Powder XRD patterns of reacted samples from Thomas et al. (2018) aged for 11 months, with a goethite XRD pattern for comparison. C1, C3, C4 and C6 refer to initial chromium concentrations of 69, 14, 6.9 and 1.7 mg L^{-1}.

In Thomas et al. (2020), benchtop XRD was used to characterize the pure and substituted green rust sulfates before reacting them with hexavalent chromium, while synchrotron-based XRD was used to characterize the reaction products. X-ray diffraction analysis of Al-substituted green rust suggested that aluminum substitution increased green rust's structural disorder, while magnesium and zinc substitution did not have a substantial effect on crystallinity and caused only minor shifts in the peak positions. The XRD patterns of the reaction products had reflections consistent with feroxyhyte, although only the pattern of the Mg-green rust oxidation product had reflections corresponding to diffraction planes that were not parallel to the octahedral sheets. One possible explanation for this observation is that chromate is able to replace sulfate in Mg-green rust's interlayer and be incorporated into an Fe(III) oxyhydroxide, the overall goal of the experiment

1.5.3   Transmission electron microscopy (TEM)

Electron microscopes were developed to overcome the limitations in resolution and magnification of visible light microscopes (Fultz and Howe 2013). The maximum resolution of a microscope is a function of the wavelength of the light used, so the use of visible light (λ=400-700 nm) limits the maximum possible resolution to approximately 200 nm, making light microscopy insufficient for studies of particles with diameters of about 500 nm. Like all matter, electrons possess a de Broglie wavelength, the value of which is a function of the electron mass and its velocity. The electron wavelength at velocities used in electron microscopy is much shorter than that of visible light (~4 pm), so the maximum resolution possible with an electron microscope is as low as 0.1 nm, small enough to distinguish individual atoms. The primary difference between TEM and scanning electron microscopy (SEM) is whether backscattered or transmitted electrons are detected (Gauvin 1997). TEM detects the internal structure of particles

in the sample by measuring electrons that pass through the particles, while SEM produces an image of the sample's surface by detecting backscattered electrons. Therefore, proper sample preparation is essential, as the sample must be thin enough for the electrons to pass through. Electrons are also typically accelerated to higher energies for TEM measurements than for SEM measurements so the electrons can pass through the sample.

To perform TEM, a very thin sample is first loaded onto a sample holder composed of a low-Z element (i.e. carbon), then mounted between the electron source and the detector (Fultz and Howe 2013). Electrons are produced by a thermal or field emission source, then accelerated by a potential difference between the cathode and anode. Because magnetism is the most effective way of manipulating an electron beam, solenoid-based lenses focus and magnify the electron beam as it approaches the sample and project it onto the imaging device. After passing through the sample, the beam's intensity is detected at many points on an imaging plate, which is used to construct a magnified image. Contrast in the image results from differences in sample thickness, concentrations of high-Z elements that scatter electrons well, diffraction of the electron beam, and many other factors. A typical TEM image of a green rust particle reacted with hexavalent chromium is shown in Figure 8a.
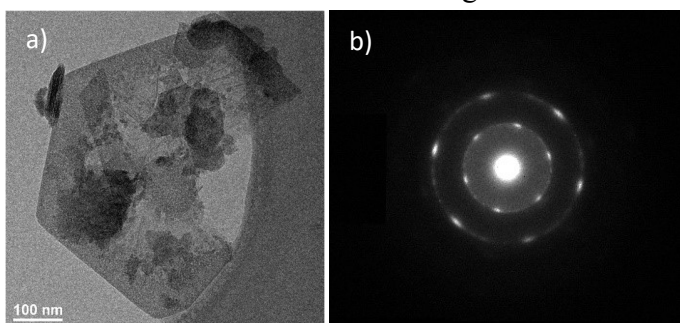

Figure 8 Typical TEM image (a) of an Al/Zn-substituted green rust particle reacted with hexavalent chromium and allowed to age for seven days. Representative SAED pattern (b) is also included.

Electron interactions with matter are similar to those of photons with similar wavelengths. Therefore, TEM instruments are capable of a wide variety of other measurements

that can characterize a sample on a smaller scale. Many of these techniques are similar to X-ray diffraction and spectroscopy methods, but a higher resolution is achievable (Fultz and Howe 2013). Selected-area electron diffraction (SAED) is used to identify crystalline phases in a sample by collecting a diffraction pattern from one or more particles in the electron beam (Gauvin 1997). The sample is exposed to a beam of high-energy electrons that can easily pass through, and a portion of these electrons are diffracted onto an imaging plate by crystallographic planes that satisfy the Bragg condition, producing a pattern similar to Figure 8b. The corresponding spacing can then be calculated and indexed to a matching phase. Another method, energy-dispersive X-ray spectroscopy (EDX), uses fluoresced X-rays to determine the elemental composition of the illuminated portion of the sample (Fultz and Howe 2013). This technique is analogous to X-ray fluorescence spectroscopy. Electrons with sufficiently high energy can excite an inner shell electron, leaving a vacancy that is filled by an electron from a higher energy shell, releasing a photon with an energy equal to the energy difference between the two shells. The emitted X-rays are detected and sorted into a spectrum by an energy-dispersive detector (see figure 9), and the elemental concentrations of the irradiated area are calculated from measured fluorescence at characteristic energies. A technique known as EDX mapping can also generate elemental composition maps by collecting an EDX spectrum at a selection of points.

This dissertation features TEM images, SAED patterns, and EDX results from three of the four studies. TEM samples were prepared by resuspension in ethanol and drop casting onto a 3 mm Cu-TEM grid covered by a porous carbon film. The samples were then loaded into a single-tilt sample holder and transferred into the TEM device, which measures under vacuum conditions. within 30 seconds to prevent oxidation of the sample. The microscope used was a FEI Tecnai TEM equipped with a Gatan Tridium imaging filter, an EDX analyzer, a charge-
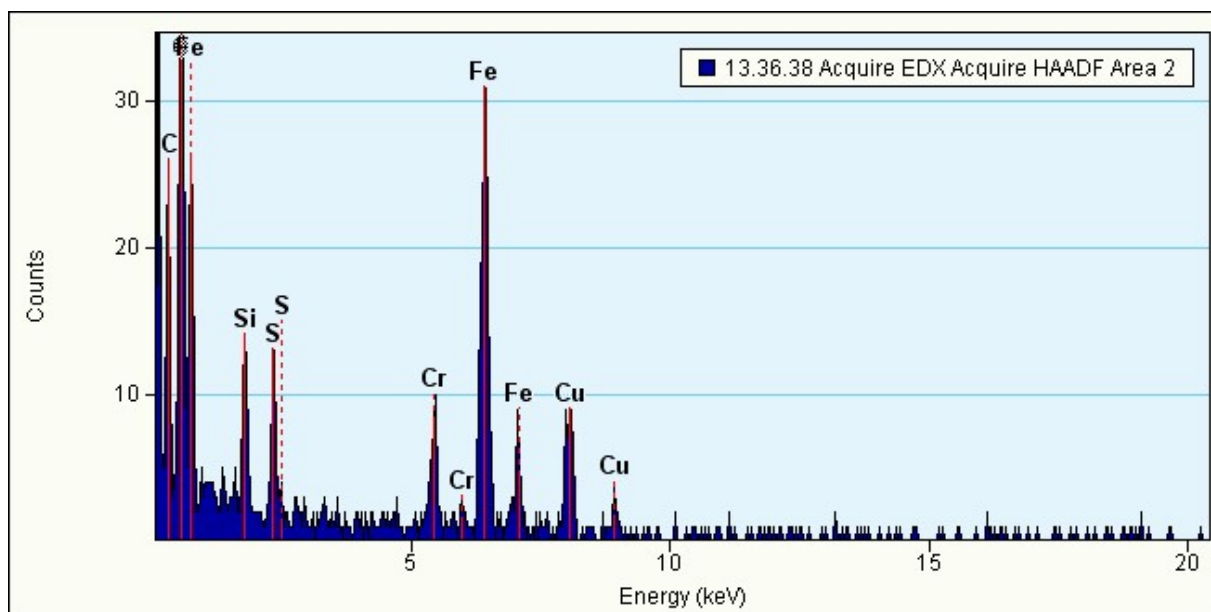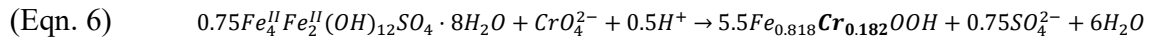
Figure 9 Example EDX spectrum produced by the transmission electron microscope at GFZ.

coupled device (CCD) camera, and a Ditabis Imaging Plate Scanner for collection of SAED

patterns. Thomas et al. (2018) and Thomas et al. (2020) used TEM imaging to show that the

reacted particles maintained their hexagonal morphology but displayed morphological changes.

In addition, particles with globular and rod-like morphologies also developed but could be

identified using the available techniques. SAED patterns showed that these particles also

maintained their hexagonal unit cells, but with a decrease in crystallinity. Analysis of the full-

width half maximum (FWHM) of the reflections in these patterns showed that their disorder was

correlated to the disorder of the corresponding reflections in the XRD patterns. An EDX analysis

showed that the Fe:Cr ratios of the reacted hexagonal particles were similar to the theoretical

ratios calculated from the balanced equation (Eqn. 6), and there was some removal of sulfate

from the green rust interlayers, as sulfur concentrations in these particles were lower than

unreacted green rust. However, this last result should be treated with caution, as sulfur X-ray

fluorescence is inefficient and measurements of sulfur concentrations using this method have a low signal-to-noise ratio.

(Eqn. 6) $\quad 0.75Fe_4^{II}Fe_2^{II}(OH)_{12}SO_4 \cdot 8H_2O + CrO_4^{2-} + 0.5H^+ \rightarrow 5.5Fe_{0.818}\boldsymbol{Cr_{0.182}}OOH + 0.75SO_4^{2-} + 6H_2O$

Perez et al. (2019) collected TEM images of the As(V)-ferrihydrite samples following a 24 hour exposure to high concentrations of aqueous Fe^{2+}. These images showed residual As(V)-ferrihydrite, easily visible because of its globular morphology. In addition, these images showed particles of green rust sulfate and goethite that had formed from ferrihydrite via a Fe^{2+}-catalyzed transformation mechanism. These images provided further evidence that these phases had formed and showed their spatial relationship to each other, which suggested that green rust sulfate was able to form topotactically from a ferrihydrite precursor. The identities of these phases were confirmed using SAED and Fourier transformation of high-resolution TEM images, which are mathematically equivalent.

2. Hexavalent Chromium Reduction by Green Rust Sulfate

The first study (Thomas et al. 2018) presented in this dissertation examined the reduction of hexavalent chromium at different concentrations by synthetic green rust sulfate. The efficacy of in vitro Cr(VI) reduction by green rust sulfate suggests that it is potentially useful for remediation of Cr-contaminated groundwater. Previous investigations studied this reaction but did not sufficiently characterize the intermediates and end products at chromate (CrO_4^{2-}) concentrations typical of contaminant plumes, hindering identification of the dominant reaction mechanisms under these conditions. Because the mobility of chromium depends on its chemical speciation, knowledge of the host phases of chromium in the reaction products is essential for the

accurate prediction of the long-term viability of green rust as an *in situ* chemical reagent for groundwater remediation.

In this study, batch reactions at varying chromate concentrations and suspension densities were performed and the intermediate and final products of this reaction were analyzed using X-ray absorption spectroscopy and electron microscopy. The reaction produced particles that maintained the initial hexagonal morphology of green rust but were topotactically transformed into poorly crystalline Fe(III) oxyhydroxysulfates coated by a Cr (oxy) hydroxide layer that results from chromate reduction at the surface. Recent studies of the behavior of Cr(III) (oxy) hydroxides in soils have revealed that reductive transformation of CrO_4^{2-} is reversible in the presence of Mn(IV) oxides, limiting the applicability of green rust for Cr remediation in some soils. Modification of the green rust reactant particles so that an insoluble, Cr(III)-bearing Fe oxide product such as goethite is produced would increase the long-term stability of the reaction products. Therefore, future studies should focus on modifying the reagent particles so that the production of these reaction products is favored.

3. Hexavalent Chromium Reduction by Cation-Substituted Green Rusts

Chromium contamination is a serious environmental issue in areas affected by leather tanning and metal plating (Saha et al. 2011), and green rust sulfate has been tested extensively as a potential material for *in situ* chemical reduction of hexavalent chromium in groundwater (Thomas et al. 2018 and references therein). The long-term stability of the reduced Cr within the reaction products depends on the stability of the Cr host phases. This in turn depends on the mechanism of the green rust-chromium reaction, as reduction of chromium at the edges of the green rust particle preferentially produces the less stable poorly-crystalline Cr hydroxide in a

reaction coupled to electron transport from the interior of the particle. These transport processes can potentially be hindered by substitution of metal cations such as Al, Mg and/or Zn for Fe within the green rust crystal, as these metal cations do not have multiple stable oxidation states and are therefore unable to accept electrons from or donate electrons to the electron transport chain. In addition, these cations may interfere with the superexchange coupling that drives rapid electron transfer (Alexandrov and Rosso 2014) to the surfaces of the green rust particle. This may instead favor the production of more stable Cr-bearing iron oxide particles, which are predicted to form when Cr is instead reduced within green rust's interlayer (Skovbjerg et al. 2006).

In the second study of Cr reduction by green rust sulfate (Thomas et al 2020), synthetic green rusts with substitutions of Al, Mg and Zn were synthesized and used to reduce hexavalent Cr in batch reactions. Reported products and mechanisms for the reaction have varied, most likely because of green rust's layered structure, where reduction at outer and interlayer surfaces might result in different products with variable stabilities (Skovbjerg et al. 2006). Based on studies of Cr(III) oxidation by biogenic Mn (IV) oxides (Villalobos et al. 2003; Landrot et al. 2012b; Pan et al. 2017), Cr mobility in oxic soils is controlled by the solubility of the Cr(III)-bearing phase. Therefore, careful engineering of green rust properties, i.e., crystal/particle size, morphology, structure, and electron availability, is essential for its optimization as a remediation reagent.

In this study, pure green rust sulfate and green rust sulfate with Al, Mg and Zn substitutions were synthesized and reacted with identical 0.67 mM chromate (CrO_4^{2-}) solutions. The reaction products were characterized by X-ray diffraction, pair distribution function analysis, X-ray absorption spectroscopy and transmission electron microscopy. In addition, a

synthetic δ-MnO_2 suspension was added to the reaction product to assess how easily Cr(III) in the products could be oxidized. It was found that Cr in the Mg-green rust reaction product had the lowest labile fraction, as 2.5% of the Cr(III) present in the reacted Mg-substituted green rust was oxidized by δ-MnO_2 within 14 days, compared to 7% of the Cr bound in the pure and Zn-substituted green rust reaction products, while 4.5% of the Cr in the Al-substituted green rust reaction product was oxidized by δ-MnO_2.

Additionally, the particle structure and Cr speciation observed during X-ray scattering and absorption analyses of this product suggested that Cr(VI) was reduced in its interlayer. The most consistent explanation for these effects is that substitution of Al and Mg, which have one possible oxidation state and no net electronic spin, disrupts electron transfer from the interior to the edges of the green rust crystal, slowing regeneration of reactive Fe(II) at the edges. If regeneration at the edges is insufficiently rapid to drive Cr reduction at these sites, a greater proportion of Cr is reduced in green rust's interlayer following exchange for sulfate, as this allows access to Fe(II) in green rust's interior. Based on the results of this and similar studies (Bond and Fendorf 2003; Skovbjerg et al. 2006; Thomas et al. 2018), further improvements can also be made to this remediation technique by treating chromate with an excess of green rust sulfate (i.e. $[Fe(II)] > 3*[Cr(VI)]$, the stoichiometric ratio of the reaction). This provides excess Fe(II) that can catalyze reductive transformation of the reaction products to more crystalline iron oxides (Vempati and Loeppert 1989; Cornell and Schwertmann 2003). Synthesis of the reactant under alkaline conditions, which has been shown to favor chromium reduction in the interlayer of Fe(II)-bearing phyllosilicates (Bishop et al. 2014, 2019), may also favor the production of a Cr-substituted Fe(III) oxyhydroxide reaction product.

4. Surface-Mediated Reduction of Arsenate by Fe^{2+}

Perez et al. (2019) tested the role of Fe oxide surfaces in mediating arsenic redox transformations in soils. To assess the fate of arsenate [As(V)] in subsurface settings, the Fe^{2+}-induced transformation of As(V)-bearing ferrihydrite to more crystalline phases under environmentally relevant anoxic subsurface conditions was investigated. At all initial ratios of Fe^{2+}(aq) to solid-bound Fe(III) in ferrihydrite [Fe(III)$_{Fh}$], formation of goethite, green rust sulfate, and were observed within the first two hours of the reaction. At low Fe^{2+}(aq)/Fe(III)$_{Fh}$ ratios (0.5 to 1), green rust sulfate and/or lepidocrocite that formed initially dissolved as the reaction progressed, and only goethite and some unreacted ferrihydrite remained after 24 h. At an Fe^{2+}(aq)/Fe(III)$_{Fh}$ ratio of 2, green rust sulfate remained stable throughout the 24 h of reaction, alongside goethite and unreacted As(V)-ferrihydrite. Despite the fact that the majority of the initial As(V)-ferrihydrite transformed to other phases, the initially adsorbed As was not released into solution during the transformation reactions, and ~99.9% of it remained bound in an Fe(III) (oxy)hydroxide phase. Nevertheless, the initial As(V) was partially reduced to As(III), most likely because of the surface-associated Fe^{2+}-goethite redox couple. The extent of As(V) reduction increased from ~34% to ~40%, as the Fe^{2+}(aq)/Fe(III)$_{Fh}$ ratio increased from 0.5 to 2.

Previous studies of Fe^{2+} interactions with Fe oxides found that adsorption of Fe^{2+} to oxide surfaces can lead to electron transfer into the interior of the mineral (Stone and Morgan 1987; Cornell and Schwertmann 2003). This destabilizes the mineral, as the ionic radius of Fe^{2+} is considerably higher than that of Fe^{3+}. As a result, the reduced mineral is in a high-energy transition state, which can lower the energy barrier and increase the rate of subsequent reaction steps. In this experiment, addition of Fe^{2+} led to both ferrihydrite transformation to goethite and the reduction of As(V) adsorbed to the ferrihydrite surface. The results of this study showed that

Fe^{2+}(aq) can catalyze transformations of poorly-crystalline Fe (oxyhydr)oxides to more crystalline phases such as goethite with lower surface adsorption capacities and the reduction of As(V) to its more labile trivalent form. However, the study was not able to demonstrate that this leads to higher As solubility. It is possible that the initial arsenic levels in this experiment were significantly lower than the adsorption capacities of all reaction and product Fe(III) (oxyhydr)oxide phases, and the equilibrium aqueous As concentrations were therefore negligible.

5. Arsenic Speciation and Mobility in a Natural Sediment

The other As-focused publication referenced in this dissertation (Wang et al., 2020) analyzed the mineralogy and As speciation in diagenetically-altered peat deposits in a lacustrine sediment basin in northern China. Areal peat deposits are widely distributed in the lacustrine sediment basins of northern China, including Hetao Basin, Datong Basin and Huhhot Basin. As has been identified as a contaminant of concern in these areas (Guo et al. 2008, 2012, 2013; Jia et al. 2017), but the Fe and As speciation controlling the mobility of As in these sediments is unknown. In this study, X-ray absorption and ^{57}Fe Mössbauer spectroscopy in combination with electron microscopy were used to analyze the S, Fe and As speciation in three centimeter-thick peat layers separated from late Pleistocene lacustrine sediments of the Hetao Basin.

It was found that the organic carbon in the peat layers promotes the microbially-driven formation of specific sulfide minerals during the diagenetic mineralization process; pyrite (FeS_2) and metastable greigite (Fe_3S_4) are found in the peat layers as the end products of these diagenetic processes. Pyrite nucleation most likely occurs via the polysulfide pathway (Wilkin and Barnes 1997; Rickard and Luther 2007), whereas greigite primarily nucleates on the surface of phyllosilicate and gypsum/anhydrite particles and within plant tissues. In particularly greigite-

rich samples, the portion of the sulfur bound in greigite was as high as 90%. The relative enrichment of reactive Fe to sulfide most likely inhibits the transformation of greigite to pyrite in layers with less organic carbon (Lennie et al. 1997).

Pyrite crystallites have As contents ranging from < 90 to 11,000 mg/kg. The majority of the As substitutes for sulfur in pyrite, which accounts for ~60 % of the bulk As (~250 mg/kg) in the pyrite-enriched peat layer. Compared to pyrite, greigite crystallites have relatively constant As contents ranging from ~500 to ~1400 mg/kg and incorporate ~40 % of the total As (~50 mg/kg) in the greigite-enriched peat layer. The XANES fitting results suggest that instead of adsorbing to the greigite surface, As forms As-sulfide bonds with sulfur contributed by greigite. This bonding environment is chemically similar to realgar and was identified as such by XANES. Ferrihydrite with high As content was also observed, in some cases as a precipitate directly on the pyrite particle surfaces, suggesting that ferrihydrite forms as an oxidation product of pyrite. The reductive dissolution of the relatively freshly-formed ferrihydrite and subsequent As re-release via mechanisms explored by Perez et al. (2019) may potentially be a source of the As found in groundwater at the Hetao Basin site (Guo et al. 2008, 2012, 2013; Jia et al. 2017).

6. Summary

Based on the results of the above laboratory studies with green rust sulfate and chromium, it appears that green rust is an effective reagent for *in situ* chemical reduction of hexavalent chromium, although its effectiveness varies. The presence of reaction sites in green rust sulfate's interlayer allows the subsequent incorporation of chromium in the interior of the recalcitrant reaction byproduct particles, but the kinetics of the interlayer reaction mechanism compared to other reaction mechanisms that produce less stable reaction products are dependent

on the reaction conditions and the properties of the green rust reactants. For example, increasing the initial aqueous Cr(VI) concentration results in a larger portion of the Cr reacting within green rust's interlayer, and isomorphic substitution of magnesium and aluminum further increases the favorability of this reaction mechanism and the effectiveness of the green rust reagent by interfering with electron transport from the particle interior to reactive sites at its surface. This instead favors chromate exchange for interlayer sulfate and sequestration of trivalent chromium within the byproduct's interior. Column- and field-scale tests of these chemically-modified green rusts should be performed in order to determine whether these lab-scale results can be reproduced in the field.

The studies in this dissertation focused on the effects of initial Cr(VI) concentration and the chemical composition of green rust on products of this reaction. However, the effects of other green rust properties such as particle size and pH-dependent surface charge have not yet been determined. Theoretically, the size of the green rust particle may have an effect on the ability of the chromate anion to diffuse into green rust's interlayer, as diffusion into the center of larger particles is a slower process. Also, as a metal hydroxide mineral, green rust has a pH-dependent surface charge that affects the ability of chromate to adsorb to the green rust particle surface (Guilbaud et al. 2013). This is the rate-limiting step of the adsorption-mediated reaction mechanism; therefore, synthesis of green rust under more alkaline conditions, leading to a negative surface charge, may hinder chromate sorption and instead favor exchange of chromate for interlayer sulfate and reduction in the interlayer.

Biogenic Mn(IV) oxides mediate the oxidation of several common metal(loid) contaminants in soils, including chromium (Landrot et al. 2012b; Butler et al. 2015; Pan et al. 2017) and arsenic (Driehaus et al. 1995), and the synthetic Mn(IV) oxide assay developed in this

study is an effective method of determining the efficacy of *in situ* chemical reduction methods in the laboratory. The method presented in this dissertation (addition of pure δ-MnO$_2$, pH of suspension adjusted to 7.0, and sonicated prior to use to ensure maximum dispersion) was designed to determine the maximum possible oxidizable fraction of Cr at circumneutral pH values in the measured reaction products in order to avoid inconsistencies in the method. The actual labile fraction, even in soils with high levels of Mn(IV) oxides, is likely to be lower. Due to these inconsistencies, this method is most useful for direct comparisons between remediation methods. Column and/or field studies are more appropriate for determining the actual stability of the reaction products.

The behavior of arsenic in soils and sediments is more complex, and further research is necessary to develop effective remediation technologies. *In situ* chemical remediation of arsenic typically depends on conversion of arsenic to its pentavalent (arsenate, which is then immobilized by Fe(III) (oxyhydr)oxides) or trivalent (allowing sequestration in Fe sulfide phases in the right chemical environments) chemical states. Although these chemical transformations are initially effective for arsenic sequestration, they appear to be reversible if groundwater conditions change, as is the case for chromium. Perez et al. (2019) found that although ferrihydrite is an effective sink for pentavalent arsenic, its presence in soils and sediments under reducing conditions can accelerate the reduction of arsenic to its trivalent form and subsequent remobilization, although remobilization was not observed under the experimental conditions used. This has implications in sediments with naturally high arsenic concentrations and arsenic-affected areas where *in situ* treatment is applied. However, this transformation depends on the unstable transition state that forms from the transfer of an electron from aqueous Fe^{2+} to ferrihydrite's interior, and the transformation of this transition state to goethite is then coupled to

the reduction of arsenate adsorbed to the particle surface. Alternatively, if arsenic is associated with a more stable Fe(III) (oxyhydr)oxide phase such as goethite or hematite, formation of the transition state that drives arsenate reduction is less favorable and arsenate is protected from reduction by Fe^{2+}. Arsenate adsorbed to goethite and hematite surfaces was resistant to reduction and desorption in the presence of Fe^{2+} (Catalano et al. 2011), and Amstaetter et al. (2010) found that As(III) oxidation to As(V) takes place under these conditions. This suggests that goethite and hematite are more effective sinks for As(V) than ferrihydrite despite their lower surface areas.

Similarly, our study of arsenic speciation in altered peat sediments provided valuable insights into arsenic partitioning into during diagenetic alterations to soil and sediments that may be applicable to contaminated sites. Because geogenic arsenic contamination is widespread in south and southeast Asia, further field studies of arsenic behavior under varying chemical regimes should be performed to refine our knowledge of As mobilization and sequestration in response to changes in groundwater redox conditions. Of particular interest is the possibility of sequestering groundwater As in sulfide phases. Although these phases can effectively sequester As, they are easily oxidized and may not be useful for *in situ* remediation of As in groundwater in environments with dynamic groundwater conditions. The stability of As within the Fe(III) oxyhydroxide phases that form following sulfide oxidation is unknown, and it is likely that the chemical conditions necessary to catalyze As reduction by this mechanism (reducing environment, sufficiently high $[Fe^{2+}]$) were not encountered within the sediments sampled in the course of this experiment. Exposure of oxidized sediment samples to these conditions as outlined in Perez et al. (2019) may provide further insights into the potential fate of As in these environments.

Pure and modified green rusts are also promising as reagents for the removal of chromium from pumped groundwater, as this treatment can occur under controlled conditions and favors the formation of stable, Cr(III) bearing goethite. Existing reagents used for this purpose include ion exchange resins and activated carbon, which can remove chromate effectively, but their disposal is difficult and expensive because the associated chromium is still in its hexavalent state. On the other hand, green rust synthesis is easy and inexpensive (only inexpensive metal sulfate salts are required), and because Cr-bearing goethite is stable, it is possible that no additional precautions must be taken during its disposal. A scientific study using the MnO_2 assay outlined above to measure the lability of Cr in the product produced in a similar green rust sulfate reaction vessel under controlled conditions could effectively determine the stability of Cr in the reacted green rust reagent. Similarly, arsenic sequestration in Fe oxide and sulfide phases can be more effectively applied to above-ground treatment of pumped groundwater, as the treatment itself and disposal of the byproducts can occur under controlled conditions. Arsenic can easily be removed from pumped groundwater by synthetic iron oxides installed in place of an ion exchange resin or activated carbon. This would reduce the cost of remediation because iron oxides can be synthesized or mined more cheaply than presently used technologies, although their use would most likely not result in a decrease in disposal costs, however, as the associated arsenic is still toxic and must be disposed of properly.

Acknowledgements

References

Alexandrov, V., and Rosso, K.M. (2014) Electron transport in pure and substituted iron oxyhydroxides by small-polaron migration. Journal of Chemical Physics, 140.

Allen, B.L., and Hajek, B.F. (1989) Mineral occurrence in soil environments. Minerals in soil environments, 1, 199–278.

Als-Nielsen, J., and McMorrow, D. (2011) Elements of Modern X-Ray Physics, 2nd Ed. John Wiley and Sons, Chichester, UK.

Amstaetter, K., Borch, T., Larese-Casanova, P., and Kappler, A. (2010) Redox Transformation of Arsenic by Fe(II)-Activated Goethite (α-FeOOH). Environmental Science & Technology, 44, 102–108.

Anger, G., Halstenberg, J., Hochgeschwender, K., Scherhag, C., Korallus, U., Knopf, H., Schmidt, P., and Ohlinger, M. (2000) Chromium Compounds. In Ullmann's Encyclopedia of Industrial Chemistry. Wiley-VCH Verlag GmbH & Co. KGaA, Weinheim, Germany.

Apte, A., Verma, S., Tare, V., and Bose, P. (2005) Oxidation of Cr(III) in tannery sludge to Cr(VI): Field observations and theoretical assessment. Journal of Hazardous Materials, 121, 215–222.

Arčon, I., van Elteren, J.T., Glass, H.J., Kodre, A., and Šlejkovec, Z. (2005) EXAFS and XANES study of arsenic in contaminated soil. X-Ray Spectrometry, 34, 435–438.

Aroyo, M.I., Müller, U., and Wondratschek, H. (2006) Historical introduction. In International Tables for Crystallography pp. 2–5. International Union of Crystallography, Chester, England.

ATSDR (2017) The ATSDR 2017 Substance Priority List.

Bach, D., Christiansen, B.C., Schild, D., and Geckeis, H. (2014) TEM study of Green Rust Sodium Sulphate ($GR_{Na,SO4}$) Interacted with Neptunyl Ions (NpO_2^+). Radiochimica Acta, 102.

Barceloux, D.G., and Barceloux, D. (1999) Chromium. Journal of Toxicology: Clinical Toxicology, 37, 173–194.

Bare, S.R. (2005) XANES measurements and interpretation. EXAFS Data Collection and Analysis Course, Advanced Photon Source, July, 26, 29.

Bechine, K., Subrt, J., Hanslik, T., Zapletal, V., Tlaskal, J., Lipka, J., Sedlak, B., and Rotter, M. (1982) Transformation of synthetic y-FeOOH (lepidocrocite) in aqueous solutions of ferrous sulphate. Zeitschrift für anorganische und allgemeine Chemie, 489, 186–196.

Bish, D.L., and Post, J.E., Eds. (2018) Modern Powder Diffraction. De Gruyter, Berlin, Boston.

Bishop, M.E., Glasser, P., Dong, H., Arey, B., and Kovarik, L. (2014) Reduction and immobilization of hexavalent chromium by microbially reduced Fe-bearing clay minerals. Geochimica et Cosmochimica Acta, 133, 186–203.

Bishop, M.E., Dong, H., Glasser, P., Briggs, B.R., Pentrak, M., Stucki, J.W., Boyanov, M.I., Kemner, K.M., and Kovarik, L. (2019) Reactivity of redox cycled Fe-bearing subsurface sediments towards hexavalent chromium reduction. Geochimica et Cosmochimica Acta, 252, 88–106.

Blakemore, J.S. (1982) Semiconducting and other major properties of gallium arsenide. Journal of Applied Physics, 53, R123–R181.

Bond, D.L., and Fendorf, S. (2003) Kinetics and Structural Constraints of Chromate Reduction by Green Rusts. Environmental Science & Technology, 37, 2750–2757.

Bowell, R.J. (1994) Sorption of arsenic by iron oxides and oxyhydroxides in soils. Applied Geochemistry, 9, 279–286.

Bowell, R.J., Alpers, C.N., Jamieson, H.E., Nordstrom, D.K., and Majzlan, J. (2014) The Environmental Geochemistry of Arsenic -- An Overview --. Reviews in Mineralogy and Geochemistry, 79, 1–16.

Brigatti, M., Lugli, C., Cibin, G., Marcelli, A., Giuli, G., Paris, E., Mottana, A., and Wu, Z. (2000) Reduction and Sorption of Chromium by Fe(II)-bearing Phyllosilicates: Chemical Treatments and X-ray Absorption Spectroscopy (XAS) Studies. Clays and Clay Minerals, 48, 272–281.

Buerge, I.J., and Hug, S.J. (1997) Kinetics and pH Dependence of Chromium (VI) Reduction by Iron (II). Environmental Science & Technology, 31, 1426–1432.

Bunker, G. (2010) Introduction to XAFS, 818–818 p. Journal of Synchrotron Radiation Vol. 18. Cambridge University Press, Cambridge.

Buresh, R.J., and Moraghan, J.T. (1976) Chemical Reduction of Nitrate by Ferrous Iron1. Journal of Environment Quality, 5, 320.

Butler, E.C., Chen, L., Hansel, C.M., Krumholz, L.R., Elwood Madden, A.S., and Lan, Y. (2015) Biological versus mineralogical chromium reduction: potential for reoxidation by manganese oxide. Environmental Science: Processes & Impacts, 17, 1930–1940.

Calvin, S. (2013) XAFS for Everyone. CRC Press, Boca Raton.

Carlson, L., and Schwertmann, U. (1980) Natural Occurrence of Feroxyhite (δ′-FeOOH). Clays and Clay Minerals, 28, 272–280.

Catalano, J.G., Luo, Y., and Otemuyiwa, B. (2011) Effect of Aqueous Fe(II) on Arsenate Sorption on Goethite and Hematite. Environmental Science & Technology, 45, 8826–8833.

Cebrián, M.E., Albores, A., Aguilar, M., and Blakely, E. (1983) Chronic arsenic poisoning in the north of Mexico. Human toxicology, 2, 121–133.

Christiansen, B.C., Balic-Zunic, T., Petit, P.-O., Frandsen, C., Mørup, S., Geckeis, H., Katerinopoulou, A., and Stipp, S.L.S. (2009) Composition and structure of an iron-bearing, layered double hydroxide (LDH) – Green rust sodium sulphate. Geochimica et Cosmochimica Acta, 73, 3579–3592.

Christiansen, B.C., Geckeis, H., Marquardt, C.M., Bauer, A., Römer, J., Wiss, T., Schild, D., and Stipp, S.L.S. (2011) Neptunyl (NpO_2) interaction with green rust. Geochimica et Cosmochimica Acta, 75, 1216–1226.

Cismasu, A.C., Michel, F.M., Tcaciuc, A.P., Tyliszczak, T., and Brown, Jr, G.E. (2011) Composition and structural aspects of naturally occurring ferrihydrite. Comptes Rendus Geoscience, 343, 210–218.

Cornell, R.M., and Schwertmann, U. (2003) The Iron Oxides. Wiley.

Cramer, S.P., Tench, O., Yocum, M., and George, G.N. (1988) A 13-element Ge detector for fluorescence EXAFS. Nuclear Instruments and Methods in Physics Research Section A: Accelerators, Spectrometers, Detectors and Associated Equipment, 266, 586–591.

Craw, D., Falconer, D., and Youngson, J.H. (2003) Environmental arsenopyrite stability and dissolution: theory,

experiment, and field observations. Chemical Geology, 199, 71–82.

Cudennec, Y., and Lecerf, A. (2006) The transformation of ferrihydrite into goethite or hematite, revisited. Journal of Solid State Chemistry, 179, 716–722.

Daus, B., Mattusch, J., Paschke, A., Wennrich, R., and Weiss, H. (2000) Kinetics of the arsenite oxidation in seepage water from a tin mill tailings pond. Talanta, 51, 1087–1095.

Delnomdedieu, M., Basti, M.M., Otvos, J.D., and Thomas, D.J. (1994) Reduction and binding of arsenate and dimethylarsinate by glutathione: a magnetic resonance study. Chemico-biological interactions, 90, 139–155.

Dixon, H.B.F. (1996) The Biochemical Action of Arsonic Acids Especially As Phosphate Analogues. In A.G.B.T.-A. in I.C. Sykes, Ed., Vol. 44, pp. 191–227. Academic Press.

Driehaus, W., Seith, R., and Jekel, M. (1995) Oxidation of arsenate(III) with manganese oxides in water treatment. Water Research, 29, 297–305.

Drits, V.A., Sakharov, B.A., and Manceau, A. (1993) Structure of Feroxyhite as Determined by Simulation of X-Ray Diffraction Curves. Clay Minerals, 28, 209–222.

Duker, A., Carranza, E., and Hale, M. (2005) Arsenic geochemistry and health. Environment International, 31, 631–641.

Dzombak, D.A., and Morel, F.M. (1990) Surface complexation modelling: Hydrous ferric oxide. John Wiley and Sons, New York.

Elleaume, P. (1992) Insertion devices for the new generation of synchrotron sources: A review (invited). Review of Scientific Instruments, 63, 321–326.

Elzinga, E.J., and Cirmo, A. (2010) Application of sequential extractions and X-ray absorption spectroscopy to determine the speciation of chromium in Northern New Jersey marsh soils developed in chromite ore processing residue (COPR). Journal of Hazardous Materials, 183, 145–154.

Fandeur, D., Juillot, F., Morin, G., Olivi, L., Cognigni, A., Ambrosi, J.-P., Guyot, F., and Fritsch, E. (2009) Synchrotron-based speciation of chromium in an Oxisol from New Caledonia: Importance of secondary Fe-

oxyhydroxides. American Mineralogist, 94, 710–719.

Fischer, W.R. (1972) Die Wirkung von zweiwertigem Eisen auf Lösung und Umwandlung von Eisen(III)-hydroxiden. In E. Schlichtling and U. Schwertmann, Eds., Pseudogley and gley. pp. 37–44. VCH, Weinheim, Germany.

Fitz, W.J., and Wenzel, W.W. (2002) Arsenic transformations in the soil–rhizosphere–plant system: fundamentals and potential application to phytoremediation. Journal of Biotechnology, 99, 259–278.

Flemming, R.L., Salzsauler, K.A., Sherriff, B.L., and Sidenko, N. V. (2005) Identification of Scorodite in Fine-grained, High-sulfide, Arsenopyrite Mine Waste Using Micro X-ray Diffraction (μXRD). The Canadian Mineralogist, 43, 1243–1254.

Fuller, C.C., Davis, J.A., and Waychunas, G.A. (1993) Surface chemistry of ferrihydrite: Part 2. Kinetics of arsenate adsorption and coprecipitation. Geochimica et Cosmochimica Acta, 57, 2271–2282.

Fultz, B., and Howe, J. (2013) Transmission Electron Microscopy and Diffractometry of Materials, 4th Ed. Springer, Berlin, Heidelberg.

Garman, S.M., Luxton, T.P., and Eick, M.J. (2004) Kinetics of Chromate Adsorption on Goethite in the Presence of Sorbed Silicic Acid. Journal of Environment Quality, 33, 1703.

Gauvin, R. (1997) Review of transmission electron microscopy for the characterization of materials p. 102910C.

Gimenez, J., Martinez, M., Depablo, J., Rovira, M., and Duro, L. (2007) Arsenic sorption onto natural hematite, magnetite, and goethite. Journal of Hazardous Materials, 141, 575–580.

Goodenough, J.B. (1955) Theory of the Role of Covalence in the Perovskite-Type Manganites [La, M(II)]MnO3. Physical Review, 100, 564–573.

——— (1958) An interpretation of the magnetic properties of the perovskite-type mixed crystals La1−xSrxCoO3−λ. Journal of Physics and Chemistry of Solids, 6, 287–297.

Guilbaud, R., White, M.L., and Poulton, S.W. (2013) Surface charge and growth of sulphate and carbonate green rust in aqueous media. Geochimica et Cosmochimica Acta, 108, 141–153.

Guo, H., Yang, S., Tang, X., Li, Y., and Shen, Z. (2008) Groundwater geochemistry and its implications for arsenic mobilization in shallow aquifers of the Hetao Basin, Inner Mongolia. Science of The Total Environment, 393, 131–144.

Guo, H., Zhang, Y., Xing, L., and Jia, Y. (2012) Spatial variation in arsenic and fluoride concentrations of shallow groundwater from the town of Shahai in the Hetao basin, Inner Mongolia. Applied Geochemistry, 27, 2187–2196.

Guo, H., Liu, C., Lu, H., Wanty, R.B., Wang, J., and Zhou, Y. (2013) Pathways of coupled arsenic and iron cycling in high arsenic groundwater of the Hetao basin, Inner Mongolia, China: An iron isotope approach. Geochimica et Cosmochimica Acta, 112, 130–145.

Guo, Z.-R., Zhang, G., Fang, J., and Dou, X. (2006) Enhanced chromium recovery from tanning wastewater. Journal of Cleaner Production, 14, 75–79.

Gurman, S.J. (1995) Interpretation of EXAFS Data. Journal of Synchrotron Radiation, 2, 56–63.

Hansen, H.C.B., and Koch, C.B. (1998) Reduction of nitrate to ammonium by sulphate green rust: activation energy and reaction mechanism. Clay Minerals, 33, 87–101.

Hansen, H.C.B., Guldberg, S., Erbs, M., and Bender Koch, C. (2001) Kinetics of nitrate reduction by green rusts-effects of interlayer anion and Fe(II) :Fe(III) ratio. Applied Clay Science, 18, 81–91.

Hargrove, R.S., and Kündig, W. (1970) Mössbauer measurements of magnetite below the Verwey transition. Solid State Communications, 8, 303–308.

Hausladen, D.M., and Fendorf, S. (2017) Hexavalent Chromium Generation within Naturally Structured Soils and Sediments. Environmental Science & Technology, 51, 2058–2067.

He, Y.T., and Traina, S.J. (2005) Cr(VI) Reduction and Immobilization by Magnetite under Alkaline pH Conditions: The Role of Passivation. Environmental Science & Technology, 39, 4499–4504.

Higgins, M.R., and Olson, T.M. (2009) Life-Cycle Case Study Comparison of Permeable Reactive Barrier versus Pump-and-Treat Remediation. Environmental Science & Technology, 43, 9432–9438.

Hossain, M.F. (2006) Arsenic contamination in Bangladesh—An overview. Agriculture, Ecosystems & Environment, 113, 1–16.

Hughes, M.F. (2002) Arsenic toxicity and potential mechanisms of action. Toxicology Letters, 133, 1–16.

James, B.R. (1996) Peer Reviewed: The Challenge of Remediating Chromium-Contaminated Soil. Environmental Science & Technology, 30, 248A-251A.

Jia, Y., Guo, H., Xi, B., Jiang, Y., Zhang, Z., Yuan, R., Yi, W., and Xue, X. (2017) Sources of groundwater salinity and potential impact on arsenic mobility in the western Hetao Basin, Inner Mongolia. Science of The Total Environment, 601–602, 691–702.

Jordan, N., Marmier, N., Lomenech, C., Giffaut, E., and Ehrhardt, J.-J. (2007) Sorption of silicates on goethite, hematite, and magnetite: Experiments and modelling. Journal of Colloid and Interface Science, 312, 224–229.

Kanamori, J. (1959) Superexchange interaction and symmetry properties of electron orbitals. Journal of Physics and Chemistry of Solids, 10, 87–98.

Karimian, N., Johnston, S.G., and Burton, E.D. (2017) Antimony and Arsenic Behavior during Fe(II)-Induced Transformation of Jarosite. Environmental Science & Technology, 51, 4259–4268.

Kendelewicz, T., Liu, P., Doyle, C.S., and Brown, G.E. (2000) Spectroscopic study of the reaction of aqueous Cr(VI) with $Fe_3O_4(111)$ surfaces. Surface Science, 469, 144–163.

Kinniburgh, D.G. (1986) General purpose adsorption isotherms. Environmental Science & Technology, 20, 895–904.

Krishna, M.V.B., Chandrasekaran, K., Karunasagar, D., and Arunachalam, J. (2001) A combined treatment approach using Fenton's reagent and zero valent iron for the removal of arsenic from drinking water. Journal of Hazardous Materials, 84, 229–240.

Lagunas, R. (1980) Sugar-arsenate esters: Thermodynamics and biochemical behavior. Archives of Biochemistry and Biophysics, 205, 67–75.

Lai, K.C.K., and Lo, I.M.C. (2008) Removal of Chromium (VI) by Acid-Washed Zero-Valent Iron under Various

Groundwater Geochemistry Conditions. Environmental Science & Technology, 42, 1238–1244.

Landrot, G., Tappero, R., Webb, S.M., and Sparks, D.L. (2012a) Arsenic and chromium speciation in an urban contaminated soil. Chemosphere, 88, 1196–1201.

Landrot, G., Ginder-Vogel, M., Livi, K., Fitts, J.P., and Sparks, D.L. (2012b) Chromium(III) Oxidation by Three Poorly-Crystalline Manganese(IV) Oxides. 1. Chromium(III)-Oxidizing Capacity. Environmental Science & Technology, 46, 11594–11600.

Latta, D., Boyanov, M., Kemner, K., O'Loughlin, E., and Scherer, M. (2015) Reaction of Uranium(VI) with Green Rusts: Effect of Interlayer Anion. Current Inorganic Chemistry, 5, 156–168.

Lear, P.R., and Stucki, J.W. (1987) Intervalence Electron Transfer and Magnetic Exchange in Reduced Nontronite. Clays and Clay Minerals, 35, 373–378.

Legrand, L., El Figuigui, A., Mercier, F., and Chausse, A. (2004) Reduction of Aqueous Chromate by Fe(II)/Fe(III) Carbonate Green Rust: Kinetic and Mechanistic Studies. Environmental Science & Technology, 38, 4587–4595.

Lennie, A. R., Redfern, S.A.T., Schofield, P.F., and Vaughan, D.J. (1995) Synthesis and Rietveld crystal structure refinement of mackinawite, tetragonal FeS. Mineralogical Magazine, 59, 677–683.

Lennie, Alistar R., England, K.E.R., and Vaughan, D.J. (1995) Transformation of synthetic mackinawite to hexagonal pyrrhotite; a kinetic study. American Mineralogist, 80, 960–967.

Lennie, A.R., Redfern, S.A.T., Champness, P.E., Stoddart, C.P., Schofield, P.F., and Vaughan, D.J. (1997) Transformation of mackinawite to greigite; an in situ X-ray powder diffraction and transmission electron microscope study. American Mineralogist, 82, 302–309.

Liamleam, W., and Annachhatre, A.P. (2007) Electron donors for biological sulfate reduction. Biotechnology Advances, 25, 452–463.

Litter, M.., and Blesa, M.. (1988) Photodissolution of iron oxides. Journal of Colloid and Interface Science, 125, 679–687.

Litter, M.I., and Blesa, M.A. (1992) Photodissolution of iron oxides. IV. A comparative study on the photodissolution of hematite, magnetite, and maghemite in EDTA media. Canadian Journal of Chemistry, 70, 2502–2510.

Liu, F., De Cristofaro, A., and Violante, A. (2001) Effect of pH, phosphate and oxalate on the adsorption/desorption of arsenate on/from goethite. Soil Science, 166, 197–208.

Loyaux-Lawniczak, S., Refait, P., Lecomte, C., Ehrhardt, J., and Genin, J.R. (1999) The reduction of chromate ions by Fe (II) layered hydroxides. Hydrology and Earth System Sciences, 3, 593–599.

Loyaux-Lawniczak, S., Refait, P., Ehrhardt, J.-J., Lecomte, P., and Génin, J.-M.R. (2000) Trapping of Cr by Formation of Ferrihydrite during the Reduction of Chromate Ions by Fe(II)−Fe(III) Hydroxysalt Green Rusts. Environmental Science & Technology, 34, 438–443.

Ludwig, R.D., Su, C., Lee, T.R., Wilkin, R.T., Acree, S.D., Ross, R.R., and Keeley, A. (2007) In Situ Chemical Reduction of Cr(VI) in Groundwater Using a Combination of Ferrous Sulfate and Sodium Dithionite: A Field Investigation. Environmental Science & Technology, 41, 5299–5305.

Maillot, F., Morin, G., Wang, Y., Bonnin, D., Ildefonse, P., Chaneac, C., and Calas, G. (2011) New insight into the structure of nanocrystalline ferrihydrite: EXAFS evidence for tetrahedrally coordinated iron (III). Geochimica et Cosmochimica Acta, 75, 2708–2720.

Majumdar, S., Peralta-Videa, J.R., Castillo-Michel, H., Hong, J., Rico, C.M., and Gardea-Torresdey, J.L. (2012) Applications of synchrotron μ-XRF to study the distribution of biologically important elements in different environmental matrices: A review. Analytica Chimica Acta, 755, 1–16.

Mamun, A. Al, Morita, M., Matsuoka, M., and Tokoro, C. (2017) Sorption mechanisms of chromate with coprecipitated ferrihydrite in aqueous solution. Journal of Hazardous Materials, 334, 142–149.

Manceau, A., and Drits, V.A. (1993) Local Structure of Ferrihydrite and Feroxyhyte by EXAFS Spectroscopy. Clay Minerals, 28, 165–184.

Manceau, A., Marcus, M.A., and Tamura, N. (2002) Quantitative Speciation of Heavy Metals in Soils and Sediments by Synchrotron X-ray Techniques. Reviews in Mineralogy and Geochemistry, 49, 341–428.

Mandaliev, P.N., Mikutta, C., Barmettler, K., Kotsev, T., and Kretzschmar, R. (2014) Arsenic Species Formed from Arsenopyrite Weathering along a Contamination Gradient in Circumneutral River Floodplain Soils. Environmental Science & Technology, 48, 208–217.

Manning, B.A., Fendorf, S.E., Bostick, B., and Suarez, D.L. (2002) Arsenic(III) Oxidation and Arsenic(V) Adsorption Reactions on Synthetic Birnessite. Environmental Science & Technology, 36, 976–981.

Margaritondo, G. (1995) A Primer in Synchrotron Radiation: Everything You Wanted to Know about SEX (Synchrotron Emission of X-rays) but Were Afraid to Ask. Journal of Synchrotron Radiation, 2, 148–154.

Michel, F.M., Ehm, L., Antao, S.M., Lee, P.L., Chupas, P.J., Liu, G., Strongin, D.R., Schoonen, M.A.A., Phillips, B.L., and Parise, J.B. (2007) The Structure of Ferrihydrite, a Nanocrystalline Material. Science, 316, 1726–1729.

Milacic, R., and Stupar, J. (1995) Fractionation and Oxidation of Chromium in Tannery Waste- and Sewage Sludge-Amended Soils. Environmental Science & Technology, 29, 506–514.

Missana, T., Maffiotte, C., and García-Gutiérrez, M. (2003) Surface reactions kinetics between nanocrystalline magnetite and uranyl. Journal of Colloid and Interface Science, 261, 154–160.

Moody, J.B. (1976) Serpentinization: a review. Lithos, 9, 125–138.

Moore, D.M., and Reynolds, R.C. (1989) X-ray Diffraction and the Identification and Analysis of Clay Minerals., 2nd Ed. Oxford University Press, Oxford.

Mullen, D.J.E., and Nowacki, W. (1972) Refinement of the crystal structures of realgar, AsS and orpiment, As2S3. Zeitschrift für Kristallographie - Crystalline Materials, 136.

Myneni, S.C. (1997) Abiotic Selenium Redox Transformations in the Presence of Fe(II,III) Oxides. Science, 278, 1106–1109.

Nachman, K.E., Graham, J.P., Price, L.B., and Silbergeld, E.K. (2005) Arsenic: A Roadblock to Potential Animal Waste Management Solutions. Environmental Health Perspectives, 113, 1123–1124.

Naz, A., Mishra, B.K., and Gupta, S.K. (2016) Human Health Risk Assessment of Chromium in Drinking Water: A

Case Study of Sukinda Chromite Mine, Odisha, India. Exposure and Health, 8, 253–264.

Newman, D.K., Kennedy, E.K., Coates, J.D., Ahmann, D., Ellis, D.J., Lovley, D.R., and Morel, F.M.M. (1997) Dissimilatory arsenate and sulfate reduction in Desulfotomaculum auripigmentum sp. nov. Archives of Microbiology, 168, 380–388.

Newville, M. (2001) EXAFS analysis using FEFF and FEFFIT. Journal of Synchrotron Radiation, 8, 96–100.

Nickson, R., McArthur, J., Burgess, W., Ahmed, K.M., Ravenscroft, P., and Rahmanñ, M. (1998) Arsenic poisoning of Bangladesh groundwater. Nature, 395, 338–338.

Nivas, B.T., Sabatini, D.A., Shiau, B.-J., and Harwell, J.H. (1996) Surfactant enhanced remediation of subsurface chromium contamination. Water Research, 30, 511–520.

Nriagu, J.O., and Simmons, M.S., Eds. (1988) Chromium in the Natural and Human Environments. Wiley, New York.

O'Loughlin, E.J., Kelly, S.D., Cook, R.E., Csencsits, R., and Kemner, K.M. (2003) Reduction of Uranium(VI) by Mixed Iron(II)/Iron(III) Hydroxide (Green Rust): Formation of UO_2 Nanoparticles. Environmental Science & Technology, 37, 721–727.

Omoregie, E.O., Couture, R.-M., Van Cappellen, P., Corkhill, C.L., Charnock, J.M., Polya, D.A., Vaughan, D., Vanbroekhoven, K., and Lloyd, J.R. (2013) Arsenic Bioremediation by Biogenic Iron Oxides and Sulfides. Applied and Environmental Microbiology, 79, 4325–4335.

Ona-Nguema, G., Morin, G., Juillot, F., Calas, G., and Brown, G.E. (2005) EXAFS Analysis of Arsenite Adsorption onto Two-Line Ferrihydrite, Hematite, Goethite, and Lepidocrocite. Environmental Science & Technology, 39, 9147–9155.

Ona-Nguema, G., Morin, G., Wang, Y., Foster, A.L., Juillot, F., Calas, G., and Brown, G.E. (2010) XANES Evidence for Rapid Arsenic(III) Oxidation at Magnetite and Ferrihydrite Surfaces by Dissolved O 2 via Fe 2+ -Mediated Reactions. Environmental Science & Technology, 44, 5416–5422.

Oremland, R.S., Dowdle, P.R., Hoeft, S., Sharp, J.O., Schaefer, J.K., Miller, L.G., Switzer Blum, J., Smith, R.L., Bloom, N.S., and Wallschlaeger, D. (2000) Bacterial dissimilatory reduction of arsenate and sulfate in

meromictic Mono Lake, California. Geochimica et Cosmochimica Acta, 64, 3073–3084.

Páez-Espino, D., Tamames, J., de Lorenzo, V., and Cánovas, D. (2009) Microbial responses to environmental arsenic. BioMetals, 22, 117–130.

Paktunc, D., and Dutrizac, J.E. (2003) Characterization of Arsenate-for-Sulfate Substitution in Synthetic Jarosite Using X-ray Diffracton and X-ray Absorption Spectroscopy. The Canadian Mineralogist, 41, 905–919.

Palmer, C.D., and Wittbrodt, P.R. (1991) Processes affecting the remediation of chromium-contaminated sites. Environmental Health Perspectives, 92, 25–40.

Pan, C., Liu, H., Catalano, J.G., Qian, A., Wang, Z., and Giammar, D.E. (2017) Rates of Cr(VI) Generation from Cr_xFe_{1-x} (OH)$_3$ Solids upon Reaction with Manganese Oxide. Environmental Science & Technology, 51, 12416–12423.

Papassiopi, N., Pinakidou, F., Katsikini, M., Antipas, G.S.E., Christou, C., Xenidis, A., and Paloura, E.C. (2014a) A XAFS study of plain and composite iron (III) and chromium (III) hydroxides. Chemosphere, 111, 169–176.

Papassiopi, N., Vaxevanidou, K., Christou, C., Karagianni, E., and Antipas, G.S.E. (2014b) Synthesis, characterization and stability of Cr(III) and Fe(III) hydroxides. Journal of Hazardous Materials, 264, 490–497.

Patrat, G., de Bergevin, F., Pernet, M., and Joubert, J.C. (1983) Structure locale de δ-FeOOH. Acta Crystallographica Section B Structural Science, 39, 165–170.

Patterson, A.L. (1939) The Scherrer Formula for X-Ray Particle Size Determination. Physical Review, 56, 978–982.

Patterson, R.R., Fendorf, S., and Fendorf, M. (1997) Reduction of Hexavalent Chromium by Amorphous Iron Sulfide. Environmental Science & Technology, 31, 2039–2044.

Peak, D., and Regier, T. (2012) Direct Observation of Tetrahedrally Coordinated Fe(III) in Ferrihydrite. Environmental Science & Technology, 46, 3163–3168.

Peryea, F.J., and Kammereck, R. (1997) Phosphate-Enhanced Movement of Arsenic Out of Lead Arsenate-Contaminated Topsoil and Through Uncontaminated Subsoil. Water, Air and Soil Pollution, 93, 243–254.

Peterson, M.L., Brown, G.E., and Parks, G.A. (1996) Direct XAFS evidence for heterogeneous redox reaction at the

aqueous chromium/magnetite interface. Colloids and Surfaces A: Physicochemical and Engineering Aspects, 107, 77–88.

Postma, D., Larsen, F., Thai, N.T., Trang, P.T.K., Jakobsen, R., Nhan, P.Q., Long, T.V., Viet, P.H., and Murray, A.S. (2012) Groundwater arsenic concentrations in Vietnam controlled by sediment age. Nature Geoscience, 5, 656–661.

Prasanna, S. V., Rao, R.A.P., and Kamath, P.V. (2006) Layered double hydroxides as potential chromate scavengers. Journal of Colloid and Interface Science, 304, 292–299.

Puls, R.W., Paul, C.J., and Powell, R.M. (1999) The application of in situ permeable reactive (zero-valent iron) barrier technology for the remediation of chromate-contaminated groundwater: a field test. Applied Geochemistry, 14, 989–1000.

Rahman, F.A., Allan, D.L., Rosen, C.J., and Sadowsky, M.J. (2004) Arsenic Availability from Chromated Copper Arsenate (CCA)–Treated Wood. Journal of Environment Quality, 33, 173.

Rahman, M.A., and Hasegawa, H. (2011) Aquatic arsenic: Phytoremediation using floating macrophytes. Chemosphere, 83, 633–646.

Rai, D., Moore, D.A., Hess, N.J., Rosso, K.M., Rao, L., and Heald, S.M. (2007) Chromium(III) hydroxide solubility in the aqueous K^+-H^+-OH^--CO_2-HCO_3^--CO_3^{2-}-H_2O system: A thermodynamic model. Journal of Solution Chemistry, 36, 1261–1285.

Randall, S.R., Sherman, D.M., and Ragnarsdottir, K.V. (2001) Sorption of As(V) on green rust ($Fe_4(II)Fe_2(III)(OH)_{12}SO_4 \cdot 3H_2O$) and lepidocrocite ($\gamma$-FeOOH): Surface complexes from EXAFS spectroscopy. Geochimica et Cosmochimica Acta, 65, 1015–1023.

Ravel, B., and Newville, M. (2005) ATHENA and ARTEMIS Interactive Graphical Data Analysis Using IFEFFIT. Physica Scripta, T115, 1007–1010.

Raven, K.P., Jain, A., and Loeppert, R.H. (1998) Arsenite and Arsenate Adsorption on Ferrihydrite: Kinetics, Equilibrium, and Adsorption Envelopes. Environmental Science & Technology, 32, 344–349.

Refait, P., Abdelmoula, M., and Génin, J.-M.R. (1998) Mechanisms of formation and structure of green rust one in

aqueous corrosion of iron in the presence of chloride ions. Corrosion Science, 40, 1547–1560.

Refait, P., Sabot, R., and Jeannin, M. (2017) Role of Al(III) and Cr(III) on the formation and oxidation of the Fe(II-III) hydroxysulfate Green Rust. Colloids and Surfaces A: Physicochemical and Engineering Aspects, 531, 203–212.

Regenspurg, S., and Peiffer, S. (2005) Arsenate and chromate incorporation in schwertmannite. Applied Geochemistry, 20, 1226–1239.

Reynolds, I.M. (1985) The nature and origin of titaniferous magnetite-rich layers in the upper zone of the Bushveld Complex; a review and synthesis. Economic Geology, 80, 1089–1108.

Rickard, D., and Luther, G.W. (2007) Chemistry of Iron Sulfides. Chemical Reviews, 107, 514–562.

Rietveld, H.M. (1969) A profile refinement method for nuclear and magnetic structures. Journal of Applied Crystallography, 2, 65–71.

Rittle, K.A., Drever, J.I., and Colberg, P.J.S. (1995) Precipitation of arsenic during bacterial sulfate reduction. Geomicrobiology Journal, 13, 1–11.

Rose, J., Masion, A., Borschneck, D., Hazemann, J.-L., Saint Macary, H., and Bottero, J.-Y. (2006) New Combination of EXAFS Spectroscopy and Density Fractionation for the Speciation of Chromium within an Andosol. Environmental Science & Technology, 40, 7602–7608.

Rumble, J.R., Bruno, T.J., and Doa, M.J., Eds. (2020) CRC handbook of chemistry and physics: A ready-reference book of chemical and physical data, 101st edit. CRC Press/Taylor & Francis Group, Boca Raton.

Saha, R., Nandi, R., and Saha, B. (2011) Sources and toxicity of hexavalent chromium. Journal of Coordination Chemistry, 64, 1782–1806.

Sampson, C.F. (1969) The lattice parameters of natural single crystal and synthetically produced goethite (α-FeOOH). Acta Crystallographica Section B Structural Crystallography and Crystal Chemistry, 25, 1683–1685.

Savage, K.S., Tingle, T.N., O'Day, P.A., Waychunas, G.A., and Bird, D.K. (2000) Arsenic speciation in pyrite and secondary weathering phases, Mother Lode Gold District, Tuolumne County, California. Applied

Geochemistry, 15, 1219–1244.

Savage, K.S., Bird, D.K., and O'Day, P.A. (2005) Arsenic speciation in synthetic jarosite. Chemical Geology, 215, 473–498.

Schindler, P.W., and Stumm, W. (1987) The Surface Chemistry of Oxides, Hydroxides and Oxide Minerals. In Werner Stumm, Ed., Aquatic Surface Chemistry: Chemical Processes at the Particle-Water Interface pp. 83–110. John Wiley and Sons, New York.

Schlegel, A., Alvarado, S.F., and Wachter, P. (1979) Optical properties of magnetite (Fe3O4). Journal of Physics C: Solid-state Physics, 12, 1157–1164.

Schoonen, M.A.A., and Barnes, H.L. (1991) Reactions forming pyrite and marcasite from solution: II. Via FeS precursors below 100°C. Geochimica et Cosmochimica Acta, 55, 1505–1514.

Schwertmann, U., and Carlson, L. (1994) Aluminum Influence on Iron Oxides: XVII. Unit-Cell Parameters and Aluminum Substitution of Natural Goethites. Soil Science Society of America Journal, 58, 256.

Schwertmann, U., and Cornell, R.M. (2008) Iron oxides in the laboratory, 2nd Edition., 2nd ed. Wiley-WCH, Weinheim, Germany.

Schwertmann, U., and Fechter, H. (1994) The Formation of Green Rust and Its Transformation to Lepidocrocite. Clay Minerals, 29, 87–92.

Schwertmann, U., Gasser, U., and Sticher, H. (1989) Chromium-for-iron substitution in synthetic goethites. Geochimica et Cosmochimica Acta, 53, 1293–1297.

Scott, N., Hatlelid, K.M., MacKenzie, N.E., and Carter, D.E. (1993) Reactions of arsenic(III) and arsenic(V) species with glutathione. Chemical Research in Toxicology, 6, 102–106.

Scott, T.B., Allen, G.C., Heard, P.J., and Randell, M.G. (2005) Reduction of U(VI) to U(IV) on the surface of magnetite. Geochimica et Cosmochimica Acta, 69, 5639–5646.

Sestu, M., Carta, D., Casula, M.F., Corrias, A., and Navarra, G. (2015) Novel interpretation of the mean structure of feroxyhyte. Journal of Solid State Chemistry, 225, 256–260.

Sharma, P., Bihari, V., Agarwal, S.K., Verma, V., Kesavachandran, C.N., Pangtey, B.S., Mathur, N., Singh, K.P., Srivastava, M., and Goel, S.K. (2012) Groundwater Contaminated with Hexavalent Chromium [Cr (VI)]: A Health Survey and Clinical Examination of Community Inhabitants (Kanpur, India). (J.E. Mendelson, Ed.) PLoS ONE, 7, e47877.

Sherman, D.M. (1985) The electronic structures of Fe3+ coordination sites in iron oxides: Applications to spectra, bonding, and magnetism. Physics and Chemistry of Minerals, 12, 161–175.

Sherman, D.M. (1990) Crystal Chemistry, Electronic Structures, and Spectra of Fe Sites in Clay Minerals: Applications to Photochemistry and Electron Transport. In L.M. Coyne, S.W.S. McKeever, and D.F. Blake, Eds., Spectroscopic Characterization of Minerals and Their Surfaces Vol. 415, pp. 284–309. American Chemical Society, Washington, DC.

Shiraki, K. (1997) Geochemical Behavior of Chromium. Shigen-Chishitsu, 47, 319–330.

Siegbahn, M. (1916) Relations between the K and L Series of the High-Frequency Spectra. Nature, 96, 676–676.

Singh, B., Sherman, D.M., Gilkes, R.J., Wells, M. a, and Mosselmans, J.F.W. (2002) Incorporation of Cr, Mn and Ni into goethite (alpha-FeOOH): mechanism from extended X-ray absorption fine structure spectroscopy. Clay Minerals, 37, 639–649.

Skinner, B.J., Erd, R.C., and Grimaldi, F.S. (1964) Greigite, the thio-spinel of iron; a new mineral. American Mineralogist, 49, 543–555.

Skovbjerg, L.L., Stipp, S.L.S., Utsunomiya, S., and Ewing, R.C. (2006) The mechanisms of reduction of hexavalent chromium by green rust sodium sulphate: Formation of Cr-goethite. Geochimica et Cosmochimica Acta, 70, 3582–3592.

Skovbjerg, L.L., Christiansen, B.C., Nedel, S., Dideriksen, K., and Stipp, S.L.S. (2010) The role of green rust in the migration of radionuclides: An overview of processes that can control mobility of radioactive elements in the environment using as examples Np, Se and Cr. Radiochimica Acta, 98, 607–612.

Sorlini, S., and Gialdini, F. (2010) Conventional oxidation treatments for the removal of arsenic with chlorine dioxide, hypochlorite, potassium permanganate and monochloramine. Water Research, 44, 5653–5659.

Spiro, T.G., Allerton, S.E., Renner, J., Terzis, A., Bils, R., and Saltman, P. (1966) The Hydrolytic Polymerization of Iron (III). Journal of the American Chemical Society, 88, 2721–2726.

Stern, E.A., Bunker, B.A., and Heald, S.M. (1980) Many-body effects on extended x-ray absorption fine structure amplitudes. Phys. Rev. B, 21, 5521–5539.

Stone, A.T., and Morgan, J.J. (1987) Reductive dissolution of metal oxides. In W. Stumm, Ed., Aquatic Surface Chemistry. John Wiley and Sons, New York.

Strauss, R., Brummer, G.W., and Barrow, N.J. (1997) Effects of crystallinity of goethite: II. Rates of sorption and desorption of phosphate. European Journal of Soil Science, 48, 101–114.

Swedlund, P.J., and Webster, J.G. (1999) Adsorption and polymerisation of silicic acid on ferrihydrite, and its effect on arsenic adsorption. Water Research, 33, 3413–3422.

Tamaura, Y., Saturno, M., Yamada, K., and Katsura, T. (1984) The Transformation of γ-FeO(OH) to Fe_3O_4 and Green Rust II in an Aqueous Solution. Bulletin of the Chemical Society of Japan, 57, 2417–2421.

Tang, Y., Michel, F.M., Zhang, L., Harrington, R., Parise, J.B., and Reeder, R.J. (2010) Structural Properties of the Cr(III)−Fe(III) (Oxy)hydroxide Compositional Series: Insights for a Nanomaterial "Solid Solution." Chemistry of Materials, 22, 3589–3598.

Tazaki, K. (2000) Formation of Banded Iron-Manganese Structures by Natural Microbial Communities. Clays and Clay Minerals, 48, 511–520.

Teo, B.K. (2012) EXAFS: basic principles and data analysis. Springer Science & Business Media, Berlin.

Thomas, A., Eiche, E., Göttlicher, J., Steininger, R., G. Benning, L., M. Freeman, H., Dideriksen, K., and Neumann, T. (2018) Products of Hexavalent Chromium Reduction by Green Rust Sodium Sulfate and Associated Reaction Mechanisms. Soil Systems, 2, 58.

Tohji, K., and Udagawa, Y. (1988) Double-crystal spectrometer for laboratory EXAFS spectroscopy. Review of Scientific Instruments, 59, 1127–1131.

Trolard, F., Bourrié, G., Abdelmoula, M., Refait, P., and Feder, F. (2007) Fougerite, a new mineral of the

pyroaurite-iowaite group: description and crystal structure. Clays and Clay Minerals, 55, 323–334.

Ufer, K., Stanjek, H., Roth, G., Dohrmann, R., Kleeberg, R., and Kaufhold, S. (2008) Quantitative phase analysis of bentonites by the Rietveld method. Clays and Clay Minerals, 56, 272–282.

Usman, M., Hanna, K., Abdelmoula, M., Zegeye, A., Faure, P., and Ruby, C. (2012) Formation of green rust via mineralogical transformation of ferric oxides (ferrihydrite, goethite and hematite). Applied Clay Science, 64, 38–43.

Utsunomiya, S., and Ewing, R.C. (2003) Application of High-Angle Annular Dark Field Scanning Transmission Electron Microscopy, Scanning Transmission Electron Microscopy-Energy Dispersive X-ray Spectrometry, and Energy-Filtered Transmission Electron Microscopy to the Characterization of Nanopar. Environmental Science & Technology, 37, 786–791.

Vempati, R.K., and Loeppert, R.H. (1989) Influence of Structural and Adsorbed Si on the Transformation of Synthetic Ferrihydrite1. Clays and Clay Minerals, 37, 273–279.

Villalobos, M., Toner, B., Bargar, J., and Sposito, G. (2003) Characterization of the manganese oxide produced by Pseudomonas putida strain MnB1. Geochimica et Cosmochimica Acta, 67, 2649–2662.

Voegelin, A., Weber, F.-A., and Kretzschmar, R. (2007) Distribution and speciation of arsenic around roots in a contaminated riparian floodplain soil: Micro-XRF element mapping and EXAFS spectroscopy. Geochimica et Cosmochimica Acta, 71, 5804–5820.

von Burg, R., and Liu, D. (1993) Chromium and hexavalent chromium. Journal of Applied Toxicology, 13, 225–230.

Wander, M.C.F., Rosso, K.M., and Schoonen, M.A.A. (2007) Structure and Charge Hopping Dynamics in Green Rust. The Journal of Physical Chemistry C, 111, 11414–11423.

Wang, H.Y., Byrne, J.M., Perez, J.P.H., Thomas, A.N., Göttlicher, J., Höfer, H.E., Mayanna, S., Kontny, A., Kappler, A., Guo, H.M., and others (2020) Arsenic sequestration in pyrite and greigite in the buried peat of As-contaminated aquifers. Geochimica et Cosmochimica Acta, 284, 107–119.

Warren, B.E. (1969) X-ray diffraction. Addison-Wesley, Reading, Mass.

Waychunas, G.., Rea, B.., Fuller, C.., and Davis, J.. (1993) Surface chemistry of ferrihydrite: Part 1. EXAFS studies of the geometry of coprecipitated and adsorbed arsenate. Geochimica et Cosmochimica Acta, 57, 2251–2269.

Webb, S.M. (2005) SIXPack: a Graphical User Interface for XAS Analysis Using IFEFFIT. Physica Scripta, T115, 1011–1014.

Wedepohl, K.H. (1995) The composition of the continental crust. Geochimica et Cosmochimica Acta, 59, 1217–1232.

West, A.R. (2014) Solid State Chemistry and its Applications, 2nd Ed. John Wiley and Sons, Chichester, UK.

Wilke, M., Farges, F., Petit, P.-E., Brown, G.E., and Martin, F. (2001) Oxidation state and coordination of Fe in minerals: An Fe K-XANES spectroscopic study. American Mineralogist, 86, 714–730.

Wilkin, R.T., and Barnes, H.L. (1997) Formation processes of framboidal pyrite. Geochimica et Cosmochimica Acta, 61, 323–339.

Wilkin, R.T., and Ford, R.G. (2006) Arsenic solid-phase partitioning in reducing sediments of a contaminated wetland. Chemical Geology, 228, 156–174.

Wilkin, R.T., Su, C., Ford, R.G., and Paul, C.J. (2005) Chromium-Removal Processes during Groundwater Remediation by a Zerovalent Iron Permeable Reactive Barrier. Environmental Science & Technology, 39, 4599–4605.

Wilkin, R.T., Lee, T.R., McNeil, M.S., Su, C., and Adair, C. (2018) Fourteen-year assessment of a permeable reactive barrier for treatment of hexavalent chromium and trichloroethylene. Permeable Reactive Barrier: Sustainable Groundwater Remediation, 99.

Williams, A.G.B., and Scherer, M.M. (2001) Kinetics of Cr(VI) Reduction by Carbonate Green Rust. Environmental Science & Technology, 35, 3488–3494.

Willmott, P. (2011) An Introduction to Synchrotron Radiation. Wiley, Hoboken, NJ.

World Health Organization, ., Ed. (2017) Guidelines for drinking-water quality, 4th ed. World Health Organization, Geneva.

Yamamoto, T. (2008) Assignment of pre-edge peaks in K-edge x-ray absorption spectra of 3d transition metal compounds: electric dipole or quadrupole? X-Ray Spectrometry, 37, 572–584.

Yee, N., Shaw, S., Benning, L.G., and Nguyen, T.H. (2006) The rate of ferrihydrite transformation to goethite via the Fe(II) pathway. American Mineralogist, 91, 92–96.

Zachara, J.M., Girvin, D.C., Schmidt, R.L., and Resch, C.T. (1987) Chromate adsorption on amorphous iron oxyhydroxide in the presence of major groundwater ions. Environmental Science & Technology, 21, 589–594.

Appendix A: Full Text of First-author Publications

A.1 Products of Hexavalent Chromium Reduction by Green Rust Sodium Sulfate and Associated Reaction Mechanisms

Products of Hexavalent Chromium Reduction by Green Rust Sodium Sulfate and Associated Reaction Mechanisms

Andrew N. Thomas [1],*, Elisabeth Eiche [1], Jörg Göttlicher [2], Ralph Steininger [2], Liane G. Benning [3,4] , Helen M. Freeman [3,† , Knud Dideriksen [5] and Thomas Neumann [6]

[1] Institute for Applied Geosciences, Karlsruhe Institute of Technology, Adenauerring 20b, Building 50.40, 76135 Karlsruhe, Germany; elisabeth.eiche@kit.edu

[2] Institute for Synchrotron Radiation, Karlsruhe Institute of Technology, Herman-von-Helmholtz Platz 1, 76344 Eggenstein-Leopoldshafen, Germany; joerg.goettlicher@kit.edu (J.G.); ralph.steininger@kit.edu (R.S.)

[3] GFZ German Research Center for Geosciences, Telegrafenberg, 14473 Potsdam, Germany; benning@gfz-potsdam.de (L.G.B.); h.m.freeman@leeds.ac.uk (H.M.F.)

[4] Department of Earth Sciences, Free University of Berlin, 12249 Berlin, Germany

[5] Nano-Science Center, Department of Chemistry, University of Copenhagen, Universitetsparken 5, 2100 Copenhagen, Denmark; knud@nano.ku.dk

[6] Department of Applied Geosciences, Technical University of Berlin, Ernst-Reuter-Platz 1, 10587 Berlin, Germany; neumann@tu-berlin.de

* Correspondence: andrew.thomas@kit.edu

† Current address: School of Chemical and Process Engineering, University of Leeds, Leeds LS29JT, UK.

check for updates

Abstract: The efficacy of in vitro Cr(VI) reduction by green rust sulfate suggests that this mineral is potentially useful for remediation of Cr-contaminated groundwater. Previous investigations studied this reaction but did not sufficiently characterize the intermediates and end products at chromate (CrO_4^{2-}) concentrations typical of contaminant plumes, hindering identification of the dominant reaction mechanisms under these conditions. In this study, batch reactions at varying chromate concentrations and suspension densities were performed and the intermediate and final products of this reaction were analyzed using X-ray absorption spectroscopy and electron microscopy. This reaction produces particles that maintain the initial hexagonal morphology of green rust but have been topotactically transformed into a poorly crystalline Fe(III) oxyhydroxysulfate and are coated by a Cr (oxy) hydroxide layer that results from chromate reduction at the surface. Recent studies of the behavior of Cr(III) (oxy) hydroxides in soils have revealed that reductive transformation of CrO_4^{2-} is reversible in the presence of Mn(IV) oxides, limiting the applicability of green rust for Cr remediation in some soils. The linkage of Cr redox speciation to existing Fe and Mn biogeochemical cycles in soils implies that modification of green rust particles to produce an insoluble, Cr(III)-bearing Fe oxide product may increase the efficacy of this technique.

Keywords: green rust sulfate; chromium; EXAFS; metal redox cycles

1. Introduction

Chromium contamination of groundwater is a common environmental problem worldwide and poses a major threat to human health due to the toxicity, carcinogenicity, and solubility of its hexavalent form. Chromium is released into the environment by industrial processes such as metal plating, wood treatment, and leather tanning [1] and exists in several oxidation states from 0 to +6, the most common of which are Cr(III) and Cr(VI), which usually takes the form of the chromate oxyanion (CrO_4^{2-}).

Cr(VI), due to its carcinogenicity, toxicity, and mobility, is hazardous even at low concentrations. Trivalent chromium, on the other hand, is an essential trace element for sugar metabolism [2] and normally does not exist at high enough concentrations to have toxic effects due to its low solubility [3] and tendency to form stable complexes with soil minerals [4]. Therefore, reductive transformation of CrO_4^{2-} to Cr^{3+} is a promising remediation strategy. Several viable remediation methods exist that are capable of driving this transformation, including Fe^{2+} and dithionite [5], zero-valent iron [6–8], and green rust, a layered Fe(II)-Fe(III) hydroxide mineral. However, several recent studies [9–11] have investigated the regeneration of chromate from Cr(III) and Cr(III)-bearing Fe(III) hydroxides in packed column experiments. These studies revealed that biogenic Mn(IV) oxides are the primary oxidant in these systems and that reductive transformation of chromate in soils may be reversible, depending on the Mn content and redox conditions of the soils as well as the solubility of the Cr(III)-bearing phase. Therefore, the use of reactive particles, such as green rust, with heterogeneous reaction mechanisms and the potential to produce less-soluble Cr(III)-bearing solid solutions is investigated here as a potential means of remediating chromium contamination.

Green rust, a member of the layered double hydroxide (LDH) family, is composed of repeating, positively charged Fe(II)-Fe(III) hydroxide sheets that alternate with an interlayer containing water, an interlayer anion, and occasionally an interlayer cation [12]. Green rusts are classified based on the identity of the interlayer anion, the most common of which are CO_3^{2-}, Cl^-, and SO_4^{2-}. Originally identified in hydric soils as fougèrite [13], it is stable within a narrow redox potential range, but destabilizes at low (<6) or very high pH values [14] and under oxidizing conditions. Green rust has also been identified as an oxidation product of zero-valent iron (ZVI) in permeable reactive barriers [15] and as a product of steel corrosion in marine environments [16].

The ability of green rust to remediate As [17–19], NO_3^- [20], NO_{2-} [21], Se(VI) [22,23], U(VI) [24], Np [25], and Cr(VI) [26–31] has been investigated extensively, with mixed results. The kinetics and byproducts of the Cr(VI)–green rust reaction have been investigated repeatedly, but the resulting product characterizations and mechanism descriptions vary, most likely due to inconsistent synthesis methods and analytical methodologies. The twin studies of Loyaux-Lawniczak et al. (1999) [26] and Loyaux-Lawniczak et al. (2000) [27] examined the solid byproducts of green rust chloride and sulfate reacted with CrO_4^{2-} using X-ray diffraction (XRD), Raman spectroscopy, and X-ray photoelectron spectroscopy (XPS): the product was identified as a poorly ordered Cr(III)-Fe(III) oxyhydroxide resembling 2-line ferrihydrite. Bond and Fendorf (2003) [28] reduced chromate with green rust sulfate, carbonate and chloride and proposed a dominant interlayer-exchange mechanism for the reaction. Extended X-ray absorption fine structure spectroscopy (EXAFS) scans of the products suggested the formation of a poorly ordered Cr(III)-Fe(III) oxyhydroxide. Williams and Scherer (2001) [29] and Legrand et al. (2004) [30] measured the kinetics of chromate reduction by green rust carbonate and identified the product as a Fe(III) oxyhydroxycarbonate. Finally, Skovbjerg et al. (2006) [31] reacted concentrated chromate solutions with freshly prepared, untreated green rust sulfate and analyzed both partially and fully reacted solid samples. This study identified Cr(III)-bearing goethite as the primary reaction product, formed via chromate exchange for sulfate in the interlayer.

Although the reduction of chromate by green rust is well-characterized, what is missing is both a detailed structural study of the byproducts and an evaluation of the mechanism of green rust oxidation at chromate concentrations characteristic of contaminant plumes. EXAFS shell fits of byproducts of this reaction are available [28], but these shell-by-shell fits are better suited for less-complex samples. Samples with multiple mineral components are often better characterized by linear combination fitting (LCF) of the k^3-weighted EXAFS region using synthesized reference standards, especially for substances with modular, repeating structural geometries (such as iron oxides). In addition, although Bond and Fendorf (2003) [28] reacted green rust with Cr concentrations characteristic of contaminant plumes (192 µM) and Skovbjerg et al. (2006) [31] characterized intermediate products of reactions with higher Cr concentrations (0.8–12.3 mM), intermediate products of batch reactions at plume concentrations have not been analyzed, so little is known about the reaction mechanism under these

conditions. Without knowledge of the structure of the Cr-bearing solids formed by this reaction and the mechanism of formation, the long-term stability of Cr immobilized by green rust in permeable reactive barriers becomes very difficult to predict.

The objective of the present study was to determine the structure and stability of the Cr-bearing products of green rust reacted with Cr(VI) at typical plume concentrations. Synthetic green rust was oxidized to completion by solutions of chromate at concentrations between 30 and 1300 μM. By adding freshly prepared green rust suspension and a chromate stock solution at a ratio sufficient to oxidize 100% of the green rust to varying volumes of water, the initial chromate concentrations and green rust suspension densities were varied systematically, allowing the analysis of products formed at different variable reaction rates. EXAFS, transmission electron microscopy (TEM), and scanning electron microscopy (SEM) were then used to characterize the intermediate and end products. This allowed us to determine the dominant reaction mechanism(s) as well as how these mechanisms vary under different reaction conditions.

2. Materials and Methods

Green rust sulfate [$Fe^{II}_4Fe^{III}_2(OH)_{12}SO_4 \cdot 2H_2O$] was synthesized using a modified version of the co-precipitation method from Géhin et al. (2002) [32]. After deoxygenating solutions of $FeSO_4 \cdot 7H_2O$ and $Fe_2(SO_4)_3 \cdot H_2O$ in doubly-deionized water (Siemens Milli-Q Plus, Lowell, Massachusetts, USA) by purging the solutions with N_2, both solutions were transferred into a glovebox (Jacomex P[Box] Compact Glove Box, Dagneux, France) under an Ar atmosphere. In the glovebox, the Fe(III) solution was added to the Fe(II) solution using a peristaltic pump (Ismatec IPC, Wertheim, Germany) at a constant rate of approximately 1 mL/min for 40 min while mixing with a magnetic stirrer to maintain solution homogeneity. The solution pH was maintained at approximately 7.0 using dropwise addition of 1 M NaOH. This method allowed the synthesis of a product with a known [Fe(II)] primarily bound in the solid fraction, and a minimal amount of side products (see Supplementary Information for explanation). After complete mixing of the two solutions, the mixture had a [Fe(II)]/[Fe(III)] ratio of 2 and the total [Fe] was approximately 0.1 M.

After aging the product for 24 h, one batch was collected by vacuum filtration using a Whatman 0.2 μm nylon membrane filter and protected from oxidation by adding glycerol. XRD measurements were obtained using a Bruker D8 Diffractometer (Karlsruhe, Germany) equipped with the EVA 100 software. X-rays were emitted from a Cu-Kα source (λ = 1.5418 Å), and data were collected at 2θ values between 2–82° with a step size of 0.02° and an average counting time of 1 s per step.

To vary the reaction rate between CrO_4^{2-} and green rust sulfate, equimolar amounts of each reagent were diluted in variable volumes of a 13.33 mmol kg^{-1} Na_2SO_4 solution, producing solutions with [CrO_4^{2-}] varying from 0.033 to 1.333 mmol kg^{-1} (see Table 1). Prior to the addition of green rust, the pH of the CrO_4^{2-} solutions and the green rust sulfate suspension were adjusted to 7.0, where geochemical modelling (PHREEQC) indicates that the dichromate ($Cr_2O_7^{2-}$) concentration is negligible. Approximately 30 mg of green rust were then added to the CrO_4^{2-} solutions as a suspension without drying or any other treatment. Separate batches of each CrO_4^{2-} solution were reacted for 24 h or 7 days before termination of the reaction by vacuum filtration through a 0.2 μm nylon membrane filter (Whatman, Little Chalfont, UK). A third batch was reacted to measure the CrO_4^{2-} reduction kinetics, and a fourth to collect samples for electron microscopy. Samples of the reaction suspension were diluted in 0.01 M HCl and filtered using a 0.2 μm syringe filter. A 30 mg sample of green rust was also suspended in the 13.33 mmol kg^{-1} diluent as a blank and characterized by XRD (see previous section).

Table 1. Approximate CrO_4^{2-} concentrations and green rust suspension densities of the six reaction solutions. All samples diluted in 13.3 mmol kg^{-1} Na$_2$SO$_4$.

Solution	Volume (mL)	[CrO$_4^{2-}$] (mg L^{-1})	Green Rust Suspension Density (mg L^{-1})
C1	50	69	600
C2	100	35	300
C3	250	14	120
C4	500	6.9	60
C5	1000	3.5	30
C6	2000	1.7	15

Aqueous CrO_4^{2-} concentrations were determined by colorimetric analyses of the filtered solutions using the 1,5-diphenylcarbazide method Environmental Protection Agency (EPA) Method 7196A) with a Perkin-Elmer Lambda 2S UV-Vis Spectrophotometer (Waltham, MA, USA) calibrated using a four-point calibration curve. The pH of the reaction system after 7 days was measured using a Wissenschaftlich-Technische-Werkstätten (WTW) pH 330 pH meter (Weilheim, Germany).

EXAFS spectra of all 24 h and 7 day reacted samples were obtained on beamline SUL-X (wiggler X-ray source) at the ANKA synchrotron facility in Eggenstein-Leopoldshafen, Germany. Data reduction and analysis of the EXAFS spectra were performed using the Athena/Artemis software package (Ravel & Newville, 2005) [33]. All Fe reference compounds were synthesized according to the standard synthesis protocols in Cornell & Schwertmann (2008) [34]. The experimental details and data analysis steps are outlined in the Supplementary Information.

All electron microscopy experiments were performed at the Potsdam Imaging and Spectral Analysis (PISA) facility at the Deutsches Geoforschungszentrum (GFZ) in Potsdam, Germany. Samples were collected from reaction C1 after 5 s (halfway point of the reaction), 1 min (reaction completion point) and 7 days of aging, and from reaction C6 after 1 min (halfway point of the reaction), 10 min (reaction completion point) and 7 days of aging.

TEM samples were prepared by drop casting the diluted suspension onto a 3 mm Cu-TEM grid coated with holey carbon film, which was then transferred to a single-tilt holder inside the anaerobic chamber. The sample holder was then transferred to the TEM instrument within 30 s to minimize the effects of oxidation. Imaging and analysis were done using a FEI Tecnai TEM (Thermo Fisher Scientific, Waltham, MA, USA) at 200 kV equipped with a Gatan Tridiem imaging filter (GIF), an energy dispersive X-ray (EDX) analyzer, to measure chemical composition, and a Gatan Orius SC200D 4K pixel cooled charge-coupled device (CCD) camera (Pleasanton, CA, USA). Selected-Area Electron Diffraction (SAED) patterns were collected using an aperture with an effective diameter of 250 nm at the image plane and a camera length of 990 mm. The SAED patterns were developed in a Ditabis Imaging Plate Scanner (Munich, Germany). TEM images were processed and converted using Gatan DigitalMicrograph, while the raw EDX data was processed using EDX Quant.

SEM samples were prepared by vacuum filtration of small volumes of suspended sample followed by adhesion of the filter paper to the SEM sample holder with carbon tape and quickly coated with carbon using BAL-TEC MED 020 (Leica Microsystems, Wetzlar, Germany) to avoid charging effects during imaging. Images were obtained using a Zeiss Ultra Plus Field Emission-Scanning Electron Microscope (FE-SEM) (Carl Zeiss AG, Oberkochen, Germany) in a high vacuum mode at acceleration voltages between 1 and 3 kV with 10 μm aperture size using an InLens secondary electron detector. Elemental analyses of the samples were performed at 20 kV with 120 μm aperture size in point and shoot mode using a Thermo Scientific Ultra Dry Energy Dispersive Spectrometry (EDX) detector (Waltham, MA, USA).

3. Results

3.1. Characterization and Stability of Sulfate Green Rust

The X-ray diffractogram of the aged synthetic green rust sulfate stabilized with glycerol is shown in Figure 1a. No side products were observed by this method, but the green rust basal plane (003) peak at ~8° 2θ is smaller in intensity relative to other green rust XRD patterns from the literature [32,35]. When suspended in 13.33 mM Na_2SO_4 (the same ionic strength as the reaction solutions), the synthetic sulfate green rust transformed to the product shown in Figure 1b. This product is dominated by a poorly crystalline phase (most likely ferrihydrite), but peaks corresponding to magnetite and sulfate green rust were also identified. The green rust basal plane reflection at ~8° 2θ is not visible, possibly because the thick layer of glycerol added to stabilize the product disproportionally decreased reflection at low incident angles.

3.2. $CrO_4{}^{2-}$ Reduction Kinetics

The time required to reduce Cr(VI) to completion showed a strong dependence on the initial Cr(VI) concentration (Figure 2). At higher concentrations (C1-C3), the $CrO_4{}^{2-}$ was reduced to completion within five minutes, while at lower $CrO_4{}^{2-}$ concentrations (C4-C6), complete reduction took 5–6 times as long. Minimal sorption of $CrO_4{}^{2-}$ to the glass beaker was shown by the blank solution, and $CrO_4{}^{2-}$ concentrations remained low until the reaction was terminated after 7 days. In all reaction systems, the pH value had decreased to between 4 and 5 by the time the reaction was terminated after 7 days.

3.3. Fe and Cr Speciation

The lack of the characteristic Cr(VI) 1s→3d pre-edge peak at 5993 eV in all 7-day reacted spectra in Figure 3 suggests that there was not a significant level of Cr(VI) in any of the samples, as would be the case if the $CrO_4{}^{2-}$ had simply adsorbed onto the surface of the product.

Fe EXAFS linear combination fits (k^3-weighted, Table 2) were obtained by fitting the Fe EXAFS data of the 24-h (Figure 4a) and 7-day (Figure 4b) samples to a set of reference standards. In every fitted sample, the dominant detected Fe-bearing phase was feroxyhyte (δ'-FeOOH), the proportion of which increases in all reactions except C5 between 24 h and 7 days. Ferrihydrite was detected at very low levels in some samples, albeit the patterns for ferrihydrite and feroxyhyte were similar. Ferrihydrite EXAFS spectra vary with the preparation method used [36], and patterns for ferrihydrite have been published [37] that more closely align with our feroxyhyte patterns than our ferrihydrite patterns do. The other phases identified by EXAFS are goethite (α-FeOOH) and lepidocrocite (γ-FeOOH), the last of which contributes more to the overall fit at the expense of the goethite and feroxyhyte-like components as the initial $CrO_4{}^{2-}$ concentration decreases.
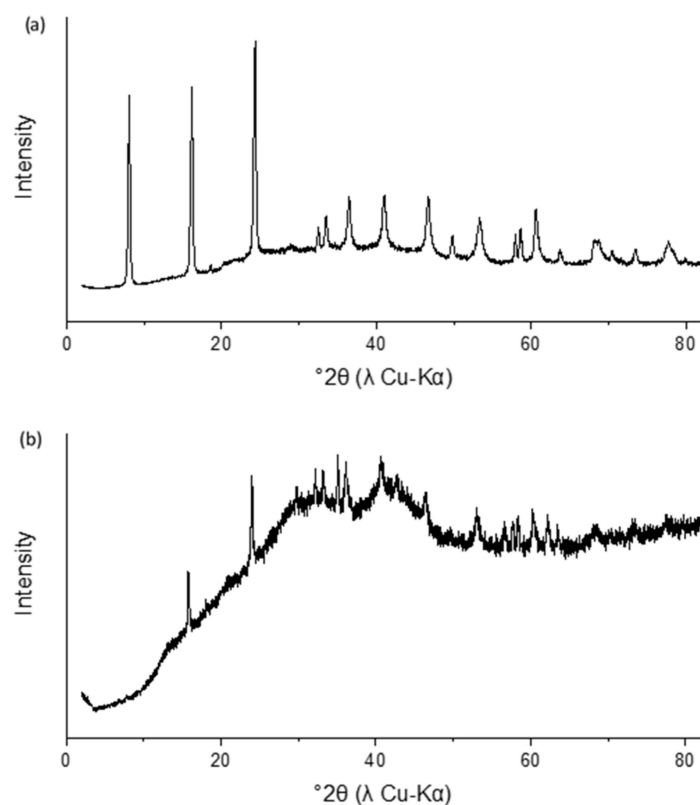
Figure 1. XRD trace of synthetic green rust sulfate (**a**) and green rust suspended in aqueous Na_2SO_4 for seven days (**b**). Transformation products include ferrihydrite and magnetite.
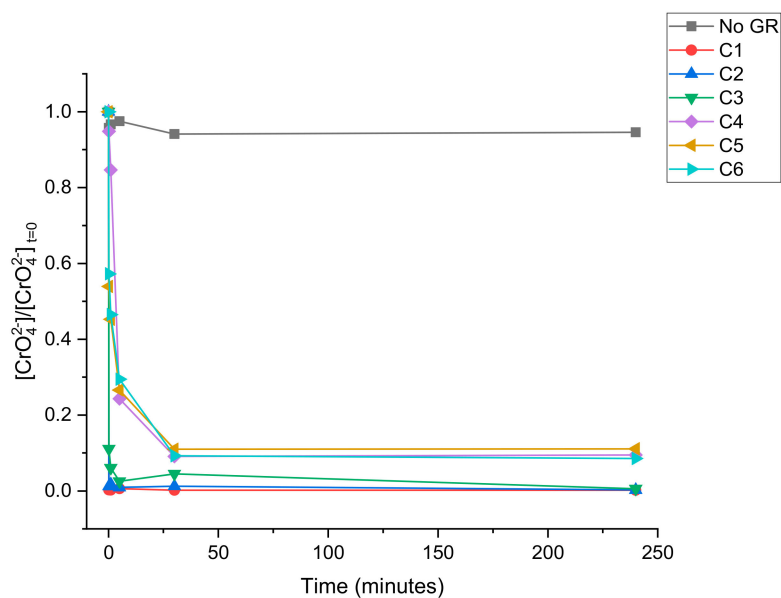

Figure 2. Reduction of Cr(VI) at variable initial CrO_4^{2-} initial concentrations and green rust suspension densities (see Table 1). Blank reaction with no green rust added also included. All measurements were performed on a single batch reaction.
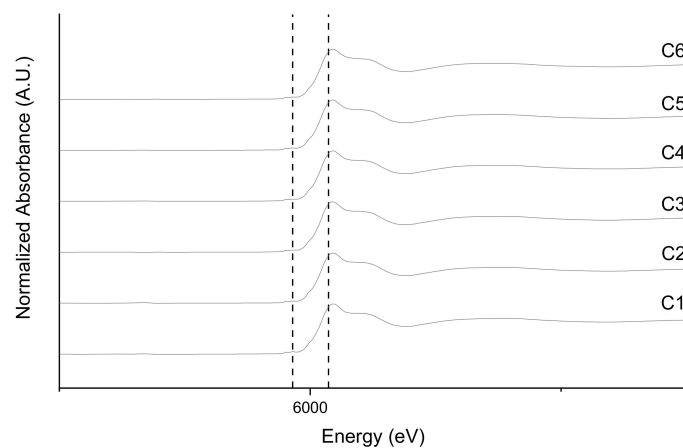
Figure 3. Cr XANES spectrum showing absence of Cr(VI) pre-edge peak (at 5993 eV) and the dominance of the Cr(III) peak (at 6007.3 eV) in samples reacted for 7 days.
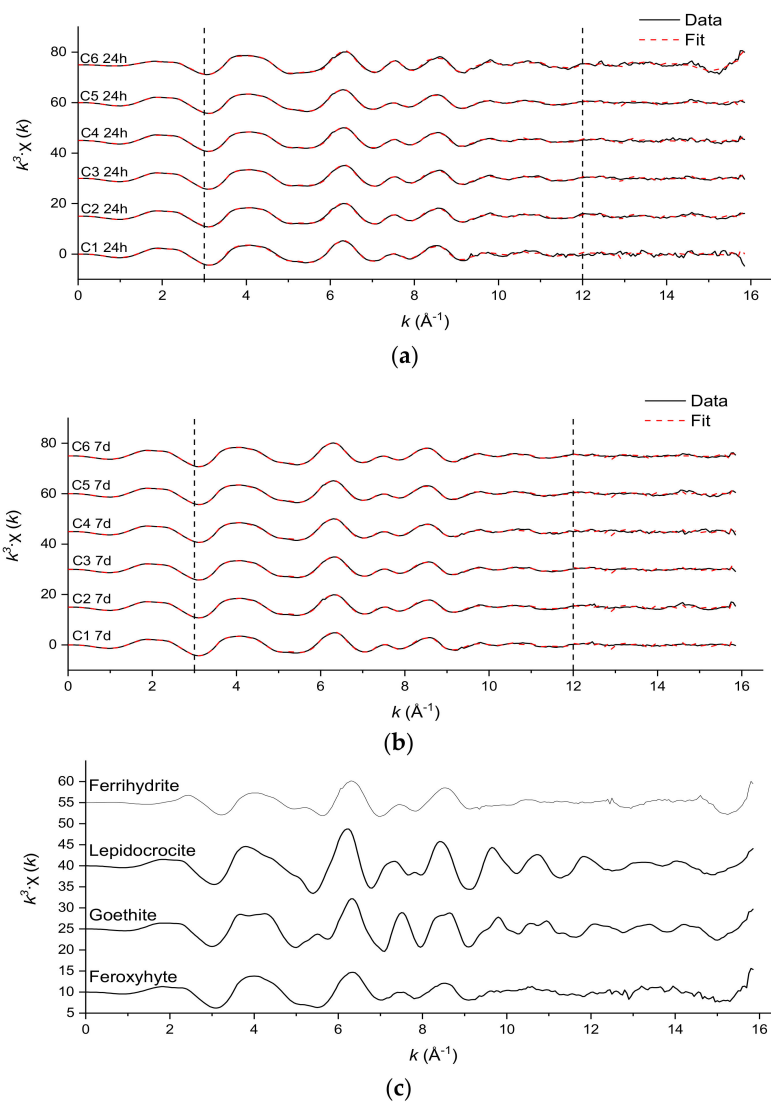

(**a**)

(**b**)

(**c**)

Figure 4. Fe k^3-weighted EXAFS spectra of samples aged for 7 days (**a**) and 24 h (**b**). Fits are linear combinations of the reference standards in (**c**). The vertical dashed lines represent the fit boundaries.

Table 2. Fe linear combination fit results and statistics of samples collected after 24 h and 7 d reaction time. Fits were constrained to no more than four standards.

| | Weights | | | | | | |
Sample	Feroxyhyte	Goethite	Lepidocrocite	Ferrihydrite	Sum	R-Factor	Reduced χ^2
C1 24 h	0.813	0.112	0.064	0.073	1.063	0.024	0.122
C1 7 d	0.902	0.139	0	0	1.041	0.0105	0.0476
C2 24 h	0.741	0.229	0.032	0	1.002	0.01	0.0472
C2 7 d	0.909	0.115	0.016	0.003	1.0	0.0114	0.0521
C3 24 h	0.746	0.243	0.027	0	1.016	0.0090	0.0435
C3 7 d	0.874	0.128	0.028	0	1.03	0.00656	0.0297
C4 24 h	0.794	0.181	0.047	0	1.022	0.00748	0.0355
C4 7 d	0.906	0.085	0.052	0.002	1.044	0.0099	0.046
C5 24 h	0.827	0.075	0.104	0.02	1.027	0.00513	0.0242
C5 7 d	0.809	0.075	0.096	0.059	1.039	0.00631	0.0303
C6 24 h	0.531	0.39	0.033	0	0.953	0.019	0.0934
C6 7 d	0.824	0.075	0.12	0.001	1.02	0.00452	0.0214

Table 3 shows the calculated parameters of the Cr EXAFs shell fits shown in Figure 5. The coordination numbers of the Cr-O and first Cr-Cr shells are fixed to literature values [38] confirmed during preliminary fits of the region R = 1.2 to 3. The outer shells were fit using pathways calculated from the Cr-substituted lepidocrocite (γ-FeOOH) structure, in which MeO_6 octahedra share edges and single corners, corresponding to Cr-Cr distances of 3.05 and 3.98 Å, respectively. The corner-sharing contribution at 3.98 Å has a coordination number between 1.5 and 2.5 in all samples, corresponding to the γ-MeOOH local structure typical of poorly crystalline Cr hydroxides, particularly those on Fe oxide surfaces [39,40].

Table 3. Fitting parameters derived from Cr EXAFS analysis of reaction products. N is the degeneracy of each shell, R is the interatomic distance, and σ^2 is the Debye-Waller parameter. Parameters marked with an asterisk (*) were kept fixed during fitting, while parameters marked § were constrained so that parameters from different shells shared the same value. R-factor reported to indicate goodness of fit.

Sample	Cr-O			Edge:	Cr-Cr		Single Corner:	Cr-Cr		*R* (%)
	N	R (Å)	σ^2 (Å^2)	N	R (Å)	σ^2 (Å^2) §	N ± 50%	R (Å)	σ^2 (Å^2) §	
C1 7 d	6 *	1.97	0.0021 ± 0.0006	3 *	3.06	0.011 ± 0.0028	2.53	3.92	0.011 ± 0.0028	1.97
C2 7 d	6 *	1.96	0.0023 ± 0.0006	3 *	3.05	0.011 ± 0.0026	2.79	3.92	0.011 ± 0.0026	1.87
C3 7 d	6 *	1.96	0.0019 ± 0.0007	3 *	3.04	0.011 ± 0.0032	2.64	3.92	0.011 ± 0.0032	2.17
C4 7 d	6 *	1.97	0.0027 ± 0.0006	3 *	3.04	0.0104 ± 0.0023	1.84	3.89	0.0104 ± 0.0023	1.95
C5 7 d	6 *	1.97	0.0022 ± 0.0006	3 *	3.03	0.01 ± 0.0022	1.76	3.89	0.01 ± 0.0022	1.92
C6 7 d	6 *	1.97	0.0026 ± 0.0006	3 *	3.03	0.01 ± 0.0023	1.79	3.88	0.01 ± 0.0023	2.15

3.4. Electron Microscopy

TEM images and SAED patterns were collected for material sampled at regular intervals during the reactions of green rust with solutions C1 and C6 (Figures 6 and 7). Each sample contained hexagonal plates up to 400–500 nm in size and up to 20 nm thick. After 5 s, reaction C1 results in a mixture of particles with hexagonal and rod-like morphologies (Figure 6a). These particles appear to be associated with each other, although no specific boundaries of the type observed by Skovbjerg et al. (2006) are seen. After 1 min of reaction time, when the green rust has been fully oxidized, the product is again dominated by wide hexagonal particles and smaller rod-like particles, which are either separated from the hexagons or located near their edges. SAED patterns for C1 samples after 1 min of aging (Figure 6b) show two sets of diffuse spots arranged hexagonally, corresponding to Bragg diffraction with d-values of ~2.5 and ~1.7 Å. The d-values roughly match the 330 and 300 spacings of green rust (accounting for slight changes in spacing due to differences in the Fe(II) and Fe(III) ionic radii) identified by Christiansen et al. (2009) [41], indicating that aspects of the original structure in the 100 direction has been preserved. Rod-like particles incorporated into the hexagonal particles are also visible in the SEM images. After 7 days of aging, the boundaries of the hexagonal particles have roughened and very faint SAED spots corresponding to the same spacings can be seen (pattern in the inset has been enhanced for visibility). Both the SEM and TEM images indicate that rod-like particles are still incorporated into the structure, and the SEM images of the particles show that they have become thicker and have a rough, amorphous surface (Figure 6c).
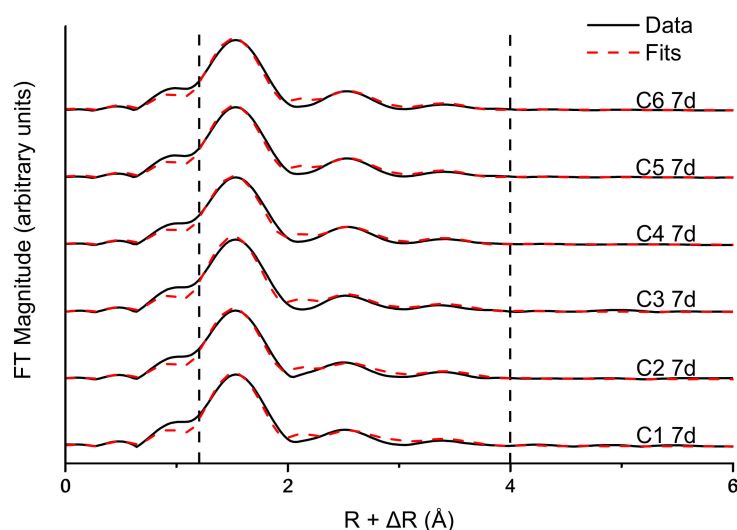

Figure 5. Fourier-transformed Cr EXAFS spectra and fits of all samples after 7 days. All data were fit over the range $k = 3$ to 10.5 Å^{-1} due to noise at high k in some samples and similar treatment of spectra in other studies (Hansel et al., 2003). Fit boundaries indicated by dotted lines at R = 1.2 and 4. Calculated fitting parameters shown in Table 3.

At the halfway point of reaction C6 at 1 min (Figure 7a), large rod-like particles have formed near the edges of the green rust crystal and a faint boundary can be seen. The interiors of the hexagonal crystals appear fractured (visible in the inset), which may be an artifact of the sample preparation or the vacuum conditions in the sample chamber. The SAED pattern shows the same hexagonally packed oxygen-derived reflections as mentioned earlier. After 10 min, when the reaction is nearing completion, the hexagonal particle morphology is maintained with goethite-like rods associated with the crystal edges and parallel crystal fractures visible in the crystal interior (Figure 7b). SAED patterns obtained from these central domains are faint (possibly due to underexposure) but show the same reflections visible in the C1 samples. SEM images also show that these particles have smooth surfaces. After 7 days, the hexagonal particles have lost much of their crystallinity, with degraded edges and a few goethite-like rods associated with the structure (Figure 7c). Very faint spots are visible in the

diffraction pattern. As aging processes are not known to transform crystalline materials to amorphous analogues, even topotactically, a more likely explanation is that residual Fe(II) in the system induced the crystallization of particles in earlier (1 min, 10 min) samples by the mechanism identified in Pedersen et al. (2005) [42], whereas Fe(II) is absent after 7 days of reaction time. Pedersen et al. [42] proposed that electron conduction from aqueous Fe^{2+} gives rise to Fe(II)-O bonds in the interior of ferrihydrite, which destabilizes the structure and leads to dissolution and re-precipitation, but the generation of structural Fe(II) would stabilize these LDH-like particles, in which Fe(II)-O_6 octahedra are more stable. The oxidation of the remaining structural Fe(II), however, leads to a restructuring of the LDH-like particles, which have low crystallinity after the reaction is complete.
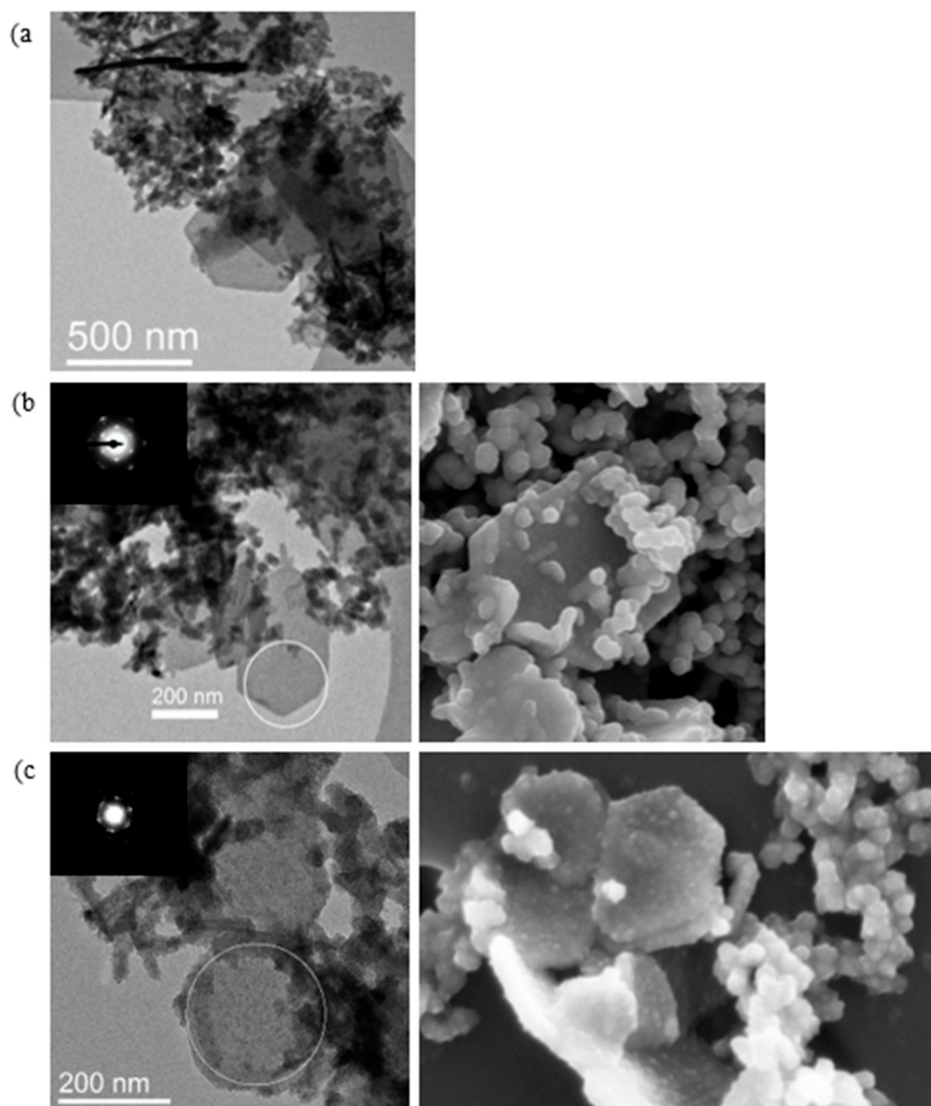
Figure 6. SEM and TEM images showing the progression of reaction C1 after 5 s (**a**), 1 min (**b**) and 7 days (**c**) of reaction time. Regions where electron diffraction measurements were obtained are circled, and the diffraction patterns are shown in the insets. Spacings of 2.5 and 1.7 Å detected after 1 min, very weak pattern detected after 7 days.
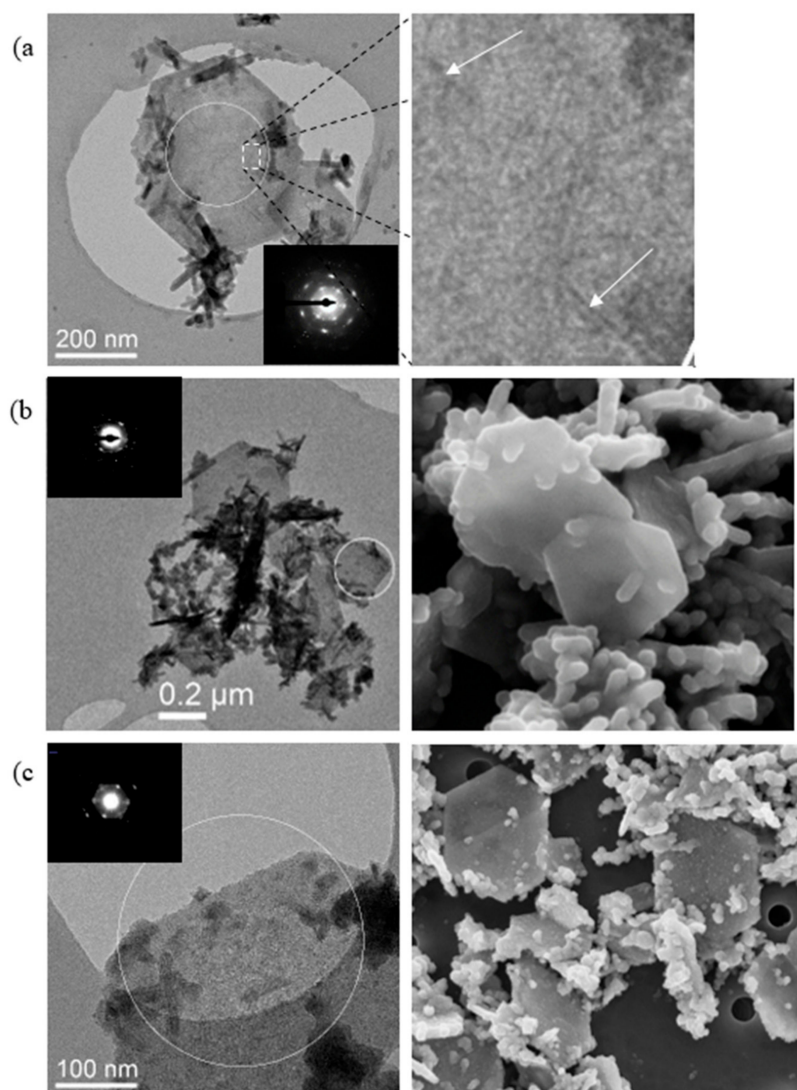
Figure 7. SEM and TEM images showing the progression of reaction C6 after 1 min (**a**), 10 min (**b**) and 7 days (**c**) of reaction time. Regions where electron diffraction measurements were obtained are circled. Spacings of 2.5 and 1.7 Å detected after 1 min and 10 min, very faint rings after 7 days.

4. Discussion

4.1. Kinetics of CrO_4^{2-} Reduction by Green Rust Sulfate

Reaction rates in this study were much faster than those observed by Bond and Fendorf (2003) [28] for a reaction between CrO_4^{2-} and green rust sulfate at similar concentrations. Skovbjerg et al. (2006) [31] also observed rapid reduction of CrO_4^{2-} and attributed the difference to the method of preparation. Drying synthetic green rust dehydrates the interlayer, which is hypothesized to decrease the exchangeability and reactivity of oxidants [14]. The green rust in this experiment was not dried or rinsed after synthesis.

Since the green rust was added as a suspension, aqueous Fe^{2+} was present at the beginning of the reaction, but at a low concentration. The resulting reaction between CrO_4^{2-} and Fe^{2+} may have been the reason for a pH drop to between 4 and 5 in each experiment. However, previous studies [43,44] suggest that the reduction rate of CrO_4^{2-} by aqueous Fe^{2+} is rapid enough to contribute to the reaction kinetics observed in this experiment, but this reaction rate is heavily dependent on pH, the behavior of which was not monitored while the reaction was in progress. It is possible that the green rust surface may have acted as a substrate, increasing the rate of reduction [31].

4.2. Composition of Observed Reaction Products

Fe EXAFS fitting results reveal that the short-range (5–6 Å) particle structure is dominated by feroxyhyte-like structural motifs (i.e., face-sharing octahedra). The Fourier-transformed Cr spectra show a prominent single corner-sharing shell at an interatomic distance of approximately 3.9 Å, characteristic of a γ-CrOOH short-range structure (Figure 8), a structure typical of poorly crystalline Cr hydroxides [38–40]. Charlet & Manceau (1992) [39] showed that EXAFS spectra of Cr coprecipitated with Fe or sorbed on Fe oxide surfaces show a double corner-sharing reflection at approximately 3.46 Å, which was not detected in the current study. This suggests that the Cr in these samples has formed a spatially distinct Cr(III) hydroxide phase, probably precipitated on the surface of Fe oxide particles. These results, combined with electron microscopy images that show that the hexagonal morphology of the green rust crystals is maintained after oxidation, suggest that the primary product is a layered Fe(III) oxyhydroxysulfate with a spatially distinct $Cr(OH)_3$ phase that forms on the particle surface or in the bulk solution.

Ferrihydrite and feroxyhyte are nano-crystalline Fe oxides. Based on published structures [36,45,46], both phases would be expected to give rise to the hexagonal arranged diffraction spots identified with SAED when probed perpendicular to the hexagon oxygen packing. As EXAFS is a short-range (<5–6 Å) technique and is unable to detect long-range crystal structure, the detection of material with a feroxyhyte- or ferrihydrite-like structure is most likely an expression of structural motifs present in both the synthesized feroxyhyte reference standard and the product. EDX spectra of these hexagonal particles also revealed unexpectedly high sulfur concentrations, indicating that sulfate is still incorporated into the structure. Rapid oxidation of the green rust crystal without displacing the interlayer sulfate anions would prevent complete transformation to another Fe(III) oxide, potentially explaining why the primary product is poorly crystalline. A topotactic redox reaction would require partial deprotonation of the Fe oxide layers to maintain the charge balance; one way this could be accomplished is the formation of the face-sharing octahedra suggested by the EXAFS fitting results. Previous studies [47,48] have claimed that a major product of rapid oxidation of green rust sulfate is a layered, poorly crystalline Fe(III) oxyhydroxysulfate, and the product of the reaction in this study appears to be similar.
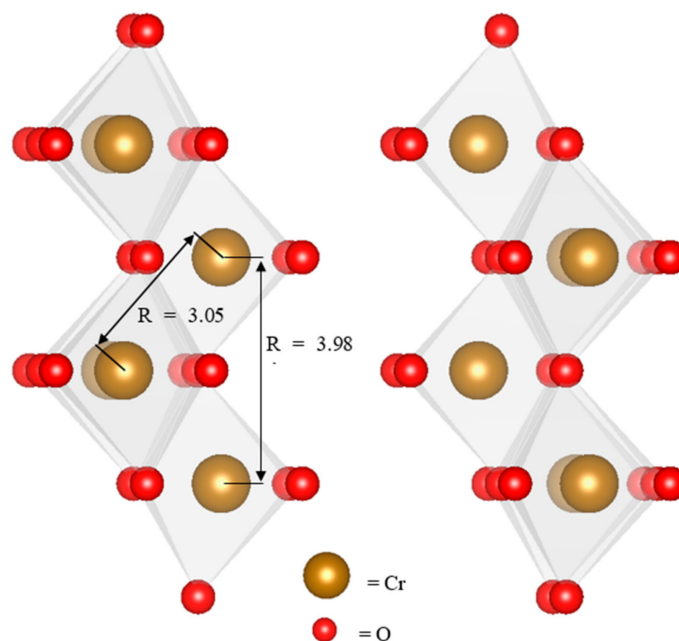

Figure 8. Γ-CrOOH short-range structure of $Cr(OH)_3$. Edge-sharing (3.05 Å) and single corner-sharing (3.98 Å) Cr-Cr distances correspond to the predominant scattering paths identified by EXAFS fitting.

Spectroscopic data also suggests that lepidocrocite and goethite are significant components of the byproduct. Needle- and rod-like particles with lengths of approximately 50 nanometers and similar morphologies to goethite are visible in TEM and SEM images, both on the hexagonal particle surfaces (see SEM images) and in separate aggregates. Sharply defined rod-like particles are no longer present after 7 days. Skovbjerg et al. (2006) [31] identified Cr(III)-bearing goethite as the primary product of this reaction, and the low crystallinity of the product in both experiments is most likely a result of Cr substitution for Fe [49]. These particles likely formed through a dissolution-precipitation mechanism while the product was aging and nucleated on the hexagonal particle surfaces or in the bulk solution. Lepidocrocite was also detected in samples obtained from reactions at lower chromate concentrations, possibly due to the formation of lepidocrocite-like structural motifs (i.e., edge-sharing octahedra) within the layered, poorly crystalline final product.

Amorphous particles can also be seen in aggregates separate from the hexagonal particles. These particles appear circular in TEM and SEM images and have very high Cr concentrations. EDX measurements show that Cr/(Fe + Cr) is between 20 and 40%, so these particles most likely formed due to reduction of chromate by aqueous Fe^{2+}. The stoichiometry of this reaction (Equation (1)) results in particles with very high Cr content.

$$0.25CrO_4^{2-} + 0.75Fe^{2+} + 2H_2O = Cr_{0.25}Fe_{0.75}(OH)_3 + H^+ \qquad (1)$$
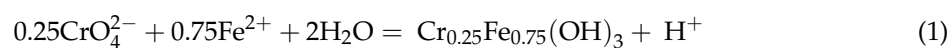
Although the rate of this reaction is pH-dependent [43,44] and therefore unknown, the visibility of these particles suggests that this reaction contributed to Cr(VI) reduction and green rust may have acted as a reaction substrate. Schwertmannite formation is favored by the conditions observed at the end of the reaction, so a substantial portion of the amorphous particles may be identified as schwertmannite.
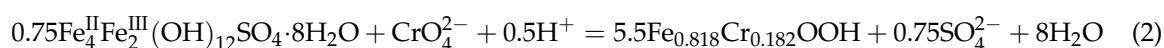
4.3. Reaction Mechanisms

As the poorly crystalline particles observed at the end of the reaction maintain their hexagonal morphologies, are feroxyhyte-like in structure and still contain sulfur, these particles were most likely to have been oxidized by means of CrO_4^{2-} reduction at the particle surface, which oxidizes Fe(II) in the interior via an electron hopping mechanism. Green rust, like many other Fe(III) oxides [50,51], is a semiconductor due to the ability of electrons to migrate between adjacent Fe(II) centers [52]. This electron hopping is fastest for electron transport within an Fe(II)/Fe(III) oxide layer, but Yao et al. (1998) [53] demonstrated that electron transport between layers is possible in green rusts and other LDHs and accelerates in response to the introduction of a potential difference (i.e., binding of chromate at the particle surface). Through this mechanism, green rust can regenerate reactive Fe(II) centers at the surface by transporting the electron "holes" produced by oxidation into the crystal's interior, which then causes a rearrangement to another Fe(III) oxide structure to balance the charge. The Fe(III) oxide produced depends on the oxidation rate; Hansen (2001) [54] gave the following succession from slow to fast reaction: magnetite, goethite, lepidocrocite, feroxyhyte and ferrihydrite. However, this mechanism, especially when rapid, may not allow the sulfate in the interlayer to escape, with the resulting charge imbalance preventing complete transformation of the product to a thermodynamically preferred crystalline Fe oxide. The partially transformed Fe(III) oxide resembled feroxyhyte and lepidocrocite spectroscopically because the layered structure was maintained, and most transformations involved deprotonation and formation of face-sharing octahedra to balance the charge. The spectroscopic resemblance of the product to feroxyhyte is most likely a consequence of this type of internal rearrangement.

The other major product of this surface oxidation reaction is the amorphous $Cr(OH)_3$ coating. This coating forms because poorly crystalline Fe(III) oxide surfaces are ideal substrates for Cr(III) precipitation [39,55], and newly produced Cr^{3+} ions continue to precipitate as $Cr(OH)_3$ at the particle surface. This Cr(III) oxyhydroxide layer passivates the surface by blocking access to the green rust structure, as observed when chromate reacts with other green rusts [30], magnetite [56] and ZVI [57].

Passivation may be responsible for the incomplete reduction of chromate in reactions C4-C6, where 10% of the chromate remains in solution at the end of the reaction.

In addition to the coated hexagonal plates, the reaction also produced rod-like particles of goethite, which can be seen in the SEM and TEM images and detected in the Fe and Cr EXAFS spectra. Skovbjerg et al. (2006) [30] identified similar Cr(III)-bearing goethites and hypothesized that these particles formed as a result of green rust oxidation through a chromate-sulfate interlayer exchange mechanism. The stoichiometry of this reaction predicts a Cr(III)-goethite solid solution with a Cr/(Cr+Fe) ratio of 0.182 (Equation (2)).

$$0.75Fe_4^{II}Fe_2^{III}(OH)_{12}SO_4 \cdot 8H_2O + CrO_4^{2-} + 0.5H^+ = 5.5Fe_{0.818}Cr_{0.182}OOH + 0.75SO_4^{2-} + 8H_2O \quad (2)$$

Schwertmann et al. (1989) [49] were not able to synthesize goethite with Cr/(Cr + Fe) mole ratios greater than 0.12, and Skovbjerg et al. (2006) [31] found that goethite particles with Cr/(Cr + Fe) greater than approximately 0.10 (as measured by EDX) underwent rearrangement and became less crystalline as the product was aged. Similarly, goethite particles produced in reactions C1 and C6 appear crystalline early in the reaction but poorly crystalline in TEM images (Figures 6 and 7) after aging the product for seven days, and the goethite component of both the Fe and Cr EXAFS fits appears to decline between 24 h and 7 days, indicating that these particles may be losing their crystallinity. A more likely explanation is the depletion of aqueous Fe^{2+}, which has been shown to catalyze the transformation of poorly crystalline Fe(III) oxyhydroxides in batch and flow-through experiments [58,59].

The most noticeable trend in these experiments is that more goethite is produced at higher initial CrO_4^{2-} concentrations. This trend matches the observations of Skovbjerg et al. (2006) [31], where Cr-substituted goethite is the primary product of reactions with much higher initial CrO_4^{2-} concentrations, while Bond and Fendorf (2003) [28] observed the formation of an amorphous product at concentrations similar to those tested in this experiment. Therefore, it appears that the CrO_4^{2-} exchange mechanism becomes more important to the reaction at higher CrO_4^{2-} concentrations. Equations (3) and (4) show the rate-limiting steps of the competing exchange and surface oxidation (assuming monodentate adsorption of Cr(VI)) mechanisms, as well as the hypothetical rate equations of these reactions. If the CrO_4^{2-} reaction order (*a*) of the exchange reaction is higher than the reaction order (*c*) of the surface oxidation reaction, this would cause Cr-substituted goethite to be favored at higher CrO_4^{2-} concentrations as observed.

$$CrO_4^{2-} + GR - SO_4 = GR - CrO_4 + SO_4^{2-} \quad \frac{d\left[CrO_4^{2-}\right]}{dt} = k_1 \frac{\left[CrO_4^{2-}\right]^a}{\left[SO_4^{2-}\right]^b} \quad (3)$$

$$CrO_4^{2-} + FeOH = FeOCrO_3^- + OH^- \cdot \frac{d\left[CrO_4^{2-}\right]}{dt} = k_2 \frac{\left[CrO_4^{2-}\right]^c}{\left[OH^-\right]^d} \quad (4)$$

4.4. Implications for Use in Permeable Reactive Barriers

The effectiveness of green rust sulfate for reducing Cr(VI) has been addressed by these experiments, but the long-term stability of the Cr(III)-bearing products of this reaction remains questionable. Due to the heterogeneity of the reaction between green rust sulfate particles and aqueous CrO_4^{2-}, the identity and morphology of the products depend on the mechanism and can therefore be changed by modifications to the particle composition. The primary product of these reactions was a hexagonal, Fe(III) oxyhydroxysulfate particle covered by a $Cr(OH)_3$ surface coating. Cr(III) oxyhydroxides are poorly characterized, but Papassiopi et al. (2014) [60] found that synthetic $Cr(OH)_3$ is more soluble than its Fe(III) analogue and did not transform to a less-soluble Cr (oxy)hydroxide during the experiment. Because CrO_4^{2-} is normally found under oxidizing conditions, $Cr(OH)_3$

dissolution is a potential pathway for the return of CrO_4^{2-} to the newly remediated groundwater if the redox conditions have not been altered, particularly in the presence of Mn(IV) oxides [61]. Studies of Cr(III) hydroxide redox behavior in soils [9–11,62] have shown that biogenic Mn(IV) oxides in soils can reverse the reductive transformation of chromate by oxidizing soluble Cr^{3+}. The limiting factor in this process is the solubility of the Cr(III)-bearing phases (incorporation into ferrihydrite decreased oxidation by 37%), so the product produced in these reactions suggests that this method is unsuitable. In addition, green rust sulfate is unstable under oxidizing conditions, and modifications to the structure or composition to prevent oxidation by other compounds might make green rust sulfate more viable for remediation. Green rust is also metastable with respect to magnetite and transforms to magnetite when diluted in water, suggesting that it may not be stable under flow conditions in aquifers unless stabilized by high Fe^{2+} concentrations in the groundwater [62].

Similarly, this study provides insights into the chemical and microbial mechanisms governing Cr speciation in natural environments. Green rust is commonly encountered in redox transition-zone sediments [13] and is believed to form as a result of microbial bioreduction of Fe oxides [63,64], and reduction by green rust and other Fe(II)-bearing minerals is most likely one of the mechanisms governing changes in Cr speciation in response to soil redox conditions. Reduction of Cr(VI) by structural Fe(II) in biogenic Fe oxides may favor the precipitation of spatially distinct Cr(III) hydroxides in soils.

5. Conclusions

This study shows that green rust sulfate can effectively remediate Cr(VI) contamination in groundwater, but the investigators have concerns about the stability of the reaction byproducts. Based on the EXAFS fitting results (Figures 4 and 5, Tables 2 and 3) and electron microscope images (Figures 6 and 7), it appears that this reaction produces a poorly crystalline Cr(III) hydroxide, as opposed to a Cr(III)-substituted Fe oxide, which would be far more stable and resistant to oxidation by Mn(IV) oxides. One potential pathway for future study is the use of green rust solid solutions to remediate Cr(VI). Cr(III)-substituted Fe(III) oxides should be viewed as the favored products of this reaction due to their increased stabilities; therefore, particles should be designed to favor the CrO_4^{2-} exchange reduction mechanism. Substitutions of metal cations such as Zn, Mg, and Al that do not have multiple oxidation states may disrupt the electron hopping chain that enables reduction of CrO_4^{2-} at the particle surface. These particles may also be more stable than pure green rust if O_2 is unable to oxidize them at their surfaces.

References

1.   Saha, R.; Nandi, R.; Saha, B. Sources and toxicity of hexavalent chromium. *J. Coord. Chem.* **2011**, *64*, 1782–1806. [CrossRef]

2. Barceloux, D.G. Chromium. *J. Toxicol. Clin. Toxicol.* **1999**, *37*, 173–194. [CrossRef] [PubMed]

3. Rai, D.; Sass, B.M.; Moore, D.A. Chromium(III) Hydrolysis Constants and Solubility of Chromium(III) Hydroxide. *Inorg. Chem.* **1987**, *26*, 345–349. [CrossRef]

4. Rai, D.; Moore, D.A.; Hess, N.J.; Rosso, K.M.; Rao, L.; Heald, S.M. Chromium(III) Hydroxide Solubility in the Aqueous K^+-H^+-OH^--CO_2-HCO_3^--CO_3^{2-}-H_2O System: A Thermodynamic Model. *J. Solut. Chem.* **2007**, *36*, 1261–1285. [CrossRef]

5. Su, C.; Ludwig, R.D. Treatment of Hexavalent Chromium in Chromite Ore Processing Solid Waste Using a Mixed Reductant Solution of Ferrous Sulfate and Sodium Dithionite. *Environ. Sci. Technol.* **2005**, *39*, 6208–6216. [CrossRef] [PubMed]

6. Puls, R.W.; Paul, C.J.; Powell, R.M. The application of in situ permeable reactive (zero-valent iron) barrier technology for the remediation of chromate-contaminated groundwater: A field test. *Appl. Geochem.* **1999**, *14*, 989–1000. [CrossRef]

7. Wilkin, R.T.; Su, C.; Ford, R.G.; Paul, C.J. Chromium-Removal Processes during Groundwater Remediation by a Zerovalent Iron Permeable Reactive Barrier. *Environ. Sci. Technol.* **2005**, *39*, 4599–4605. [CrossRef] [PubMed]

8. Kumpiene, J.; Ore, S.; Renella, G.; Mench, M.; Lagerkvist, A.; Maurice, C. Assessment of zerovalent iron for stabilization of chromium, copper, and arsenic in soil. *Environ. Pollut.* **2006**, *144*, 62–69. [CrossRef] [PubMed]

9. Hausladen, D.M.; Fendorf, S. Hexavalent Chromium Generation within Naturally Structured Soils and Sediments. *Environ. Sci. Technol.* **2017**, *51*, 2058–2067. [CrossRef] [PubMed]

10. Pan, C.; Liu, H.; Catalano, J.G.; Qian, A.; Wang, Z.; Giammar, D.E. Rates of Cr(VI) Generation from $Cr_xFe_{1-x}(OH)_3$ Solids upon Reaction with Manganese Oxide. *Environ. Sci. Technol.* **2017**, *51*, 12416–12423. [CrossRef] [PubMed]

11. Varadharajan, C.; Beller, H.R.; Bill, M.; Brodie, E.L.; Conrad, M.E.; Han, R.; Irwin, C.; Larsen, J.T.; Lim, H.C.; Molins, S.; et al. Reoxidation of Chromium(III) Products Formed under Different Biogeochemical Regimes. *Environ. Sci. Technol.* **2017**, *51*, 4918–4927. [CrossRef] [PubMed]

12. Christiansen, B.C.; Dideriksen, K.; Katz, A.; Nedel, S.; Bovet, N.; Sorensen, H.O.; Frandsen, C.; Gundlach, C.; Andersson, M.P.; Stipp, S.L. Incorporation of monovalent cations in sulfate green rust. *Inorg. Chem.* **2014**, *53*, 8887–8894. [CrossRef] [PubMed]

13. Trolard, F.; Bourrié, G.; Abdelmoula, M.; Refait, P.; Feder, F. Fougerite, a new mineral of the pyroaurite-iowaite group: Description and crystal structure. *Clays Clay Miner.* **2007**, *55*, 323–334. [CrossRef]

14. Lewis, D.G. Factors influencing the stability and properties of green rusts. *Adv. Geoecol.* **1997**, *30*, 345–372.

15. Roh, Y.; Lee, S.Y.; Elless, M.P. Characterization of corrosion products in the permeable reactive barriers. *Environ. Geol.* **2000**, *40*, 184–194. [CrossRef]

16. Refait, P.; Memet, J.B.; Bon, C.; Sabot, R.; Génin, J.M.R. Formation of the Fe(II)–Fe(III) hydroxysulphate green rust during marine corrosion of steel. *Corros. Sci.* **2003**, *45*, 833–845. [CrossRef]

17. Su, C.; Puls, R.W. Significance of Iron(II,III) Hydroxycarbonate Green Rust in Arsenic Remediation Using Zerovalent Iron in Laboratory Column Tests. *Environ. Sci. Technol.* **2004**, *38*, 5224–5231. [CrossRef] [PubMed]

18. Jönsson, J.; Sherman, D.M. Sorption of As(III) and As(V) to siderite, green rust (fougerite) and magnetite: Implications for arsenic release in anoxic groundwaters. *Chem. Geol.* **2008**, *255*, 173–181. [CrossRef]

19. Perez, J.P.H.; Freeman, H.M.; Schuessler, J.A.; Benning, L.G. The interfacial reactivity of arsenic species with green rust sulfate (GR_{SO4}). *Sci. Total Environ.* **2019**, *648*, 1161–1170. [CrossRef] [PubMed]

20. Hansen, H. Kinetics of nitrate reduction by green rusts—Effects of interlayer anion and Fe(II):Fe(III) ratio. *Appl. Clay Sci.* **2001**, *18*, 81–91. [CrossRef]

21. Hansen, H.C.B.; Borggaard, O.K.; Sørensen, J. Evaluation of the free energy of formation of Fe(II)-Fe(III) hydroxide-sulphate (green rust) and its reduction of nitrite. *Geochim. Cosmochim. Acta* **1994**, *58*, 2599–2608. [CrossRef]

22. Myneni, S.C. Abiotic Selenium Redox Transformations in the Presence of Fe(II,III) Oxides. *Science* **1997**, *278*, 1106–1109. [CrossRef]

23. Borsig, N.; Scheinost, A.C.; Shaw, S.; Schild, D.; Neumann, T. Retention and multiphase transformation of selenium oxyanions during the formation of magnetite via iron(II) hydroxide and green rust. *Dalton Trans.* **2018**, *47*, 11002–11015. [CrossRef] [PubMed]

24. O'Loughlin, E.J.; Kelly, S.D.; Cook, R.E.; Csencsits, R.; Kemner, K.M. Reduction of Uranium(VI) by Mixed Iron(II)/Iron(III) Hydroxide (Green Rust): Formation of UO$_2$Nanoparticles. *Environ. Sci. Technol.* **2003**, *37*, 721–727. [CrossRef] [PubMed]

25. Christiansen, B.C.; Geckeis, H.; Marquardt, C.M.; Bauer, A.; Römer, J.; Wiss, T.; Schild, D.; Stipp, S.L.S. Neptunyl (Np) interaction with green rust. *Geochim. Cosmochim. Acta* **2011**, *75*, 1216–1226. [CrossRef]

26. Loyaux-Lawniczak, S.; Refait, P.; Lecomte, P.; Ehrhardt, J.J.; Génin, J.M.R. The reduction of chromate ions by Fe(II) layered hydroxides. *Hydrol. Earth Syst. Sci.* **1999**, *3*, 593–599. [CrossRef]

27. Loyaux-Lawniczak, S.; Refait, P.; Ehrhardt, J.-J.; Lecomte, P.; Génin, J.-M.R. Trapping of Cr by Formation of Ferrihydrite during the Reduction of Chromate Ions by Fe(II)−Fe(III) Hydroxysalt Green Rusts. *Environ. Sci. Technol.* **2000**, *34*, 438–443. [CrossRef]

28. Bond, D.L.; Fendorf, S. Kinetics and Structural Constraints of Chromate Reduction by Green Rusts. *Environ. Sci. Technol.* **2003**, *37*, 2750–2757. [CrossRef] [PubMed]

29. Williams, A.G.B.; Scherer, M.M. Kinetics of Cr(VI) Reduction by Carbonate Green Rust. *Environ. Sci. Technol.* **2001**, *35*, 3488–3494. [CrossRef] [PubMed]

30. Legrand, L.; El Figuigui, A.; Mercier, F.; Chausse, A. Reduction of Aqueous Chromate by Fe(II)/Fe(III) Carbonate Green Rust: Kinetic and Mechanistic Studies. *Environ. Sci. Technol.* **2004**, *38*, 4587–4595. [CrossRef] [PubMed]

31. Skovbjerg, L.L.; Stipp, S.L.S.; Utsunomiya, S.; Ewing, R.C. The mechanisms of reduction of hexavalent chromium by green rust sodium sulphate: Formation of Cr-goethite. *Geochim. Cosmochim. Acta* **2006**, *70*, 3582–3592. [CrossRef]

32. Géhin, A.; Ruby, C.; Abdelmoula, M.; Benali, O.; Ghanbaja, J.; Refait, P.; Génin, J.-M.R. Synthesis of Fe(II-III) hydroxysulphate green rust by coprecipitation. *Solid State Sci.* **2002**, *4*, 61–66. [CrossRef]

33. Ravel, B.; Newville, M. ATHENA and ARTEMIS Interactive Graphical Data Analysisusing IFEFFIT. *Physica Scr.* **2005**, *12*, 537–541. [CrossRef]

34. Cornell, R.M.; Schwertmann, U. *Iron Oxides in the Laboratory*, 2nd ed.; Wiley-VCH: Weinheim, Germany, 2008.

35. Simon, L.; François, M.; Refait, P.; Renaudin, G.; Lelaurain, M.; Génin, J.-M.R. Structure of the Fe(II-III) layered double hydroxysulphate green rust two from Rietveld analysis. *Solid State Sci.* **2003**, *5*, 327–334. [CrossRef]

36. Manceau, A.; Drits, V.A. Local Structure of Ferrihydrite and Feroxyhite by Exafs Spectroscopy. *Clay Miner.* **2018**, *28*, 165–184. [CrossRef]

37. Maillot, F.; Morin, G.; Wang, Y.; Bonnin, D.; Ildefonse, P.; Chaneac, C.; Calas, G. New insight into the structure of nanocrystalline ferrihydrite: EXAFS evidence for tetrahedrally coordinated iron(III). *Geochim. Cosmochim. Acta* **2011**, *75*, 2708–2720. [CrossRef]

38. Papassiopi, N.; Pinakidou, F.; Katsikini, M.; Antipas, G.S.; Christou, C.; Xenidis, A.; Paloura, E.C. A XAFS study of plain and composite iron(III) and chromium(III) hydroxides. *Chemosphere* **2014**, *111*, 169–176. [CrossRef] [PubMed]

39. Charlet, L.; Manceau, A.A. X-ray absorption spectroscopic study of the sorption of Cr(III) at the oxide-water interface. *J. Colloid Interface Sci.* **1992**, *148*, 443–458. [CrossRef]

40. Frommer, J.; Nachtegaal, M.; Czekaj, I.; Kretzschmar, R. The Cr X-ray absorption K-edge structure of poorly crystalline Fe(III)-Cr(III)-oxyhydroxides. *Am. Mineral.* **2010**, *95*, 1202–1213. [CrossRef]

41. Christiansen, B.C.; Balic-Zunic, T.; Petit, P.O.; Frandsen, C.; Mørup, S.; Geckeis, H.; Katerinopoulou, A.; Stipp, S.L.S. Composition and structure of an iron-bearing, layered double hydroxide (LDH)—Green rust sodium sulphate. *Geochim. Cosmochim. Acta* **2009**, *73*, 3579–3592. [CrossRef]

42. Pedersen, H.D.; Postma, D.; Jakobsen, R.; Larsen, O. Fast transformation of iron oxyhydroxides by the catalytic action of aqueous Fe(II). *Geochim. Cosmochim. Acta* **2005**, *69*, 3967–3977. [CrossRef]

43. Buerge, I.J.; Hug, S.J. Kinetics and pH Dependence of Chromium(VI) Reduction by Iron(II). *Environ. Sci. Technol.* **1997**, *31*, 1426–1432. [CrossRef]

44. Sedlak, D.L.; Chan, P.G. Reduction of hexavalent chromium by ferrous iron. *Geochim. Cosmochim. Acta* **1997**, *61*, 2185–2192. [CrossRef]

45. Jansen, E.; Kyek, A.; Schäfer, W.; Schwertmann, U. The structure of six-line ferrihydrite. *Appl. Phys. A Mater. Sci. Process.* **2002**, *74*, s1004–s1006. [CrossRef]

46. Michel, F.M.; Ehm, L.; Antao, S.M.; Lee, P.L.; Chupas, P.J.; Liu, G.; Strongin, D.R.; Schoonen, M.A.; Phillips, B.L.; Parise, J.B. The structure of ferrihydrite, a nanocrystalline material. *Science* **2007**, *316*, 1726–1729. [CrossRef] [PubMed]

47. Hansen, H.C.B.; Bender Koch, C. Reduction of nitrate to ammonium by sulphate green rust: Activation energy and reaction mechanism. *Clay Miner.* **1998**, *33*, 87–101. [CrossRef]

48. Antony, H.; Legrand, L.; Chaussé, A. Carbonate and sulphate green rusts—Mechanisms of oxidation and reduction. *Electrochim. Acta* **2008**, *53*, 7146–7156. [CrossRef]

49. Schwertmann, U.; Gasser, U.; Sticher, H. Chromium-for-iron substitution in synthetic goethites. *Geochim. Cosmochim. Acta* **1989**, *53*, 1293–1297. [CrossRef]

50. Schrupp, D.; Sing, M.; Tsunekawa, M.; Fujiwara, H.; Kasai, S.; Sekiyama, A.; Suga, S.; Muro, T.; Brabers, V.A.M.; Claessen, R. High-energy photoemission on Fe_3O_4: Small polaron physics and the Verwey transition. *Europhys. Lett.* **2005**, *70*, 789–795. [CrossRef]

51. Katz, J.E.; Zhang, X.; Attenkofer, K.; Chapman, K.W.; Frandsen, C.; Zarzycki, P.; Rosso, K.M.; Falcone, R.W.; Waychunas, G.A.; Gilbert, B. Electron small polarons and their mobility in iron (oxyhydr)oxide nanoparticles. *Science* **2012**, *337*, 1200–1203. [CrossRef] [PubMed]

52. Wander, M.C.F.; Rosso, K.M.; Schoonen, M.A.A. Structure and Charge Hopping Dynamics in Green Rust. *J. Phys. Chem. C* **2007**, *111*, 11414–11423. [CrossRef]

53. Yao, K.; Taniguchi, M.; Nakata, M.; Takahashi, M.; Yamagishi, A. Electrochemical Scanning Tunneling Microscopy Observation of Ordered Surface Layers on an Anionic Clay-Modified Electrode. *Langmuir* **1998**, *14*, 2890–2895. [CrossRef]

54. Hansen, H.C.B. Environmental chemistry of iron (II)–iron (III) LDHs (green rusts). In *Layered Double Hydroxides: Present and Future*; Rives, V., Ed.; Nova Science Publishers Inc.: New York, NY, USA, 2001; pp. 413–434.

55. Garg, A.; Matijevic, E. Preparation and properties of uniformly coated inorganic colloidal particles. 2. Chromium hydrous oxide on hematite. *Langmuir* **1988**, *4*, 38–44. [CrossRef]

56. Kendelewicz, T.; Liu, P.; Doyle, C.S.; Brown, G.E. Spectroscopic study of the reaction of aqueous Cr(VI) with Fe_3O_4 (111) surfaces. *Surf. Sci.* **2000**, *469*, 144–163. [CrossRef]

57. Lai, K.C.K.; Lo, I.M.C. Removal of chromium (VI) by acid-washed zero-valent iron under various groundwater geochemistry conditions. *Environ. Sci. Technol.* **2008**, *42*, 1238–1244. [CrossRef] [PubMed]

58. Yang, L.; Steefel, C.I.; Marcus, M.A.; Bargar, J.R. Kinetics of Fe(II)-catalyzed transformation of 6-line ferrihydrite under anaerobic flow conditions. *Environ. Sci. Technol.* **2010**, *44*, 5469–5475. [CrossRef] [PubMed]

59. Boland, D.D.; Collins, R.N.; Miller, C.J.; Glover, C.J.; Waite, T.D. Effect of solution and solid-phase conditions on the Fe(II)-accelerated transformation of ferrihydrite to lepidocrocite and goethite. *Environ. Sci. Technol.* **2014**, *48*, 5477–5485. [CrossRef] [PubMed]

60. Papassiopi, N.; Vaxevanidou, K.; Christou, C.; Karagianni, E.; Antipas, G.S. Synthesis, characterization and stability of Cr(III) and Fe(III) hydroxides. *J. Hazard. Mater.* **2014**, *264*, 490–497. [CrossRef] [PubMed]

61. Landrot, G.; Ginder-Vogel, M.; Livi, K.; Fitts, J.P.; Sparks, D.L. Chromium(III) oxidation by three poorly-crystalline manganese(IV) oxides. 1. Chromium(III)-oxidizing capacity. *Environ. Sci. Technol.* **2012**, *46*, 11594–11600. [CrossRef] [PubMed]

62. Bartlett, R.; James, B. Behavior of chromium in soils: III. Oxidation 1. *J. Environ. Qual.* **1979**, *8*, 31–35. [CrossRef]

63. Fredrickson, J.K.; Zachara, J.M.; Kennedy, D.W.; Dong, H.; Onstott, T.C.; Hinman, N.W.; Li, S.-M. Biogenic iron mineralization accompanying the dissimilatory reduction of hydrous ferric oxide by a groundwater bacterium. *Geochim. Cosmochim. Acta* **1998**, *62*, 3239–3257. [CrossRef]

64. Ona-Nguema, G.; Abdelmoula, M.; Jorand, F.; Benali, O.; Block, J.-C.; Génin, J.-M.R. Iron(II,III) Hydroxycarbonate Green Rust Formation and Stabilization from Lepidocrocite Bioreduction. *Environ. Sci. Technol.* **2002**, *36*, 16–20. [CrossRef] [PubMed]

Appendix A: Full Text of First-author Publications

A.2 Effects of metal cation substitution on hexavalent chromium reduction by green rust

Effects of metal cation substitution on hexavalent chromium reduction by green rust

Andrew N. Thomas[1]*[iD], Elisabeth Eiche[1], Jörg Göttlicher[2], Ralph Steininger[2], Liane G. Benning[3,4], Helen M. Freeman[3,7], Dominique J. Tobler[5], Marco Mangayayam[5], Knud Dideriksen[5] and Thomas Neumann[6]

Abstract

Chromium contamination is a serious environmental issue in areas affected by leather tanning and metal plating, and green rust sulfate has been tested extensively as a potential material for in situ chemical reduction of hexavalent chromium in groundwater. Reported products and mechanisms for the reaction have varied, most likely because of green rust's layered structure, as reduction at outer and interlayer surfaces might produce different reaction products with variable stabilities. Based on studies of Cr(III) oxidation by biogenic Mn (IV) oxides, Cr mobility in oxic soils is controlled by the solubility of the Cr(III)-bearing phase. Therefore, careful engineering of green rust properties, i.e., crystal/particle size, morphology, structure, and electron availability, is essential for its optimization as a remediation reagent. In the present study, pure green rust sulfate and green rust sulfate with Al, Mg and Zn substitutions were synthesized and reacted with identical chromate (CrO_4^{2-}) solutions. The reaction products were characterized by X-ray diffraction, pair distribution function analysis, X-ray absorption spectroscopy and transmission electron microscopy and treated with synthetic δ-MnO_2 to assess how easily Cr(III) in the products could be oxidized. It was found that Mg substitution had the most beneficial effect on Cr lability in the product. Less than 2.5% of the Cr(III) present in the reacted Mg-GR was reoxidized by δ-MnO_2 within 14 days, and the particle structure and Cr speciation observed during X-ray scattering and absorption analyses of this product suggested that Cr(VI) was reduced in its interlayer. Reduction in the interlayer lead to the linkage of newly-formed Cr(III) to hydroxyl groups in the adjacent octahedral layers, which resulted in increased structural coherency between these layers, distinctive rim domains, sequestration of Cr(III) in insoluble Fe oxide bonding environments resistant to reoxidation and partial transformation to Cr(III)-substituted feroxyhyte. Based on the results of this study of hexavalent chromium reduction by green rust sulfate and other studies, further improvements can also be made to this remediation technique by reacting chromate with a large excess of green rust sulfate, which provides excess Fe(II) that can catalyze transformation to more crystalline iron oxides, and synthesis of the reactant under alkaline conditions, which has been shown to favor chromium reduction in the interlayer of Fe(II)-bearing phyllosilicates.

Keywords: Chromium, Green rust, X-ray absorption spectroscopy, Remediation

Introduction

Chromium is a common groundwater contaminant suitable for remediation by in situ chemical reduction [1, 2]. Geogenic chromium is associated with surficial ultramafic outcroppings, while anthropogenic chromium contamination typically results from chromium mining, metal plating facilities, tanneries and wood and

*Correspondence: andrew.thomas@kit.edu
[1] Institute of Applied Geosciences, Karlsruhe Institute of Technology, 76137 Karlsruhe, Germany
Full list of author information is available at the end of the article

paper treatment plants [3]. Once chromium enters soil and groundwater, its solubility and toxicity depend on its chemical speciation. In its trivalent form, chromium is insoluble and non-toxic, and is even an essential trace metal for sugar metabolism [4]. However, in its hexavalent oxidation state, chromium takes the form of chromate (CrO_4^{2-}), a highly soluble, toxic and carcinogenic compound. Redox transformations between the two forms occur in response to changing redox conditions; these transformations are often mediated by other metal biogeochemical cycles. Cr(III) oxidation to Cr(VI) is primarily mediated by biogenic Mn(IV) oxides [5–7], and the synthetic counterpart δ-MnO_2 has been used to assess the lability of synthetic Cr(III)-bearing phases [8, 9]. However, no published study to date has used this method to assess the stability of Cr(III) carrier phases generated by a lab-scale in situ chemical reduction study.

Because the trivalent form of Cr is less soluble and toxic than its hexavalent form, chemical reduction of Cr is a potential remediation strategy referred to as in situ chemical reduction (ISCR) when used for remediation purposes. However, to work effectively, it is advantageous that any applied reduction method produces an insoluble Cr(III)-bearing product that is resistant to oxidation. At earth surface conditions, Cr(III) typically precipitates as a poorly-crystalline hydroxide [10, 11], which is vulnerable to dissolution and subsequent re-oxidation. On the other hand, coprecipitation of Cr(III) with Fe oxides results in a Cr(III) carrier phase that is more insoluble and resistant to oxidation. Therefore, any applied ISCR method should attempt to produce a Cr(III)-substituted Fe(III) oxyhydroxide product.

Green rust (GR) is a Fe (II)–Fe (III) layered double hydroxide (LDH) and has been shown to effectively reduce various contaminants causing their immobilisation, including chromium, yet in many cases the actual reduction mechanisms are still unclear. Green rust is composed of brucite-like $Fe(OH)_2$ sheets in which a portion of the Fe^{2+} has been replaced by Fe^{3+}, giving the sheets a positive charge. This positive charge is balanced by interlayer anions, where cations such as Na^+ are also present [12]. There are two types of green rust, distinguished by their interlayer spacings and associated anions. Green rust 1 has a narrow interlayer spacing of ~ 8 Å occupied by chloride or carbonate, while green rust 2 has a broad interlayer spacing (~ 11 Å) typically occupied by sulfate, which allows exchange of tetrahedral oxyanions and subsequently reduction and sequestration of these substances in the reaction product's interlayer [13–15]. Therefore, it is a promising reagent for exchange and/or reduction of selected groundwater contaminants such as As [16, 17], NO_3^- [18, 19], U (VI) [15, 20], Se (VI) [21, 22], Np [23] and Cr(VI) [13, 14, 24–28].

The most commonly-identified product of chromate reduction by green rust is a poorly-crystalline Cr(III)–Fe (III) oxyhydroxide [13, 24, 25] or a Cr(III)–Fe (III) oxyhydroxycarbonate when green rust carbonate is used [26, 27]. However, Cr(III)-bearing goethite has also been observed to form [14] at the green rust particle rims when Cr concentrations are high and an excess of green rust is added to a batch reaction. Bond and Fendorf [13] and Skovbjerg et al. [14] concluded that these products formed due to exchange of chromate for interlayer sulfate followed by reduction. More recently, our previous study [28] reacted green rust with a series of initial chromium concentrations typical of contaminant plumes and determined that the speciation of chromium in the reaction product is correlated to the initial concentration. Although more goethite was found in the reaction products formed at higher initial concentrations, Cr(III) hydroxide, presumably located on the oxidized green rust particle surfaces, was the primary Cr(III) carrier phase produced. A similar side product was also identified by Legrand et al. [27]. The variable Cr(III) carrier phases identified under varying reaction conditions suggest that several reaction mechanisms are possible: reduction at the particle surface coupled to electron donation from the particle's interior is expected to produce Cr(III) hydroxide, while Cr(III)-bearing Fe(III) oxyhydroxides can form when Cr(VI) is reduced in the interlayer following exchange of chromate for sulfate.

Like magnetite, green rust is a low-bandwidth semiconductor, and electron transfer from structural Fe(II) in the particles' interior to the surface is possible via a polaron hopping mechanism [29]. A polaron is a quasiparticle consisting of an electron (hole) and the associated distortions in the surrounding lattice [30]. According to the polaron hopping model, which matches empirical observations [31, 32] of electron conductivity in metal oxides and other polaronic insulators, electron conduction can only take place via Fe(II)–Fe(III) charge transfer steps, each of which depends on superexchange coupling induced by intermediate cation-centered octahedra [29], as this transition would otherwise be spin-forbidden [33]. Incorporation of divalent and trivalent cations that have no net spin and only a single available oxidation state (e.g. Al^{3+}, Mg^{2+} and Zn^{2+}) may prevent or slow regeneration of Fe(II) at the particle surface, as these cations canot accept or donate electrons as part of a transfer chain [34] and may interfere with the superexchange coupling [35] that drives the rapid electron transfer modelled by Wander et al. [29]. In this case, Cr(VI) may only be able to access Fe(II) in the green rust crystal interior by exchanging for interlayer sulfate, which would lead to Cr(III) incorporation into a Fe(III) oxide product, although passivation of the particle may be an issue, as formation of an

interlayer precipitate may hinder access to interior Fe(II). Since reduction at the surface depends on conduction of interior electrons to the surface, changes in the green rust particle's electrical conductivity can lead to changes in the dominant reaction mechanism. Despite this, few studies have measured the Cr reactivity of green rusts with cation impurities incorporated into the octahedral layer. Ruby et al. [36] investigated the structure and formation of Al-substituted green rust sulfate, while recent studies ofits reactivity with hexavalent chromium found that it reduced Cr(VI) more quickly than unsubstituted green rust, suggesting that cation-substituted green rusts may be more effective in situ chemical reduction reagents than the pure form. Green rust sulfates with isomorphic substitutions of Mg^{2+} [37] and Zn^{2+} [38] have also been synthesized, but no published study has investigated their reactivity.

Previous investigations of chromate reduction by green rust have returned inconsistent results, possibly due to variations in synthesis techniques and reaction conditions across multiple studies. In the present study, pure sulfate GR and sulfate GR with isomorphic substitution of Al, Mg, and Zn were synthesized and reacted with Cr(VI). The lability of Cr(III) in the reaction products was then determined by measuring the release of Cr(VI) after treatment with synthetic δ-MnO_2, the synthetic counterpart of biogenic Mn oxide which has been used to assess Cr lability in previous studies [7–9]. The structure and Cr speciation of these products were also determined using transmission electron microscopy (TEM), X-ray absorption spectroscopy (XAS), X-ray diffraction (XRD) and pair distribution function (PDF) analysis.

Methods/experimental
Green rust and feroxyhte synthesis and characterization
All green rusts (green rust sulfate, Al-GR, Mg-GR, Zn-GR) were synthesized using the method from Géhin et al. [39] with metal sulfate salt reagents added to N_2-purged Milli-Q water. The total metal concentration in all synthesis batches was 0.1 mol kg^{-1}, with divalent to trivalent cation ratios of 3:1. To synthesize the substituted green rusts, the synthesis solutions prior to titration by NaOH were prepared by replacing 10% of the Fe^{2+} or Fe^{3+} by the desired cation (see Table 1). After synthesis, the green rusts were aged in solution for 48 h. The composition of the solid phase was then calculated by subtracting the values measured using ICP-OES, and aqueous Fe^{2+} concentrations were measured using the ferrozine method [40] after centrifuging the green rust suspensions and filtering the supernatant using the aforementioned 0.2 μm syinge filters. Feroxyhyte (δ-FeOOH) was synthesized using a method utilizing rapid $Fe^{2+}_{(aq)}$

Table 1 Summary of green rust chemical compositions and associated Fe^{2+} concentrations

Reactant	Expected chemical composition[a]	$[Fe^{2+}]_{(aq)}$ (mmol L^{-1})[b]
GR-SO$_4$	$Fe^{II}_4 Fe^{III}_2 (OH)_{12} SO_4 \cdot 2H_2O$	25
Al-GR	$Fe^{II}_4 Fe^{III}_{1.9} Al_{0.1} (OH)_{12} SO_4 \cdot 2H_2O$	27
Mg-GR	$Fe^{II}_{3.8} Mg_{0.2} Fe^{III}_2 (OH)_{12} SO_4 \cdot 2H_2O$	23
Zn-GR	$Fe^{II}_{3.8} Zn_{0.2} Fe^{III}_2 (OH)_{12} SO_4 \cdot 2H_2O$	23

[a] Based on ratio of cations in solution prior to titration

[b] Expected $[Fe^{2+}]_{(aq)}$ is 20–25 mmol L^{-1}

oxidation by H_2O_2 [41] and used as a characterization standard for the reacted green rust samples.

δ-MnO_2 synthesis
Vernalite (δ-MnO_2), which resembles natural biogenic Mn (VI) oxides [42], was synthesized using the "redox" method of Villalobos et al. [43]. $MnCl_2$ was added slowly to a $KMnO_4$ solution while maintaining a pH of 7 using NaOH. The product was first rinsed several times with 1 M NaCl to remove the remaining Mn^{2+}, then with Milli-Q water before further purification using dialysis. Vernalite was kept in suspension by sonication and adjusted to pH 7.5 before use in re-oxidation batch reactors.

Batch reactions
Three replicate batch reactors were set-up for each synthesized green rust type: one for solid phase characterization and two to measure Cr(VI) reduction and Cr(III) re-oxidation by δ-MnO_2. All batch reactions were performed in an anaerobic chamber with an Ar atmosphere. In each reactor, an aliquot of green rust suspension with about 0.2 mmol of Fe (II) was added to a 100 mL 0.67 mmol kg^{-1} K_2CrO_4 solution in an acid-washed borosilicate beaker ([Fe(II)]/[Cr(VI)] $\leq$ 3, slight excess of Cr(VI) to ensure complete oxidation and prevent the Fe^{2+}-catalyzed transformation of reaction products), with the pH of all solutions adjusted to 7. The batch reactions were not shielded from the light as this would have prevented sample removal, and the reaction temperature and pH were not controlled to allow direct comparison to similar studies that followed the same procedure [14, 28]. The first reaction was terminated after 7 days by filtration (0.2 μm, Whatman nylon membrane filter), and solid samples were removed for further characterization. Aging for 7 days allowed incipient transformation of the initial metastable intermediate [14, 28]. In the second and third reactors, suspension aliquots were periodically removed and filtered during the first hour of the

Thomas *et al. Geochem Trans* (2020) 21:2

Page 4 of 16

reaction to monitor the removal of Cr(VI) by GR reduction; after 7 days, colloidal, synthetic δ-MnO$_2$ was added to the remaining suspension. Samples removed prior to and 1 and 2 weeks after δ-MnO$_2$ addition were treated with 10 mM Na$_2$HPO$_4$ for 24 h to desorb chromate from mineral surfaces, followed by filtration. [Cr(VI)] in all samples was measured using the 1,5-diphenylcarbazide method (US Environmental Protection Agency (EPA) method 7196A) with a Perkin-Elmer Lambda 2S UV-Vis Spectrophotometer calibrated using a four-point calibration curve. In addition, measurement of [Fe^{2+}$_{(aq)}$] by the ferrozine method was attempted, but the results are not shown here because [Fe^{2+}$_{(aq)}$] decreased to below the limit of detection within ten seconds.

X-ray diffraction (XRD) and pair distribution function (PDF) analyses

Benchtop XRD measurements were performed using a Bruker D8 Diffractometer. Unreacted green rust samples were removed from suspension by filtration, treated with glycerol to prevent oxidation, and transferred as a paste to a standard Si powder specimen holder. X-rays were emitted from a Cu-Kα source (λ = 1.5418 Å), and data were collected at 2θ values between 2 and 82° with a step size of 0.02° and an average counting time of 1 s per step. Background diffraction patterns were collected by measuring an empty sample holder, and the XRD-BS software was used to remove the background from the sample data.

Synchrotron X-ray scattering measurements of reacted samples were performed at beamline 11-ID-B at the Advanced Photon Source (APS) at Argonne National Laboratory, using an X-ray energy of 58.66 keV (λ=0.2113 Å). Samples were ground and transferred into glass capillaries sealed with paraffin, then measured at a distance of ~18 cm (PDF) and 100 cm (XRD) using a 40 cm × 40 cm amorphous Si 2D detector. An empty glass capillary and a CeO$_2$ standard were also measured for background subtraction and calibration of the Laue patterns, respectively. The collected patterns were converted to 1D data using the Fit2D software after calibrating the geometry of the setup using the CeO$_2$ standard. For high resolution XRD, the I(Q) data collected at 100 cm was treated with the software GSAS-II [44] to perform background subtraction, and to convert the incident beam energy to Cu-Kα (λ=1.5406 Å) for comparison with lab based XRD. Full width half maximum (FWHM) values for the green rust {213} reflection were determined using the peak fitting extension in OriginPro 2018. PDF patterns were extracted from the data collected at 18 cm using the software PDFGetX3 [45], including background subtraction and corrections for incoherent scattering and non-linear detector efficiency

as well as normalization to the sample's average atomic scattering cross-section [46]. The composition of the sample was set at Fe$_{0.5}$Cr$_{0.12}$O$_{0.38}$ due to the stoichiometry of the reaction. Fourier transformation of the reduced structure function Q[S(Q)$^{-1}$] was performed using a maximum Q-value of 20 Å^{-1} to yield G (r), the reduced pair distribution function.

X-ray absorption spectroscopic (XAS) analyses and data processing

Bulk XAS spectra of all reacted samples were collected at the SUL-X beamline at the ANKA synchrotron facility in Eggenstein-Leopoldshafen, Germany, which operates at 2.5 GeV. The incident beam was scanned through the Cr and Fe K-edges (set at 5989 eV and 7112 eV for metallic Cr and Fe, respectively), using a Si (111) crystal pair monochromator with a fixed-beam exit. Higher-order harmonics were removed from the incident beam using a grazing incidence mirror. Three replicates of each spectrum were measured in both transmission and fluorescence mode in a range of -200 to 1000 eV relative to the absorption edge. Transmission spectra were obtained using three Oxford Instruments IC-type ionization chambers with Kapton windows, and fluorescence measurements were obtained using a Gresham 7-element Si (Li) detector. All spectra were calibrated with a Cr or Fe metal foil placed between ionization chambers 2 and 3.

Fe and Cr XAS data were processed and analyzed using the Demeter software package [47]. All analyses were performed on spectra obtained in transmission mode. After calibrating the spectral energies using reference metal foil spectra, a merged spectrum was produced by averaging the three replicate spectra in μ(E)-space. The merged spectra were then normalized using a first-order pre-edge function and a third-order post-edge spline function to model the background absorption.

For Cr X-ray absorption near-edge spectroscopy (XANES) linear combination fitting, the derivative of each μ(E) spectrum was fitted to two reference standards (Cr(III)-bearing ferrihydrite and Cr(III) hydroxide [48, 49]) in the XANES region (-20 to $+30$ eV). No further constraints were placed on the fit. Fe K-edge extended X-ray absorption fine-structure spectroscopy (EXAFS) fitting was also performed, and due to the similarity of the spectra to feroxyhite, the procedure for fitting of a feroxyhyte spectrum outlined in Manceau and Drits [50] was followed. Where possible, the k^3-weighted EXAFS spectra were Fourier transformed over a k-range of 4–14 Å^{-1}; other ranges were used when the data at high k-values was too noisy or a Co K-edge was present in this region (oxGR). Shell-fitting was performed using the Artemis software. Theoretical Fe phase and amplitude functions were calculated from the crystal structure of hematite

Thomas *et al. Geochem Trans*   (2020) 21:2

Page 5 of 16

[51] with no further modifications. During fitting, S_0^2 was fixed at 0.9 and all σ^2 values were fixed at 0.015, as the fitted value of this parameter tended to converge to 0.015 when the fits were performed. All fits were performed using three single-scattering paths: Fe–O (1.98 Å), edge-sharing Fe–Fe (3.01 Å), and corner-sharing Fe–Fe (3.4 Å). Other single- and multiple-scattering pathways were tested but ultimately excluded because they failed to improve the fit or produced unphysical parameter solutions. A more detailed outline of the Fe K-edge EXAFS fitting procedure is included in Additional file 1: Appendix 2.

Electron microscopy

Scanning electron microscopy (SEM) images of unreacted green rusts were recorded on an FEI Quanta 3D FEG microscope. Samples were prepared inside an anaerobic chamber by filtering an aliquot of a green rust suspension through a 0.2 μm nylon filter, and the paste was transferred to an SEM sample holder. The samples were then immediately transferred to the microscope's vacuum chamber to prevent oxidation. Images were obtained in high vacuum mode at an accelerating voltage of 20 kV using an Everhart-Thornly secondary electron detector.

Higher resolution images of green rust samples reacted with Cr(VI) were recorded using a TEM on samples prepared by transferring several drops of a sonicated suspension in ethanol to a 3 mm Cu-TEM grid coated with a holey amorphous carbon film. The TEM grids were then transferred to a FEI Tecnai TEM operated at 200 kV and equipped with a Gatan Tridiem imaging filter (GIF), a

Fishione high-angle annular dark field detector, an energy dispersive X-ray (EDX) analyzer to measure chemical composition and a Gatan Orius SC200D 4 K pixel cooled CCD camera. Selected-area electron diffraction (SAED) patterns were collected using plates with an aperture of ca. 200–300 nm and developed in a Ditabis Imaging Plate Scanner. The d-spaces and FWHM values were calculated from manual measurements obtained using the ImageJ software. TEM images were processed and converted using Gatan DigitalMicrograph, while the raw EDX data was processed using EDX Quant.

Results and discussion
Characterization, reduction of Cr(VI) and reaction product stability

Based on the measurements shown in Table 1, all green rust suspensions have similar aqueous Fe^{2+} concentrations which are similar to the expected concentrations based on the 2:1 ratio of Fe(II) to Fe(III) in green rust sulfate. Mg- and Zn-GR are associated with slightly lower Fe^{2+} concentrations, however, most likely because 10% of the Fe(II) in these suspensions (compared to pure GR) is replaced by Mg or Zn. As aqueous Fe^{2+} can also reduce Cr(VI) [11, 48, 52], the inconsistent Fe^{2+} concentrations shown in Table 1 may result in differing Cr-bearing phases in the products of these reactions, as discussed later.

Figure 1 shows the benchtop XRD patterns of the synthetic green rusts prior to reaction with hexavalent chromium. All patterns had the same green rust 2 peaks predicted by the crystal structure from Simon et al. [53],
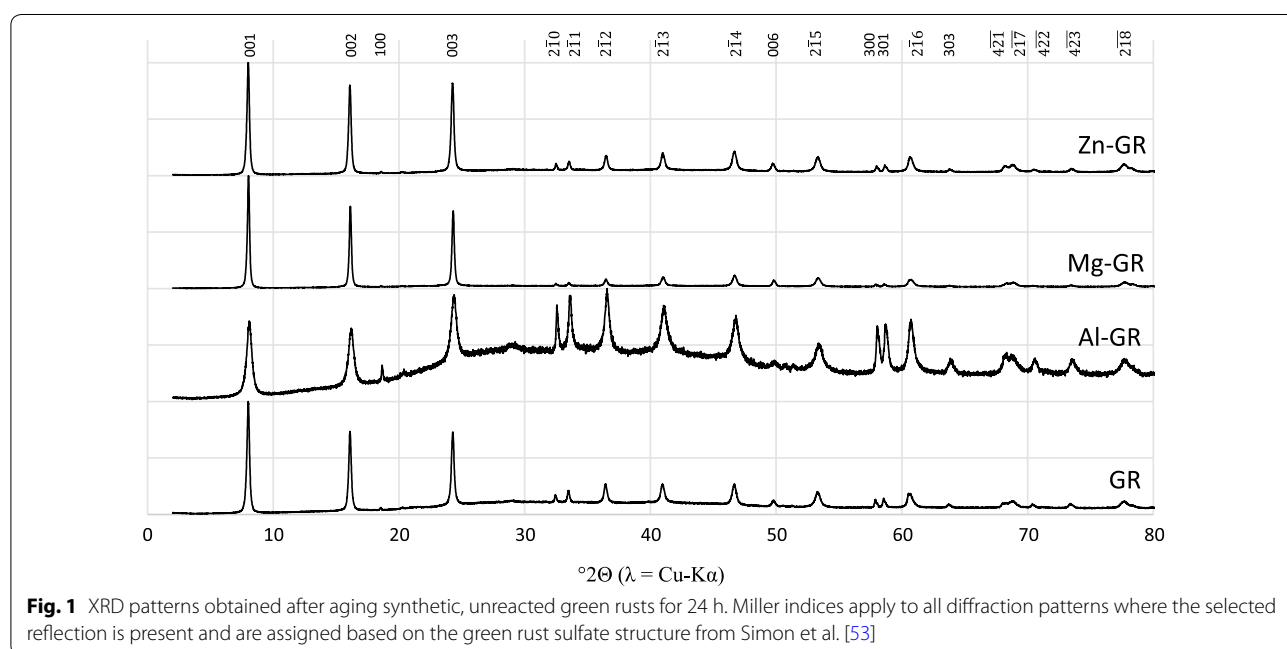

Fig. 1 XRD patterns obtained after aging synthetic, unreacted green rusts for 24 h. Miller indices apply to all diffraction patterns where the selected reflection is present and are assigned based on the green rust sulfate structure from Simon et al. [53]

but there were differences in peak amplitude and shape. Al substitution for Fe(III) resulted in an 87% increase in the FWHM of the {213} peak at 41° 2θ relative to GR, suggesting that Al substitution either increases the structural disorder or decreases the crystallite size in the green rust as observed in previous studies [36]. Representative SEM images (Fig. 2) show that all green rusts have a characteristic hexagonal morphology, but the substituted green rust particle morphologies are more irregular than pure green rust. In addition, it is clear that the substituted green rusts have broader particle size distributions, possibly due to non-uniform incorporation of Al, Mg and Zn.

The removal of chromate by the various green rust sulfates is shown in Fig. 3a. In all cases, chromate concentrations are reduced to below the detection limit (0.04 mg kg^{-1}, below the WHO-recommended limit of 0.05 mg kg^{-1}) after 10 min of reaction time; however, Cr(VI) is removed from solution much more rapidly by pure green rust and Al-GR, while substitution by zinc and magnesium led to slower removal of Cr(VI) from solution. This may be due to differences in particle size (Fig. 2) and/or [Fe$^{2+}_{(aq)}$] concentration; several Mg-GR and Zn-GR particles with diameters near 700 nm are visible, possibly indicating that Mg-GR and Zn-GR have lower reactive surface areas, and Fe^{2+} reacts more rapidly with chromate than structural Fe(II) [52]. Our previous study [28] measured Cr(VI) reduction at different chromium concentrations, finding that green rust consistently reduces all chromium in solution, but the reaction rate decreases with the chromium concentration.
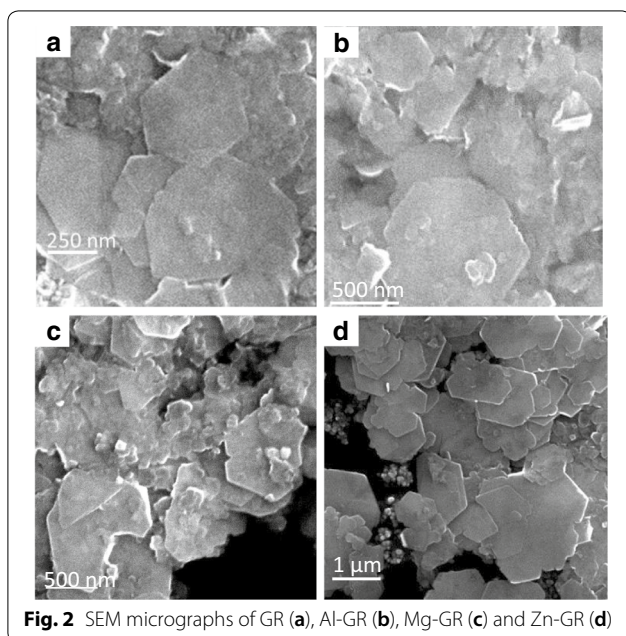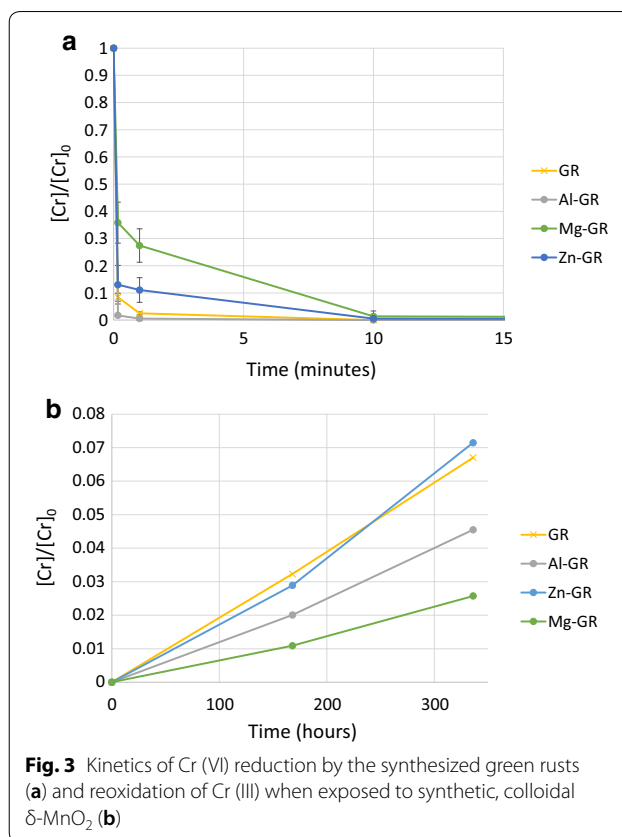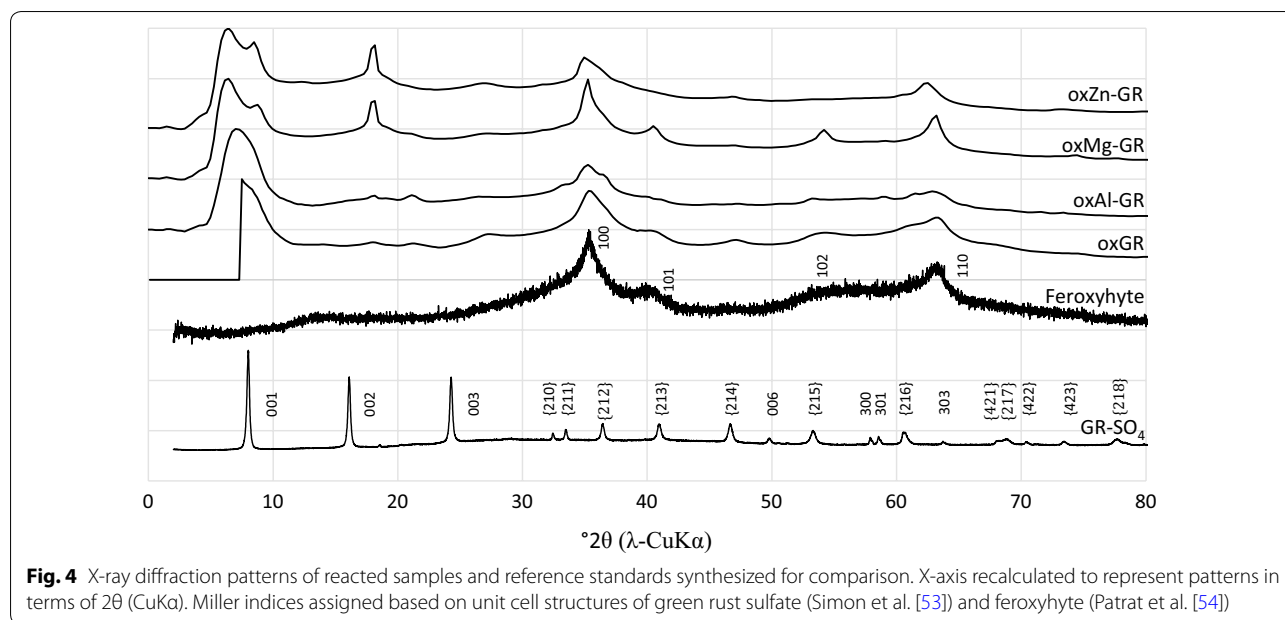

Fig. 3 Kinetics of Cr (VI) reduction by the synthesized green rusts (**a**) and reoxidation of Cr (III) when exposed to synthetic, colloidal δ-MnO$_2$ (**b**)

It is unknown whether the differences in reaction rate between the green rusts tested in the present study are consistent at other chromium concentrations. Figure 3b shows the release of chromate, i.e. re-oxidation of Cr(III) to Cr(VI) by colloidal δ-MnO$_2$. Approximately 7% of the reduced chromium in the pure green rust and Zn-bearing green rust reaction products were re-oxidized ([Cr]=2.4 mg kg^{-1}), compared to 2.5% ([Cr] = 0.9 mg kg^{-1}) and 4.5% ([Cr] = 1.6 mg kg^{-1}) of the Cr in the product of Mg- and Al-bearing green rust, respectively. These differences most likely result from differences in the particle structure and Cr speciation of the reaction byproducts, which are discussed below.

Long-range order structure and particle morphology of reaction products

Synchrotron XRD patterns of solids formed after reacting the GRs with Cr for 7 days are shown in Fig. 4. For simplicity, all reaction products in this publication will be identified as oxGR (oxidized green rust sulfate) or ox*n*-GR (*n*=Al, Mg or Zn). Two broad reflections at 2.55 Å (2θ = 35.2°) and 1.46 Å (2θ = 63.7°) are the most notable features present in each pattern. These spacings were also observed in the oxidized green rust diffraction patterns from Skovbjerg et al. [14] and are characteristic of

Fig. 2 SEM micrographs of GR (**a**), Al-GR (**b**), Mg-GR (**c**) and Zn-GR (**d**)

Thomas *et al. Geochem Trans*   (2020) 21:2

Page 7 of 16

Fig. 4 X-ray diffraction patterns of reacted samples and reference standards synthesized for comparison. X-axis recalculated to represent patterns in terms of 2θ (CuKα). Miller indices assigned based on unit cell structures of green rust sulfate (Simon et al. [53]) and feroxyhyte (Patrat et al. [54])

many Fe oxides with hexagonal symmetry such as ferrihydrite and feroxyhyte [54, 55] and most likely indicate a residual hexagonal symmetry remaining after oxidation and restructuring of the green rust. However, the broadness of these peaks suggests structural disorder in the [001] crystallographic direction. In the case of oxMg-GR, partial transformation to feroxyhyte is also evident, as the broad 2.55 Å and 1.46 Å reflections are sharper and several minor feroxyhyte reflections at ~40.5° (101) and 54.2° 2θ (102) are also visible in this XRD pattern. Every sample is also partially composed of a residual layered ferric green rust structure, as shown by a broad, diffuse reflection below 8° 2θ [14], which is much more prominent in the wet sample diffraction pattern (Additional file 1: Fig. S1) obtained using a Bragg-Bretano instrument. Therefore, the broadening of this peak is most likely due to drying of the sample prior to measurement, which can dehydrate the interlayer to a variable degree and cause stacking distance variability in the [001] direction. A reflection at about 10.4 Å (2θ = 8.5°) is also visible in the oxMg-GR and oxZn-GR patterns; this reflection is similar to the (001) reflection in green rust sulfate and suggests that the original, hydrated structure has been preserved to some extent. These reflections are also visible in Additional file 1: Figure S1, but the data is much noisier and many minor peaks are not visible. In addition, a minor reflection at 4.9 Å (2θ = 18.1°) is present in the oxMg-GR and oxZn-GR patterns, but the authors were unable to identify the source of this peak. This spacing does not correspond to any known iron oxide structure.

Figure 5 shows TEM images of the various green rust samples after reaction with aqueous chromate. In all samples, the pseudo-hexagonal morphology of the reactant particles remains preserved after oxidation and the particle diameters are similar to those measured in Fig. 2, but the particle edges are more irregular, particularly in the case of oxAl-GR. This sample also has many irregular particular aggregates, but several pseudo-hexagonal particles are visible, particularly the particle from which the SAED pattern was obtained. Higher-contrast domains at the rims of some oxMg- and oxZn-GR hexagonal particles are visible, which are also associated with lower density in the interior domains of the same particle (more easily visible in the STEM (scanning transmission electron microscopy) images, Fig. 5e–f). Although particles with these rim-like domains are present in both oxMg-GR and oxZn-GR, they are more prevalent in oxMg-GR. Particles with similar morphologies were identified by Skovbjerg et al. [14], but the rim domains in the present study are more poorly-defined than the domains that formed at chromium levels high enough to oxidize 60% of the Fe(II) bound in green rust. This study concluded that these features formed due to Cr reduction by green rust from the rim inwards. Particles with other morphologies (i.e. rods and amorphous aggregates) are also visible.

In the SAED patterns collected from selected hexagonal particles, two hexagonal sets of reflections corresponding to d-spacings of ~2.5 and ~1.47 Å are also visible in all samples (see Fig. 5 insets) with variable sharpness. These patterns confirm the hexagonal symmetry of the product when observed from the [001] direction and
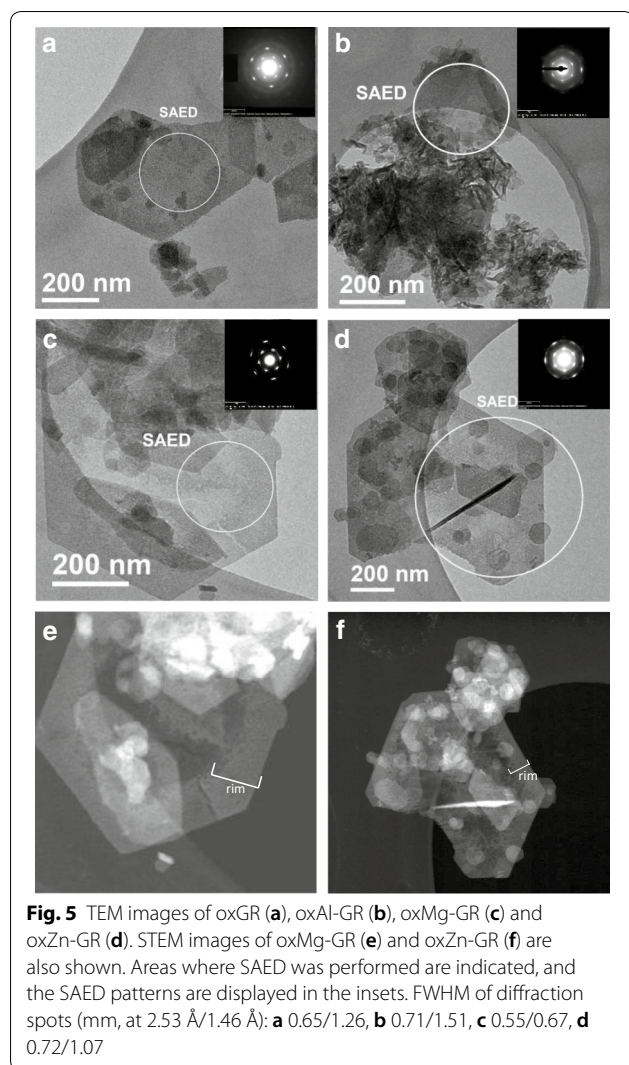
Fig. 5 TEM images of oxGR (**a**), oxAl-GR (**b**), oxMg-GR (**c**) and oxZn-GR (**d**). STEM images of oxMg-GR (**e**) and oxZn-GR (**f**) are also shown. Areas where SAED was performed are indicated, and the SAED patterns are displayed in the insets. FWHM of diffraction spots (mm, at 2.53 Å/1.46 Å): **a** 0.65/1.26, **b** 0.71/1.51, **c** 0.55/0.67, **d** 0.72/1.07

Table 2 Elemental ratios determined by EDX. Values are averages calculated from measurements of all selected areas

Sample	[Cr]/([Cr+Fe])[a]	[Fe]/[S]
oxGR	0.19 (0.02) (n = 2)	4.21 (1.68) (n = 2)
oxAl-GR	0.142 (0.012) (n = 2)	13.90 (2.20) (n = 2)
oxMg-GR	0.158 (0.052) (n = 7)	31.19 (14.45) (n = 7)
oxZn-GR	0.179 (0.074) (n = 8)	13.72 (6.94) (n = 8)

Elemental ratios and uncertainties calculated from all EDX measurements taken from hexagonal particles

[a] Expected ratio (reaction stoichiometry) is ca. 0.18

or depletion. Cr/Fe+Cr ratios are similar to the ratio (~ 0.18) predicted by the reaction's stoichiometry (Eq. 1). The value of this ratio is not expected to vary for different topotactic reaction mechanisms, as three structural Fe (II) atoms are necessary to reduce one Cr(VI) atom in all cases. The Fe/S ratios, which can serve as proxies for exchange of interlayer sulfate, vary widely between samples, although many of these measurements have a large standard deviation. OxGR has a measured Fe/S ratio of 4.2, lower than the unreacted green rust ratio of 6.0 (Eq. 1) [12, 39], although the sample size of this measurement is not large enough to determine whether this difference is statistically significant.

$$0.75Fe_4^{II}Fe_2^{II}(OH)_{12}SO_4 \cdot 8H_2O + CrO_4^{2-} + 0.5H^+$$
$$\rightarrow 5.5Fe_{0.818}Cr_{0.182}OOH + 0.75SO_4^{2-} + 8H_2O \tag{1}$$

On the other hand, oxMg-GR has a significantly higher Fe/S ratio than oxZn-GR and the ratio in unreacted green rust sulfate (~ 6.0), and it is likely that sulfur has been depleted in this sample, possibly by chromate exchange for sulfate and its subsequent reduction in the interlayer.

PDF and XAS characterization of short-range order structure of reaction products

The reduced pair distribution functions G(r) calculated for all reaction products produced in this study (Fig. 6) are nearly identical to those observed by Yin et al. [56], who characterized the oxidation products of 3:1 (i.e. [Fe(III)]/[Fe(II)] = 3) oxidized green rust chloride single sheets separated by dodecanoate intercalation (single-sheet iron oxide, SSI) and green rust sulfate oxidized by an excess of Cr(VI), respectively. These studies hypothesized that oxidation of the brucite-like layer caused dislocation of part of the Fe (III) into the interlayer, which manifests in the PDF as a splitting of the single green rust peak at ~ 3.20 Å [Fe(II)–Fe(II) and Fe(II)–Fe(III) edge sharing] into two peaks at approximately 3.04 Å [Fe(III)–Fe(III) edge-sharing] and 3.41 Å [Fe(III)–Fe(III) corner

indicate that there is some coherence between adjacent sheets along this axis. The oxidation product for which the smallest proportion of Cr was oxidized by δ-MnO₂, oxMg-GR, had a SAED pattern with the lowest calculated peak FWHM values (mm, inner ring/outer ring = 0.55/0.67) when measuring in the direction of the center of the pattern, suggesting increased coherency between hydroxide sheets. The corresponding peaks (at 34° and 63.2° 2θ) are also sharpest in the oxMg-GR diffraction pattern (Fig. 4b).

Elemental concentration ratios measured by EDX and averaged over all measured hexagonal particles in each sample are shown in Table 2. Spectra taken from non-hexagonal particles were excluded from these calculations. These elemental ratios can determine whether certain elements are enriched or depleted in the various oxGR's that formed during the reactions and also provide insights into the mechanisms that drive enrichment
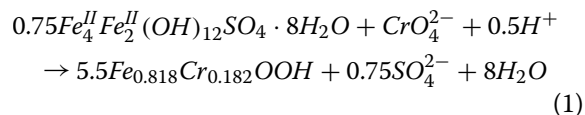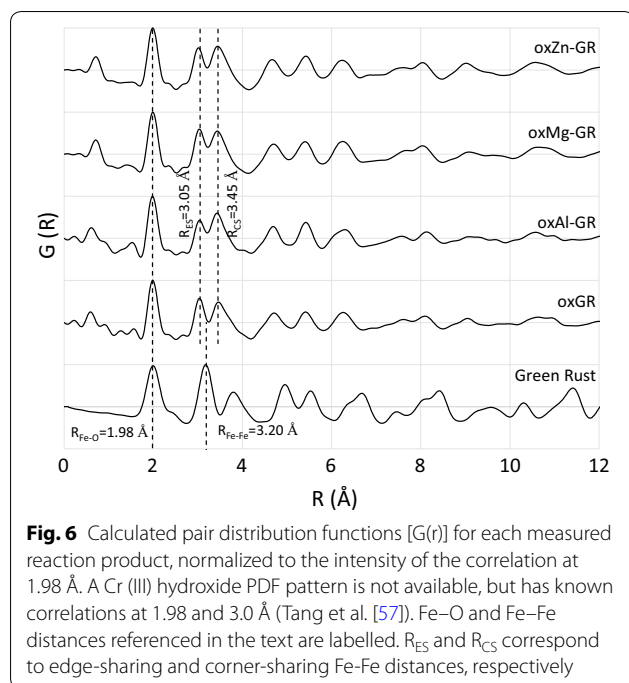
Thomas *et al. Geochem Trans*   (2020) 21:2

Page 9 of 16

Fig. 6 Calculated pair distribution functions [G(r)] for each measured reaction product, normalized to the intensity of the correlation at 1.98 Å. A Cr (III) hydroxide PDF pattern is not available, but has known correlations at 1.98 and 3.0 Å (Tang et al. [57]). Fe–O and Fe–Fe distances referenced in the text are labelled. R_{ES} and R_{CS} correspond to edge-sharing and corner-sharing Fe-Fe distances, respectively

Fig. 7 Fourier transformed Fe K-edge EXAFS spectra and fits after 7 days reaction time, as well as a feroxyhyte spectrum for comparison . Fit statistics and sample-specific fitting parameters outlined in Table 3. Fits performed over an R-range of 1.1–3.5 Å

sharing], both of which can be seen in the reaction products in Fig. 6, although the peak positions differ slightly (3.05 and 3.45 Å). The XRD (Fig. 4) and SAED (Fig. 5) patterns indicate that there is some coherence between the stacked, oxidized layers, but the associated intersheet correlations most likely have amplitudes too low to be visible in the PDF patterns, as random Fe dislocations may remove atomic correlations while leaving the stacking in the [001] direction coherent enough to generate identifiable XRD and SAED reflections.

However, there are significant differences in peak intensity from the Yin et al. [56] PDFs at low R-values, particularly between 3.0 and 3.5 Å. The amplitudes of the peaks at 3.05 Å and 3.45 Å are very similar in the present study's PDF patterns while the intensity at 3.41 Å in Yin et al. [56] is greater. Oxidation of 2:1 green rust sulfate (i.e. [Fe(II)]/[Fe(III)] = 2) produces a lower layer charge than oxidation of 3:1 green rust chloride, and therefore requires a smaller degree of internal rearrangement and deprotonation/hydroxylation to balance this layer charge. In addition, Tang et al. [57] found that PDF patterns of Cr(III) hydroxide have prominent pair correlations at 1.98 Å and ~3.0 Å, which may also contribute to the amplitudes of the peaks at 1.98 and 3.03 Å in Fig. 6, but do not have high enough amplitudes at higher R to contribute to the pattern in this region due to the small (> 10 Å) domain sizes.

Figure 7 shows the Fe EXAFS shell-by-shell fits of all reacted green rust products and a feroxyhyte reference standard for comparison, and the associated fit results
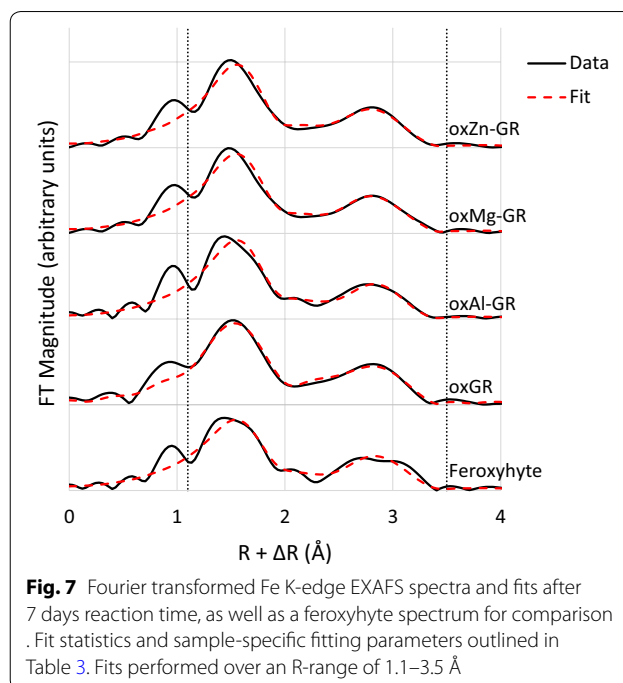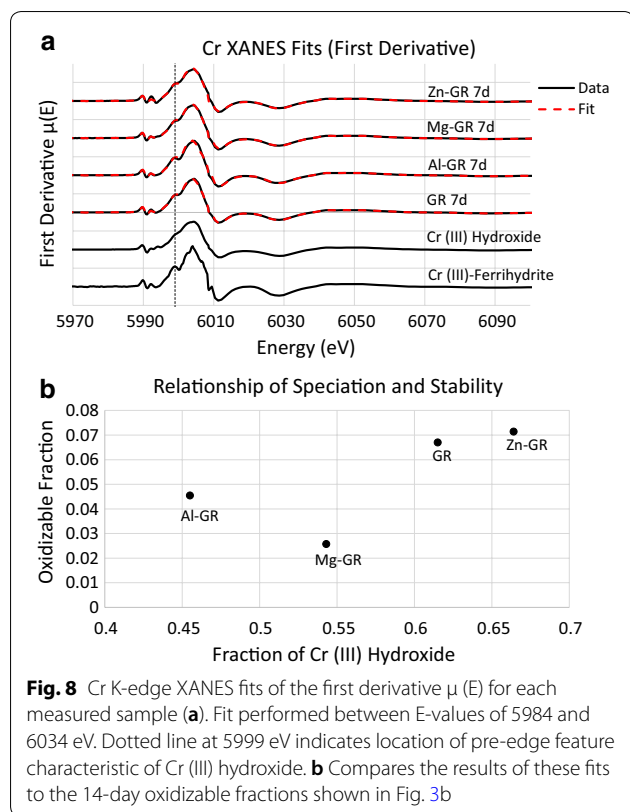
are listed in Table 3. The short-range (< 4 Å) bonding environment of Fe in these samples is characterized by a mix of edge- and corner-sharing MeO_6 octahedral linkages at distances of ~ 3.04 and 3.4 Å, which matches the structure predicted by PDF. The second- and third-shell coordination numbers have ratios similar to the apparent intensity ratios of the corresponding PDF peaks (Fig. 6), and the sums of these coordination numbers are all close to six. Because each Fe octahredron is also surrounded by six Fe in unreacted green rust sulfate, this supports the formation mechanism suggested by the PDF, as Fe dislocated into the interlayer is still bound to Fe remaining in the octahedral layer. The Fe EXAFS spectra also show that the Fe-bearing phases in all samples resemble feroxyhyte, particularly oxMg-GR, but there are significant differences. All samples have more edge-sharing Fe than feroxyhyte, particularly oxGR and oxZn-GR as well as oxMg-GR, even though feroxyhyte is identifiable in the latter sample by XRD. This may be due to features such as the brucite-like sheet inherited after the transformation, as this sheet, which is dominated by edge-sharing linkages, has fewer vacancies than a similar feroxyhyte structure [54, 58] if the transformation is topotactic. In addition, the two shells at 3.04 and 3.41 Å are distinct in the feroxyhyte spectrum but merged into a single shell in the sample spectra, suggesting that these samples have a significantly higher degree of structural disorder than synthetic feroxyhyte.

XANES linear combination fits were also performed on all Cr K-edge XAS spectra, using synthetic Cr(III)

Thomas *et al. Geochem Trans*   (2020) 21:2

Page 10 of 16

Table 3 EXAFS fitting parameters for all Fe K-edge EXAFS spectra

Sample	k-range	R-value	S_0^2	Shell: ΔE_0 (eV)	Fe–O CN	R (Å)	σ^2 (Å^{-2})	Fe–Fe (edge-sharing) CN	R (Å)	σ^2 (Å^{-2})	Fe–Fe (corner-sharing) CN	R (Å)	σ^2 (Å^{-2})
Feroxyhyte	4–14	0.014	0.9*	−4.19	6*	1.98	0.013	2.80 ± 13%	3.03	0.015*	2.39 ± 20%	3.41	0.015*
oxGR	4–11	0.004	0.9*	−4.63	6*	1.98*	0.011	3.88 ± 10%	3.05	0.015*	2.49 ± 20%	3.41	0.015*
oxAl-GR	4–14	0.011	0.9*	−4.56	6*	1.98*	0.012	3.19 ± 12%	3.04	0.015*	2.59 ± 20%	3.38	0.015*
oxMg-GR	4–13	0.008	0.9*	−4.11	6*	1.98*	0.012	3.18 ± 10%	3.02	0.015*	2.23 ± 20%	3.41	0.015*
oxZn-GR	4–13	0.006	0.9*	−4.2	6*	1.98*	0.012	3.73 ± 10%	3.05	0.015*	2.26 ± 20%	3.41	0.015*

*Parameter was fixed during fitting

Fig. 8 Cr K-edge XANES fits of the first derivative μ (E) for each measured sample (**a**). Fit performed between E-values of 5984 and 6034 eV. Dotted line at 5999 eV indicates location of pre-edge feature characteristic of Cr (III) hydroxide. **b** Compares the results of these fits to the 14-day oxidizable fractions shown in Fig. 3b

high errors, but as the amount of Cr(III) hydroxide detected in each sample and the fitted values match the relative prominence of the characteristic Cr(III)-ferrihydrite features, errors in these values are unlikely to be as high as suggested by the fitting software. Cr(III)-bearing ferrihydrite is the expected product of Cr(VI) reduction by $Fe^{2+}_{(aq)}$ under circumneutral conditions [11, 48, 52]; however, as differences in $Fe^{2+}_{(aq)}$ concentrations are minimal (Table 1), this likely has little effect on the speciation of Cr in the product. A portion of the green rust is also expected to dissolve when added to the chromate solutions due to the relatively high solubility of green rust, which likely affects the reactions performed in this study. However, as the initial pH values of the chromate solutions are identical, meaningful differences in the behavior of each batch reaction due to green rust dissolution are not expected, but possible. Cr speciation is correlated to the fraction of Cr(III) oxidizible by δ-MnO_2 after 14 days (Fig. 8b), but it is clear that oxMg-GR is an exception to the overall trend, as the fraction oxidized by δ-MnO_2 is lower than predicted. Therefore, it is likely that the low Cr lability in this product is the result of other factors such as partial conversion to feroxyhyte instead of depending purely on the Cr speciation.

Based on the XRD, PDF and XAS results, all oxidized samples appear to have maintained a layered structure composed of stacked SSI (Fig. 9) similar to those characterized by Yin et al. [56], with variable coherency and partial transformation to feroxyhyte in the case of oxMg-GR. Following oxidation (regardless of mechanism), the resulting strain causes displacement of Fe(III) octahedra into an interlayer region labelled in Fig. 9 as the diffuse octahedral layer. Fe octahedral positions within this layer are not defined in a unit cell, as Fe displacements are random, but the uniform geometry of Fe octahedra ensures that the diffuse octahedral layer has a uniform thickness, allowing the particle to maintain its periodicity in the [001] direction. The actual basal plane spacings depend on the species present in the interlayer, including water. In the presence of sulfate, the original structure remains, as the (001) reflection is still visible in a diffraction pattern of the undried samples (Additional file 1: Figure

hydroxide and Cr(III)-bearing ferrihydrite as reference standards (Fig. 8a, fit results and statistics shown in Table 4). Cr(III)-bearing ferrihydrite, which is used here in the absence of other Cr(III)-bearing Fe oxyhydroxide reference standards, can be identified in the XANES spectra by characteristic pre-edge features at 5993 and 5999 eV visible in the derivative of the μ (E) spectrum [57]. EXAFS fits were not performed due to the difficulty of differentiating scattering by Fe and Cr; the distortion of the immediate (hydr)oxide bonding environment as Cr is incorporated into increasingly crystalline solids is more easily detectable using XANES fitting [57]. The proportion of Cr(III) hydroxide in each fit varies between 0.54 and 0.66. The proportions of each reference standard fit to the spectra have relatively

Table 4 Summary of Cr-XANES LCF fitting parameters

Weighing factors	Cr (OH)$_3$	Cr-ferrihydrite	Sum	R-value	Reduced Chi squared
GR 7d	0.62 (4)	0.40 (4)	1.02	0.003225	0.00202
AlGR 7d	0.57 (5)	0.45 (5)	1.02	0.00584	0.00377
MgGR 7d	0.54 (5)	0.45 (5)	0.99	0.00693	0.00418
ZnGR 7d	0.66 (3)	0.36 (3)	1.02	0.00183	0.00116

Fig. 9 Probable structure of the reaction product. The brucite-like layers present in green rust are preserved, but some octahedra are displaced into the diffuse octahedral layer. The interlayer spacing is determined by the presence of sulfate, water and hydrated Cr (III)
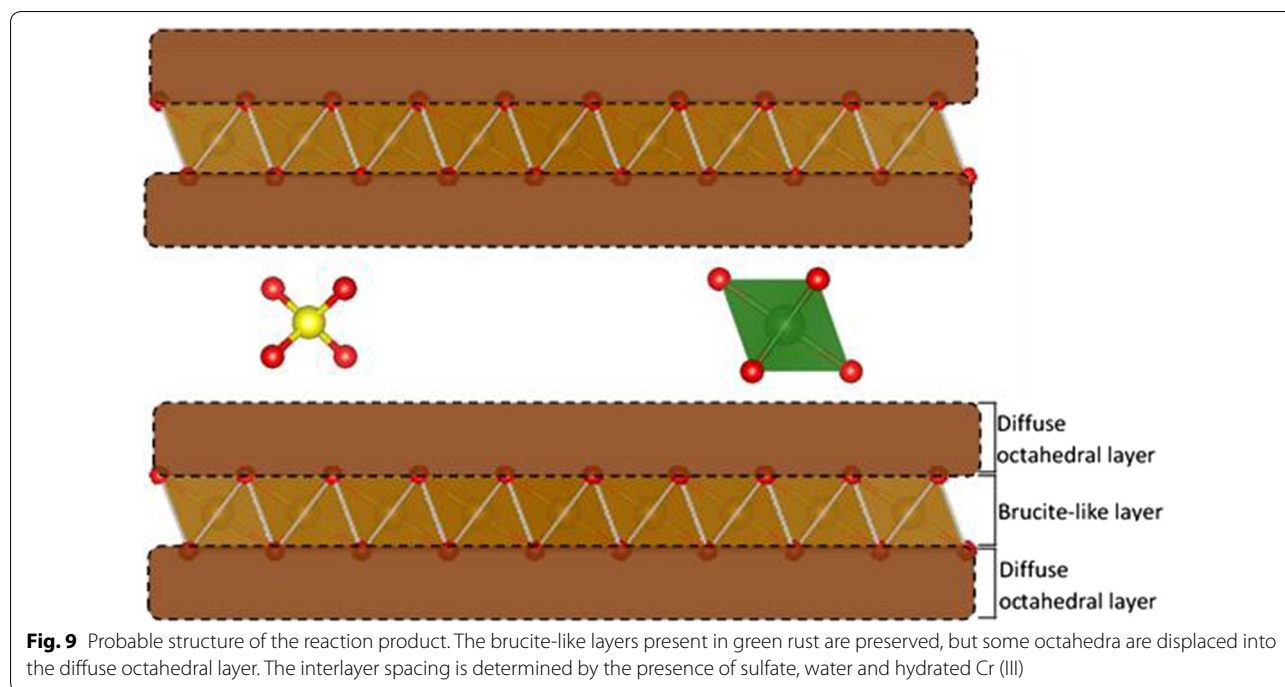
S1). However, displacement of Fe octahedra disrupts the hydrogen bonding in the basal layer that maintains the crystallographic coherence across layers, and as a result, many non-basal plane spacings are no longer detected or very faint in the diffraction patterns. These peaks in the XRD are broad, indicating poor coherence within the ab plane of the reaction products. In this case, linkage of adjacent layers and transformation to feroxyhyte is sterically inhibited by sulfate and the structure is better described as a metastable ferric green rust. However, if sulfate is removed by exchange for chromate prior to the Fe(II)–Cr(VI) electron transfer, adjacent layers can be linked by either covalent bonding with Cr(III) or hydrogen bonding with residual H_2O; this can lead to the topotactic formation of other Fe oxides such as feroxyhyte. Feroxyhyte forms due to the linkage of adjacent layers, as the two phases have similar layered structures and hexagonal symmetries, so following linkage of two oxidized octahedral layers, only a slight reorganization is necessary for this transformation. This reaction mechanism was also proposed by Skovbjerg et al. [14] and our previous study [28], but appears to vary slightly depending on the initial chromium concentration, as higher concentrations favor chromate exchange for interlayer sulfate. The effects of initial chromium concentration on the substituted green rusts are unknown. In addition, the XRD patterns of some samples (oxMg-GR and oxGR, to a lesser extent) with higher non-basal plane crystallinity appear to have partially transformed to feroxyhyte, as

characteristic feroxyhyte XRD peaks are visible in these diffraction patterns, although oxMg-GR is the only product in which this transformation is clear.

Cr(III) hydroxides are also present in the samples and may make a contribution to the PDF pattern between 0 and 10 Å, especially the correlations at 1.98 and 3.0 Å. A PDF pattern of Cr(III) hydroxide is not available; for peak positions and amplitudes, see Tang et al. [57]. Chromium reduced in the interlayer can form Cr(III) hydroxide domains ($[Cr^{3+}]$ is very high in the interlayer following reduction) or bind to adjacent diffuse octahedral layers. Interior Cr(III) hydroxide domains may have formed in oxMg-GR, as the low lability of Cr in this sample despite its relatively high Cr(III) hydroxide content suggests that this phase may be somehow sequestered. It should be noted that this is a metastable, transitional structure that will likely eventually transform to a mixture of Cr(III)-bearing goethite and Cr(III) hydroxide.

Effects of cation substitution on reaction mechanisms and byproducts

Substitution of Al, Mg and Zn for Fe in green rust sulfate alters the morphology, structure and chemical properties of the mineral [36, 37, 59, 60], which could result in substantial changes in reactivity and reaction mechanism when exposed to hexavalent chromium. Green rust [29], like magnetite and other Fe oxides [33], is a semiconductor, potentially allowing reduction of chromate at its surface and rims by electron transport from

Thomas *et al. Geochem Trans* (2020) 21:2

Page 13 of 16

within the particle"s interior. Conduction within green rust is best modelled by a "polaron hopping" mechanism that transports electrons and electron holes in a series of of Fe(II)–Fe(III) charge transfer steps rather than through a delocalized conduction band [29]. Density functional theory (DFT) modelling of polaron hopping within a green rust-like $Fe(OH)_2$ plane showed that the potential rate of electron hole propagation at 300 K reaches 10^{10} s^{-1} in the case of transfer between next-nearest neighbor FeO_6 octahedra (sites Fe1 and Fe2 in Fig. 10), 10^8 times the rate of any other transfer mechanism. The most important parameter controlling the rate of charge transfer was the electronic coupling matrix element (V_{ab}), which represents superexchange processes that link the electron spin states of magnetic cations (i.e. transmission metal cations with a net spin) covalently bound to a shared ligand [35, 61, 62] as a consequence of the Pauli exclusion principle. This coupling mechanism allows Fe^{3+} ligand field transitions, which drive electron transfer and would otherwise be forbidden by the spin-selection rule [33]. Next-nearest neighbor Fe atoms in green rust are not coupled directly by superexchange since they do not share a bridging –OH ligand, but are effectively coupled since both Fe octahedra participate in superexchange interactions with intermediate Fe(III) and Fe(II) octahedra (at sites Me^{3+} and Me^{2+} in Fig. 10). This rapid charge-hopping mechanism allows the regeneration of electron holes at the crystal edges resulting from chromate reduction and therefore continued reduction at the surface as long as it is not passivated. Oxidation by this mechanism would preserve the morphology and structure of the green rust, as it doesn't require exchange of chromate for sulfate. The continued presence of sulfate

in the interlayer sterically inhibits linkages between adjacent layers but maintains the particle structure by linking adjacent layers via electrostatic interactions. Antony et al. [63] observed a reaction product with this structure when oxidizing green rust sulfate with O_2, and our previous study [28] found a similar result. On the other hand, if chromate exchanges for sulfate and is reduced by nearby Fe(II), a new 3-dimensional structure can form as adjacent layers are linked. In this case, transformation to other Fe oxides such as feroxyhyte (as seen in the present study) or goethite [14] is possible.

Cation substitution is expected to alter this intrasheet conductivity, depending on the properties of the substituted cation. Since Al^{3+}, Mg^{2+} and Zn^{2+} are not capable of donating or accepting electrons, as they do not have additional stable oxidation states, incorporation of these cations along the electron transfer chain at sufficient concentrations ($\geq 10\%$) can lower the rate of electron conduction to the particle surface [34, 64], and this effect may be stronger when electron transport is only possible in two dimensions. In addition, since these ions also have full or empty valence orbitals and therefore no net spin, they are unable to induce superexchange interactions with adjacent FeO_6 octahedra when substituted at the Me^{2+} and Me^{3+} sites in Fig. 10 and therefore lower the rate of Fe(II)→Fe(III) charge transfer. Mg substitution appears to have this effect, as the partial transformation to feroxyhyte, lower levels of Cr(III) hydroxide in the Cr K-edge XAS spectra and low S concentrations measured in oxMg-GR by EDX suggest that chromate exchange for sulfate is taking place during these reactions, which leads to the formation of a more stable product. Al-GR also produces a product more resistant to oxidation by δ-MnO_2 than pure green rust with a lower proportion of Cr(III) hydroxide. On the other hand, Zn substitution appears to have the opposite effect, as oxZn-GR was primarily composed of Cr(III) hydroxide and a layered, incoherently-stacked product as expected when Cr(VI) is reduced by electrons transferred to the crystal edges from its interior. As a non-magnetic cation, Zn^{2+} is also unable to couple the electron spin states of adjacent Fe-centered octahedra, and Zn substitution is expected to favor interlayer reduction of Cr(VI), and some evidence for this reaction exists in the form of the rim-like domains observed in the oxZn-GR TEM images. However, as Cr hydroxide is still the dominant Cr carrier phase in this sample, it is possible that other factors favor oxidative transformation of Zn-GR to a stacked SSI reaction product instead.

Additionally, cation substitution can lead to thermodynamic constraints on the reaction mechanism. For example, Zn^{2+} has a similar ionic radius to Fe^{2+} and is therefore easily incorporated at Fe(II) sites in green rust,
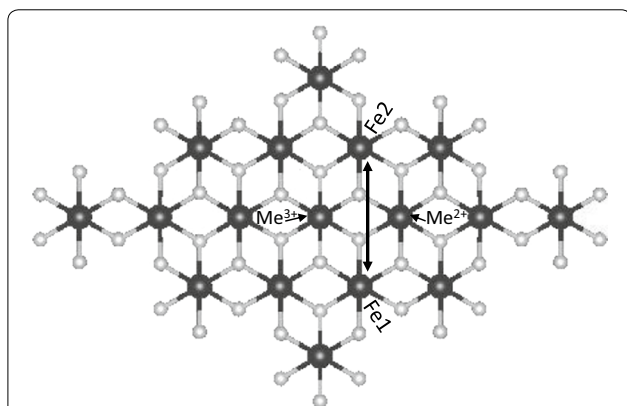

Fig. 10 Brucite-like sheet used to demonstrate electron transfer between Fe-centered octahedra. Electron transport is between next-nearest neighbor Fe sites labelled Fe1 and Fe2, which are coupled via superexchange with atoms at the neighboring sites Me^{2+} and Me^{3+}

Thomas *et al. Geochem Trans*   (2020) 21:2

Page 14 of 16

phyllosilicates and other mixed-valence Fe oxides such as magnetite [65]. However, divalent metal substitution in Fe(III) (oxyhydr)oxides is generally not favorable because of its effects on the crystal field stabilization energy [66], differences in atomic radius, and effects on charge balance. Gerth [67] synthesized goethite with relatively high levels of Zn (Zn/Zn + Fe = 0.07), and Manceau et al. [68] identified natural goethite with approximately 2% substitution of Zn for Fe, so Zn incorporation into a Fe (III) oxide product is possible but most likely not thermodynamically favorable in this system, particularly because Zn substitution at the Fe(II) site is so high (13.5%). Instead, when ZnGR is oxidized by Cr(VI), the presence of a divalent cation with a higher ionic radius such as Zn^{2+} within the octahedral sheet may reduce the structural strain resulting from oxidation relative to other green rusts, possible including pure green rust sulfate. Therefore, the stacked SSI product is most likely more stable and crystalline, so chromate exchange for sulfate and collapse of the stacked SSI layers is less favorable. As a result, Cr(VI) reduction at the particle surface coupled to electron transfer from the interior is probably a more dominant reaction mechanism, producing Cr(III) hydroxide as the dominant Cr carrier phase in oxZn-GR.

Conclusion

Laboratory-scale experiments are only the first step in developing and implementing an effective in situ remediation method, but the results presented here suggest that the controlled substitution of cations into green rust can significantly improve its ability to remediate hexavalent chromium contamination. In particular, the increased stability of the reaction products in the case of Mg substitution represents a significant improvement compared to existing particle-based in situ chemical reduction methods, and the reactants can be simply and inexpensively synthesized from sulfate salts available in bulk as agricultural chemicals. Mg^{2+} is abundant in soils and non-toxic, and due to its similar ionic radius to Fe^{2+} (0.072 nm vs. 0.078 nm, Shannon [69]), can easily substitute for structural Fe (II) and is a common substituent in green rusts identified in natural soils [37].

This technique is best applied by adding a large excess of ex situ-synthesized Mg-substituted green rust to a Cr-contaminated site. Excess Fe (III) allows the formation of more-crystalline Fe (III) oxides with lower levels of Cr incorporation [14], and excess Fe (II) can catalyze more rapid formation of these oxides [70–72] via a dissolution-precipitation mechanism. These oxides may also be a sink for other metal contaminants often associated with chromium contamination at former metal plating sites such as Ni^{2+}, Cd^{2+} and Cu^{2+} [3]. In addition, under the reaction conditions tested in the present study (pH = 7.0),

the green rust surface is positively charged [73], which should favor sorption of chromate at the particle surface followed by reduction. Synthesizing green rust under more alkaline conditions (pH > 8.0) may favor exchange of chromate for interlayer sulfate, as observed when reacting chromate with Fe (II)-bearing smectites [74, 75]. A study of these reactions at different initial chromium concentrations would also be useful for determining the reproducibility of these results under variable conditions. Finally, higher or lower levels of isomorphic substitution may also have an effect on the reactivities and reaction byproducts of these green rusts.

Supplementary information

> **Additional file 1.** Includes x-ray diffraction patterns obtained using benchtop equipment as well as a more detailed description of the XAS data analysis procedure.

Abbreviations
ISCR: In situ chemical reduction; TEM: Transmission electron microscopy; XAS: X-ray absorption spectroscopy; XRD: X-ray diffraction; PDF: Pair distribution function; ICP-OES: Inductively-coupled plasma optical emission spectroscopy; FWHM: Full width half maximum; XANES: X-ray absorption near-edge spectroscopy; EXAFS: Extended X-ray absorption fine-structure spectroscopy; SEM: Scanning electron microscopy; EDX: Energy dispersive X-ray spectroscopy; SAED: Selected-area electron diffraction; STEM: Scanning transmission electron microscopy; DFT: Density functional theory; GR: Green rust; SSI: Single-sheet iron oxided.

Authors' contributions
AT designed and performed the study. EE, LB, DT and TN provided lab space and access to scientific instruments. JG and RS assisted with XAS measurements at the ANKA beamline. HF and MM performed electron microscopy and PDF measurements, respectively. KD assisted with interpretation of results and elucidation of the reaction mechanism. All authors assisted with writing the manuscript and approved its submission. All authors read and approved the final manuscript.

Availability of data and materials
Data sets are available without restriction from the authors on request (andrew.thomas@kit.edu).

Thomas *et al. Geochem Trans*   (2020) 21:2

Page 15 of 16

Author details
[1] Institute of Applied Geosciences, Karlsruhe Institute of Technology, 76137 Karlsruhe, Germany. [2] Institute of Synchrotron Radiation, Karlsruhe Institute of Technology, 76344 Eggenstein-Leopoldshafen, Germany. [3] GFZ German Research Center for Geosciences, Telegrafenberg, 14473 Potsdam, Germany. [4] Department of Earth Sciences, Free University of Berlin, 12249 Berlin, Germany. [5] Nano-Science Center, Department of Chemistry, University of Copenhagen, 2100 Copenhagen, Denmark. [6] Department of Applied Geosciences, Technical University of Berlin, 10587 Berlin, Germany. [7] Present Address: School of Chemical and Processing Engineering, University of Leeds, Leeds LS29JT, UK.

References
1. Puls RW, Paul CJ, Powell RM (1999) The application of in situ permeable reactive (zero-valent iron) barrier technology for the remediation of chromate-contaminated groundwater: a field test. Appl Geochem 14(8):989–1000
2. Ludwig RD, Su C, Lee TR, Wilkin RT, Acree SD, Ross RR et al (2007) In situ chemical reduction of Cr(VI) in groundwater using a combination of ferrous sulfate and sodium dithionite: a field investigation. Environ Sci Technol 41(15):5299–5305. https://doi.org/10.1021/es070025z
3. Saha R, Nandi R, Saha B (2011) Sources and toxicity of hexavalent chromium. J Coord Chem 64(10):1782–1806
4. Barceloux DG, Barceloux D (1999) Chromium. J Toxicol Clin Toxicol 37:173–194
5. Landrot G, Ginder-Vogel M, Livi K, Fitts JP, Sparks DL (2012) Chromium(III) oxidation by three poorly-crystalline manganese(IV) oxides. 1. Chromium(III)-oxidizing capacity. Environ Sci Technol 46(21):11594–11600. https://doi.org/10.1021/es302383y
6. Bartlett R, James B (1979) Behavior of chromium in soils: III. Oxidation 1. J Environ Qual. 8(1):31
7. Hausladen DM, Fendorf S (2017) Hexavalent chromium generation within naturally structured soils and sediments. Environ Sci Technol 51(4):2058–2067. https://doi.org/10.1021/acs.est.6b04039
8. Pan C, Liu H, Catalano JG, Qian A, Wang Z, Giammar DE (2017) Rates of Cr(VI) generation from Cr x Fe 1–x (OH) 3 solids upon reaction with manganese oxide. Environ Sci Technol 51(21):12416–12423. https://doi.org/10.1021/acs.est.7b04097
9. Varadharajan C, Beller HR, Bill M, Brodie EL, Conrad ME, Han R et al (2017) Reoxidation of chromium(III) products formed under different biogeochemical regimes. Environ Sci Technol 51(9):4918–4927. https://doi.org/10.1021/acs.est.6b06044
10. Rai D, Sass BM, Moore DA (1987) Chromium(III) hydrolysis constants and solubility of chromium(III) hydroxide. ChemInform. https://doi.org/10.1002/chin.198720020
11. Papassiopi N, Vaxevanidou K, Christou C, Karagianni E, Antipas GSE (2014) Synthesis, characterization and stability of Cr(III) and Fe(III) hydroxides. J Hazard Mater 264:490–497
12. Christiansen BC, Dideriksen K, Katz A, Nedel S, Bovet N, Sørensen HO et al (2014) Incorporation of monovalent cations in sulfate green rust. Inorg Chem 53(17):8887–8894. https://doi.org/10.1021/ic500495a
13. Bond DL, Fendorf S (2003) Kinetics and structural constraints of chromate reduction by green rusts. Environ Sci Technol 37(12):2750–2757. https://doi.org/10.1021/es026341p
14. Skovbjerg LL, Stipp SLS, Utsunomiya S, Ewing RC (2006) The mechanisms of reduction of hexavalent chromium by green rust sodium sulphate: formation of Cr-goethite. Geochim Cosmochim Acta 70(14):3582–3592
15. O'Loughlin EJ, Kelly SD, Cook RE, Csencsits R, Kemner KM (2003) Reduction of uranium(VI) by mixed iron(II)/iron(III) hydroxide (green rust): formation of UO 2 nanoparticles. Environ Sci Technol 37(4):721–727. https://doi.org/10.1021/es0208409
16. Jönsson J, Sherman DM (2008) Sorption of As(III) and As(V) to siderite, green rust (fougerite) and magnetite: implications for arsenic release in anoxic groundwaters. Chem Geol 255(1–2):173–181
17. Perez JPH, Freeman HM, Schuessler JA, Benning LG (2019) The interfacial reactivity of arsenic species with green rust sulfate (GRSO4). Sci Total Environ 648:1161–1170
18. Hansen HCB, Koch CB (1998) Reduction of nitrate to ammonium by sulphate green rust: activation energy and reaction mechanism. Clay Miner 33(01):87–101
19. Hansen HCB, Guldberg S, Erbs M, Bender Koch C (2001) Kinetics of nitrate reduction by green rusts-effects of interlayer anion and Fe(II):Fe(III) ratio. Appl Clay Sci 18(1–2):81–91
20. Latta D, Boyanov M, Kemner K, O'Loughlin E, Scherer M (2015) Reaction of uranium(VI) with green rusts: effect of interlayer anion. Curr Inorg Chem. 5(3):156–168
21. Myneni SC (1997) Abiotic selenium redox transformations in the presence of Fe(II, III) oxides. Science (80-) 278(5340):1106–1109. https://doi.org/10.1126/science.278.5340.1106
22. Refait P, Simon L, Génin JMR (2000) Reduction of SeO42- anions and anoxic formation of iron(II)–Iron(III) hydroxy-selenate green rust. Environ Sci Technol 34(5):819–825
23. Christiansen BC, Geckeis H, Marquardt CM, Bauer A, Römer J, Wiss T et al (2011) Neptunyl (NpO2) interaction with green rust. Geochim Cosmochim Acta 75(5):1216–1226
24. Loyaux-Lawniczak S, Refait P, Lecomte C, Ehrhardt J, Genin JR (1999) The reduction of chromate ions by Fe (II) layered hydroxides. Hydrol Earth Syst Sci 3:593–599
25. Loyaux-Lawniczak S, Refait P, Ehrhardt JJ, Lecomte P, Génin JMR (2000) Trapping of Cr by formation of ferrihydrite during the reduction of chromate ions by Fe(II)—Fe(III) hydroxysalt green rusts. Environ Sci Technol. 34(3):438–443. https://doi.org/10.1021/es9903779
26. Williams AGB, Scherer MM (2001) Kinetics of Cr(VI) Reduction by Carbonate Green Rust. Environ Sci Technol. 35(17):3488–3494. https://doi.org/10.1021/es010579g
27. Legrand L, El Figuigui A, Mercier F, Chausse A (2004) Reduction of aqueous chromate by Fe(II)/Fe(III) carbonate green rust: kinetic and mechanistic studies. Environ Sci Technol 38(17):4587–4595. https://doi.org/10.1021/es035447x
28. Thomas A, Eiche E, Göttlicher J, Steininger R, Benning LG, Freeman HM et al (2018) Products of hexavalent chromium reduction by green rust sodium sulfate and associated reaction mechanisms. Soil Syst. 2(4):58
29. Wander MCF, Rosso KM, Schoonen MAA (2007) Structure and charge hopping dynamics in green rust. J Phys Chem C 111(30):11414–11423. https://doi.org/10.1021/jp072762n
30. Alexandrov AS, Mott NF. Polarons and Bipolarons. World Scientific; 1996. https://www.worldscientific.com/worldscibooks/10.1142/2784
31. Ederth J, Hoel A, Niklasson GA, Granqvist CG (2004) Small polaron formation in porous WO3−x nanoparticle films. J Appl Phys 96(10):5722–5726. https://doi.org/10.1063/1.1804617
32. Katz JE, Zhang X, Attenkofer K, Chapman KW, Frandsen C, Zarzycki P et al (2012) Electron small polarons and their mobility in iron (oxyhydr) oxide nanoparticles. Science (80-) 337(6099):1200–1203. https://doi.org/10.1126/science.1223598
33. Sherman DM. Crystal chemistry, electronic structures, and spectra of fe sites in clay minerals: applications to photochemistry and electron transport. In: Coyne LM, McKeever SWS, Blake DF, editors. Spectroscopic characterization of minerals and their surfaces. Washington, DC: American Chemical Society; 1990. p. 284–309. (ACS Symposium Series; vol. 415). http://pubs.acs.org/doi/book/10.1021/bk-1990-0415
34. Alexandrov V, Rosso KM (2014) Electron transport in pure and substituted iron oxyhydroxides by small-polaron migration. J Chem Phys. https://doi.org/10.1063/1.4882065
35. Kanamori J (1959) Superexchange interaction and symmetry properties of electron orbitals. J Phys Chem Solids 10(2–3):87–98
36. Ruby C, Abdelmoula M, Aissa R, Medjahdi G, Brunelli M, François M (2008) Aluminium substitution in iron(II-III)-layered double hydroxides: formation and cationic order. J Solid State Chem 181(9):2285–2291
37. Refait P, Abdelmoula M, Trolard F, Génin JMR, Bourkié G (2001) Mössbauer and XAS study of a green rust mineral; the partial substitution of Fe2+ by Mg2+. Am Mineral 86(5–6):731–739

Thomas *et al. Geochem Trans*   (2020) 21:2

Page 16 of 16

38. Ahmed IAM, Shaw S, Benning LG (2008) Formation of hydroxysulphate and hydroxycarbonate green rusts in the presence of zinc using time-resolved in situ small and wide angle X-ray scattering. Mineral Mag 72(1):159–162

39. Géhin A, Ruby C, Abdelmoula M, Benali O, Ghanbaja J, Refait P et al (2002) Synthesis of Fe(II-III) hydroxysulphate green rust by coprecipitation. Solid State Sci 4(1):61–66

40. Gibbs CR (1976) Characterization and application of FerroZine iron reagent as a ferrous iron indicator. Anal Chem 48(8):1197–1201. https://doi.org/10.1021/ac50002a034

41. Carlson L, Schwertmann U (1980) Natural occurrence of feroxyhite (δ′-FeOOH). Clays Clay Miner 28(4):272–280

42. Villalobos M, Lanson B, Manceau A, Toner B, Sposito G (2006) Structural model for the biogenic Mn oxide produced by *Pseudomonas putida*. Am Mineral 91(4):489–502

43. Villalobos M, Toner B, Bargar J, Sposito G (2003) Characterization of the manganese oxide produced by *Pseudomonas putida* strain MnB1. Geochim Cosmochim Acta 67(14):2649–2662

44. Toby BH, Von Dreele RB (2013) GSAS-II : the genesis of a modern open-source all purpose crystallography software package. J Appl Crystallogr 46(2):544–549

45. Juhás P, Davis T, Farrow CL, Billinge SJL (2013) PDFgetX3: a rapid and highly automatable program for processing powder diffraction data into total scattering pair distribution functions. J Appl Crystallogr 46(2):560–566

46. Egami T, Billinge SJL (2012) Underneath the Bragg peaks: structural analysis of complex materials, 2nd edn. Elsevier, Oxford

47. Ravel B, Newville M (2005) ATHENA and ARTEMIS interactive graphical data analysis using IFEFFIT. Phys Scr T115:1007–1010

48. Papassiopi N, Pinakidou F, Katsikini M, Antipas GSE, Christou C, Xenidis A et al (2014) A XAFS study of plain and composite iron (III) and chromium (III) hydroxides. Chemosphere 111:169–176

49. Schwertmann U, Cornell RM (2008) Iron oxides in the laboratory, 2nd edition, 2nd edn. Wiley-WCH, Weinheim

50. Manceau A, Drits VA (1993) Local structure of ferrihydrite and feroxyhyte by EXAFS spectroscopy. Clay Miner 28(02):165–184

51. Blake RL, Hessevick RE, Zoltai T, Finger LW (1966) Refinement of the hematite structure. Am Mineral 51(1–2):123–129

52. Buerge IJ, Hug SJ (1997) Kinetics and pH dependence of chromium (VI) reduction by iron (II). Environ Sci Technol. 31(5):1426–1432. https://doi.org/10.1021/es960672i

53. Simon L, François M, Refait P, Renaudin G, Lelaurain M, Génin JMR (2003) Structure of the Fe(II-III) layered double hydroxysulphate green rust two from Rietveld analysis. Solid State Sci 5(2):327–334

54. Patrat G, de Bergevin F, Pernet M, Joubert JC (1983) Structure locale de δ-FeOOH. Acta Crystallogr Sect B: Struct Sci 39(2):165–170

55. Michel FM, Ehm L, Antao SM, Lee PL, Chupas PJ, Liu G et al (2007) The structure of ferrihydrite, a nanocrystalline material. Science (80-) 316(5832):1726–1729. https://doi.org/10.1126/science.1142525

56. Yin Z, Dideriksen K, Abdelmoula M, Ruby C, Michel FM, Bjerrum MJ et al (2019) Structure of single sheet iron oxides produced from surfactant interlayered green rusts. Appl Clay Sci 170:86–96

57. Tang Y, Michel FM, Zhang L, Harrington R, Parise JB, Reeder RJ (2010) Structural properties of the Cr(III)—Fe(III) (Oxy)hydroxide compositional series: insights for a nanomaterial "solid solution". Chem Mater 22(12):3589–3598. https://doi.org/10.1021/cm1000472

58. Drits VA, Sakharov BA, Manceau A (1993) Structure of feroxyhite as determined by simulation of X-ray diffraction curves. Clay Miner 28(2):209–222

59. Refait P, Sabot R, Jeannin M (2017) Role of Al(III) and Cr(III) on the formation and oxidation of the Fe(II-III) hydroxysulfate green rust. Colloids Surfaces A Physicochem Eng Asp 531:203–212. https://doi.org/10.1016/j.colsurfa.2017.08.006

60. Zhang H, Wen X, Wang Y (2007) Synthesis and characterization of sulfate and dodecylbenzenesulfonate intercalated zinc-iron layered double hydroxides by one-step coprecipitation route. J Solid State Chem 180(5):1636–1647

61. Goodenough JB (1955) Theory of the role of covalence in the perovskite-type manganites [La, M(II)]MnO$_3$. Phys Rev 100(2):564–573. https://doi.org/10.1103/PhysRev.100.564

62. Goodenough JB (1958) An interpretation of the magnetic properties of the perovskite-type mixed crystals La1−xSrxCoO3−λ. J Phys Chem Solids 6(2–3):287–297

63. Antony H, Legrand L, Chaussé A (2008) Carbonate and sulphate green rusts—mechanisms of oxidation and reduction. Electrochim Acta 53(24):7146–7156

64. Latta DE, Bachman JE, Scherer MM (2012) Fe Electron transfer and atom exchange in goethite: influence of Al-substitution and anion sorption. Environ Sci Technol 46(19):10614–10623. https://doi.org/10.1021/es302094a

65. Sidhu PS, Gilkes RJ, Posner AM (1978) The synthesis and some properties of Co, Ni, Zn, Cu, Mn and Cd substituted magnetites. J Inorg Nucl Chem 40(3):429–435

66. Dawson BSW, Fergusson JE, Campbell AS, Cutler EJB (1985) Distribution of elements in some Fe-Mn nodules and an iron-pan in some gley soils of New Zealand. Geoderma 35(2):127–143

67. Gerth J (1990) Unit-cell dimensions of pure and trace metal-associated goethites. Geochim Cosmochim Acta 54(2):363–371

68. Manceau A, Schlegel ML, Musso M, Sole VA, Gauthier C, Petit PE et al (2000) Crystal chemistry of trace elements in natural and synthetic goethite. Geochim Cosmochim Acta 64(21):3643–3661

69. Shannon RD (1976) Revised effective ionic radii and systematic studies of interatomic distances in halides and chalcogenides. Acta Crystallogr Sect A. 32(5):751–767

70. Boland DD, Collins RN, Miller CJ, Glover CJ, Waite TD (2014) Effect of solution and solid-phase conditions on the Fe(II)-accelerated transformation of ferrihydrite to lepidocrocite and goethite. Environ Sci Technol 48(10):5477–5485. https://doi.org/10.1021/es4043275

71. Yang L, Steefel CI, Marcus MA, Bargar JR (2010) Kinetics of Fe(II)-catalyzed transformation of 6-line ferrihydrite under anaerobic flow conditions. Environ Sci Technol. 44(14):5469–5475. https://doi.org/10.1021/es1007565

72. Pedersen HD, Postma D, Jakobsen R, Larsen O (2005) Fast transformation of iron oxyhydroxides by the catalytic action of aqueous Fe (II). Geochim Cosmochim Acta 69(16):3967–3977

73. Guilbaud R, White ML, Poulton SW (2013) Surface charge and growth of sulphate and carbonate green rust in aqueous media. Geochim Cosmochim Acta. 108:141–153. https://doi.org/10.1016/j.gca.2013.01.017

74. Bishop ME, Dong H, Glasser P, Briggs BR, Pentrak M, Stucki JW et al (2019) Reactivity of redox cycled Fe-bearing subsurface sediments towards hexavalent chromium reduction. Geochim Cosmochim Acta. 252:88–106. https://doi.org/10.1016/j.gca.2019.02.039

75. Bishop ME, Glasser P, Dong H, Arey B, Kovarik L (2014) Reduction and immobilization of hexavalent chromium by microbially reduced Fe-bearing clay minerals. Geochim Cosmochim Acta. 133:186–203. https://doi.org/10.1016/j.gca.2014.02.040

Publisher's Note

Appendix B: Full Text of Second-author Publications

B.1 Adsorption and Reduction of Arsenate during the Fe^{2+}-Induced Transformation of Ferrihydrite

Article

Adsorption and Reduction of Arsenate during the Fe²⁺-Induced Transformation of Ferrihydrite

Jeffrey Paulo H. Perez,*[†,‡] Dominique J. Tobler,[§] Andrew N. Thomas,[∥] Helen M. Freeman,[†,#] Knud Dideriksen,[§,¶] Jörg Radnik,[⊥] and Liane G. Benning[†,‡,Δ]

[†]GFZ German Research Center for Geosciences, Telegrafenberg, 14473 Potsdam, Germany

[‡]Department of Earth Sciences, Free University of Berlin, 12249 Berlin, Germany

[§]Nano-Science Center, Department of Chemistry, University of Copenhagen, 2100 Copenhagen, Denmark

[∥]Institute of Applied Geosciences, Karlsruhe Institute of Technology, 76137 Karlsruhe, Germany

[#]School of Chemical and Process Engineering, University of Leeds, Leeds LS2 9JT, United Kingdom

[¶]Geological Survey of Denmark and Greenland (GEUS), 1350 Copenhagen K, Denmark

[⊥]Federal Institute for Materials Research and Testing (BAM), 12205 Berlin, Germany

[Δ]School of Earth and Environment, University of Leeds, Leeds LS2 9JT, United Kingdom

Ⓢ Supporting Information

ABSTRACT: Iron (oxyhydr)oxides play an important role in controlling the mobility and toxicity of arsenic (As) in contaminated soils and groundwaters. Dynamic changes in subsurface geochemical conditions can impact As sequestration and remobilization since the fate of As is highly dependent on the dominant iron mineral phases present and, specifically, the pathways through which these form or transform. To assess the fate of arsenate [As(V)] in subsurface settings, we have investigated the Fe²⁺-induced transformation of As(V)-bearing ferrihydrite (As(V)-FH) to more crystalline phases under environmentally relevant anoxic subsurface conditions. Specifically, we examined the influence of varying $Fe^{2+}_{(aq)}/Fe(III)_{solid}$ ratios (0.5, 1, 2) on the behavior and speciation of mineral-bound As species during the transformation of As(V)-FH to crystalline iron-bearing phases at circumneutral pH conditions. At all $Fe^{2+}_{(aq)}/Fe(III)_{solid}$ ratios, goethite (GT), green rust sulfate (GR_{SO4}), and lepidocrocite (LP) formed within the first 2 h of reaction. At low ratios (0.5 to 1), initially formed GR_{SO4} and/or LP dissolved as the reaction progressed, and only GT and some unreacted FH remained after 24 h. At $Fe^{2+}_{(aq)}/Fe(III)_{solid}$ ratio of 2, GR_{SO4} remained stable throughout the 24 h of reaction, alongside GT and unreacted As(V)-FH. Despite the fact that majority of the starting As(V)-FH transformed to other phases, the initially adsorbed As was not released into solution during the transformation reactions, and ~99.9% of it remained mineral-bound. Nevertheless, the initial As(V) became partially reduced to As(III), most likely because of the surface-associated Fe²⁺-GT redox couple. The extent of As(V) reduction increased from ~34% to ~40%, as the $Fe^{2+}_{(aq)}/Fe(III)_{solid}$ ratio increased from 0.5 to 2. Overall, our results provide important insights into transformation pathways of iron (oxyhydr)oxide minerals in As contaminated, anoxic soils and sediments and demonstrate the impact that such transformations can have on As mobility and also importantly oxidation state and, hence, toxicity in these environments.

KEYWORDS: arsenic, ferrihydrite, goethite, green rust, mineral transformation, XAS, XPS
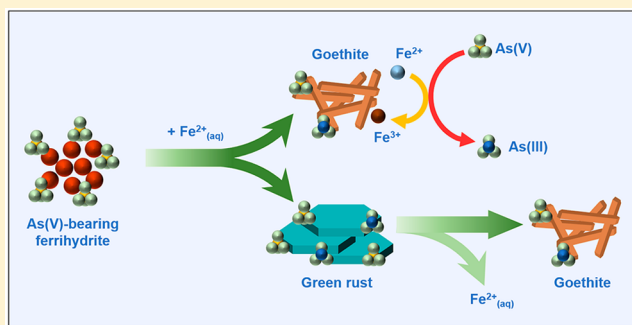
INTRODUCTION

Ferrihydrite (FH) is a nanoparticulate ferric oxyhydroxide mineral commonly found in natural and engineered environments (e.g., soils, groundwater, acid mine drainage, and acid sulfate soils).[1,2] FH can sequester considerable amounts of trace or toxic elements via adsorption or coprecipitation due to its high specific surface area (from 120 to 850 m² g⁻¹) and reactivity.[3−8] However, FH is thermodynamically metastable and usually transforms to more crystalline iron (oxyhydr)-oxides (e.g., goethite, hematite, lepidocrocite, green rust, or

magnetite),[1] whereby any adsorbed or incorporated compounds can be remobilized and redistributed. FH transformation in oxic, ambient conditions and at circumneutral pH

is very slow (months to years),[9] and the rates, mechanisms, and pathways of transformation strongly depend on physicochemical factors including pH,[10−12] temperature,[11,12] and the presence of inorganic ions[4,12−14] and organic ligands.[15,16]

In anoxic and nonsulfidic environments, FH transformations can occur more rapidly (within hours or days) due to the presence of aqueous ferrous iron ($Fe^{2+}_{(aq)}$),[17−20] generated by dissimilatory iron-reducing bacteria.[21,22] FH transformation usually starts by an initial adsorption of aqueous Fe^{2+} onto FH surface sites and the oxidation of this surface-bound Fe(II) to surface Fe(III) species by loss of an electron to the FH solid. This electron is then conducted through the FH and eventually leads to a release of $Fe^{2+}_{(aq)}$.[23−26] This electron conduction process creates "reactive" surface sites, which in turn initiates the dissolution of FH and recrystallization to goethite (GT) and/or lepidocrocite (LP).[17,27] If the aqueous Fe^{2+} is in excess compared to the solid Fe(III) (oxyhydr)oxide (e.g., FH, GT, and LP), it can transform to mixed-valent Fe minerals such as green rust (GR) and magnetite (MGT).[28−30] Hence, FH transformations can lead to a variety of Fe mineral phases, and each of these phases has different sorption and redox properties. In turn, this will affect biogeochemical cycling of iron and nutrients[21] and importantly also the sequestration of FH-bound toxic elements.

Arsenic is a persistent contaminant affecting groundwater resources worldwide due to its widespread occurrence and distribution.[31,32] Its mobility in the environment can be greatly influenced by its interaction with mineral phases such as iron (oxhydr)oxides, which have been shown to be highly effective substrates for the sequestration of As in contaminated groundwater. However, the adsorption capacity of iron (oxyhydr)oxides varies dramatically and is also strongly affected by the As oxidation state, which can quickly change during Fe redox transformations. Among the various iron (oxyhydr)oxides, FH, which is often the first Fe phase forming in subsurface near-neutral environments, exhibits one of the highest adsorption affinities for both As(III) and As(V) , while most crystalline Fe phases have far lower As adsorption affinities.[33−38] Under anoxic conditions and in the presence of $Fe^{2+}_{(aq)}$, FH readily transforms to crystalline Fe phases, and this can be accompanied by the release and remobilization of As back into the aqueous phase or the As can become associated with the newly formed Fe phases. However, the mechanisms and pathways of these processes during the intertransformation of the various iron (oxyhydr)oxides is, however, so far poorly understood or quantified.

To the best of our knowledge, only a few studies examined the Fe^{2+}-induced transformation of As-bearing FH under anoxic conditions. Pedersen et al.[39] used ^{55}Fe and ^{73}As radiotracers to monitor the transformation of As(V)-coprecipitated FH at pH 6.5 and at varying $Fe^{2+}_{(aq)}$ concentrations (0 to 1 mM), an Fe(III)$_{FH}$ loading of 0.5 mM, and As/Fe$_{solid}$ ratios between 0.001 to 0.005. They showed that after 5 days, LP and GT formed at low [$Fe^{2+}_{(aq)}$], while GT and MGT formed at higher [$Fe^{2+}_{(aq)}$]. They also inferred that the coprecipitated As had little to no effect on the FH transformation rates and that most of the As remained associated with the solids. More recently, Masue-Slowey et al.[40] investigated the Fe^{2+}-induced transformation of As(V)-adsorbed FH. They used higher As/Fe$_{solid}$ ratios (0.013 to 0.05), higher Fe(III)$_{FH}$ loadings (20 mM), and also up to 2 mM of $Fe^{2+}_{(aq)}$ concentration. They showed that LP and MGT

formed instead of GT, and that the preadsorbed As retarded FH transformation. These studies have provided insights into the mineralogical changes that occur when As-bearing FH is reacted with varying [$Fe^{2+}_{(aq)}$] and revealed how the transformation rates can be affected by the presence of As. However, the fate, bonding environment, or redox state of the coprecipitated or adsorbed As during the crystallizations remains elusive. The questions of whether transformation reactions in systems where higher amounts of As are associated with the initial FH will cause As release, and what happens if As is only adsorbed to FH rather than coprecipitated are still open. Moreover, As oxidation state could be affected by these redox reactions, and this would affect the toxicity of As in the subsurface. Lastly, the previously tested conditions do not favor GR formation; however, GR phases may be a key substrate for As sequestration in Fe-rich and oxygen-poor subsurface environments (e.g., gley soils or contaminated aquifers), particularly as they can adsorb large amounts of As.[33,41] Thus, GR formation, stability, and behavior with respect to As has to be evaluated.

Herein, we aim to fill a part of this knowledge gap by describing a study in which we performed batch experiments under anoxic conditions and examined the Fe^{2+}-induced transformation of As(V)-bearing FH. Experiments were carried out at pH 6.5 with FH onto which As(V) was adsorbed and was subsequently reacted at varying $Fe^{2+}_{(aq)}$/Fe(III)$_{solid}$ ratios for up to 24 h. In particular, we tested $Fe^{2+}_{(aq)}$/Fe(III)$_{solid}$ concentrations and ratios that were higher than in the above-mentioned studies but that have been shown to favor the formation of GR.[29,41] The mineralogical transformations of As(V)-FH and the fate of As in these processes were assessed using conventional laboratory and synchrotron-based X-ray scattering and spectroscopic techniques, and the resulting products were imaged using electron microscopy. Our results provide new insights on the influence of iron (oxyhydr)oxide mineral transformations on the speciation and hence mobility and toxicity of As in contaminated subsurface environments.

■ EXPERIMENTAL SECTION

General Methods. All glass- and plastic-wares were cleaned in 5 M HCl for 24 h, followed by thorough rinsing with Milli-Q water (~18.2 MΩ·cm). All chemicals were ACS reagent grade from Sigma-Aldrich and Acros Organics and were used as received. Stock solutions were prepared inside the anaerobic chamber (97% N_2, 3% H_2, Coy Laboratory Products, Inc.) using O_2-free water, which was obtained by purging Milli-Q water with O_2-free nitrogen for at least 4 h.

Synthesis of Two-Line FH. Two-line FH was synthesized using the method described by Schwertmann and Cornell[42] by slowly titrating 0.1 M $Fe_2(SO_4)_3$·5H_2O with 1 M NaOH to pH ≈ 7. The resulting suspension was washed using six cycles of centrifugation (9000 rpm, 5 min) and redispersion in Milli-Q water to remove excess solutes. Afterward, the FH slurry was purged with O_2-free N_2 for at least 4 h to remove O_2 and then immediately transferred into the anaerobic chamber. The amount of synthesized FH was determined based on the total iron concentration of an aliquot of the suspension dissolved in 0.3 M HNO_3. The total Fe concentration was analyzed by flame atomic absorption spectrometry (AAS, PerkinElmer AAS Analyst 800). Each batch of FH (~88.3 mM Fe(III)$_{solid}$) was prepared fresh and used on the day of synthesis.

Batch Transformation Experiments. All batch experiments were performed in triplicate at room temperature inside
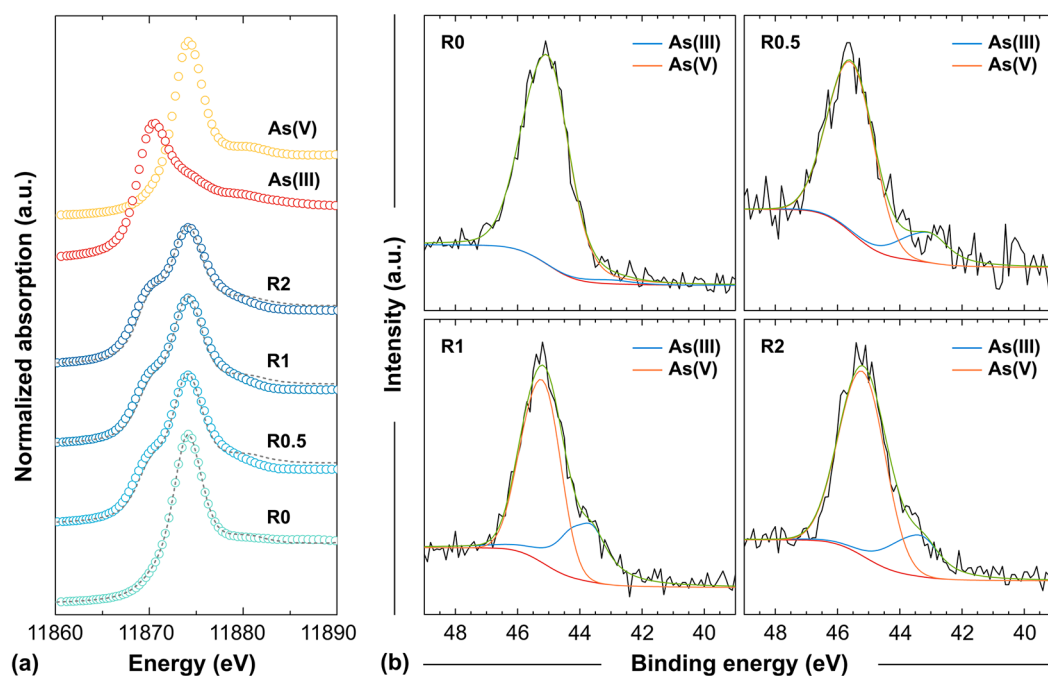
Figure 1. (a) Normalized As K-edge XANES spectra of the end-products. Fits (gray dashed lines) are linear combinations of the As reference standards (i.e., As(III) and As(V) adsorbed on GT). (b) Deconvoluted high-resolution As 3d XPS spectra of the end-products (calibrated to yield adventitious C 1s peak at 285.0 eV). Details of the fitting parameters and statistics for the quantification of As speciation based from the As K-edge XANES and XPS data can be found in Tables S-2 and S-4, respectively.

the anaerobic chamber. To prepare As(V)-bearing FH, an aliquot of the washed FH was resuspended in a 0.1 M NaCl solution buffered at pH 6.5 using 0.05 M morpholinoethanesulfonic acid (MOPS). After pH equilibration, the resulting FH suspension was then spiked with an aliquot from an As(V) stock solution prepared from $Na_2HAsO_4 \cdot 7H_2O$. The resulting suspensions [41.6 mM $Fe(III)_{solid}$, 1.33 mM As(V)] were stirred at 350 rpm for 24 h to ensure As(V) adsorption onto FH (Figure S-1). Afterward, aliquots of 0.5 M $FeSO_4$ were added to the As(V)-bearing FH suspension to achieve $Fe^{2+}_{(aq)}$/$Fe(III)_{solid}$ ratios of 0.5, 1, or 2 (denoted as R0.5, R1, and R2 from here on). A control experiment without $FeSO_4$ addition (no aqueous Fe^{2+}, R0) was also conducted. The resulting mixtures were stirred at 350 rpm for 24 h, with aliquots of the suspension being removed after 0.5, 1, 2, 4, 8, and 24 h. Parts of the collected suspensions were filtered through 0.22 μm syringe filters, and the resulting solutions were acidified with HNO_3 and stored at 4 °C until the concentrations of aqueous As were analyzed by inductively coupled plasma optical emission spectrometry (ICP-OES, Varian 720ES), following the method described by Perez et al.[33] Further analytical details can be found in the Supporting Information (Text S-1, Table S-1). The remainder of the collected suspensions was used to characterize the solid phase. For this, the suspension was filtered using 0.22 μm polycarbonate membrane filters, and the obtained solids were dried in a desiccator inside the chamber, ground, and stored until use in crimped headspace vials inside the anaerobic chamber.

Mineral Characterization and Thermodynamic Modeling. The solids were analyzed by a suite of laboratory- and synchrotron-based characterization techniques to determine their structure and composition, particle sizes and morphologies, surface properties, as well as As and Fe redox states. Detailed information on sample preparation to minimize

oxidation and on solid characterization can be found in the Supporting Information (Text S-2). Mineralogical changes in the solid phase during the reaction were monitored by X-ray powder diffraction (XRD) using a Bruker D8 powder diffractometer (Cu Kα radiation, λ = 1.5406 Å). The morphology, size, structure, and chemical composition of the final solids (collected after 24 h) were characterized by transmission electron microscopy (TEM) and scanning electron microscopy (SEM). TEM micrographs and selected area electron diffraction (SAED) patterns were recorded using a FEI Tecnai G2 F20 X-Twin FEG TEM, operated at 200 keV and equipped with a Gatan Imaging Filter (GIF) Tridiem. SEM images were acquired using a ZEISS Ultra Plus FE-SEM operated in high vacuum mode at an acceleration voltage of 3 kV with 10 μm aperture size using an InLens secondary electron detector. The local structure was investigated using pair distribution function (PDF) analysis. The high energy X-ray scattering data used for PDF analysis were collected at the 11-ID-B beamline of the Advanced Photon Source (Argonne National Laboratory, USA). X-ray absorption spectroscopic (XAS) analyses were carried out to monitor the changes in As oxidation state and to quantify the Fe phases in the final solids. Fe K-edge extended X-ray absorption fine structure (EXAFS) spectra were collected at the SUL-X beamline of Angström-quelle Karlsruhe (ANKA, Karlsruhe, Germany), and the As K-edge X-ray absorption near-edge structure (XANES) data were collected at the BM23 beamline of the European Synchrotron Radiation Facility (ESRF, Grenoble, France). The Fe K-edge EXAFS spectra of synthetic iron (oxyhydr)oxide mineral samples [i.e., FH,[42] GT,[42,43] LP,[42] GR sulfate (GR_{SO_4})[33]] were also collected as reference standards for Fe phase quantification. As K-edge XANES spectra of As(III)- and As(V)-interacted GT samples were also collected and were used as reference standards for the determination of As oxidation state.

Table 1. Arsenic Oxidation State and Mineralogical Composition of the End-Products of As(V)-Bearing FH Transformation with Varying $Fe^{2+}_{(aq)}/Fe(III)_{solid}$ Ratios (R)

| | As oxidation state | | | Fe phase composition | | | | | | | |
| | As K-edge XANES | | | Fe−K edge EXAFS | | | | PDF | | | |
ratio	As(III)	As(V)	red. χ^2	FH	GT	GR	red. χ^2	FH	GT	GR	goodness of fit (R_w)
0	4.1 ± 0.1	95.9 ± 0.1	0.001	100				100			0.208
0.5	33.6 ± 1.8	66.4 ± 1.7	0.014	17 ± 4	83 ± 3		0.221	70 ± 3	30 ± 1		0.205
1	34.3 ± 1.8	65.7 ± 1.8	0.015	15 ± 1	85 ± 1		2.663	22 ± 5	78 ± 3		0.150
2	42.4 ± 1.8	57.6 ± 1.7	0.013	11 ± 2	84 ± 2	5 ± 1	0.226		92 ± 3	8 ± 1	0.175
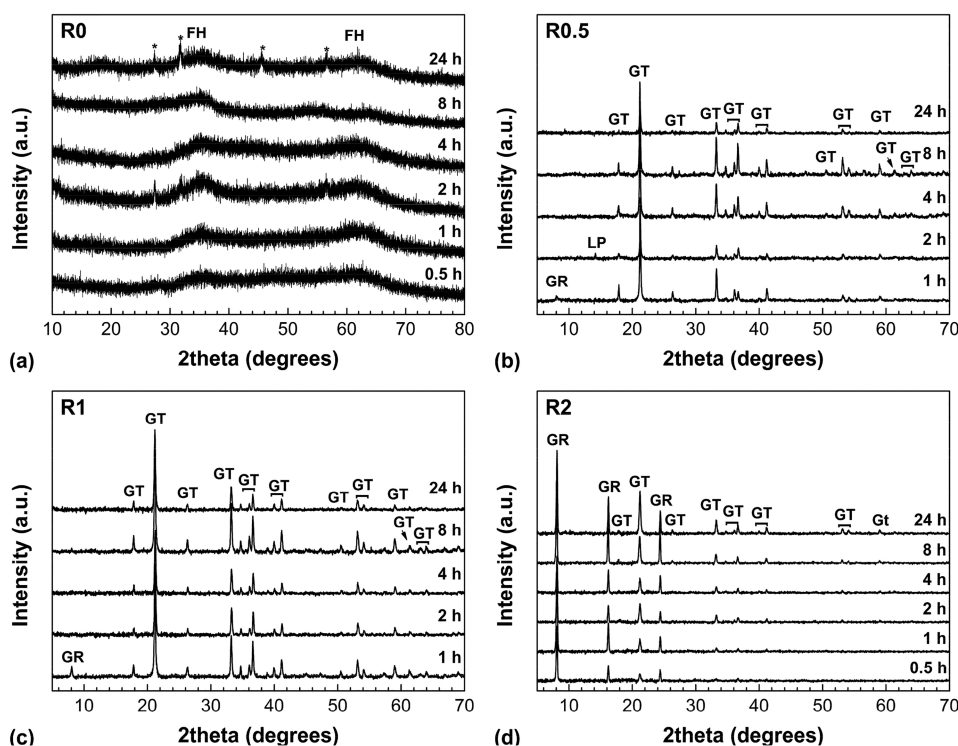
Figure 2. XRD patterns showing the change in mineralogical composition in the solid samples during the 24 h transformation of As(V)-bearing FH at varying $Fe^{2+}_{(aq)}/Fe(III)_{solid}$ ratios (R): (a) control (0), (b) 0.5, (c) 1, and (d) 2. The '*' denotes peaks for halite (NaCl) from the background electrolyte. XRD patterns for R0.5 and R1 at 0.5 h are not shown because no crystalline mineral phases were detected. Note that the increased peak intensity of GR_{SO4} (001) comes from preferential orientation of GR_{SO4} plate-like particles along the [001] zone axis during XRD sample preparation.

X-ray photoelectron spectroscopy (XPS) measurements were performed using a KRATOS Axis Ultra DLD to determine the surface chemistry of the solids. To predict Fe and As speciation and Fe phase stability in the studied system, thermodynamic modeling was carried out using Geochemist's Workbench (GWB)[44] with the MINTEQ thermodynamic database (see Supporting Information Text S-2 for details). Missing thermodynamic data of mineral phases in the Fe−S−H_2O system (e.g., GR_{SO4}) were manually added to the MINTEQ database.[45,46]

RESULTS AND DISCUSSION

Aqueous Behavior and Speciation of Mineral-Bound As Species. The aqueous concentrations of As revealed that barely any As was released (<0.15%, Figure S-1) during the Fe^{2+}-induced transformation of As(V)-bearing FH to GT ± GR. This is consistent with the high uptake capacity of synthetic iron (oxyhydr)oxides for As species determined in the adsorption experiments (Figure S-2). Similar minimal As

release (<1%) was also reported in previous Fe^{2+}-catalyzed transformation experiments of As(V)-bearing ferrihydrite[39,47] and As(V)/Sb(V)-bearing jarosite.[45,46] Moreover, it has also been shown that As removal efficiencies were even higher in experiments wherein As was coprecipitated with iron (oxyhydr)oxides compared to those adsorbed onto presynthesized iron (oxyhydr)oxides.[39,48,49]

The oxidation state of As associated with the solids after 24 h of reaction as probed by As K-edge XANES (Figure 1a) showed that the initial FH-bound As(V) was partially reduced to As(III) when the initial As(V)-bearing FH reacted with aqueous Fe^{2+} under anoxic conditions. The degree of As(V) reduction slightly increased from 33.6 ± 1.8% to 42.4 ± 1.8% as the $Fe^{2+}_{(aq)}/Fe(III)_{solid}$ ratio increased from 0.5 to 2 (see Table 1). This trend was also confirmed by high-resolution XPS of the final solids (Figure 1b), which showed the presence of a shoulder at a binding energy of ~44 eV, indicative of As(III) (see Table S-3 for As reference binding energies). Due to the uncertainty of the XPS measurements (see Table S-4), a fully quantitative determination of the As(III) contents was
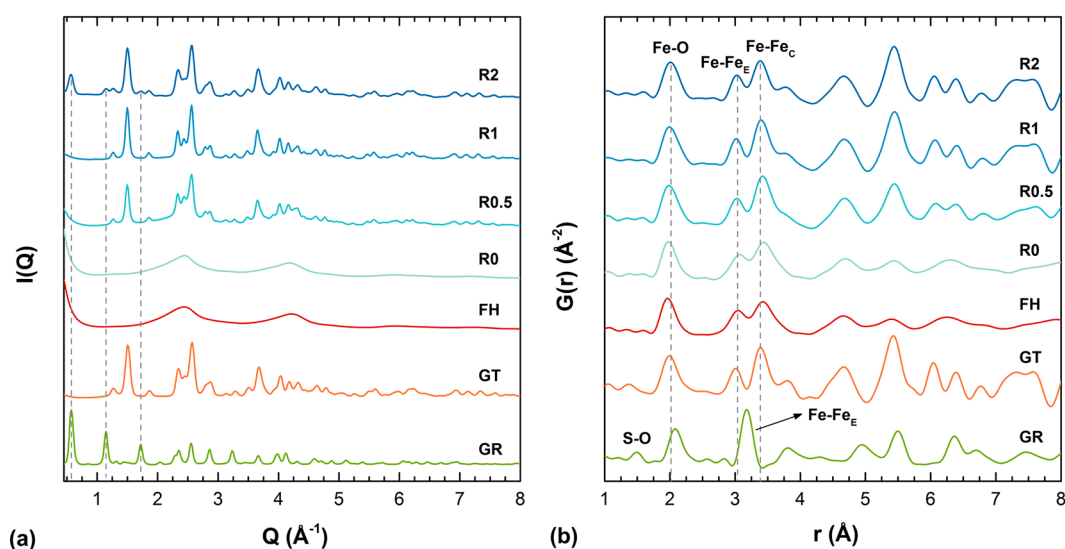
Figure 3. High-energy X-ray scattering data of the end-products after the 24 h transformation of As(V)-bearing FH at varying $Fe^{2+}_{(aq)}/Fe(III)_{solid}$ ratios (R): (a) high-energy XRD patterns $[I(Q)]$. GR (00*l*) reflections in the R2 end-product are indicated by gray dashed lines, while all the other peaks in the transformation end-products can be assigned to GT (except for the R0 end-product, which is naturally still pure As(V)-bearing FH). The patterns of the reference materials (i.e., FH, GT, and GR) are shown for comparison; and (b) PDFs $[G(r)]$ of the low *r*-value region showing the short-range structure of the solids. The full PDFs are shown in Figure S-4. Fe–Fe$_E$ and Fe–Fe$_c$ refer to edge- and corner-sharing pairs, respectively.
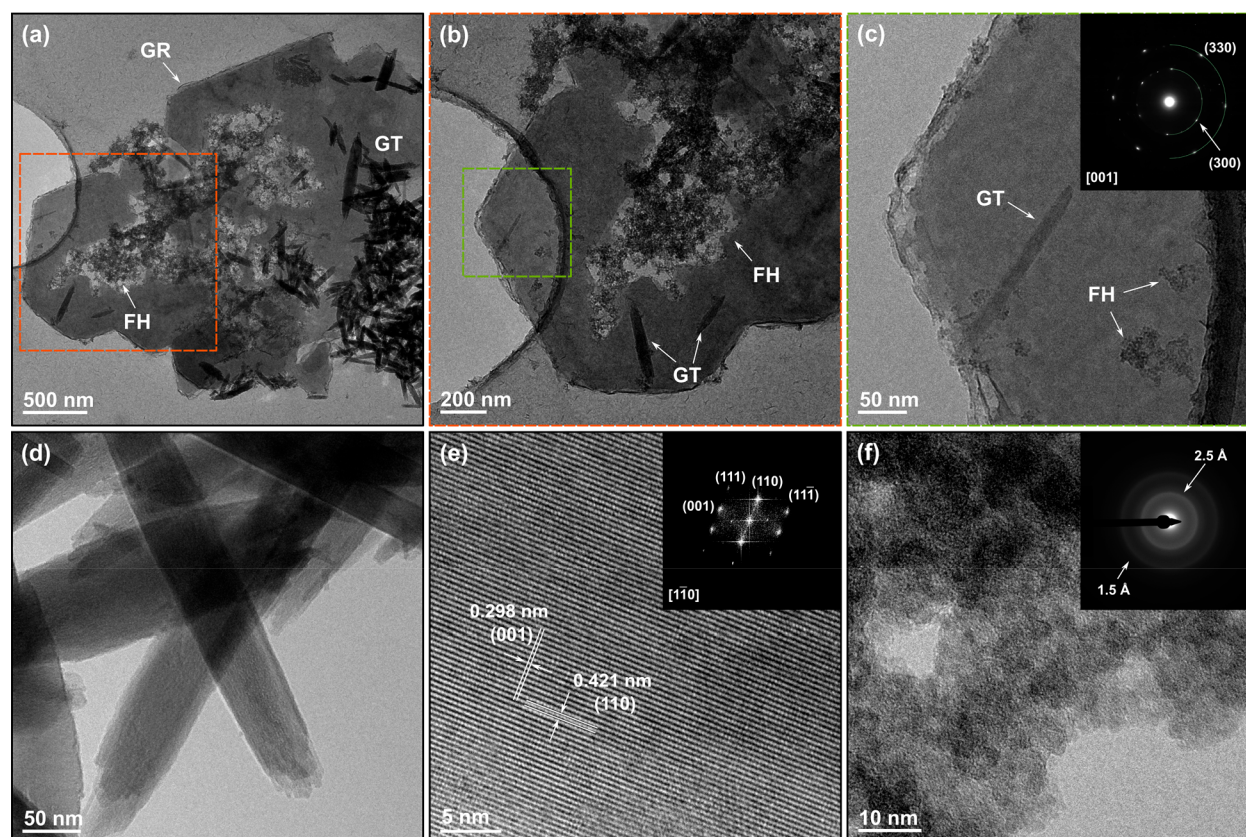
Figure 4. TEM images of Fe phases following the 24 h transformation of As(V)-bearing FH at $Fe^{2+}_{(aq)}/Fe(III)_{solid}$ ratio of 2: (a) overview showing the close association between GR$_{SO4}$ (dark gray, >300 nm wide hexagonal platelets), GT (ca. 50 nm wide black rods), and unreacted FH (aggregates of ~3 nm sized particles); (b) blow-up of the orange marked area in (a); (c) GR$_{SO4}$ particle seen in green marked area in (b) with the SAED pattern in inset; (d) GT nanorods and the corresponding (e) HRTEM image with the fast Fourier transformation (FFT) pattern in the inset showing the lattice fringes for (001) and (110) planes of GT (in *Pbnm* spacegroup); (f) As(V)-bearing FH nanoparticles with the SAED pattern in the inset. The SAED pattern of GR$_{SO4}$ was indexed according to the proposed structure of Christiansen et al.[56]
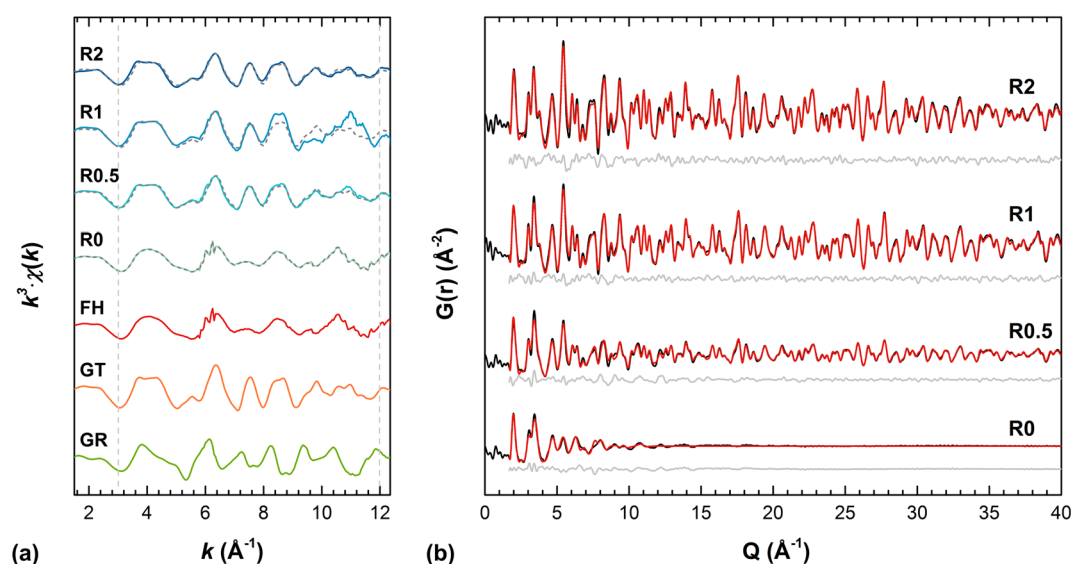
Figure 5. (a) k^3-weighted $\chi(k)$ Fe K-edge EXAFS spectra of transformation end-products following the 24 h transformation of As(V)-bearing FH with varying $Fe^{2+}_{(aq)}$ concentrations ($Fe^{2+}_{(aq)}/Fe(III)_{solid}$ ratios from 0 to 2). Fits (gray dashed lines) are least-squares linear combinations of the reference materials (i.e., lower three patterns FH, GT, and GR_{SO4}). Fit boundaries are indicated by the vertical dashed lines (k-range = 3–12 Å^{-1}). (b) Fits of PDFs of same end-products ($Fe^{2+}_{(aq)}/Fe(III)_{solid}$ ratio from 0 to 2). The black curves represent the experimental data, whereas red and light gray curves represent the calculated pattern and the residuals. Details of the fitting method for Fe K-edge EXAFS and PDF conducted in Athena[57] and PDFgui[58] can be found in Supporting Information Text S-9.

difficult, but XPS confirmed its presence. Furthermore, XPS analyses showed that the initial As(V) was still the primary valence state in the near surface region (top 10 nm of the samples). A possible reduction of As(V) due to X-ray beam damage is negligible as shown by analysis of the control (R0).

Thermodynamic calculations based on the Eh-pH conditions used in our experiments (Figure S-3) suggest that, at equilibrium, all initially adsorbed As(V) species should have been reduced to As(III) during the transformation. The partial reduction of As(V) to As(III) after 24 h observed in our data is likely a result of kinetic limitations since it might take longer time scales for full reduction.

Mineralogical Transformation of As(V)-Bearing FH. In the absence of aqueous Fe^{2+}, the As(V)-bearing FH did not transform to other iron (oxyhydr)oxides (R0, Figure 2a). While barely any As was released during the reactions, exposure of the initial As(V)-bearing FH to varying aqueous Fe^{2+} concentrations led to its rapid transformation into more crystalline iron (oxyhydr)oxides. At $Fe^{2+}_{(aq)}/Fe(III)_{solid}$ ratios of 0.5 and 1 (R0.5 and R1, Figure 2b,c, respectively), goethite (GT) formed within the first hour and dominated the pattern over the remaining 24 h. Small amounts of green rust sulfate (GR_{SO4}) and lepidocrocite (LP, only in R0.5) also formed in the R0.5 and R1 experiments. However, both phases dissolved, as supported by aqueous Fe^{2+} release (Figure S-1), which then precipitated as goethite after 2 h. At an $Fe^{2+}_{(aq)}/Fe(III)_{solid}$ ratio of 2 (R2, Figure 2d), both GT and GR_{SO4} formed rapidly within the first 30 min but both also remained present throughout the 24 h of reaction.

The high energy XRD pattern $[I(Q)]$ of the mineral end-products (Figure 3a) corroborated the laboratory-based XRD data (Figure 2), with the main end-product being GT and with some GR_{SO4} forming at the highest tested $Fe^{2+}_{(aq)}/Fe(III)_{solid}$ ratio of 2. The broad humps at Q-values of ~2.4 and ~4.2 Å^{-1} for R0.5 and, in part, R1 stem from unreacted FH, the presence of which was not unexpected in the end-product material

because previous studies[50−52] have shown that As can slow down the transformation of FH to crystalline iron (oxyhydr)-oxides. The PDF analyses (Figures 3b and S-4) were used to derive the characteristic interatomic distances in the mineral-end products. The atomic pair correlations at r-values < 4 Å (Figure 3b) correspond to the atomic arrangements in the Fe−O polyhedra in iron (oxyhydr)oxides. The first peak at ~2.0 Å matches first neighbor Fe−O pairs, while peaks at ~3.0 and ~3.4 Å represent edge- and corner-sharing Fe−Fe pairs (Fe−Fe$_E$, Fe−Fe$_C$), respectively. Changes in peak positions and intensities for these Fe−Fe pairs are a consequence of the presence of mixed iron (oxyhydr)oxides (i.e., GT, FH ± GR_{SO4}) in these solids, when compared with the standard materials (spectra labeled GT, FH, and GR in Figure 3a,b).

TEM and SEM analyses of the transformation end-products confirmed that GT was the main product with FH still present in all experiments after 24 h. As shown before with XRD and PDF, GR_{SO4} was only present in reactions with $Fe^{2+}_{(aq)}/Fe(III)_{solid}$ = 2 (Figures 4a, S-5, and S-6). GR_{SO4} was identified by its thin hexagonal plate-like particles (Figure 4b),[33,53,54] GT by its distinctive crystalline nanorod (Figure 4d), and FH by its ~3 nm-sized particle aggregates (Figures 4f and S-5). SEM images of the end-products also revealed that particle lengths of the GT nanorods gradually decreased with increasing $Fe^{2+}_{(aq)}/Fe(III)_{solid}$ ratios (Figures S-6 and S-7). Both TEM and SEM images confirmed that GT was the dominant mineral phase in all experiments (Figures 4a, S-5, and S-6) and that FH was closely associated with GT and GR_{SO4} (Figure 4a,b). It is important to note that, often, FH was observed to seemingly "fill" voids in GR_{SO4} particles (Figures 4a,b and S-5c). Such features could indicate that the GR_{SO4} particles were still forming from the As(V)-bearing FH precursor after 24 h, or that the formed GR_{SO4} crystals are dissolving from the center, as previously suggested by Skovbjerg et al.[55] However, dissolution of the GR_{SO4} from the exposed crystal edges (Figure 4c) cannot be excluded.

From the evaluation of the Fe K-edge EXAFS and PDF data (Figure 5, Table 1), we determined the relative amounts (% mol Fe) of the reaction transformation end-products. The Fe K-edge EXAFS data (Figure 5a) confirmed GT ($\geq$84%) as the main mineral phase in all Fe^{2+}-spiked experiments, with GR only accounting for ~5% in the system with $Fe^{2+}_{(aq)}/Fe(III)_{solid}$ = 2. The EXAFS fitting revealed that the amount of remnant As(V)-FH after 24 h was inversely proportional to the Fe^{2+} concentration added to the As(V)-bearing FH. Interestingly, the amount of As(V)-FH derived from the PDF data (Figure 5b) followed a similar trend to the EXAFS data, but unreacted FH could not be identified in the R2 end-product PDF pattern. This was most likely due to its low relative amount in the sample (from EXAFS $\approx$ 11%). However, the biggest difference in the relative phase amounts between PDF and EXAFS fitting was seen in the R0.5 end-product. PDF indicates ~70% FH compared to ~16% from the EXAFS evaluation, which naturally also impacted the proportion of GT in this sample. Upon closer inspection, PDF of the R0.5 end-product (Figure 3b) seems to lack the characteristic GT features observed in R1 and R2 samples. For example, the small but sharp peak at $r \approx 3.8$ Å is missing, and both the peak at 5.5 Å and the double peaks at 6−6.5 Å are also poorly developed. Thus, the bonding environment at ~3.8 to ~7 Å does not exactly resemble GT. From this, we suspect that there is a short-range distortion in the Fe octahedra that is uncharacteristic of GT. This results in the large discrepancy between the PDF and EXAFS Fe phase quantification. Despite the variation between the calculated proportions of Fe phases from EXAFS and PDF data, and considering both experimental, analytical, and fitting uncertainties, the results show that both the extent of FH transformation to GT and/or GR increases as the $Fe^{2+}_{(aq)}/Fe(III)_{solid}$ ratios increase.[27]

Overall, the compositions of the mineral end-products as determined with XRD, PDF, TEM, SEM, and EXAFS at the end of the 24-h Fe^{2+}-induced As(V)-bearing FH transformation are consistent with each other and also match the predicted phases from thermodynamic calculations for the Fe−S−H$_2$O system (Figure S-8).

Mechanism of As(V)-Ferrihydrite Transformation and As Redox Transformation. Iron redox cycling in subsurface environments highly impacts the mobility and toxicity of As in contaminated sediments and groundwaters. Specifically, mineral transformations involving iron (oxyhydr)oxides are important since, especially under reducing conditions, such transformation reactions can change the oxidation state of mineral-associated As, which in turn controls As toxicity as well as the extent to which As will be sorbed by minerals. Thus, such reactions may not only release As back into the environment, but these processes could render As to be present in the more toxic form.

Our results demonstrated that the initial As(V)-bearing FH rapidly transforms to GT and to a lesser extent to GR$_{SO4}$ and lepidocrocite upon the addition of Fe^{2+} (Figure 2). We also showed that the transformation rate of FH increased with increasing $Fe^{2+}_{(aq)}/Fe(III)_{solid}$ ratios. This is seen, for example, by the appearance of crystalline Fe phases already after 30 min in experiments with an $Fe^{2+}_{(aq)}/Fe(III)_{solid}$ ratio of 2 (Figure 2d), compared to 1 h at lower ratios or in the lower relative abundance of FH in the end-products at higher $Fe^{2+}_{(aq)}/Fe(III)_{solid}$ ratios (Figure 5). Furthermore, the absence of LP at $Fe^{2+}_{(aq)}/Fe(III)_{solid}$ ratios >0.5 indicates that the transformation was very fast because LP formation requires low

levels of FH-surface-adsorbed Fe^{2+}.[17,39,45] Moreover, the smaller GT nanorods obtained at higher $Fe^{2+}_{(aq)}/Fe(III)_{solid}$ ratios (Figure S-6) indicate faster FH transformation rates because higher nucleation rates lead to smaller crystals.

GR$_{SO4}$ formed under all tested conditions alongside with GT, but disappeared already after 2 h at lower $Fe^{2+}_{(aq)}/Fe(III)_{solid}$ ratios (<2), and it transformed into the thermodynamically more stable GT (Figure 2b,c). At $Fe^{2+}_{(aq)}/Fe(III)_{solid}$ = 2, GR$_{SO4}$ remained throughout the reaction as expected based on previous Fe^{2+}-induced FH transformation experiments where a similar $Fe^{2+}_{(aq)}/Fe(III)_{solid}$ ratio was employed without the addition of As.[28,29,59] However, in contrast to the As-free FH experiments, which only formed GR, the R2 end-products in the current study also contained FH and GT. Arsenic species have been shown to hinder iron (oxyhydr)oxide transformations.[30,45,60] Thus, the incomplete conversion of As(V)-bearing FH into GT and/or GR$_{SO4}$ (Figures 4 and 5) is likely a consequence of crystallite poisoning by the surface-bound As species. Specifically, As species have been shown to inhibit Fe−O−Fe polymerization, thereby inducing distortions in the Fe bonding environment and inhibiting crystal nucleation and growth.[50−52]

The solid-state characterization results and electron microscopy images further suggest that GR$_{SO4}$ formed independently of GT during the Fe^{2+}-induced transformation of As(V)-bearing FH. The XRD data (Figure 2) document the rapid and simultaneous occurrence of GT and GR$_{SO4}$ in the early stages of transformation and thus suggest that both Fe phases formed directly from FH. This is also supported by the calculated Gibbs free energies ($\Delta G_{rxn}°$), which showed that the formation of GR$_{SO4}$ is more thermodynamically favored from a FH precursor (Table 2, eq 2) compared to GT (Table 2, eq 3). Moreover, the added Fe^{2+} rapidly hydrolyzed, as evidenced by

Table 2. Calculated Gibbs Free Energies ($\Delta G_r°$) at 25 °C

	chemical reaction	$\Delta G_{rxn}°$ (kJ mol^{-1})[a]
	Mineral Formation	
1	$Fe^{III}(OH)_3 \rightarrow \alpha\text{-}Fe^{III}OOH + H_2O$	−20.4
2	$4Fe^{2+} + 2Fe^{III}(OH)_3 + SO_4^{2-} + 6H_2O \rightarrow Fe^{II}_4Fe^{III}_2(OH)_{12}SO_4 + 6H^+$	124.2
3	$4Fe^{2+} + 2\alpha\text{-}Fe^{III}OOH + SO_4^{2-} + 8H_2O \rightarrow Fe^{II}_4Fe^{III}_2(OH)_{12}SO_4 + 6H^+$	598.4
	Redox Reactions	
4	$Fe^{II}_4Fe^{III}_2(OH)_{12}SO_4 + 2H_2As^VO_4^- \rightleftharpoons 6\alpha\text{-}Fe^{III}OOH + 2As^{III}(OH)_3 + SO_4^{2-} + 2H_2O$	−122.2
5	$Fe^{II}_4Fe^{III}_2(OH)_{12}SO_4 + 2HAs^VO_4^{2-} + 2H^+ \rightleftharpoons 6\alpha\text{-}Fe^{III}OOH + 2As^{III}(OH)_3 + SO_4^{2-} + 2H_2O$	−202.0
6	$Fe^{II}_4Fe^{III}_2(OH)_{12}SO_4 + 2H_2As^VO_4^- + 4H_2O \rightleftharpoons 6Fe^{III}(OH)_3 + 2As^{III}(OH)_3 + SO_4^{2-}$	0.2
7	$Fe^{II}_4Fe^{III}_2(OH)_{12}SO_4 + 2HAs^VO_4^{2-} + 4H_2O + 2H^+ \rightleftharpoons 6Fe^{III}(OH)_3 + 2As^{III}(OH)_3 + SO_4^{2-}$	−79.6
8	$2Fe^{2+} + H_2As^VO_4^- + 3H_2O \rightleftharpoons 2\alpha\text{-}Fe^{III}OOH + As^{III}(OH)_3 + 3H^+$	21.4
9	$2Fe^{2+} + HAs^VO_4^{2-} + 3H_2O \rightleftharpoons 2\alpha\text{-}Fe^{III}OOH + As^{III}(OH)_3 + 2H^+$	−18.5
10	$2Fe^{2+} + H_2As^VO_4^- + 5H_2O \rightleftharpoons 2Fe^{III}(OH)_3 + As^{III}(OH)_3 + 3H^+$	62.2
11	$2Fe^{2+} + HAs^VO_4^{2-} + 3H_2O \rightleftharpoons 2Fe^{III}(OH)_3 + As^{III}(OH)_3 + 2H^+$	22.3
12	$2Fe^{2+} + H_2As^VO_4^- + 3H^+ \rightleftharpoons 2Fe^{3+} + As^{III}(OH)_3 + H_2O$	23.2
13	$2Fe^{2+} + HAs^VO_4^{2-} + 4H^+ \rightleftharpoons 2Fe^{3+} + As^{III}(OH)_3 + H_2O$	−16.7

[a]Values calculated from the standard Gibbs free energies ($\Delta G_f°$) of minerals and aqueous species (Table S-6).

the quick decrease in aqueous Fe^{2+} concentration (Figure S-1a), and thus the simultaneous formation of GT and GR_{SO4} from FH is likely. The formation of GT from FH is well documented,[24,27,61] while the formation pathways and mechanisms of GR phases from other iron (oxyhydr)oxides are far less studied.[28,59] Sumoondur et al.,[29] however, reported a similar observation wherein GR_{SO4} formed directly from pure FH (no As added, $Fe^{2+}_{(aq)}/Fe(III)_{solid}$ ratios of 0.5 to 2) within the first 10 min of the Fe^{2+}-catalyzed transformation reaction as monitored by synchrotron-based *in situ* time-resolved energy dispersive X-ray diffraction.

During the transformation reaction of the As(V)-bearing FH a minor initial release of As (<0.15%, Figure S-1b) from its surface was observed. The initial As release is a result of the dissolution of FH, which can have surface areas up to 850 m^2 g^{-1},[3] and the formation of GT and GR phases, which both have lower surface areas. This released As was quickly adsorbed by the newly formed GT and/or GR particles (Figure S-1b). However, the possibility of incorporation of As into the structure of GT cannot be ruled out, especially since the ionic radius of As(V) is similar to tetrahedrally coordinated Fe,[1] although such phenomenon has not yet been documented.[39]

A more relevant finding of this study is that the initial As(V) was partially reduced to As(III) during the Fe^{2+}-induced transformation of As(V)-bearing FH, and this reduction (i.e., As(III)/As(V) ratio) increased with increasing $Fe^{2+}_{(aq)}/Fe(III)_{solid}$ ratio. Based on the calculated $\Delta G_{rxn}°$ values (Table 2, eqs 4−7), the most thermodynamically feasible reductant in the Fe−As−S−H$_2$O system is GR_{SO4}, yet no study to date has been able to document such reduction of As(V) to As(III) by GR.[41,62,63] Moreover, the formation and stability of the GR in the experiments R0.5 and R1 were substantially lower compared to the R2 experiment (Figure 2). This suggests that another redox couple may have induced As(V) reduction. The most likely candidate is the surface-associated Fe^{2+} and GT redox couple (Table 2, eqs 8−9), which has been shown to reduce other groundwater contaminants such as carbon tetrachloride,[64] nitrobenzene,[65,66] and chromate.[67] The surface-associated Fe^{2+}-GT redox couple might also explain why As(V) reduction was only observed at high Fe^{2+} concentrations during the Fe^{2+}-catalyzed transformation of As(V)/Sb(V)-jarosite ([Fe(III)$_{jarosite}$ = 21.8 mM, [$Fe^{2+}_{(aq)}$] = 0 to 20 mM, As/Fe$_{solid}$ = 0.003).[45] These authors noted that, in their experiments, LP was the dominant mineral phase at low Fe^{2+} concentrations, while GT was the primary end-product (with minor GR_{SO4}, <10%) at higher Fe^{2+} concentrations.

It must be noted, however, that As(V) reduction has not been observed previously upon interaction with Fe^{2+}-activated synthetic GT (e.g., Amstaetter et al.[68]), who examined the interactions at a $Fe^{2+}_{(aq)}/Fe(III)_{solid}$ ratio of 0.03, which is approximately 15 to 55 times lower than the ratios used in this study. Since the reduction reaction is driven by Fe^{2+} concentration, the low Fe^{2+} concentration used in their study could explain why they did not observe any As(V) reduction to As(III) in their system. However, a question arises whether As(V) could be reduced to As(III) at lower $Fe^{2+}_{(aq)}/Fe(III)_{solid}$ ratios and $Fe(III)_{FH}$ loadings similar to those reported by Pedersen et al.[39] and Masue-Slowey et al.,[40] especially since the mineralogical composition of the end-products is different from what we observed in our study.

Overall, these redox transformations have important implications for the mobility and toxicity of As. The partial reduction of As(V) to As(III), as documented in this study, is an unexpected and also detrimental consequence as such reduction results in the generation of far more toxic and mobile As species.[69] On the positive side, the sorption capacities of these Fe mineral phases toward As species is very high, and therefore, we observed no significant As release. Noteworthy, however, is the fact that invariably real subsurface environments are significantly more complex. The presence of many different mineral substrates and the variation in mineral sorption capacities will be affected by Eh/pH conditions[70] and the presence of other inorganic ions[33,69] (e.g., silicate and phosphate anions) or organic ligands[71−74] all competing with As for active surface sites and influencing the mechanisms and pathways of Fe (oxyhydr)oxide transformation.

■ CONCLUSION

In subsurface environments, iron-bearing mineral transformations can massively impact the mobility and toxicity of contaminants since these mineral phases serve as toxic element sinks that can control and even prevent release and further transport contaminants in soils and groundwaters. In this study, we followed the transformation of As(V)-bearing ferrihydrite, catalyzed by aqueous Fe^{2+}, under anoxic conditions as it converts to more crystalline iron (oxyhydr)-oxides. Higher Fe^{2+} concentrations resulted in the formation of both GT and GR phases, while lower Fe^{2+} concentrations led to a GT end-product. However, at all the tested conditions, the conversion of ferrihydrite was incomplete, and our data indicate that this was a consequence of As surface complexation. Analyses of the mineral-bound As species also revealed partial reduction of initial As(V) to As(III), although no significant release of As was observed during the transformation. Overall, our results highlight the need to understand such intertransformations among iron (oxyhydr)oxide in subsurface environments where aqueous Fe^{2+} is present as it will impact As sequestration, mobilization, and transport.

■ ASSOCIATED CONTENT

ⓢ Supporting Information

The Supporting Information is available free of charge on the ACS Publications website at DOI: 10.1021/acsearthspace-chem.9b00031.

> Detailed information on mineral characterization and analytical techniques, additional mineral characterization data (TEM, SEM, XAS, PDF), XPS reference data, and thermodynamic calculations (PDF)

■ AUTHOR INFORMATION

Corresponding Author
*E-mail: jpperez@gfz-potsdam.de.
ORCID ⊙
Jeffrey Paulo H. Perez: 0000-0002-0256-0576
Dominique J. Tobler: 0000-0001-8532-1855
Jörg Radnik: 0000-0003-0302-6815

■ REFERENCES

(1) Cornell, R. M.; Schwertmann, U. *The Iron Oxides: Structure, Properties, Reactions, Occurrences and Uses*, 2nd ed.; Wiley-VCH Verlag GmbH & Co. KGaA: Weinheim, FRG, 2003.

(2) Karimian, N.; Johnston, S. G.; Burton, E. D. Iron and sulfur cycling in acid sulfate soil wetlands under dynamic redox conditions: A review. *Chemosphere* 2018, 197, 803–816.

(3) Jambor, J. L.; Dutrizac, J. E. Occurrence and constitution of natural and synthetic ferrihydrite, a widespread iron oxyhydroxide. *Chem. Rev.* 1998, 98 (7), 2549–2586.

(4) Cornell, R. M. The influence of some divalent cations on the transformation of ferrihydrite to more crystalline products. *Clay Miner.* 1988, 23 (3), 329–332.

(5) Vu, H. P.; Shaw, S.; Brinza, L.; Benning, L. G. Crystallization of hematite (α-Fe$_2$O$_3$) under alkaline condition: The effects of Pb. *Cryst. Growth Des.* 2010, 10 (4), 1544–1551.

(6) Vu, H. P.; Shaw, S.; Brinza, L.; Benning, L. G. Partitioning of Pb(II) during goethite and hematite crystallization: Implications for Pb transport in natural systems. *Appl. Geochem.* 2013, 39, 119–128.

(7) Brinza, L.; Vu, H. P.; Shaw, S.; Mosselmans, J. F. W.; Benning, L. G. Effect of Mo and V on the hydrothermal crystallization of hematite from ferrihydrite: An *in situ* energy dispersive X-ray diffraction and X-ray absorption spectroscopy study. *Cryst. Growth Des.* 2015, 15 (10), 4768–4780.

(8) Brinza, L.; Vu, H. P.; Neamtu, M.; Benning, L. G. Experimental and simulation results of the adsorption of Mo and V onto ferrihydrite. *Sci. Rep.* 2019, 9 (1), 1365.

(9) Schwertmann, U.; Stanjek, H.; Becher, H. H. Long-term in vitro transformation of 2-line ferrihydrite to goethite/hematite at 4, 10, 15 and 25 °C. *Clay Miner.* 2004, 39 (4), 433–438.

(10) Schwertmann, U.; Murad, E. Effect of pH on the formation of goethite and hematite from ferrihydrite. *Clays Clay Miner.* 1983, 31 (4), 277–284.

(11) Das, S.; Hendry, M. J.; Essilfie-Dughan, J. Transformation of two-line ferrihydrite to goethite and hematite as a function of pH and temperature. *Environ. Sci. Technol.* 2011, 45 (1), 268–275.

(12) Shaw, S.; Pepper, S. E.; Bryan, N. D.; Livens, F. R. The kinetics and mechanisms of goethite and hematite crystallization under alkaline conditions, and in the presence of phosphate. *Am. Mineral.* 2005, 90 (11–12), 1852–1860.

(13) Jang, J.-H.; Dempsey, B. A.; Catchen, G. L.; Burgos, W. D. Effects of Zn(II), Cu(II), Mn(II), Fe(II), NO$_3^-$, or SO$_4^{2-}$ at pH 6.5 and 8.5 on transformations of hydrous ferric oxide (HFO) as evidenced by Mössbauer spectroscopy. *Colloids Surf., A* 2003, 221 (1), 55–68.

(14) Vempati, R.; Loeppert, R. H. Influence of structural and adsorbed Si on the transformation of synthetic ferrihydrite. *Clays Clay Miner.* 1989, 37 (3), 273–279.

(15) Cornell, R. M.; Schneider, W. Formation of goethite from ferrihydrite at physiological pH under the influence of cysteine. *Polyhedron* 1989, 8 (2), 149–155.

(16) Cornell, R. M. Comparison and classification of the effects of simple ions and molecules upon the transformation of ferrihydrite into more crystalline products. *Z. Pflanzenernaehr. Bodenkd.* 1987, 150 (5), 304–307.

(17) Hansel, C. M.; Benner, S. G.; Fendorf, S. Competing Fe(II)-induced mineralization pathways of ferrihydrite. *Environ. Sci. Technol.* 2005, 39 (18), 7147–7153.

(18) Tronc, E.; Belleville, P.; Jolivet, J. P.; Livage, J. Transformation of ferric hydroxide into spinel by iron(II) adsorption. *Langmuir* 1992, 8 (1), 313–319.

(19) Liu, H.; Li, P.; Zhu, M.; Wei, Y.; Sun, Y. Fe(II)-induced transformation from ferrihydrite to lepidocrocite and goethite. *J. Solid State Chem.* 2007, 180 (7), 2121–2128.

(20) Yang, L.; Steefel, C. I.; Marcus, M. A.; Bargar, J. R. Kinetics of Fe(II)-catalyzed transformation of 6-line ferrihydrite under anaerobic flow conditions. *Environ. Sci. Technol.* 2010, 44 (14), 5469–5475.

(21) Kappler, A.; Straub, K. L. Geomicrobiological cycling of iron. *Reviews in Mineralogy and Geochemistry* 2005, 59 (1), 85–108.

(22) Fortin, D.; Langley, S. Formation and occurrence of biogenic iron-rich minerals. *Earth-Sci. Rev.* 2005, 72 (1), 1–19.

(23) Hiemstra, T.; van Riemsdijk, W. H. Adsorption and surface oxidation of Fe(II) on metal (hydr)oxides. *Geochim. Cosmochim. Acta* 2007, 71 (24), 5913–5933.

(24) Gorski, C. A.; Scherer, M. M. Fe^{2+} sorption at the Fe oxide-water interface: A revised conceptual framework. In *Aquatic Redox Chemistry*; Tratnyek, P. G., Grundl, T. J., Haderlein, S. B., Eds.; American Chemical Society: 2011; Vol. 1071, pp 315–343.

(25) Katz, J. E.; Zhang, X.; Attenkofer, K.; Chapman, K. W.; Frandsen, C.; Zarzycki, P.; Rosso, K. M.; Falcone, R. W.; Waychunas, G. A.; Gilbert, B. Electron small polarons and their mobility in iron (oxyhydr)oxide nanoparticles. *Science* 2012, 337 (6099), 1200–1203.

(26) Williams, A. G. B.; Scherer, M. M. Spectroscopic evidence for Fe(II)–Fe(III) electron transfer at the iron oxide–water interface. *Environ. Sci. Technol.* 2004, 38 (18), 4782–4790.

(27) Boland, D. D.; Collins, R. N.; Miller, C. J.; Glover, C. J.; Waite, T. D. Effect of solution and solid-phase conditions on the Fe(II)-accelerated transformation of ferrihydrite to lepidocrocite and goethite. *Environ. Sci. Technol.* 2014, 48 (10), 5477–5485.

(28) Ahmed, I. A. M.; Benning, L. G.; Kakonyi, G.; Sumoondur, A. D.; Terrill, N. J.; Shaw, S. Formation of green rust sulfate: A combined *in situ* time-resolved X-ray scattering and electrochemical study. *Langmuir* 2010, 26 (9), 6593–6603.

(29) Sumoondur, A.; Shaw, S.; Ahmed, I.; Benning, L. G. Green rust as a precursor for magnetite: An *in situ* synchrotron based study. *Mineral. Mag.* 2008, 72 (1), 201–204.

(30) Wang, Y.; Morin, G.; Ona-Nguema, G.; Brown, G. E. Arsenic(III) and arsenic(V) speciation during transformation of lepidocrocite to magnetite. *Environ. Sci. Technol.* 2014, 48 (24), 14282–14290.

(31) Vaughan, D. J. Arsenic. *Elements* 2006, 2 (2), 71–75.

(32) Smedley, P. L.; Kinniburgh, D. G. A review of the source, behaviour and distribution of arsenic in natural waters. *Appl. Geochem.* 2002, 17 (5), 517–568.

(33) Perez, J. P. H.; Freeman, H. M.; Schuessler, J. A.; Benning, L. G. The interfacial reactivity of arsenic species with green rust sulfate (GR_{SO_4}). *Sci. Total Environ.* **2019**, *648*, 1161−1170.

(34) Raven, K. P.; Jain, A.; Loeppert, R. H. Arsenite and arsenate adsorption on ferrihydrite: Kinetics, equilibrium, and adsorption envelopes. *Environ. Sci. Technol.* **1998**, *32* (3), 344−349.

(35) Mamindy-Pajany, Y.; Hurel, C.; Marmier, N.; Roméo, M. Arsenic adsorption onto hematite and goethite. *C. R. Chim.* **2009**, *12* (8), 876−881.

(36) Tang, W.; Li, Q.; Gao, S.; Shang, J. K. Arsenic (III,V) removal from aqueous solution by ultrafine α-Fe_2O_3 nanoparticles synthesized from solvent thermal method. *J. Hazard. Mater.* **2011**, *192* (1), 131−138.

(37) Lin, S.; Lu, D.; Liu, Z. Removal of arsenic contaminants with magnetic γ-Fe_2O_3 nanoparticles. *Chem. Eng. J.* **2012**, *211−212*, 46−52.

(38) Feng, L.; Cao, M.; Ma, X.; Zhu, Y.; Hu, C. Superparamagnetic high-surface-area Fe_3O_4 nanoparticles as adsorbents for arsenic removal. *J. Hazard. Mater.* **2012**, *217−218*, 439−446.

(39) Pedersen, H. D.; Postma, D.; Jakobsen, R. Release of arsenic associated with the reduction and transformation of iron oxides. *Geochim. Cosmochim. Acta* **2006**, *70* (16), 4116−4129.

(40) Masue-Slowey, Y.; Loeppert, R. H.; Fendorf, S. Alteration of ferrihydrite reductive dissolution and transformation by adsorbed As and structural Al: Implications for As retention. *Geochim. Cosmochim. Acta* **2011**, *75* (3), 870−886.

(41) Jönsson, J.; Sherman, D. M. Sorption of As(III) and As(V) to siderite, green rust (fougerite) and magnetite: Implications for arsenic release in anoxic groundwaters. *Chem. Geol.* **2008**, *255* (1−2), 173−181.

(42) Schwertmann, U.; Cornell, R. M. *Iron Oxides in the Laboratory: Preparation and Characterization*, 2nd ed.; Wiley-VCH Verlag GmbH & Co. KGaA: Weinheim, FRG, 2000; p 188.

(43) Atkinson, R. J.; Posner, A. M.; Quirk, J. P. Adsorption of potential-determining ions at the ferric oxide-aqueous electrolyte interface. *J. Phys. Chem.* **1967**, *71* (3), 550−558.

(44) Bethke, C. M. *Geochemical and Biogeochemical Reaction Modeling*; Cambridge University Press: 2010.

(45) Karimian, N.; Johnston, S. G.; Burton, E. D. Antimony and arsenic behavior during Fe(II)-induced transformation of jarosite. *Environ. Sci. Technol.* **2017**, *51* (8), 4259−4268.

(46) Karimian, N.; Johnston, S. G.; Burton, E. D. Antimony and arsenic partitioning during Fe^{2+}-induced transformation of jarosite under acidic conditions. *Chemosphere* **2018**, *195*, 515−523.

(47) Gomez, M. A.; Jim Hendry, M.; Hossain, A.; Das, S.; Elouatik, S. Abiotic reduction of 2-line ferrihydrite: Effects on adsorbed arsenate, molybdate, and nickel. *RSC Adv.* **2013**, *3* (48), 25812−25822.

(48) Asta, M. P.; Cama, J.; Martínez, M.; Giménez, J. Arsenic removal by goethite and jarosite in acidic conditions and its environmental implications. *J. Hazard. Mater.* **2009**, *171* (1), 965−972.

(49) Park, J. H.; Han, Y.-S.; Ahn, J. S. Comparison of arsenic co-precipitation and adsorption by iron minerals and the mechanism of arsenic natural attenuation in a mine stream. *Water Res.* **2016**, *106*, 295−303.

(50) Waychunas, G. A.; Rea, B. A.; Fuller, C. C.; Davis, J. A. Surface chemistry of ferrihydrite: Part 1. EXAFS studies of the geometry of coprecipitated and adsorbed arsenate. *Geochim. Cosmochim. Acta* **1993**, *57* (10), 2251−2269.

(51) Richmond, W. R.; Loan, M.; Morton, J.; Parkinson, G. M. Arsenic removal from aqueous solution via ferrihydrite crystallization control. *Environ. Sci. Technol.* **2004**, *38* (8), 2368−2372.

(52) Rancourt, D. G.; Fortin, D.; Pichler, T.; Thibault, P.-J.; Lamarche, G.; Morris, R. V.; Mercier, P. H. J. Mineralogy of a natural As-rich hydrous ferric oxide coprecipitate formed by mixing of hydrothermal fluid and seawater: Implications regarding surface complexation and color banding in ferrihydrite deposits. *Am. Mineral.* **2001**, *86* (7−8), 834−851.

(53) Freeman, H. M.; Perez, J. P. H.; Hondow, N.; Benning, L. G.; Brown, A. P. Beam-induced oxidation of mixed-valent Fe (oxyhydr)-oxides (green rust) monitored by STEM-EELS. *Micron* **2019**, DOI: 10.1016/j.micron.2019.02.002.

(54) Perez, J. P. H.; Mangayayam, M. C.; Rubio, S. N.; Freeman, H. M.; Tobler, D. J.; Benning, L. G. Intercalation of aromatic sulfonates in 'green rust' via ion exchange. *Energy Procedia* **2018**, *146*, 179−187.

(55) Skovbjerg, L. L.; Stipp, S. L. S.; Utsunomiya, S.; Ewing, R. C. The mechanisms of reduction of hexavalent chromium by green rust sodium sulphate: Formation of Cr-goethite. *Geochim. Cosmochim. Acta* **2006**, *70* (14), 3582−3592.

(56) Christiansen, B. C.; Balic-Zunic, T.; Petit, P. O.; Frandsen, C.; Mørup, S.; Geckeis, H.; Katerinopoulou, A.; Stipp, S. L. S. Composition and structure of an iron-bearing, layered double hydroxide (LDH) − Green rust sodium sulphate. *Geochim. Cosmochim. Acta* **2009**, *73* (12), 3579−3592.

(57) Ravel, B.; Newville, M. ATHENA, ARTEMIS, HEPHAESTUS: Data analysis for X-ray absorption spectroscopy using IFEFFIT. *J. Synchrotron Radiat.* **2005**, *12* (4), 537−541.

(58) Farrow, C. L.; Juhas, P.; Liu, J. W.; Bryndin, D.; Božin, E. S.; Bloch, J.; Th, P.; Billinge, S. J. L. PDFfit2 and PDFgui: Computer programs for studying nanostructure in crystals. *J. Phys.: Condens. Matter* **2007**, *19* (33), 335219.

(59) Usman, M.; Hanna, K.; Abdelmoula, M.; Zegeye, A.; Faure, P.; Ruby, C. Formation of green rust via mineralogical transformation of ferric oxides (ferrihydrite, goethite and hematite). *Appl. Clay Sci.* **2012**, *64*, 38−43.

(60) Su, C.; Puls, R. W. Significance of iron(II,III) hydroxycarbonate green rust in arsenic remediation using zerovalent iron in laboratory column tests. *Environ. Sci. Technol.* **2004**, *38* (19), 5224−5231.

(61) Yee, N.; Shaw, S.; Benning, L. G.; Nguyen, T. H. The rate of ferrihydrite transformation to goethite via the Fe(II) pathway. *Am. Mineral.* **2006**, *91* (1), 92−96.

(62) Wang, Y.; Morin, G.; Ona-Nguema, G.; Juillot, F.; Guyot, F.; Calas, G.; Brown, G. E. Evidence for different surface speciation of arsenite and arsenate on green rust: An EXAFS and XANES Study. *Environ. Sci. Technol.* **2010**, *44* (1), 109−115.

(63) Randall, S. R.; Sherman, D. M.; Ragnarsdottir, K. V. Sorption of As(V) on green rust ($Fe_4(II)Fe_2(III)(OH)_{12}SO_4 \cdot 3H_2O$) and lepidocrocite ($\gamma$-FeOOH): Surface complexes from EXAFS spectroscopy. *Geochim. Cosmochim. Acta* **2001**, *65* (7), 1015−1023.

(64) Amonette, J. E.; Workman, D. J.; Kennedy, D. W.; Fruchter, J. S.; Gorby, Y. A. Dechlorination of carbon tetrachloride by Fe(II) associated with goethite. *Environ. Sci. Technol.* **2000**, *34* (21), 4606−4613.

(65) Stewart, S. M.; Hofstetter, T. B.; Joshi, P.; Gorski, C. A. Linking thermodynamics to pollutant reduction kinetics by Fe^{2+} bound to iron oxides. *Environ. Sci. Technol.* **2018**, *52* (10), 5600−5609.

(66) Gorski, C. A.; Edwards, R.; Sander, M.; Hofstetter, T. B.; Stewart, S. M. Thermodynamic characterization of iron oxide−aqueous Fe^{2+} redox couples. *Environ. Sci. Technol.* **2016**, *50* (16), 8538−8547.

(67) Buerge, I. J.; Hug, S. J. Influence of mineral surfaces on chromium(VI) reduction by iron(II). *Environ. Sci. Technol.* **1999**, *33* (23), 4285−4291.

(68) Amstaetter, K.; Borch, T.; Larese-Casanova, P.; Kappler, A. Redox transformation of arsenic by Fe(II)-activated goethite (α-FeOOH). *Environ. Sci. Technol.* **2010**, *44* (1), 102−108.

(69) Roberts, L. C.; Hug, S. J.; Ruettimann, T.; Billah, M. M.; Khan, A. W.; Rahman, M. T. Arsenic removal with iron(II) and iron(III) in waters with high silicate and phosphate concentrations. *Environ. Sci. Technol.* **2004**, *38* (1), 307−315.

(70) Root, R. A.; Dixit, S.; Campbell, K. M.; Jew, A. D.; Hering, J. G.; O'Day, P. A. Arsenic sequestration by sorption processes in high-iron sediments. *Geochim. Cosmochim. Acta* **2007**, *71* (23), 5782−5803.

(71) Zhou, Z.; Latta, D. E.; Noor, N.; Thompson, A.; Borch, T.; Scherer, M. M. Fe(II)-catalyzed transformation of organic matter−

ferrihydrite coprecipitates: A closer look using e isotopes. *Environ. Sci. Technol.* **2018**, *52* (19), 11142−11150.

(72) Chen, C.; Sparks, D. L. Fe(II)-induced mineral transformation of ferrihydrite−organic matter adsorption and co-precipitation complexes in the absence and presence of As(III). *ACS Earth and Space Chemistry* **2018**, *2* (11), 1095−1101.

(73) Chen, C.; Kukkadapu, R.; Sparks, D. L. Influence of coprecipitated organic matter on $Fe^{2+(aq)}$-catalyzed transformation of ferrihydrite: Implications for carbon dynamics. *Environ. Sci. Technol.* **2015**, *49* (18), 10927−10936.

(74) Hu, S.; Lu, Y.; Peng, L.; Wang, P.; Zhu, M.; Dohnalkova, A. C.; Chen, H.; Lin, Z.; Dang, Z.; Shi, Z. Coupled kinetics of ferrihydrite transformation and As(V) sequestration under the effect of humic acids: A mechanistic and quantitative study. *Environ. Sci. Technol.* **2018**, *52* (20), 11632−11641.

Appendix B: Full Text of Second-author Publications

B.2 Arsenic sequestration in pyrite and greigite in the buried peat of As-contaminated aquifers

Arsenic sequestration in pyrite and greigite in the buried peat of As-contaminated aquifers

12 authors, including:

Hongyan Wang
Karlsruhe Institute of Technology
8 PUBLICATIONS   84 CITATIONS

SEE PROFILE

Jeffrey Paulo H. Perez
Helmholtz-Zentrum Potsdam - Deutsches GeoForschungsZentrum GFZ
18 PUBLICATIONS   110 CITATIONS

SEE PROFILE

Andrew Thomas
Karlsruhe Institute of Technology
10 PUBLICATIONS   26 CITATIONS

SEE PROFILE

Joerg Goettlicher
Karlsruhe Institute of Technology
272 PUBLICATIONS   2,549 CITATIONS

SEE PROFILE

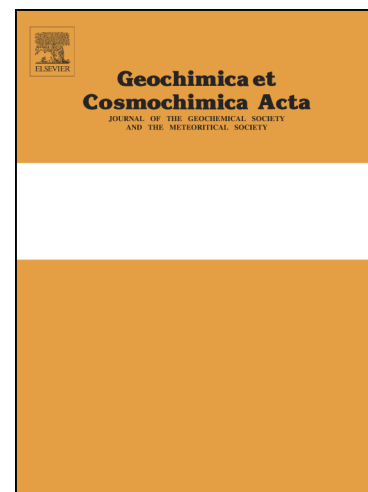Some of the authors of this publication are also working on these related projects:

Project Metabolic Survival Strategies of Iron(II)-oxidizing Bacteria from Freshwater Ecosystems View project

Project Formation kinetics and interfacial reactivities of 'green rust' minerals (Metal-Aid) View project

Journal Pre-proofs

Arsenic sequestration in pyrite and greigite in the buried peat of As-contaminated aquifers

H.Y. Wang, J.M. Byrne, J.P.H. Perez, A.N. Thomas, J. Göttlicher, H.E. Höfer, S. Mayanna, A. Kontny, A. Kappler, H.M. Guo, L.G. Benning, S. Norra

Arsenic sequestration in pyrite and greigite in the buried peat of As-contaminated aquifers

H.Y. Wang[a*], J.M. Byrne[b], J.P.H. Perez[c,d], A.N. Thomas[a], J. Göttlicher[e], H.E. Höfer[f], S. Mayanna[c], A. Kontny[a], A. Kappler[b], H.M. Guo[g], L.G. Benning[c,d], S. Norra[a]

[a]Institute of Applied Geoscience, Working Group of Environmental Mineralogy and Environmental System Analysis, Karlsruhe Institute of Technology (KIT), 76131 Karlsruhe, Germany

[b]Geomicrobiology, Center for Applied Geosciences, University of Tuebingen, 72074 Tuebingen, Germany

[c]GFZ German Research Center for Geoscience, 14473 Potsdam, Germany

[d]Department of Earth Sciences, Freie Universität Berlin, 12249 Berlin, Germany

[e]Institute of Synchrotron Radiation, Karlsruhe Institute of Technology (KIT), 76131 Karlsruhe, Germany

[f]Institute of Geoscience, Goethe University, 60438 Frankfurt, Germany

[g]State key Laboratory of Biogeology and Environmental Geology, China University of Geoscience, 100083 Beijing, China

1

Abstract

Detrital peat (organic carbon-enriched deposit) with high arsenic (As) content is widely distributed in sediments where groundwater As contamination exists. Iron sulfides often persist in these sediments under anoxic conditions. However, the mechanisms and pathways of formation of iron sulfides and its potential contribution in controlling As mobility are still poorly understood. In this study, we examined three As-contaminated peat sediments from the Hetao Basin in China to gain better understanding of the complex interplay between iron sulfides formation and As mobility. We employed high-resolution spectroscopic techniques, including X-ray absorption spectroscopy and ^{57}Fe Mössbauer spectroscopy, coupled with electron microscopy to determine the speciation of iron sulfides and the associated As in the peat sediments.

Pyrite (FeS_2) and metastable greigite (Fe_3S_4) persisted in peat as end-members of S and Fe diagenetic pathways. The Fe-rich phyllosilicates and decaying plant tissues provided the ideal micro-environments for pyrite and greigite nucleation. Pyrite formation most likely occurred via the polysulfides pathway in the surface water-sediments interface during early diagenetic process, while the relative enrichment of reactive Fe compared to sulfide possibly inhibited the transformation of greigite to pyrite in such Fe-rich sediments.

Our results revealed that the peat sediments could act as a stable sink for As immobilization under steady groundwater anoxic conditions, with As content up to 250 mg/kg and large proportions (40 to 60 wt.% As) sequestered in pyrite and greigite. Pyrite crystallites had up to 1 wt.% As content through the replacement of the S^{-I} sites. Greigite crystallites had a relatively constant As content ranging from ~500 to ~1,400 mg/kg. Instead of being adsorbed or structurally incorporated, arsenic formed distinct arsenic sulfide phase in the greigite-enriched sediments, which was analogous to realgar. The transfer of As from iron sulfides to ferrihydrite temporarily retarded As release into

groundwater under slightly oxic groundwater conditions. However, the reductive dissolution of ferrihydrite and potential subsequent As re-release could be a source of As in groundwater under disturbed redox conditions.

Keywords: peat; arsenic; greigite; pyrite; sediment biogeochemistry; early diagenesis

Introduction

Over a hundred million people are exposed to groundwater with high levels of arsenic (As) (> 10 μg/L) globally, particularly in South and Southeast Asia including the Ganges-Brahmaputra-Megha, Red River and Mekong Deltas and the basins belong to the Yangtze and Yellow River catchments (Winkel et al., 2008; Fendorf et al., 2010; Wang et al., 2019 b). It is widely accepted that microbial reduction of Fe (oxyhydr)oxides coupled to organic carbon oxidation causes the release of Fe (oxyhydr)oxides-bound As into groundwater (Nickson et al., 1998; Islam et al., 2004; Guo et al., 2013). The reactivity and availability of organic matter, partitioning of As in solids and the presence of other redox-active species (e.g., NO_3^-, SO_4^{2-}) largely influence As speciation and partitioning between groundwater and solid phases (O'Day et al., 2004 b; Langner et al., 2012; Stuckey et al., 2015 a; Zhu et al., 2017; Smith et al., 2017).

Peat is a heterogeneous mixture of (partly) decayed plant materials that accumulate anaerobically (Naafs et al., 2019). Abundant reactive organic matter provides electrons for the reductive transformation of Fe (oxyhydr)oxides, thereby influencing the behavior of trace elements that are bound onto Fe (oxyhydr)oxides such as As. In the As contaminated aquifers in South and Southeast of Asia, peat formed in Holocene epoch or the last glacial period is widely embedded in the sediments (McArthur et al., 2001; Wang et al., 2018; Wang et al., 2019b). Influence of the buried peat for As mobilization has been extensively discussed in terms of reductive dissolution of Fe(III) (oxyhydr)oxides. On one hand, dissolved organic matter degraded from plants in the peat lenses can be transported to different locations by groundwater flow, stimulate microbial reduction of Fe(III) (oxyhydr)oxides and As(V) reduction and thereby releasing arsenic into groundwater (McArthur et al. 2001, 2004; Anawar et al. 2003; Fendorf et al., 2010). On the other hand, the detrital peat buried in the sediments can serve as a special sink for As. Following the reductive

dissolution of Fe(III) (oxyhydr)oxides and As(V) species, mobilized As(III) species can be subsequently sequestrated by sulfides, with sulfide arising from reduced organic sulfide in peat or microbial reduction of SO_4^{2-} (Stuckey et al., 2015 b; Wang et al., 2018; Knappová et al., 2019). Furthermore, recent research shows that reactive organic thiol groups formed by incorporating inorganic sulfide into organic carbon can adsorb As in contaminated peatlands, providing another sink for As (Langner et al., 2012, 2013; Wang et al., 2018). Therefore, the influence of peat for As behavior is complex and affected by Fe-C-S coupled mineralization pathways. Understanding the diagenetic process in the peat layers and related As speciation are vital to gain better understanding on the influence of peat sediments in As immobilization in contaminated anoxic environments.

Arsenic-Fe sulfides associations are common features in peat layers, and act an important role for As immobilization. Iron sulfides found in the natural sediments mainly include mackinawite (nominally "FeS"), greigite and pyrite (Wilkin and Ford, 2006; Pickard et al., 2017; Knappová et al., 2019). Recent research suggests that Fe sulfides are main As carriers in the detrital peat of As contaminated aquifer in South and Southeast of Asia. For example, arsenic is mainly sequestrated in pyrite found in peat from Mekong River Delta and Bangladesh (Lowers et al., 2007; Stuckey et al., 2015 b; Wang et al., 2018). Several studies have been conducted to study the mechanisms of Fe sulfides formation as well as the adsorption/incorporation behavior of As in the laboratory scale (Benning et al., 2000; Bostick and Fendorf, 2003; Blanchard et al., 2007; Kirk et al., 2010; Le et al., 2017). However, the diagenetic formation process in natural settings and adsorption/incorporation mechanisms for As are still not sufficiently understood because Fe sulfides and related As species are difficult to characterize and quantify due to its oxygen-sensitive nature and poorly crystalline properties.

Based on the assumption that diagenetic process especially Fe sulfides formation in the peat can influence As partitioning in sediments and groundwater, we separated three peat lenses from the sediments of Hetao Basin, an important inland basin draining Yellow river with As contaminated groundwater. Using these, we seek to (1) define the S and Fe diagenetic minerals in peat lenses, (2) investigate As speciation in both peat sediments and specific Fe sulfides, and (3) evaluate the potential role of peat layers in controlling the toxicity and mobility of As in aquifers. The buried peat in the Hetao Basin formed either by over-flowed flood debris or swamps is analogous to other peat formed in As contaminated aquifers in South and Southeast Asia, therefore the research results can be applicable to comparable subsurface environments.

2. Material and Methods

2.1 Field area

The Hetao Basin is a typical inland basin lying in the central part of Inner Mongolia (China) with the Lang Mountains in the North and the Yellow River in the South, covering an area of about 13,000 km^2. In the early time of late Pleistocene (~120 ka) epoch, the Yellow River began to flow through the Hetao paleolake. At the same time, the paleolake started to shrink due to the cooling climate (Jia et al., 2016). Salt marshes as well as oxbow lakes were generated as a result of paleolake shrinkage and frequent movement of the Yellow River channels (Cai et al., 2019), resulting in the accumulation of organic matter. The study site was located in the flat plain of northwestern Hetao Basin which was one of most As contaminated area. The stratigraphy of the late Pleistocene and the Holocene covered a depth around 150 m, whereas the Holocene sediments primarily included alluvial-fluvial sediments with thicknesses of ~10 m (Deng et al., 2009). Further detailed information about the study area such as hydrological conditions were outlined in a previous study (Zhang et al., 2020).

2.2 Sediments collection, bulk geochemistry composition and mineral phase analysis

Two multilevel wells, K1 (41°0′9.00′′N, 106°57′59.20′′E) and K2 (41°1′2.10′′N, 106°57′24.50′′E), were selected in the study area. The wells were drilled in October 2015 by the China University of Geosciences (Beijing) (CUGB) using a circulatory drilling method. After bringing the cores to the surface, they were split into 10 cm sections according to lithology and color variations observed visually, and then capped and placed into N_2-purged Mylar bags. More detailed information about well construction and sediments sampling information has been reported by Zhang et al. (2020). Groundwater samples from different depths (sampling length: 1 m) were collected after the wells were constructed and then analyzed at CUGB. The geochemical and mineralogical composition of the sediments were analyzed at the Karlsruhe Institute of Technology (KIT). Methods for the groundwater sampling, geochemical analysis, and determination of elemental and organic carbon content and isotopic composition are detailed in the supplementary information (**Supplementary text 1**). Methods for mineralogical characterization of magnetically separated minerals, and sequential extractions of Fe-bearing phases in the bulk sediments are shown in the supplementary information (**Supplementary text 2 and Supplementary Table S1**). The magnetic susceptibility measurements of the peat sediments are described in detail in **Supplementary text 3**.
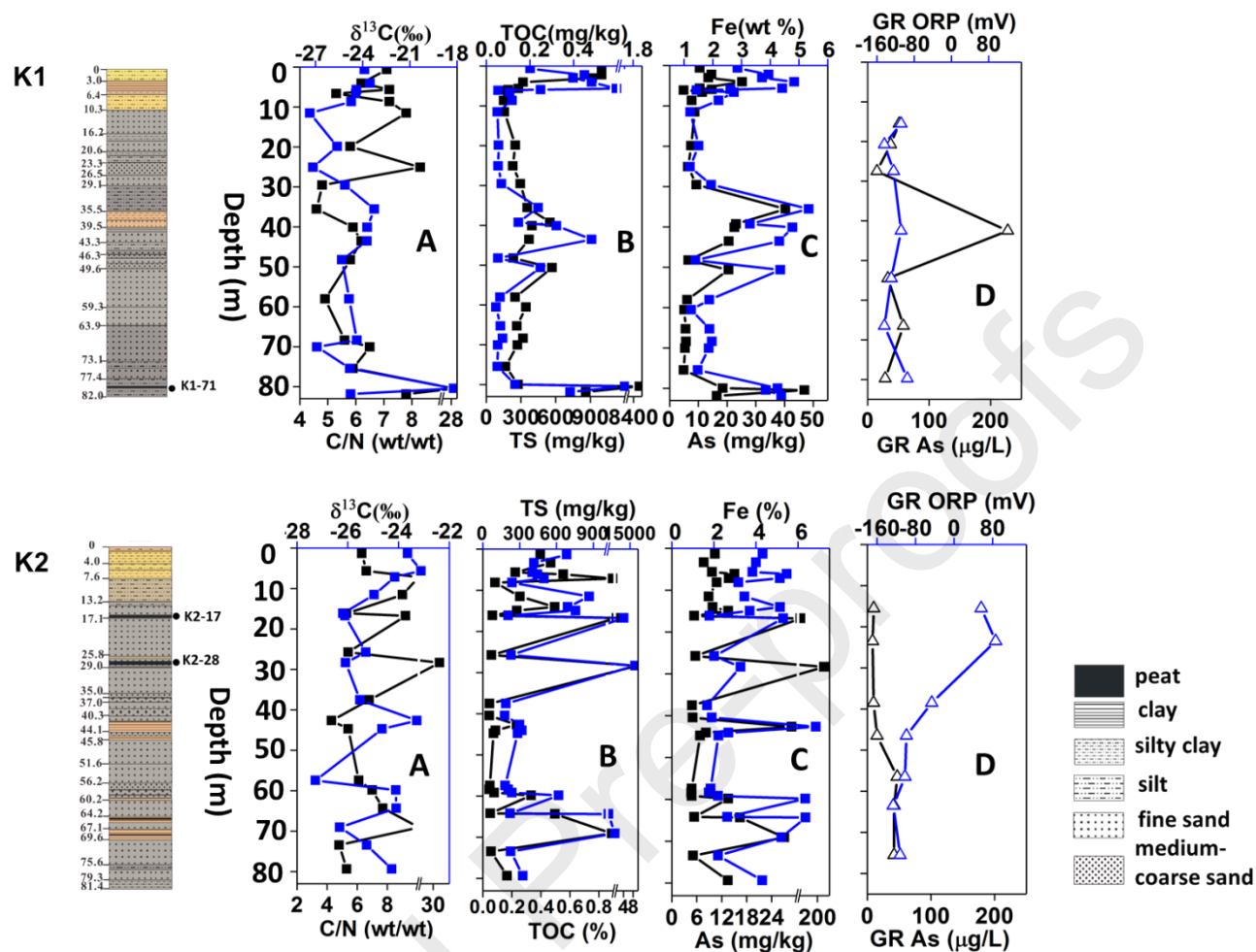
Fig. 1 Lithology and elemental content in the sediments profiles as well as groundwater redox conditions and As concentrations from different depths: (A) Isotope signature of organic carbon (δ^{13}Corg, blue) and ratio of organic carbon to total nitrogen (C/N, black); (B) total sulfur content (TS, blue) and total organic carbon (TOC, black); (C) total Fe (blue) and As content (black); and (D) groundwater redox conditions (GW ORP, blue) and As concentrations (black). Drawing color of the cores represents the visualized sediments colors, layers labeled with black dots (K1-71, K2-17, and K2-28) represent the analyzed peat sediments.

2.3 ^{57}Fe Mössbauer analysis

A section of peat was separated from each intact core for Mössbauer analysis at the University of Tübingen. Inside the glovebox (pure nitrogen atmosphere), dried powders of peat samples were loaded into Plexiglas holders (area 1 cm^2), forming a thin disc. Samples were kept in airtight jars under anoxic conditions at -20 °C until measurement. Holders were inserted into a closed-cycle exchange gas cryostat (Janis cryogenics) under a backflow of He to minimize exposure to air. Spectra were collected at 20 K using a constant acceleration drive system (WissEL) in transmission mode with a ^{57}Co/Rh source. All spectra were calibrated against a 7-μm thick α-^{57}Fe foil that was measured at room temperature. Analysis was carried out using Recoil (University of Ottawa) and the Voigt Based Fitting (VBF) routine (Rancourt and Ping, 1991). The half width at half maximum (HWHM) was constrained to 0.13 mm/s during fitting.

2.4 Scanning Electron Microscopy (SEM) and Electron probe microanalysis (EPMA)

Thin sections for SEM imaging and EPMA analysis were prepared at KIT. A section of peat was separated from intact cores, and embedded in an arsenic free-resin in the glovebox after drying (Araldite, 2020). Sections of 1-mm thickness were cut and polished down to a thickness of 80 μm. Thin sections were stored in the glovebox until analysis.

Carbon-coated thin sections were used for SEM imaging and EPMA analysis. SEM images were acquired at the GFZ German Research Center for Geosciences using a Zeiss Ultra Plus FE-SEM at an acceleration voltage of 3 kV with10 μm aperture distance using an In-lens secondary electron detector. Following mineral observations using SEM, selected particles and areas were analyzed at Goethe University by wavelength spectrometer electron probe microanalysis (EPMA, JEOL 8900). The operating conditions were 20 keV accelerating voltage and 20 nA beam current. Iron, S, Si, Ca, Mg and As concentrations were quantified using peak counting times of 10 s for Fe, S, Si, Ca, Mg, and 60 s for As. The detection limit for As was about 90 mg/kg. For As, S and Fe

9

mapping, pixel size was set to 0.1 μm × 0.1 μm. The analysis volume for particles was approximately 0.2 μm – 0.3 μm based on the Monte Carlo simulations.

2.5 As, S and Fe K-edge X-ray absorption spectroscopic analysis

The speciation and local bonding environment of As, S and Fe in selected peat samples were characterized using X-ray absorption spectroscopy (XAS) analysis at the SUL-X beamline at the ANKA synchrotron radiation facility (KIT). Samples were collected from each peat and ground into powder after drying in the glovebox. A sample mass for Fe K-edge XAS analysis was calculated by the program XAFSmass and mixed with boron nitride (Sigma-Aldrich) prior to analysis (Klementiev, 2012). For As and Fe K-edge XAS analysis, powdered samples were suspended in deoxygenated water in the glovebox, drop-casted onto Kapton tape, and sealed using a second piece of Kapton tape. Arsenic K-edge EXAFS spectra for sample K2-28 was analyzed at the BM23 beamline of the European Synchrotron Radiation Facility (ESRF, Grenoble, France) using the same sample preparation method. For S K-edge XAS measurements, dried peat samples were directly loaded onto the Kapton tape surface. Three scans to 12 scans were collected per sample for each As, Fe and S K-edge XAS spectrum. Data reduction and analysis of XAS spectra were performed using Athena software package (Ravel and Newville, 2005). Experimental and data analysis procedures can be found in the supplementary information (**Supplementary text 4**).

3. Results

3.1 Geochemical composition of peat sediments

Surface sediments (~10 m) from cores K1 and K2 were yellowish to brownish in color and fine-grained with a silt/clay like texture, whereas gray aquifer sediments with interbedded brown/gray clay lenses were found at a depth of ~10 m (K1) and ~14 m (K2) to 82 m (maximum sampled

10

depth) (**Fig. 1**). In borehole K1, a ~5 cm thick black peat band located between 80.4 and 80.5 m (K1-71) was composed of a poorly sorted mixture of fine sand, clay and small amounts of medium sand. In borehole K2, a ~5 cm poorly sorted clay peat band was found at a depth of 16.7 - 16.8 m (K2-17), and a peat layer composed of fine sand and visible detrital plant materials with thickness of at least of 10 cm was observed at a depth of 28.3 - 28.4 m (K2-28).

Arsenic content in the sediments was found to be between 4.7 mg/kg to 40.3 mg/kg (except for the peat layers) with generally higher content found in clay sediments (**Table 1**). Meanwhile, clay sediments had slightly higher Fe content (3.94% in average) than silt (2.86% in average) and sand (1.46 % in average) (**Table 1**). Peat sediments showed significantly higher total organic carbon (TOC) and total sulfur (TS) content, and C/N ratios than in the underlying and overlying sediments (**Fig. 1 and Table 1**). Much higher As content was found in the peat lenses (up to ~ 250 mg/kg) in comparison with other sediments (**Fig. 1 and Table 1**). In comparison with peats K1-71 and K2-17, peat K2-28 had much higher organic matter as well as total S content (**Table 1**).

Table 1 Geochemical compositions of studied peat sediments and comparison with other sediments.

Sample name	Depth (m)	As (mg/kg)	Fe (%)	TOC (%)	TS (mg/kg)	C_{org}/N ratio	$\delta^{13}Corg$ (‰)
K1-71	~ 80.4	46.9	3.85	1.70	8,836	29.1	-18.2
K2-17	~ 16.7	59.2	5.31	1.33	11,020	9.2	-26.1
K2-28	~ 28.3	256	3.27	9.52	155,970	31.6	-26.1
clay/silty clay	-	18.6 ± 8.9	3.94 ± 0.72	0.40 ± 0.20	365 ± 156	5.9 ± 1.2	-23.7 ± 0.5
silt	-	12.0 ± 5.1	2.86 ± 0.70	0.24 ± 0.14	376 ± 265	7.1 ± 2.4	-24.1 ± 0.5
sand	-	6.0 ± 1.4	1.46 ± 0.26	0.06 ± 0.01	163 ± 67	6.2 ± 1.3	-25.7 ± 0.9

3.2 Fe-containing phases in the peat sediments

3.2.1 Fe K-edge XAS and ^{57}Fe Mössbauer analysis

The pre-edge inflection point near 7112 eV and primary inflection point near 7119 eV in the first derivative Fe K-edge XANES spectra suggested that Fe sulfides were abundant in the peat lenses (**Supplementary Fig. S3)** (O'Day et al., 2004 a). The results of Fe K-edge extended X-ray absorption fine structure (EXAFS) linear combination fitting (LCF) revealed that, aside from phyllosilicates (~53% and ~66%), greigite (~23% and ~42%) was the primary Fe-bearing mineral phase in K2-17 and K1-71, respectively. Meanwhile, pyrite (~22%) and ferrihydrite (~17%) in combination with phyllosilicates (~59%) were the dominant Fe-bearing phases in K2-28 (**Fig. 2 a and Table 2**).
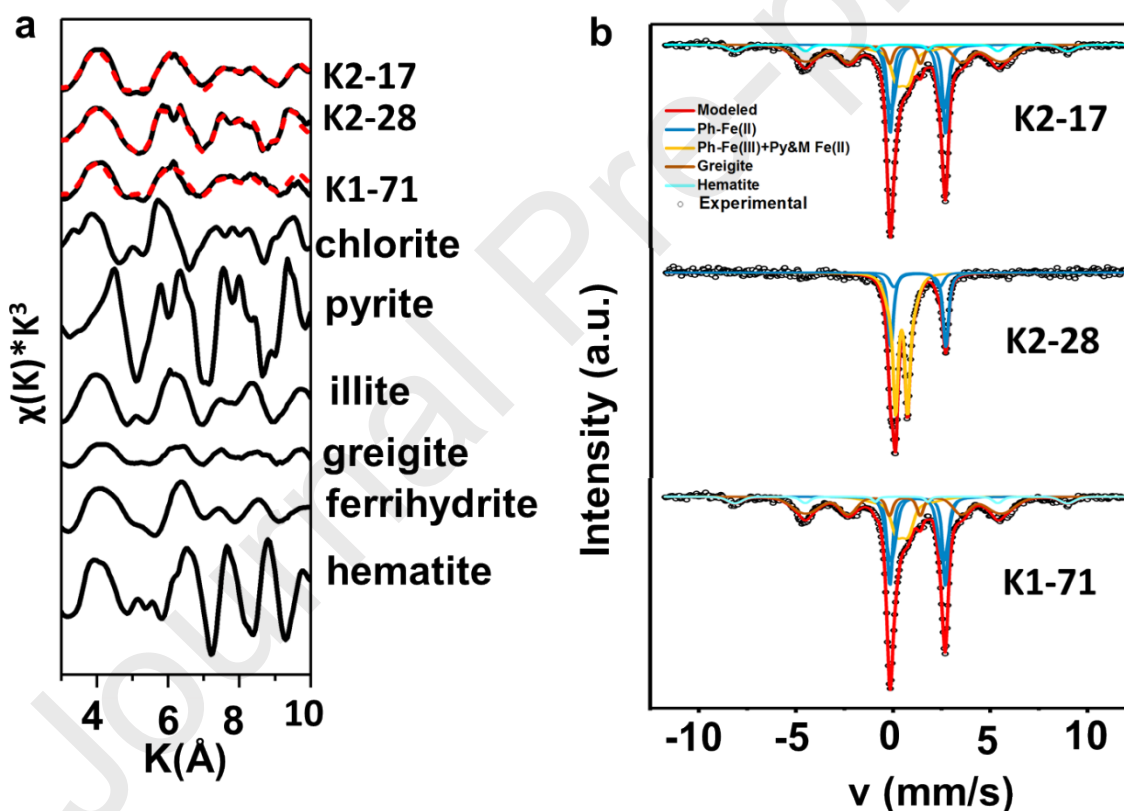

Fig. 2 (a) LCF fitting results of Fe K-edge EXAFS. Black lines represent experimental data for samples and model compound spectra used for fitting, and red dashed lines represent LCF fits. (b)

[57]Fe Mössbauer spectra collected at 20 K for peat sediments, ph: phyllosilicates; py: pyrite; M: mackinawite.

[57]Fe Mössbauer spectroscopy was used to identify Fe-bearing mineral phases as a complementary technique to synchrotron-based Fe K-edge EXAFS (**Fig. 2 b**). The parameters of the narrow sextet in the peat samples K2-17 and K1-71 were typical of greigite (magnetic hyperfine field of 31.2 T and 32.0 T, isomer shift: 0.59 and 0.57, quadrupole shift of 0.00 and -0.04) (Vandenberghe et al., 1992), comprising ~27% and ~30% of the Fe phases, respectively (**Supplementary Table S6**). Differences less than 10% in the greigite component between the Fe K-edge EXAFS and Mössbauer spectroscopy fits in peat sediments K2-17 and K1-71 is considered to be acceptable (Thomas-Arrigo et al., 2014; Chen et al., 2017).

Unfortunately, the similarity of phyllosilicates Fe(III) and pyritic Fe(II) in the Mössbauer spectra at 20 K can result to misidentification of pyrite in peat samples K2-17 and K2-28. However, the Fe K-edge EXAFS spectra of pyrite and phyllosilicates can be easily distinguished (O'Day et al., 2004 a), and these fitting results matched the Mössbauer spectroscopy fits (**Table 2 and Supplementary Table S6**). Furthermore, an expected ferrihydrite sextet in the 20 K Mössbauer spectra was not observed, even in sample K2-28, while Fe (oxyhydr)oxides were detected by Fe K-edge EXAFS. The magnetic ordering temperature of ferrihydrite is strongly dependent on the mineral purity, crystallite size and crystallinity, and as such the absence of a ferrihydrite sextet in the Mössbauer spectra does not necessarily mean that it is absent, as shown using other spectroscopic measurements (Wang et al., 2016). The presence of ferrihydrite in the K2-28 peat sample was further confirmed by measurements of magnetic susceptibility, which decreased in value from -192 ℃ to 0 ℃ (**Supplementary Fig. S2**) (Pannalal et al., 2005).

3.2.2 Texture and morphologies of Fe-bearing phases (SEM-EDX analysis)

13

The Fe-bearing minerals texture and morphologies were evaluated according to SEM-EDX analysis based on the known minerals which were obtained by Fe K-edge XAS and Fe Mössbauer analysis.

Greigite aggregates nucleated in detrital silicates and decaying plant tissues, and less in gypsum/anhydrite (**Fig. 3**). The grain size ranged from ~80 nm to ~500 nm, whereas diverse crystallite habits were observed, including cuboidal, prismatic, and elongated particles. Neoformation of pyrite was also primarily occurred in confined spaces including plant tissues, phyllosilicates grains. The diameters of framboidal pyrites ranged from ~5 μm to ~40 μm (**Fig. 3**). Framboidal crystallites showed either octahedral, cubic (~2 μm in diameter) or spherical crystal habits (~1 μm in diameter). Massive pyrite crystals occurred with octahedral, cubic or irregular habits, with diameters up to ~10 μm. Ferrihydrite was found to be associated with pyrite particles.
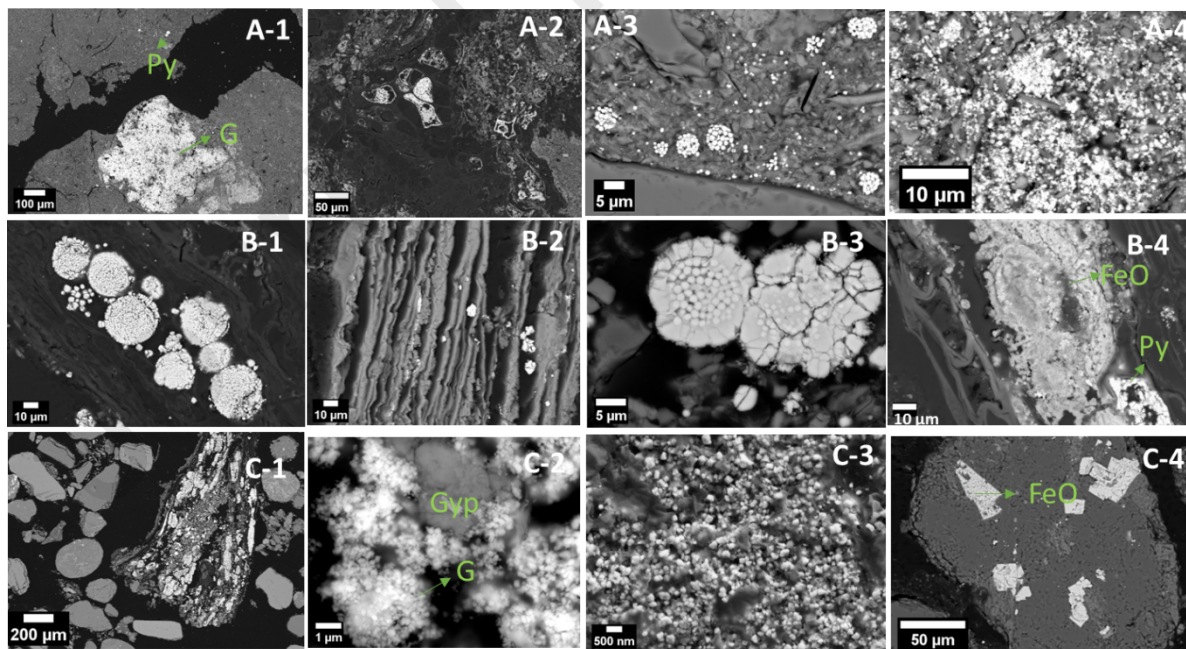
Fig. 3 Representative images of peat samples (A) K2-17, (B) K2-28 and (C) K1-71. (A-1) Representative greigite (G) and framboidal pyrite (Py) areas as indicated. (A-2) Greigite/pyrites nucleation in plant cells. (A-3) and (A-4) Nucleation of pyrites/greigite in phyllosilicates. (B-1) Framboidal and massive pyrites nucleation in plant tissues. (B-2) Massive pyrites nucleation in the phyllosilicates. (B-3) Framboidal pyrites nucleation in phyllosilicates. Overgrowth rims and interior crystallites were visible. (B-4) Mixture of ferrihydrite and pyrites in plant tissues/cells. (C-1) Greigite nucleation in phyllosilicates. (C-2) Greigite (G) nucleation in gypsum/anhydrite (Gyp). (C-3) Scattered electron images to show greigite grains. (C-4) Clastic iron oxides (FeO) in the sediment matrix.

3.3 Sulfur speciation in the peat sediments

Sulfur speciation in the peat sediments was analyzed by S K-edge XANES spectra. Based on the primary white line positions, the presence of reduced organosulfur species can be ruled out since they often have white line positions at > 2472 eV (Manceau and Nagy, 2012).The primary inflection points at ~2469.1 eV and ~2471.1 eV in K2-17 and ~2469.1 eV in K1-71 revealed that inorganic sulfides were the primary sulfur-bearing phases, whereas the pronounced inflection points of ~2471.2 eV and ~2481.6 eV in peat sample K2-28 corresponded to inorganic sulfides and SO_4^{2-} from evaporites, respectively (**Fig. 4**). Iron monosulfide minerals (FeS) were not used in the XANES and XANES first derivative LCF fitting because their characteristic features were not observed in either Fe K-edge XAS analysis or sequential experiments (**Fig.2 a** and **Supplementary Table S2**). Sulfur K-edge first derivative XANES LCF fitting showed that S^{2-} is the dominant S-bearing phase in K1-71 (~93%) and K2-17 (~70%). In sample K2-28, ~30% and ~60% of S was in the form of S^{-1} and zero-valent sulfur (S_0), respectively (**Fig. 4 and Table 2**).
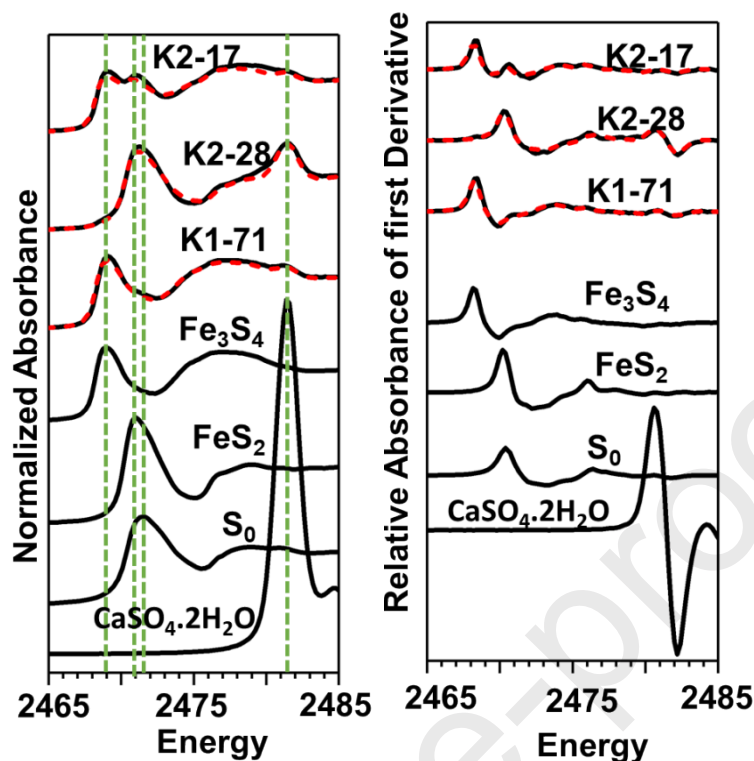
Fig. 4 Results of LCF fitting for S K-edge XANES and first derivative K-edge XANES spectra. Black lines represent experimental data, whereas red dashed lines represent the fits. Green dashed lines represent inflection points of selected model compounds.

3.4 Arsenic speciation and distribution in the peat sediments

3.4.1 As K-edge XAS analysis

The peat sediments of K1-71 and K2-17 both had white line energies near 11870 eV, which most likely indicates As(III) species were coordinated by sulfide (Smith et al., 2005). Arsenian pyrite/arsenopyrite detected in sample K2-17 do not seem to be major sinks for As due to the absence of the associated white line at ~11867.6 eV and the minimal pyrite content (< 5%) (**Fig. 5 A and Table 2**). The first shells of the Fourier-transformed EXAFS spectra of K2-17 and K1-71 were comparable with the As(III)-O bond distance (~1.7 Å), while the second shell was consistent with the As(III)-S bond distance (~2.3 Å) (Bostick and Fendorf, 2003) (**Fig. 5 D**). First

derivative K-edge XANES LCF fitting shows that ~ 40% of As is in the form of As-sulfide compounds in K2-17 and K1-71 while around 50% of As is in the form of arsenite (**Table 2**).

In peat K2-28, two inflection points occurred at ~11868 eV and ~11874 eV (**Fig. 5 A**), suggesting that the sample was mainly composed of arsenopyrite/arsenian pyrite (~11868 eV) and arsenate (~11874 eV). First derivative As K-edge XANES LCF fitting showed that ~61% and ~27% of As was presented as arsenopyrite/arsenian pyrite and As(V) species, respectively (**Table 2**).
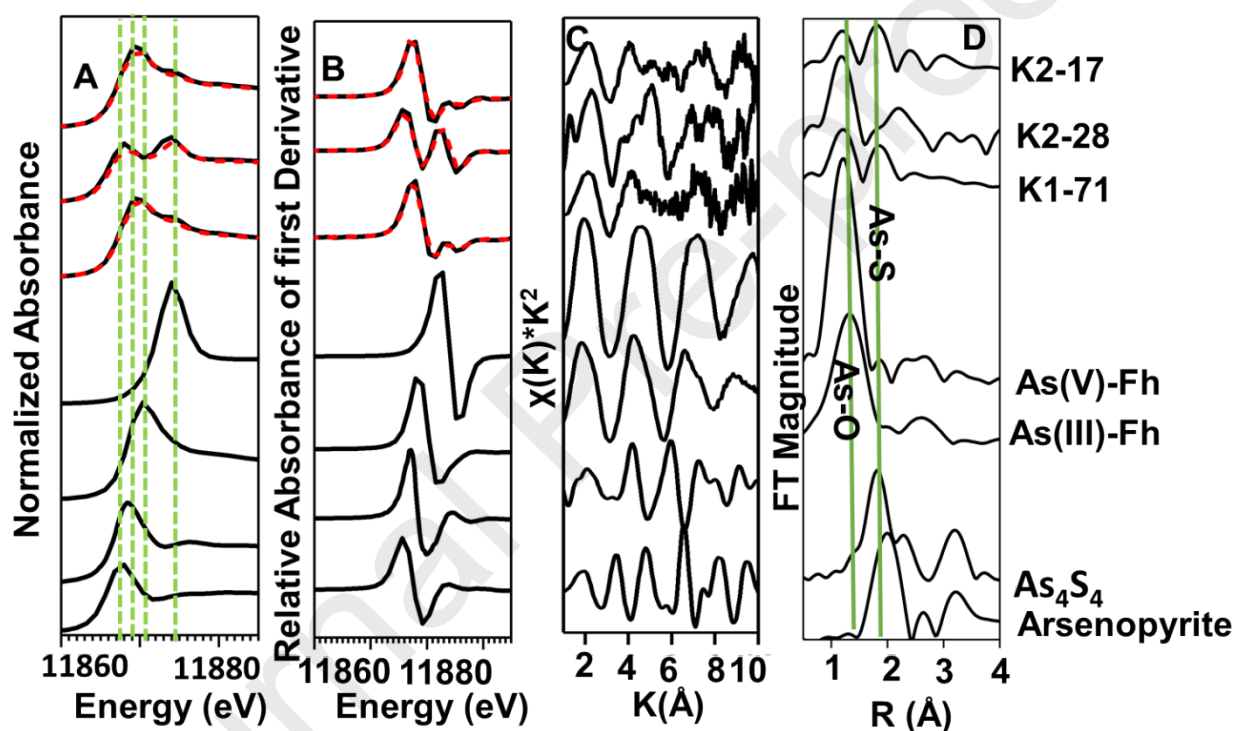

Fig. 5 As K-edge (A) XANES and (B) first-derivative XANES spectra of peat sediments and selected model compounds. The red dashed lines represent fits and the green dashed lines represent inflection points of selected model compounds (i.e., As(III)/As(V) adsorbed onto ferrihydrite, realgar (As_4S_4), arsenopyrite). (C) The k^2 weighted x(k) EXAFS spectra and their corresponding Fourier-transformations (D) The green lines represent the As-O and As-S bonding distances.

17

Table 2 Summary of S, Fe and As K-edge XANES or EXAFS LCF fitting results

Sample	Mineralogical composition (% mol S)				
	XANES first-derivative				
	pyrite	greigite	S_0	$CaSO_4 \cdot 2H_2O$	R^2
K2-17	14 (2.6)	70 (4.1)	15 (3)	1 (0.4)	0.091
K2-28	30 (2.0)	-	61 (2.9)	9 (0.4)	0.039
K1-71	-	93 (1.2)	5 (1.1)	2 (0.3)	0.058

Sample	Mineralogical composition (% mol As)				
	XANES first-derivative				
	realgar	arsenopyrite	As (III)-Fh	As (V)-Fh	R^2
K2-17	47 (6.9)	0 (4.2)	46 (2.1)	7 (1.5)	0.0245
K2-28	8(5.0)	61 (6)	3.8 (2.4)	27 (1.7)	0.0516
K1-71	41 (0.5)	-	50 (1.8)	10 (1.1)	0.0197

Sample	Mineralogical composition (% mol Fe)						
	EXAFS						
	pyrite	greigite	chlorite	illite	hematite	ferrihydrite	R^2
K2-17	3 (0.8)	23 (2.5)	19 (1.5)	47 (3.9)	8 (0.9)	-	0.0469
K2-28	23 (0.9)	-	39 (1.4)	18 (3.1)	-	21 (6.4)	0.0445
K1-71	-	42 (4.5)	24 (2.8)	29 (3.7)	5 (6.8)	-	0.1581

3.4.2 Arsenic content and distribution in pyrite and greigite

Arsenic content of the pyrite and greigite grains was measured by EPMA and summarized in **Table 3**. Arsenic content in the pyrite grains ranged from < 90 mg/kg (detection limit of EPMA) to ~11,000 mg/kg in both K2-17 and K2-28, respectively. Weak linear least squares fit was obtained for the As:S atomic ratio in the pyrite grains ($R^2 = 0.26$) (**Fig. 6**). Framboidal rims with over-grown pyrite crystallites contained more As than the framboid centers evidenced by two framboid measurements (**Supplementary Table S5**). Arsenic distributions in pyrites were heterogeneous, while the spatial distribution of As fluorescence intensities in the framboids showed a different picture compared to S and Fe (**Fig. 7**). Ferrihydrite aggregates had average As content about 4,000 mg/kg, which was comparable with the average As content in pyrite measured using EPMA in peat K2-28 (**Supplementary Table S5**).

Table 3 Arsenic content in pyrite and greigite grains in the peat sediments based on the EPMA analyses.

Sample name	Mineral	S/Fe (avg. atomic %)	Min [As] (mg/kg)	Max [As] (mg/kg)	Average [As] ± SD (mg/kg)	n
K2-17	pyrite	2.00	< 90	11,040	5,205 ± 5,155	8
	greigite	1.24	460	1,380	1,024 ±341	5
K2-28	pyrite	2.00	170	11,450	3,760 ± 3,523	22
K1-71	greigite	1.31	480	1,270	895 ± 321	8

In contrast to pyrite, arsenic had a relatively homogeneous distribution in the greigite grains ranging from 500 to 1,400 mg/kg (**Table 3**). Spatial As distribution was similar to the distribution of S and Fe fluorescence intensities (**Fig. 7**). Unfortunately, the result obtained from EPMA analysis may slightly underestimate the As content in the pyrite and greigite, while the total weight percent of S and Fe is 80% and 93% (on average) for greigite and pyrite, respectively (**Supplementary Table S5**). Except Fe (oxyhydr)oxides and sulfides, Fe-bearing phyllosilicates, especially clay minerals such as illite and chlorite, can also incorporate/adsorb As (Fakhreddine et al., 2015). However, our results showed that the influence from phyllosilicates was limited, as shown by the S/Fe atom ratios of pyrite and greigite which were similar to the stoichiometric ratios (**Table 2**). Furthermore, the distribution patterns of elements including Si, Mg and K, which are the main components of phyllosilicates, do not show any correlations with As distributions (**Supplementary Fig. S4**).
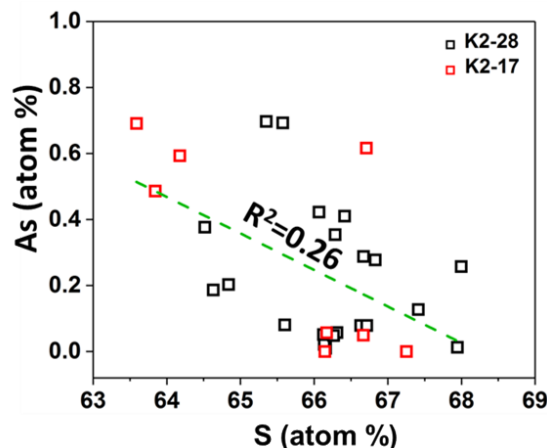
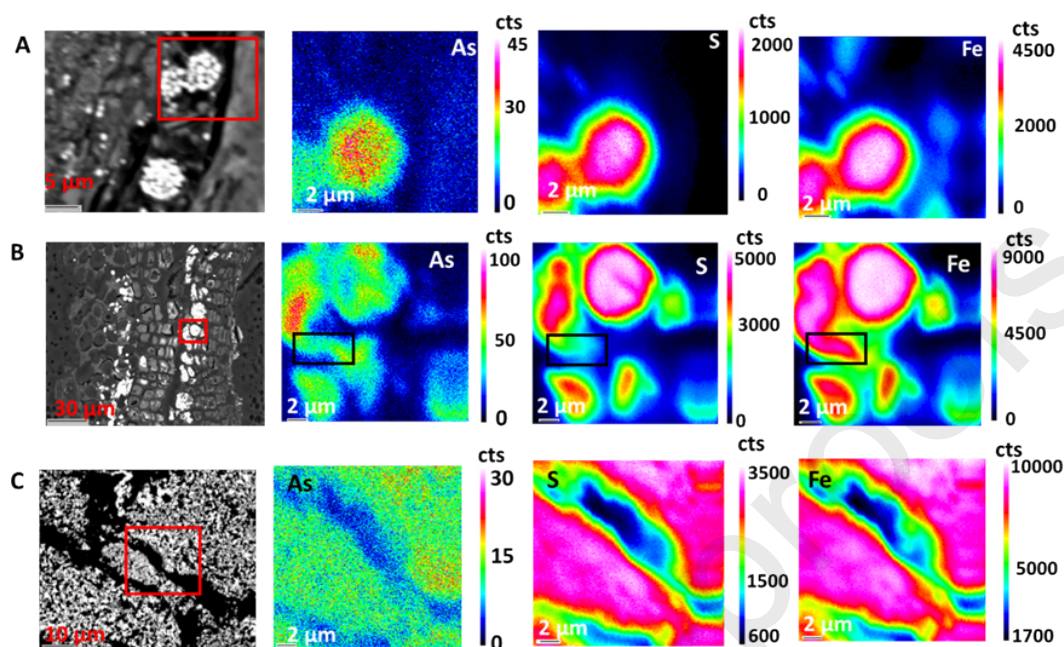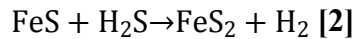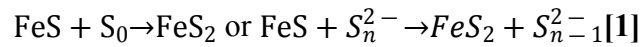**Fig. 6** Sulfur *vs* As atomic ratio measured by EPMA in peat samples.

Fig. 7 Elemental mapping images of S, Fe and As elements obtained by EPMA, mapping area is indicated by red rectangle. (A) Map of framboidal pyrites area in sample K2-17. (B) Map of pyrites area in sample K2-28 which has nucleated in plant tissues, mapping area is indicated by a black rectangle corresponding to ferrihydrite (C) Map of greigite area in sample K1-71.

4. Discussion

4.1 Diagenetic formation of Fe sulfides

The main minerals in the peat sediments include quartz, feldspar, carbonates and clay minerals, which has similar composition with the other sediments in the cores (Wang et al., 2019 a). This suggests that the peat sediments have the same provenance with other sediments. Furthermore, the Fe sulfides found in the peat are likely of authigenic origin which can only be transported via small scales because they are susceptible to oxidation (Lowers et al., 2007). Therefore, the Fe sulfides found in the peat sediments were formed *in situ*.

20

Two proposed mechanisms, which are still under debate, can explain this pyrite formation via mackinawite (nominally "FeS") transformation, either by "FeS" reacting with polysulfides/elemental sulfur (S_0) (**Eq. 1**) or "FeS" reacting with H_2S (**Eq. 2**) (Benning et al., 2000):

$$FeS + S_0 \rightarrow FeS_2 \text{ or } FeS + S_n^{2-} \rightarrow FeS_2 + S_{n-1}^{2-} \textbf{[1]}$$

$$FeS + H_2S \rightarrow FeS_2 + H_2 \textbf{ [2]}$$

Reaction between S_0 precipitates and mackinawite [**eq. 1**] is most likely the dominant mechanism of pyrite formation since large proportions of S_0 (60% of total S) are detected together with pyrite. S_0 could have formed though sulfide oxidation coupled with Fe(III) reduction in such Fe-enriched sediments. Formation of pyrite via the polysulfides/S_0 pathway is typical in the oxic-anoxic transition zone of sediments (Berner, 1970; Neumann et al., 2005; Koeksoy et al., 2019), In the early diagenetic stage, the degradation of organic matter in the saturated water provides electrons for the reductive dissolution of SO_4^{2-} and Fe(III). This is followed by the subsequent precipitation of "FeS" upon saturation of Fe(II) and S(-II), and thereby resulting in the formation of pyrite via "FeS" reacting with S_0. The inhomogeneous framboid and euhedral pyrite sizes distribution could indicate unsteady geochemical conditions (Wilkin et al., 1996, 1997). The overgrowth of framboid, as well as the filled texture, is usually related to the secondary diagenetic growth of pyrite after formation in the surface water-sediment interface during early diagenetic process (Wilkin and Barnes, 1997), and the growth rate is limited by the sulfide supply, which can be constrained by labile organic matter in the sulfidic conditions or availability of SO_4^{2-} in porewater.

Greigite is a metastable iron sulfide mineral that is suggested to form as an intermediate during the oxidative transformation of mackinawite to pyrite (Vasiliev et al., 2008; Rickard and Luther, 2007; Pickard et al., 2017). However, the formation pathway and preservation mechanisms of this

metastable mineral phase are still not fully understood, even though it has been increasingly recognized as an important sedimentary mineral. There have been few studies that show transformation of mackinawite to pyrite can be inhibited in natural sediments settings (Wilkin and Ford, 2006; Holmkvist et al., 2011; Burton et al., 2011). This is the case in one of the peats (K1-71) from Hetao Basin, wherein greigite is shown in the sample. In comparison with pyrite-dominant peats, greigite-dominant peats have less organic matter and sulfur content, whereas the Fe content is comparable. This can be attributed to the likely precipitation of mackinawite which could remove sulfide from the pore water. The excess Fe^{2+} could exhaust sulfide, therefore, preventing polysulfide/S_0 formation and the subsequent transformation of greigite to pyrite. The lower sulfide flux in greigite-dominant layers compared to pyrite-dominant layers can be related to the limited labile organic carbon content or lower SO_4^{2-} concentration. This further emphasizes the importance of polysulfides/S_0 for the transformation of metastable iron sulfide precursors to pyrite under anoxic conditions in natural sediments. However, formation of greigite from a mackinawite precursor also requires an oxidant (Wilkin and Barnes, 1997; Schippers and Jørgensen, 2002; Hunger and Benning 2007). In the surface water-sediments interface, penetration of oxidants such as O_2 and NO_3^- or metabolic activities of the SO_4^{2-} reducing bacteria probably favors the oxidation of FeS into greigite while polysulfides/S_0 is limited (Rickard, 1969; Picard et al., 2018; Mansor et al., 2019).

Phyllosilicates and decaying plant tissues provide the ideal micro-environments for pyrite/greigite nucleation and growth. Reactive Fe^{2+} provided by Fe-rich phyllosilicates via chemical or microbial reduction can induce supersaturation and precipitation of mackinawite on the silicates surface and subsequent transformation into pyrite/greigite. Some sulfate reducing bacteria such as *Desulfovibrio sp.* can reduce organic sulfur species into inorganic sulfides, which can also drive

mackinawite formation in tissues (Alschuler et al., 1983). In addition, plant tissues can provide active surface area and decrease the oversaturation required for Fe sulfide nucleation (Rickard et al., 2007). Since organic sulfur is not detected in the S K-edge XANES spectra (< 5%) of the peat samples, it suggests that microbial reduction of organic sulfur could have provided the inorganic sulfide needed for the formation of the mackinawite precursor. This result is contrary with previous study which has shown that inorganic sulfide is coupled with organic carbon as thiol functional groups, which in turn can sequester metalloids such as As (Langer et al., 2012; Wang et al., 2018). This might be a result of the differences in the ratio of reactive Fe to sulfur. The high abundance of reactive iron can remove inorganic sulfide in such Fe-rich sediments, thereby inhibiting transformation of inorganic sulfide to thiol functional groups.

4.2 Arsenic incorporation into Fe sulfides

Although relatively weakly correlated, the liner relationship between the S and As atomic ratios suggests that As possibly substitutes for S in the crystal structure of pyrite to form arsenian pyrite. The incorporation of As into pyrites is further evidenced by the As K-edge derivative XANES fits. In the pyrite-dominant peat sediments, our XANES data showed that approximate 60% of As exists as As(-I). The pyrite sequestration mechanism for As is consistent with previous studies of pyritic As sequestration mechanisms in natural sediments at low temperatures (Savage et al., 2000; Lowers et al., 2007). Arsenic content in the pyrite particles is between < 90 mg/kg to 11,000 mg/kg with an average value around 5,000 mg/kg, showing that pyrite plays an important role for As sequestration in peat sediments. The similar maximum pyrite As concentrations in sediments from Bangladesh and the Hetao Basin suggests that the maximum As content incorporated into pyrite grains is around 1 wt.% under typical aquifer conditions (Lowers et al.,2007). The heterogeneous distributions of As in pyrite can be related to pyrite growth rates as well as contact time with

porewater. The slightly higher As concentrations found in the framboid over-growth rims as well as massive pyrites could be related to longer crystallization time, leading to enhanced As incorporation from the surrounding pore water into the pyrite structure (Lowers et al., 2007; Neumann et al., 2013). Moreover, the resulting arsenian pyrites are still expected to be able to adsorb pore water As in the form of As(III) or As(V) species, or form As-S precipitates (Bostick and Fendorf, 2003; Qiu et al., 2018). This is consistent with our field observation that As concentration is relatively low in the groundwater with blackish-suspended particles, which likely corresponds to pyrite.

To our knowledge, adsorption and/or incorporation of As by greigite in both lab-scale batch reactions and in engineered and natural aquatic environments are still poorly investigated. The average As content of greigite particles as measured by EPMA, when multiplied by the amount of greigite determined in our samples, is comparable to the fraction of As bound in As sulfide (**Supplementary text 5**). Therefore, our results show that greigite is an important sink for As in the peat sediments with relatively lower S and organic carbon content and is primarily coordinated to sulfur within these particles, which is analogous to realgar evidenced by As K-edge XANES fitting. During greigite formation, oxidation of mackinawite coupled with As(III) species reduction may cause the surface precipitation of greigite and realgar. The findings in our study is consistent with the model predictions by Gallegos et al., (2008), where they argued that the formation of greigite is thermodynamically favorable by the reaction of As(III) species and mackinawite. Realgar and orpiment are also potential As carrier phases in the sulfidic sediments (O'Day et al., 2004 a). However, greigite formation also uses up the available sulfide, therefore limiting As sulfides (i.e., realgar, orpiment) formation. Furthermore, it can also be constrained by relatively

lower As concentrations in the pore water since As sulfide formation needs high porewater As concentration (O'Day et al., 2004 b; Langner et al., 2012).

4.3 Significance of peat sediments for As mobilization process in aquifers

Our study clearly shows that Fe sulfides including greigite and pyrite formed in peat lenses could be important As sinks in contaminated aquifers. Sulfide flux controls Fe sulfides formation, while the sulfide flux would be in turn controlled either by labile organic matter in peat or SO_4^{2-} flux in the SO_4^{2-} limited groundwater (Lowers et al., 2007). In comparison to Fe (oxyhydr)oxides, greigite and pyrite are more thermodynamically stable under these sub-oxic conditions. Therefore, As release caused by reductive dissolution of iron (oxyhydr)oxides would not happen in the groundwater, and competitive adsorption between dissolved phosphate and silica and As on the reactive surfaces of Fe sulfides also cannot occur.

However, oxidation of arsenian pyrite to ferrihydrite-As(V) species can be ongoing process under slightly oxic conditions, as we have observed in the peat layer K2-28 (**Fig. 1**). Transferring As from surface or structure of arsenian pyrite onto ferrihydrite can temporarily retards the As release, which is supported by the similar average As content found in the ferrihydrite and pyrite as well as low As concentrations (< 10 μg/L) in the groundwater (**Fig. 1**). However, ferrihydrite can potentially be reduced under disturbed groundwater redox conditions, which may cause elevated As concentration in the groundwater, since Fe sulfides re-formation is constrained by labile organic carbon. Groundwater redox conditions in draining delta or basins of South and Southeast Asia frequently experience anthropogenic perturbations, as well as seasonal fluctuations (Harvey et al., 2002; Fendorf et al., 2010), making Fe sulfides as an As source with respect to potential As remobilization. In recent years, *in situ* formation of Fe sulfides is suggested to remediate

groundwater As pollution (Keimowitz et al., 2007; Pi et al., 2017). However, it is not suggested to apply it in such naturally unmanaged aquifer.

Previous studies also suggested that reactive organic carbon can be transported to other area by groundwater flow, therefore stimulating As release following by Fe (oxyhydr)oxides and As(V) species reduction (McArthur et al., 2001,2004; Fendorf et al., 2010), but there is no solid evidence to prove that. Our study indicates that the labile organic matter buried in the peat sediments from aquifer can already be exhausted by early diagenetic Fe and S reduction. Our findings are consistent with the results found by Stuckey et al. (2015b), wherein organic matter leached from Mangrove deposits from Mekong delta cannot be able to simulate Fe (oxyhydr)oxides reduction.

5. Summary and Conclusion

Detrital peat formed from swamps or excessive flood debris is common in the As-contaminated aquifer of South and South-east Asia. To investigate the mineral diagenesis and sequestration behavior for As in these organic carbon-rich deposits, three peat lenses were retrieved from two cores with depths up to 80 m in the Hetao Basin.

Simultaneous microbial reduction of organic and inorganic sulfate favored Fe sulfide nucleation in the decaying plant tissues and phyllosilicates. Greigite and pyrite formed in surface water-sediment interface as the diagenetic minerals were stable in peat sediments under anoxic conditions. Excessive Fe(II) compared to sulfide due to lower sulfide flux potentially inhibited pyrite formation in the sulfidic porewater.

Peat sediments show a stable sink for As under steady anoxic conditions with As concentrations up to 250 mg/kg. Pyrite crystallites can have As content up to 11,000 mg/kg, with a majority of the As(-I) substitutes for S(-I) in the pyrite structure. Arsenic content in the greigite grains is

relatively homogeneous, ranging from ~500 to ~1,400 mg/kg. We suggest that As forms distinct As sulfide precipitates in greigite-rich peats, as indicated by our As K-edge XAS data.

Anthropogenic perturbations and seasonal fluctuation of groundwater tables can largely change the groundwater redox conditions, for example, recharge of surface water caused by groundwater extraction infiltrates O_2 into groundwater. The increase of redox potential can induce Fe sulfides (e.g. pyrite and greigite) transfer to Fe (oxyhydr)oxides and temporarily retard As release into groundwater. However, reductive dissolution may in turn release As from the newly-formed iron (oxyhydr)oxide phase, as there is insufficient organic matter for transformation of these phases to Fe sulfide minerals and sequestration of As.

Acknowledgement

Reference

Altschuler, Z.S., Schnepfe, M.M., Silber, C.C., Simon, F.O. (1983) Sulfur diagenesis in Everglades peat and origin of pyrite in coal. *Sci*. **221(4607)**, 221-227.

Anawar, H. M., Akai, J., Komaki, K., Terao, H., Yoshioka, T., Ishizuka, T., Safiullah S., Kato, K. (2003) Geochemical occurrence of arsenic in groundwater of Bangladesh: sources and mobilization processes. *J. Geochem. Explor*. **77(2-3)**, 109-131.

Benning, L. G., Wilkin, R. T., Barnes, H. L. (2000) Reaction pathways in the Fe–S system below 100 ℃. *Chem. Geol*. **167(1-2)**, 25-51.

Berner, R.A., (1970) Sedimentary pyrite formation. *Am. J. Sci*. **268(1)**, 1-23.

Blanchard, M., Alfredsson, M., Brodholt, J., Wright, K., Catlow, C. R. A. (2007) Arsenic incorporation into FeS2 pyrite and its influence on dissolution: a DFT study. *Geochim. Cosmochim. Acta*. **71(3)**, 624-630.

Bostick, B.C., Fendorf, S. (2003) Arsenite sorption on troilite (FeS) and pyrite (FeS2). *Geochim. Cosmochim. Acta*. **67(5)**, 909-921.

Burton, E. D., Johnston, S. G., Bush, R. T. (2011) Microbial sulfidogenesis in ferrihydrite-rich environments: Effects on iron mineralogy and arsenic mobility. *Geochim. Cosmochim. Acta*. **75(11)**, 3072-3087.

Cai, M., Ye, P., Yang, X., Li, C. (2019) Vegetation and climate change in the Hetao Basin (Northern China) during the last interglacial-glacial cycle. *J. Asian. Earth. Sci*. **171**, 1-8.

Chen, C., Kukkadapu, R.K., Lazareva, O., Sparks, D.L. (2017) Solid-phase Fe speciation along the vertical redox gradients in floodplains using XAS and Mössbauer spectroscopies. *Environ. Sci. Technol*. **51(14)**, 7903-7912.

Deng, Y., Wang, Y., Ma, T. (2009) Isotope and minor element geochemistry of high arsenic groundwater from Hangjinhouqi, the Hetao Plain, Inner Mongolia. *Appl. Geochem*. **24(4)**, 587-599.

Fakhreddine S, Dittmar J, Phipps D, et al. (2015) Geochemical Triggers of Arsenic Mobilization during Managed Aquifer Recharge. *Environ. Sci. Technol*. **49(13)**,7802-7809.

Fendorf, S., Michael, H. A., van Geen, A. (2010) Spatial and temporal variations of groundwater arsenic in South and Southeast Asia. *Sci*. **328(5982)**, 1123-1127.

Gallegos, T. J., Han, Y. S., Hayes, K. F. (2008) Model predictions of realgar precipitation by reaction of As (III) with synthetic mackinawite under anoxic conditions. *Environ. Sci. Technol*. **42(24)**, 9338-9343.

Guo, H., Liu, C., Lu, H., Wanty, R. B., Wang, J., Zhou, Y. (2013) Pathways of coupled arsenic and iron cycling in high arsenic groundwater of the Hetao basin, Inner Mongolia, China: An iron isotope approach. *Geochim. Cosmochim. Acta*. **112**, 130-145.

Harvey, C. F., Swartz, C. H., Badruzzaman, A. B. M., Keon-Blute, N., Yu, W., Ali, M. A., Jay J., Beckie R., Niedan V., Brabander D., Oates P. M., Ashfaque K. N., Islam S., Hemond H. F., Ahmed M. F. (2002) Arsenic mobility and groundwater extraction in Bangladesh. *Sci.* **298(5598)**, 1602-1606.

Holmkvist, L., Ferdelman T. G., J□rgensen B. B. (2011) A cryptic sulfur cycle driven by iron in the methane zone of marine sediment (Aarhus Bay, Denmark). *Geochim. Cosmochim. Acta*. 3581-3599.

Hunger, S., Benning, L. G. (2007) Greigite: a true intermediate on the polysulfide pathway to pyrite. *Geochem. Trans*. **8(1)**, 1.

Islam, F. S., Gault, A. G., Boothman, C., Polya, D. A., Charnock, J. M., Chatterjee, D., Lloyd, J. R. (2004) Role of metal-reducing bacteria in arsenic release from Bengal delta sediments. *Nature*. **430(6995)**, 68.

Jia, L., Zhang, X., Ye, P., Zhao, X., He, Z., He, X., Zhou, Q., Li, J., Ye, M., Wang, Z., Meng, J. (2016) Development of the alluvial and lacustrine terraces on the northern margin of the Hetao Basin, Inner Mongolia, China: Implications for the evolution of the Yellow River in the Hetao area since the late Pleistocene. *Geomorphol* **263**, 87-98.

Keimowitz, A. R., Mailloux, B. J., Cole, P., Stute, M., Simpson, H. J., Chillrud, S. N. (2007) Laboratory investigations of enhanced sulfate reduction as a groundwater arsenic remediation strategy. *Environ. Sci. & technol* **41(19)**, 6718-6724.

Kirk, M. F., Roden, E. E., Crossey, L. J., Brealey, A. J., Spilde, M. N. (2010) Experimental analysis of arsenic precipitation during microbial sulfate and iron reduction in model aquifer sediment reactors. *Geochim. Cosmochim. Acta* **74(9)**, 2538-2555.

Klementiev, K. V. (2012) XAFSmass. A program for calculating the mass of XAFS samples.

Knappová, M., Drahota, P., Falteisek, L., Culka, A., Penížek, V., Trubač, J., Mihaljevič M., Matoušek, T. (2019) Microbial sulfidogenesis of arsenic in naturally contaminated wetland soil. *Geochim. Cosmochim. Acta*. **267**, 33-50.

Kocar, B.D., Borch, T., Fendorf, S. (2010) Arsenic repartitioning during biogenic sulfidization and transformation of ferrihydrite. *Geochim. Cosmochim. Acta*. **74(3)**, 980-994.

Koeksoy, E., Sundman, A., Byrne, J.M., Lohmayer, R., Planer-Friedrich, B., Halevy, I., Konhauser, K.O., Kappler, A. (2019) Formation of green rust and elemental sulfur in an analogue for oxygenated ferro-euxinic transition zones of Precambrian oceans. *Geology*. **47(3)**, 211-214.

Langner, P., Mikutta, C., Kretzschmar, R. (2012) Arsenic sequestration by organic sulphur in peat. *Nat. Geosci*. **5(1)**, 66.

29

Langner, P., Mikutta, C., Suess, E., Marcus, M. A., Kretzschmar, R. (2013) Spatial distribution and speciation of arsenic in peat studied with microfocused X-ray fluorescence spectrometry and X-ray absorption spectroscopy. *Environ. Sci. Technol*. **47(17)**, 9706-9714.

Le, P. P., Blanchard, M., Brest, J., Boulliard, J. C., Ikogou, M., Stetten, L., Wang, S., Landort G., Morin, G. (2017) Arsenic Incorporation in Pyrite at Ambient Temperature at Both Tetrahedral SI and Octahedral FeII Sites: Evidence from EXAFS-DFT Analysis. *Environ. Sci. Technol*. **51(1)**, 150-158.

Lowers, H. A., Breit, G. N., Foster, A. L., Whitney, J., Yount, J., Uddin, M. N., Muneem, A. A. (2007) Arsenic incorporation into authigenic pyrite, Bengal Basin sediment, Bangladesh. *Geochim. Cosmochim. Acta*. **71(11)**, 2699-2717.

Manceau, A. and Nagy, K.L. (2012) Quantitative analysis of sulfur functional groups in natural organic matter by XANES spectroscopy. *Geochim. Cosmochim. Acta*. **99**, 206-223.

McArthur, J. M., Banerjee, D. M., Hudson-Edwards, K. A., Mishra, R., Purohit, R., Ravenscroft, P., Cronin A., Howarth R. J.,Chatterjee A, Talukder T., Lowry, D., Houghton S., Chadha D.K (2004) Natural organic matter in sedimentary basins and its relation to arsenic in anoxic ground water: the example of West Bengal and its worldwide implications. *Appl. Geochem.* **19(8)**, 1255-1293.

McArthur, J. M., Ravenscroft, P., Safiulla, S., Thirlwall, M. F. (2001) Arsenic in groundwater: testing pollution mechanisms for sedimentary aquifers in Bangladesh. *Water Resour. Res*. **37(1)**, 109-117.

Mansor, M., Berti, D., Hochella M. F., Murayama M., Xu, J., (2019) Phase, morphology, elemental composition, and formation mechanisms of biogenic and abiogenic Fe-Cu-sulfide nanoparticles: A comparative study on their occurrences under anoxic conditions. *Am. Min.***104 (5),** 703-717.

Naafs, B. D. A., Inglis, G. N., Blewett, J., McClymont E. L., Lauretano V., Xie, S., Evershed, R. P., Pancost, R. D. (2019) The potential of biomarker proxies to trace climate, vegetation, and biogeochemical processes in peat: A review. *Glob Planet Change*, **179**, 57-79.

Neumann, T., Rausch, N., Leipe, T., Dellwig, O., Berner, Z., Böttcher, M.E. (2005) Intense pyrite formation under low-sulfate conditions in the Achterwasser lagoon, SW Baltic Sea. *Geochim. Cosmochim. Acta*. **69(14)**, 3619-3630.

Nickson, R., McArthur, J., Burgess, W., Ahmed, K. M., Ravenscroft, P., Rahmanñ, M. (1998) Arsenic poisoning of Bangladesh groundwater. *Nature*, **395(6700)**, 338.

O'Day, P.A., Rivera Jr, N., Root, R., Carroll, S.A., (2004 a) X-ray absorption spectroscopic study of Fe reference compounds for the analysis of natural sediments. *Am. Mineral.* **89(4)**, 572-585.

O'Day, P. A., Vlassopoulos, D., Root, R., Rivera, N. (2004 b) The influence of sulfur and iron on dissolved arsenic concentrations in the shallow subsurface under changing redox conditions. *Proc. Natl. Acad. Sci.* **101(38)**, 13703-13708.

Pannalal, S.J., Crowe, S.A., Cioppa, M.T., Symons, D.T., Sturm, A. and Fowle, D.A. (2005) Room-temperature magnetic properties of ferrihydrite: A potential magnetic remanence carrier? *Earth Planet. Sci. Lett*. **236(3-4)**, 856-870.

Pi, K., Wang, Y., Xie, X., Ma, T., Liu, Y., Su, C., Zhu, Y., Wang, Z. (2017) Remediation of arsenic-contaminated groundwater by in-situ stimulating biogenic precipitation of iron sulfides. *Water Res*. **109**, 337-346.

Picard, A., Gartman, A., Clarke D. R., Girguis P. R. (2018) Sulfate-reducing bacteria influence the nucleation and growth of mackinawite and greigite. *Geochim. Cosmochim. Acta*. **220**, 367-384.

Pickard D., Mussmann M., Steadman J. A. (2017) Sedimentary Sulfides. *Elements*. **13(2)**, 117-122.

Qiu, G., Gao, T., Hong, J., Luo, Y., Liu, L., Tan, W., Liu, F. (2018) Mechanisms of interaction between arsenian pyrite and aqueous arsenite under anoxic and oxic conditions. *Geochim. Cosmochim. Acta*. **228**, 205-219.

Rancourt, D.G., Ping, J.Y. (1991) Voigt-based methods for arbitrary-shape static hyperfine parameter distributions in Mössbauer spectroscopy. *Nucl. Instrum. Methods Phys. Res*: Beam Interactions with Materials and Atoms. **58(1)**, 85-97.

Ravel, B. and Newville, M.A.T.H.E.N.A. (2005) ATHENA, ARTEMIS, HEPHAESTUS: data analysis for X-ray absorption spectroscopy using IFEFFIT. *J. Synchrotron Radiat*. **12(4)**, 537-541.

Rickard D. T. (1969) The microbiological formation of iron sulfides. *Stockholm Contrib. Geol.* **20**, 49-66.

Rickard D. and Luther G. W. (2007) Chemistry of Iron Sulfides. *Chem. Rev*. **107(2)**, 514-562.

Rickard, D., Grimes, S., Butler, I., Oldroyd, A. and Davies, K.L. (2007) Botanical constraints on pyrite formation. *Chem. Geol*, **236(3-4)**, 228-246.

Savage, K.S., Tingle, T.N., O'Day, P.A., Waychunas, G.A. and Bird, D.K. (2000) Arsenic speciation in pyrite and secondary weathering phases, Mother Lode gold district, Tuolumne County, California. *Appl. Geochem*. **15(8)**, 1219-1244.

Schippers, A., Jørgensen, B.B. (2002) Biogeochemistry of pyrite and iron sulfide oxidation in marine sediments. *Geochim. Cosmochim. Acta*. **66(1)**, 85-92.

Smith, P.G., Koch, I., Gordon, R.A., Mandoli, D.F., Chapman, B.D., Reimer, K.J. (2005) X-ray absorption near-edge structure analysis of arsenic species for application to biological environmental samples. *Environ. Sci. Technol*. **39(1)**, 248-254.

Smith, R. L., Kent, D. B., Repert, D. A., Böhlke, J. K. (2017) Anoxic nitrate reduction coupled with iron oxidation and attenuation of dissolved arsenic and phosphate in a sand and gravel aquifer. *Geochim. Cosmochim. Acta.* **196**, 102-120.

Stuckey, J. W., Schaefer, M. V., Benner, S. G., Fendorf, S. (2015 a) Reactivity and speciation of mineral-associated arsenic in seasonal and permanent wetlands of the Mekong Delta. *Geochim. Cosmochim. Acta*. **171**, 143-155.

Stuckey, J. W., Schaefer, M. V., Kocar, B. D., Dittmar, J., Pacheco, J. L., Benner, S. G., Fendorf, S. (2015 b) Peat formation concentrates arsenic within sediment deposits of the Mekong Delta. *Geochim. Cosmochim. Acta*. **149**, 190-205.

Thomas-Arrigo, L.K., Mikutta, C., Byrne, J., Barmettler, K., Kappler, A., Kretzschmar, R. (2014) Iron and arsenic speciation and distribution in organic flocs from streambeds of an arsenic-enriched peatland. *Environ. Sci. Technol*. **48(22)**, 13218-13228.

Upadhyaya, G., Jackson, J., Clancy, T. M., Hyun, S. P., Brown, J., Hayes, K. F., Raskin, L. (2010) Simultaneous removal of nitrate and arsenic from drinking water sources utilizing a fixed-bed bioreactor system. *Water Res*. **44(17**), 4958-4969.

Vandenberghe, R.E., De Grave, E., De Bakker, P.M.A., Krs, M. and Hus, J.J. (1992) Mössbauer effect study of natural greigite. *Hyperfine Interact*. **68(1-4)**, 319-322.

Vasiliev, I., Franke, C., Meeldijk, J. D., Dekkers, M. J., Langereis, C. G., Krijgsman, W. (2008) Putative greigite magnetofossils from the Pliocene epoch. *Nat. Geosci*. **1(11)**, 782.

Wang, H. Y., Guo, H. M., Xiu, W., Bauer, J., Sun, G. X., Tang, X. H., Norra, S. (2019 a) Indications that weathering of evaporite minerals affects groundwater salinity and As mobilization in aquifers of the northwestern Hetao Basin, China. *Appl. Geochem*. **109**, 104416.

Wang, X., Zhu, M., Koopal, L.K., Li, W., Xu, W., Liu, F., Zhang, J., Liu, Q., Feng, X., Sparks, D.L. (2016) Effects of crystallite size on the structure and magnetism of ferrihydrite. *Environ. Sci.: Nano*. **3(1)**, 190-202.

Wang, Y., Le Pape, P., Morin, G., Asta, M. P., King, G., Bártová, B., Suvorova, E., Frutschi, M., lkogou, M., Cong Pham V.H., Le Vo, P., Herman, F., Charlet, L, Bernier-Latmani B., (2018) Arsenic speciation in Mekong Delta sediments depends on their depositional environment. *Environ. Sci. Technol*. **52(6)**, 3431-3439.

Wang, Y., Pi, K., Fendorf, S., Deng, Y., Xie, X. (2019 b) Sedimentogenesis and hydrobiogeochemistry of high arsenic Late Pleistocene-Holocene aquifer systems. *Earth-Sci. Rev*. **189**, 79-98.

Wilkin, R. T., Arthur, M. A., Dean, W. E. (1997) History of water-column anoxia in the Black Sea indicated by pyrite framboid size distributions. *Earth Planet. Sci. Lett*. **148(3-4)**, 517-525.

Wilkin, R. T., Barnes, H. L., Brantley, S. L. (1996) The size distribution of framboidal pyrite in modern sediments: an indicator of redox conditions. *Geochim. Cosmochim. Acta*. **60(20)**, 3897-3912.

Wilkin, R. T., Ford, R. G. (2006) Arsenic solid-phase partitioning in reducing sediments of a contaminated wetland. *Chem. Geol*. **228(1-3)**, 156-174.

Wilkin, R.T. and Barnes, H.L. (1997) Formation processes of framboidal pyrite. *Geochim. Cosmochim. Acta*. **61(2)**, 323-339.

Winkel, L., Berg, M., Amini, M., Hug, S. J., Johnson, C. A. (2008) Predicting groundwater arsenic contamination in Southeast Asia from surface parameters. *Nat. Geosci*. **1(8)**, 536.

Wolthers, M., Charlet, L., van Der Weijden, C.H., Van der Linde, P.R., Rickard, D. (2005) Arsenic mobility in the ambient sulfidic environment: Sorption of arsenic (V) and arsenic (III) onto disordered mackinawite. *Geochim. Cosmochim. Acta*. **69(14)**, 3483-3492.

Zhang, Z., Guo, H. M., Liu, S., Weng, H. C., Han, S. B., Gao, Z. P. (2020) Mechanisms of groundwater arsenic variations induced by extraction in the western Hetao Basin, Inner Mongolia, China. *J. Hydrol*. **583(124599)**, 1-13.

Zhu, Y. G., Xue, X. M., Kappler, A., Rosen, B. P., Meharg, A. A. (2017) Linking genes to microbial biogeochemical cycling: lessons from arsenic. *Environ. Sci. Technol*. **51(13)**, 7326-7339.